Contribution à la caractérisation non destructive des milieux complexes : Ultrasons diffus et non-linéarité

Cédric Payan

Aix Marseille Université

Contribution à la caractérisation non destructive des milieux complexes : Ultrasons diffus et non-linéarité

Habilitation à Diriger des Recherches

Cédric Payan

Soutenue le 9 juin 2015 à l'IUT Aix Marseille, Aix en Provence

Composition du jury

Gilles Corneloup	Professeur	Aix Marseille Univ., LMA CNRS UPR 7051	Examinateur
Paul Johnson	Directeur de Recherches	Los Alamos National Laboratory (USA)	Président
Jean Kergomard	Directeur de Recherches	LMA CNRS UPR 7051	Examinateur
Philippe Roux	Directeur de Recherches	ISTerre, Grenoble	Rapporteur
Jean Salin	Ingénieur Chercheur	EDF R&D, Chatou	Examinateur
Marco Scalerandi	Professeur	Polytecnico di Torino (Italie)	Rapporteur
Vincent Tournat	Directeur de Recherches	LAUM CNRS UMR 6613	Rapporteur

« A toi »

Léo Ferre

Table des illustrations

Figure 1 : [STE12] Extrait du management du vieillissement des structures en béton 10
Figure 2 : Adapté de [NAG98]. Evolution de la non-linéarité comparée à celle de la vitesse et de l'atténuation des ondes face à un endommagement en fatigue. 11
Figure 3 : Le béton, matériau multi échelle 11
Figure 4 : Effets non linéaires à l'échelle micro et macroscopique 12
Figure 5 : Quantification de la non-linéarité 13
Figure 6 : Phénomènes « non classiques » 14
Figure 7 : Loi de comportement phénoménologique 14
Figure 8 : Dispositif expérimental pour la mesure d'harmoniques 15
Figure 9 : Principe de la mesure de résonance non linéaire 16
Figure 10 : Influence de la géométrie sur la déformation 17
Figure 11 : Evolution de la non-linéarité pour différents états du béton. 18
Figure 12 : Schéma de principe de la mesure quantitative 19
Figure 13 : Compilation des résultats face à un endommagement thermique et corrélation avec la microstructure. 19
Figure 14 : Corrélation entre la non-linéarité et l'aire moyenne de contact entre deux cristaux de gypse. 20
Figure 15 : (a) Schéma de principe expérimental (b) Exemple numérique de focalisation en surface. (c) Forme de la tache focale dans le volume au moment de la focalisation (simulation numérique) 21
Figure 16 : Evolution de la non-linéarité en présence de (a) une fissure provoquée par corrosion et (b) carbonatation à différentes profondeurs. 22
Figure 17 : (a) Focalisation de plus en plus tardive en fonction de l'amplitude dans du béton endommagé à 400°C. (b) Variation relative de vitesse en fonction de l'amplitude pour quatre éprouvettes de béton endommagées thermiquement. 23
Figure 18 : Paramètre non linéaire α en fonction de la profondeur de pénétration pour le jeu complet d'éprouvette. En haut à droite, image issue de mesure de tomographie X de l'éprouvette 400°C, confirmant la présence de fissures (rouge) à l'interface granulat/ciment localisées dans le premier centimètre de profondeur. En vert, schématisation de la non-linéarité mesurée en profondeur. En bas à droite, comparaison de la mesure absolue par retournement temporel avec les mesures quantitatives de résonance. TR = retournement temporel, NRUS = résonance. 23
Figure 19 : Développement Mesures Physiques 24
Figure 20 : Diffusion multiple des ondes dans le béton 25
Figure 21 : (a) Signal ultrasonore diffus. (b) Représentation de la densité spectrale d'énergie en fonction du temps (courbe en pointillés) et la solution lissée (trait plein) selon l'Equation(2) 27
Figure 22 : D'après [TUR96]. Cartographie de la fissure. a) surface latérale de l'éprouvette, b) éprouvette de béton de l'étude c) plan longitudinal central, d) géométrie latérale de la fissure, obtenue par ressuage. 28

Figure 23 : Evolution de l'ATME en fonction de la profondeur d'une entaille (rouge) et d'une fissure réelle (bleu) 29
Figure 24 : Image à un instant donné de l'énergie diffuse dans le béton. (a) Fissure ouverte. (b) Même fissure avec un point de contact entre les lèvres. 30
Figure 25 : Distribution spatiale des contacts le long de la fissure, et évolution de l'ATME en fonction du nombre de points de contact distribués linéairement sur une hauteur totale de fissure de 5 cm 30
Figure 26 : Variation de l'ATME en fonction de la distance à la surface d'un contact de 1 mm de longueur entre les lèvres de fissure 30
Figure 27 : Simulation numérique des fissures exploitées lors des expériences (0, 1, 3 et 5.5 cm). 31
Figure 28 : Variation de l'ATME en fonction de la hauteur de fissure pour une densité de contacts optimisée, comparaison aux résultats expérimentaux. 31
Figure 29 : (a) Dispositif expérimental. (b) Zoom sur la fissure. (c) Schéma de principe de l'acquisition. (d) comportement de la fissure en traction et compression 33
Figure 30 : (a) Signaux expérimentaux. En bleu, les ondes diffuses. En rouge, la basse fréquence. (b) Zoom sur un signal. Estimation de l'ATME et de l'amplitude de la basse fréquence A. 33
Figure 31 : Compilation des résultats pour toutes les éprouvettes. (a) non fissurée. (b) fissure 1cm, (c) 3cm et (d) 5,5cm. Les flèches indiquent le sens de déplacement dynamique qui est le même pour toutes les figures. s est la pente des évolutions. Δt est l'excursion maximale de l'ATME durant un cycle. 34
Figure 32 : Evolution de l'excursion maximale de l'ATME en fonction de la profondeur des fissures 35
Figure 33 : Evolution de la non-linéarité mesurée par modulation sur les mêmes éprouvettes en fonction de la profondeur des fissures 35
Figure 34 : Dispositif de contrôle optique du nuage de microbulles 38
Figure 35 : (a) Dispositif expérimental. (b) exemple de spectre avec (en bas) et sans (en haut) présence de bulle résonante. 39
Figure 36 : Comparaison des histogrammes optiques et acoustiques 39
Figure 37 : (a) Résonateur de Helmholtz employé. (b) Spectre fréquentiel donnant la fréquence de résonance avec (dessous) et sans bulle (dessus). (c) Détermination du taux de vide par le modèle de Wood. 40
Figure 38 : Description du modèle de résonateur diphasique 41
Figure 39 : Courbes de résonances à différentes amplitudes obtenues numériquement sur un nuage de bulles à basse fréquence (à gauche) et expérimentalement sur du grès [Ten98] (à droite) 41
Figure 40 : Courbes de résonances non linéaires pour différents taux de vide obtenus par la fréquence de résonance à faible amplitude (régime linéaire) 42
Figure 41 : (a) Bulle accrochée à un fil. (b) Modulations de temps de vol et d'amplitude des impulsions ultrasonores en fonction de la variation de rayon (c) de la bulle. 43
Figure 42 : Principe de la mesure absolue de rayon en mode continu. En transparence le temps pendant lequel la basse fréquence fait vibrer la bulle. 44

Figure 43 : Rapport des enveloppes et détermination du rayon pour une basse fréquence en mode (a) balayage en fréquence 30kHz-60kHz, (b) continue 60kHz et (c) impulsionnelle. En transparence le temps pendant lequel la basse fréquence est en marche. Pour comparaison, une mesure optique du rayon de la bulle est également effectuée. 44
Figure 44 : Comparaisons entre les mesures de rayon de bulles acoustiques et optiques pour différents types de basses fréquences. 45
Figure 45 : (a) [ADA99] différentes type de défauts dans un joint de colle. (b) Définition d'un bon et mauvais collage 46
Figure 46 : (a) Rupture adhésive. (b) Rupture cohésive. 46
Figure 47 : (a) Dispositif expérimental. (b) Traitement des signaux. (c) Exemple de signatures non linéaires 47
Figure 48 : Signatures non linéaires pour les éprouvettes (a) de référence, (b) avec défaut d'adhésion et (c) défaut de cohésion. 47
Figure 49 : Eprouvettes réalisée selon la norme NF EN 2243-1 48
Figure 50 : (a) Configuration expérimentale et exemple de signaux transmis. (b) Image Cscan ultrasonore correspondante. (c) Faciès de rupture (Al = aluminium, E= Epoxy) 49
Figure 51 : Exemple de surfaces collées corrigées pour deux lots et correction de la contrainte à la rupture. 49
Figure 52 : Echographe Visulasonics Vevo 770 (à gauche). Image de la sonde employée et des chambres de culture remplies de cellules (au milieu). Exemple d'image échographique obtenue (à droite). 50
Figure 53 : (A gauche) Paramètre de non-linéarité en fonction de différents temps d'exposition à l'agent chimiothérapeutique cisplatinum (0, 6, 12, 24 et 48 heures). (A droite) Histogrammes de tailles des cellules mesurés avec un compteur de cellules pour différents temps d'exposition à l'agent chimiothérapeutique. 51
Figure 54 : Triptyque des apports scientifiques développés dans ce manuscrit 55
Figure 55 : [Michele Griffa] Photographie d'une section de béton « modèle » avec des billes de verre comme aggrégats. 56
Figure 56 : Résonance non linéaire pour plusieurs modes de résonance d'un même échantillon et estimation de la déformation volumique et de cisaillement associée. 57
Figure 57 : [VAK05]. A gauche : Mise en évidence du décalage de la fréquence de résonance et de phénomènes d'hystérésis. A droite : retour à l'équilibre après différentes sollicitations. 58
Figure 58 : [REN13] (a) Mise en résonance d'un échantillon et mesure simultanée de la vitesse de propagation. (b) Basse fréquence. (c) Evolution du module élastique obtenu à partir des mesures de vitesses avant, pendant, et après la mise en résonance. 58
Figure 59 : Résultats de la simulation numérique obtenus avec les paramètres physiques issus de [REN13] 59
Figure 60 : Application du retournement temporel à l'échelle d'un mur. 60

SOMMAIRE

Table des illustrations **3**
SOMMAIRE **6**
I. Introduction **7**
II. Elasticité non linéaire : potentiel, limitations et perspectives **10**
1. CND du béton : contexte et problématique 10
2. Elasticité non linéaire : Non-linéarité « classique »/ «non classique » 12
3. Estimation de la non-linéarité « classique » 14
4. Estimation de la non-linéarité « non classique » 16
5. CND du béton par acoustique non linéaire : limitations 17
6. Mesure quantitative globale par résonance non linéaire 18
7. Mesure locale par retournement temporel 20
8. Conclusion 23
III. Ultrasons diffus : tirer parti du « bruit » **25**
1. Motivation : CND du béton par méthodes acoustiques 25
2. Les ultrasons diffus pour le CND du béton 26
3. Caractérisation de fissures réelles 27
4. Simulation numérique de la diffusion 29
5. Ultrasons diffus sous chargement dynamique 32
6. Conclusion 35
IV. Extensions thématiques **36**
1. Introduction 36
2. Les bulles : Engazement du sodium liquide 37
3. Les bulles : mesure absolue de rayon hors résonance 42
4. Caractérisation de l'adhésion 45
5. Le suivi de la mort cellulaire 50
6. Conclusion 52
V. Synthèse, Conclusion et perspectives **53**
1. Synthèse 53
2. Conclusion 55
3. Perspectives 55
VI. Bibliographie **61**
VII. Curriculum Vitae **66**
VIII. Liste des publications **72**
IX. Sélection d'articles internationaux publiés **79**

I. Introduction

Afin de mieux comprendre mes orientations scientifiques, il me semble important de commencer ce manuscrit par un bref historique. Je suis arrivé en 2004 au Laboratoire de Caractérisation Non Destructive (LCND) qui était équipe d'accueil EA3153, rapidement intégré au Laboratoire Universitaire en Evolution CIME (Contrôle Ingénierie MEcanique) jusqu'en 2006, puis de nouveau sous tutelle de l'Université de la Méditerranée jusqu'en 2012. Le LCND est localisé dans les locaux de l'Institut Universitaire de Technologie d'Aix en Provence, département Génie Mécanique et Productique, j'y ai préparé et soutenu un doctorat de Mécanique obtenu en 2007. L'axe de recherche principal du laboratoire, qui en fait un de ses atouts majeurs, est la caractérisation non destructive des matériaux et structures réels. Insistons sur le mot « réel » qui sous-entend la connaissance et la prise en compte du matériau, de sa microstructure, du procédé de fabrication, du contexte (température, environnement, accessibilité) dans lequel la caractérisation ou le contrôle sera réalisé. Cette originalité fait que le LCND est largement reconnu et ses actions de recherches se font en étroite collaboration avec l'industrie (EDF, CEA, SAFRAN, EADS, Saint Gobain …). Depuis 2012, il est intégré au Laboratoire de Mécanique et d'Acoustique (LMA, CNRS UPR7051) au sein de l'équipe Ondes et Imagerie. L'intégration du LCND au LMA est l'occasion de participer à de nouveaux thèmes de recherche comme les ultrasons médicaux, ou la simulation numérique.

En 2004, j'ai eu la chance de choisir mon sujet de thèse, parmi plusieurs thèmes liés à la Caractérisation Non Destructive (CND) du béton proposés par le LCND. Les méthodes issues de l'acoustique non linéaire semblaient prometteuses pour le CND des matériaux homogènes, la transposition au béton était une question ouverte à l'époque. J'ai choisi ce thème toujours un peu par hasard à l'époque. Il me semble important de souligner qu'en 2004, les applications pratiques de l'acoustique non linéaire étaient rares. Les échos de la communauté scientifique à l'époque étaient plutôt pessimistes quant au succès de ces recherches. Cependant, les progrès en termes d'instrumentation depuis les années 2000 ont permis de lever des verrous technologiques rendant « accessibles » les équipements associés.

Ayant rapidement repéré le Los Alamos National Laboratory (LANL) comme leader dans cette thématique appliquée à la géophysique, j'ai contacté Paul Johnson qui a gentiment répondu, nous donnant rendez-vous à Lyon pour la soutenance d'une thèse sur le sujet. J'avais à l'époque quelques difficultés expérimentales. Il m'a alors suggéré d'étudier la « coda » des ondes qui était un thème en vue en géophysique, et m'a invité à la conférence annuelle sur l'élasticité non linéaire qu'il organisait. Deux mois de bibliographie sur le sujet, d'expérimentations, de traitement des données et les premiers résultats (très préliminaires) sont présentés à cette conférence. Depuis, ses visites régulières au LCND tout au long de ma thèse ont permis des avancées rapides et significatives. C'est lui qui m'a poussé à publier mon premier article au « JASA » (Journal of the Acoustical Society of America). Il a enfin été président de mon jury de thèse. Depuis, les collaborations avec le LANL perdurent et s'amplifient. J'y ai effectué un séjour invité de six mois en 2011. Ce séjour fut très enrichissant sur le plan scientifique (et personnel), cela a sans doute été un tournant dans ma

vision et mes orientations scientifique. Les échanges ont perdurés avec l'accueil de Pierre-Yves Le Bas (LANL) au LMA pendant quatre mois en 2013. Nous continuons à travailler en étroite concertation en nous impliquant mutuellement dans les projets de recherches respectifs auxquels nous participons.

Depuis ma thèse, supportée par les projets académiques, l'industrie, et les collaborations internationales, la majorité des avancées scientifiques a été réalisée dans le domaine du CND ultrasonore du béton. Ce thème sera un point central de ce mémoire. Cependant, j'ai également étudié d'autres thématiques qui feront l'objet du dernier chapitre. Il expose l'extension des méthodes associées à des thèmes divers comme la caractérisation des microbulles pour l'industrie nucléaire et la médecine, le CND des joints de colle pour l'aéronautique ou encore le suivi de la mort cellulaire.

L'expertise développée au fil des années, fil conducteur entre tous ces thèmes de recherche, concerne la physique des phénomènes (linéaires ou non) régissant la propagation d'ondes dans les milieux complexes. Au regard du matériau, de sa microstructure, ou du milieu de propagation, je me suis attaché à proposer des pistes pour mieux comprendre la signification des grandeurs mesurées, à développer de nouvelles méthodes permettant de les évaluer et à en déduire des caractéristiques physiques du milieu. Ces différents thèmes sont abordés dans ce manuscrit.

Le premier chapitre expose la motivation de l'utilisation de l'élasticité non linéaire, dont la sensibilité à l'endommagement est désormais avérée, pour le CND du béton. Les fondements physiques sont rappelés ainsi que les phénomènes associés. Physiquement, l'estimation de la non-linéarité dans les milieux comme le béton, nécessite la connaissance de l'état de déformation du milieu. L'estimation de la déformation n'est pas chose simple, ainsi, beaucoup d'études ignorent ce point, ayant pour conséquence de ne proposer que des variations relatives entre un état « endommagé » et un état « sain ». Cette méconnaissance peut même donner lieu à de fausses interprétations. Une méthode globale fondée sur la résonance est exposée. La simulation numérique permet d'estimer la déformation dans le matériau et fournit ainsi des valeurs absolues de non-linéarité. Cette méthode est appliquée au cas de l'endommagement thermique, validée par l'évolution de la microstructure. Une méthode locale, utilisant le principe physique du retournement temporel est employée afin de localiser de l'énergie en un point donné et mesurer la non-linéarité. Le bon accord entre les méthodes globales et locales, confirmée par des données de tomographie X, valide le concept.

Le deuxième chapitre est consacré à la multi-diffusion des ondes élastiques dans le béton. Ce phénomène, souvent traité comme du bruit en CND, est ici mis à profit. La littérature montre que la complexité de la propagation des ondes dans un milieu fortement hétérogène peut être simplifiée et décrite par une équation de diffusion similaire à celle de la chaleur. La diffusion est alors décrite par deux paramètres seulement. Ce concept est ici employé pour caractériser des macro-fissures dans du béton. Les fissures considérées ici sont réelles et leur morphologie est prise en compte dans un modèle numérique afin de valider les observations expérimentales. Les zones partiellement ouvertes le long de la fissure sont visibles. Dans le but d'obtenir des informations sur les zones fermées de la fissure, une méthode de mesure sous chargement dynamique est développée.

Le troisième chapitre expose l'extension des méthodes présentées à d'autres thématiques. La première concerne la caractérisation de microbulles. Les bulles résonantes ont de fortes propriétés non linéaires qui peuvent être mises à profit pour mesurer leur rayon. L'application à la mesure d'histogramme de nuages de bulles poly dispersés est présentée, validée par mesures optiques. Une méthode originale applicable à une bulle unique, mais aussi à n'importe quelle inclusion dans un milieu, est développée. La seconde concerne la transposition des méthodes non linéaires au cas de la caractérisation de joints de colle structuraux avec pour but d'estimer le niveau d'adhésion. Les défauts d'adhésion sont détectés par cartographie des déformations d'un joint sous charge. Le champ de déformation est obtenu pas Cscan ultrasonore haute fréquence. La troisième concerne le suivi de la mort cellulaire suite à une chimiothérapie. Les résultats de suivi dans le temps montrent que les cellules ont une réponse non linéaire accrue au moment de leur fragmentation (analogie avec les fissures dans les solides).

Ce manuscrit est clôturé par une conclusion soulignant l'importance de la prise en compte de la physique des phénomènes. Les outils de simulations numériques utilisés tout au long de ces travaux sont une voie possible. La mise en perspective de ces différents résultats est abordée associée à un projet de recherche permettant de répondre aux questions encore ouvertes : Quelle est l'origine physique de la non-linéarité observée dans le béton, les roches… ? Peut-on théoriquement décrire de façon unifiée l'ensemble des phénomènes observés ? Que reste-t-il à accomplir pour voir un jour ces méthodes appliquées industriellement ?

II. Elasticité non linéaire : potentiel, limitations et perspectives

Collaborations:
Laboratoire : V. Garnier, J. Moysan, N. Chaouch, F. Bouchaala, J.P. Zardan, H. Ramanasse
Los Alamos National Laboratory (LANL, USA): P. Johnson, T.J. Ulrich, P.Y. Le Bas, T.A. Saleh, M.C. Remillieux
Swiss Federal Laboratories for Materials Science and Technology (EMPA, Suisse) : M. Griffa, P. Schuetz
Laboratoire Matériaux et Durabilité des Constructions (LMDC, France) : J.P. Balayssac
EDF R&D : J. Salin
EPRI : M. Guimaraes
Saint Gobain Recherche : I. Berline, G. Counil
Projets/contrats associés : [P3,4,6,7]/[C1,7,9]
Publications internationales associées : [1,4,6,7,15,17,19,20]

1. CND du béton : contexte et problématique

Le contexte concerne l'énergie nucléaire, en France comme dans beaucoup de pays ayant choisi cette source d'énergie. Les centrales arrivant en fin de vie théorique doivent être requalifiées pour continuer à être exploitées. L'Autorité de Sureté Nucléaire demande des garanties quant au potentiel de vie restant de ces ouvrages en béton. Figure 1, la courbe exponentielle des couts de réparation en fonction du temps, donc du taux de dégradation, montre tout l'intérêt pour l'exploitant de disposer d'une méthode permettant la caractérisation précoce de l'endommagement. C'est dans ce contexte que le CND du béton est en plein essor depuis la fin des années 1990.

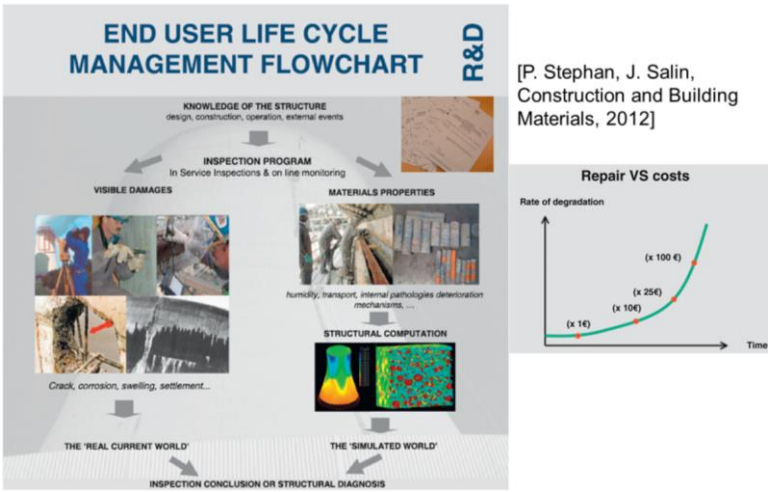

Figure 1 : [STE12] Extrait du management du vieillissement des structures en béton

Dans le même temps, pendant les années 1990, les progrès de l'instrumentation aidant, de plus en plus d'articles scientifiques concernant l'acoustique non linéaire et ses applications à la détection précoce de l'endommagement des solides sont publiés. Les mots clés « nonlinear acoustics damage » dans *google scholar* donnent en première ligne un fameux article de Peter Nagy [NAG98] comparant la sensibilité des paramètres linéaires (Figure 2) que sont la vitesse et l'atténuation des ondes, à un paramètre non linéaire qui sera explicité dans la suite. Il apparait que la sensibilité du paramètre non linéaire est décuplée, permettant une détection

précoce de l'endommagement. Cette courbe d'évolution est à mettre en parallèle de celle fournie Figure 1.

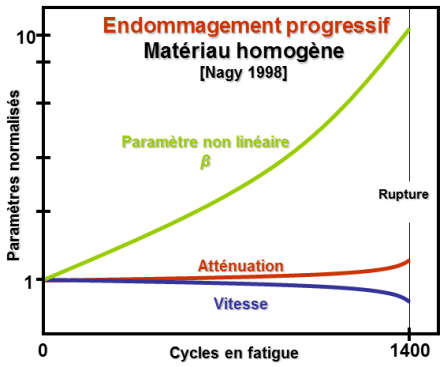

Figure 2 : Adapté de [NAG98]. Evolution de la non-linéarité comparée à celle de la vitesse et de l'atténuation des ondes face à un endommagement en fatigue.

Cette sensibilité est reconnue à la fin des années 1990 pour les matériaux homogènes de nature métallique, mais rien ne laisse penser que ces méthodes soient facilement transposables au cas du béton qui est un matériau très hétérogène et microfissuré par nature.

La problématique du CND du béton est complexe car elle implique des phénomènes à toutes les échelles (Figure 3). Un bon exemple est la carbonatation, une réaction chimique entre le CO_2 contenu dans l'air et le ciment. Cette réaction chimique est illustrée Figure 3 à l'échelle micrométrique. Avec le temps, un front de carbonatation, avec un pH inférieur à celui du ciment, pénètre les premiers centimètres de béton (béton dit de peau) jusqu'à atteindre les premières barres de renfort. Cette pénétration se fait par le réseau de porosité ou par des fissures d'origine mécanique.

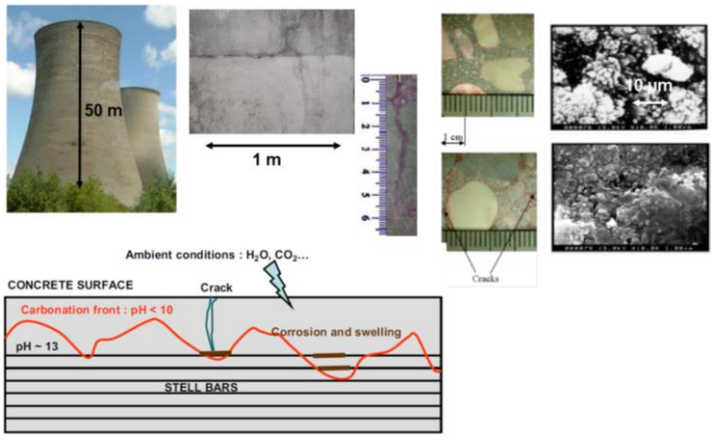

Figure 3 : Le béton, matériau multi échelle

Il s'en suit une dépassivation des aciers, entrainant la corrosion des armatures. Cela provoque un gonflement des barres, créant un réseau de micro fissures (échelle millimétrique) avant de coalescer et former une fissure débouchante en surface (échelle centimétrique). Fissure qui, en fonction des sollicitations mécanique, peut se propager jusqu'à entrainer à terme, au fil des agressions extérieures, la ruine de l'ouvrage. Les échelles à aborder s'étalent donc du micromètre à plus de 100m pour l'exemple des tours aéroréfrigérantes.

La suite de ce chapitre aborde les fondements de l'élasticité non linéaire ainsi que la particularité des matériaux tels le béton.

2. Elasticité non linéaire : Non-linéarité « classique »/ «non classique »

En acoustique linéaire, le principe de superposition indique que deux ondes se propageant dans un milieu n'interagissent pas. Le champ résultant est la somme de celui créé par la première et la seconde. Cependant, lorsque le milieu est non linéaire, ce principe n'est plus valide, le champ résultant est pour partie la somme des deux contributions, mais des contributions supplémentaires apparaissent à cause de l'interaction entre les deux ondes. Une onde perturbe le milieu, la seconde, lors de sa propagation, transite à travers ce milieu perturbé, transportant avec elle les informations relatives à cette perturbation. Au passage d'une seule onde, c'est elle-même qui perturbe le milieu et transporte les informations non linéaires. Le principe physique, simplifié au cas 1D, est résumé Figure 4.

A l'échelle macroscopique, la loi de comportement n'est pas linéaire et dépend à l'ordre deux (ou plus) des déformations. Les paramètres non linéaires associés (β Figure 4) caractérisent le comportement élastique non linéaire. A l'échelle microscopique, la vitesse des ondes dépendant de la dérivée de la contrainte en fonction de la déformation, va, par voie de conséquences, dépend également du niveau de déformation. Il en résulte une distorsion de l'onde avec les creux qui ont tendance à rattraper les bosses (Figure 4) ou inversement, selon le signe de β. La théorie simplifiée ici au cas du 1D est fondée sur la théorie de l'élasticité de Landau et Lifshitz [LAN86].

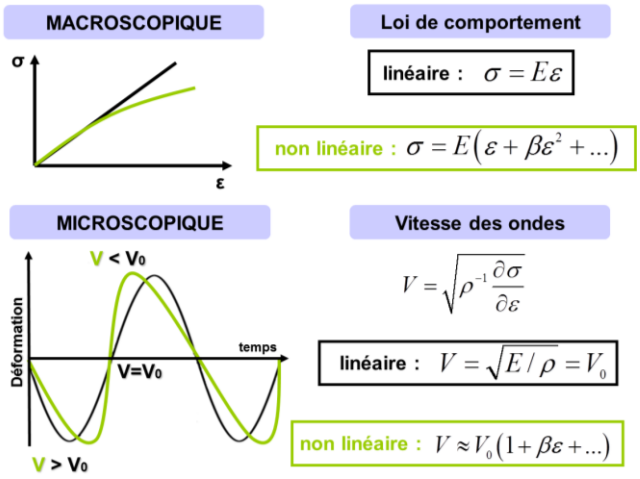

Figure 4 : Effets non linéaires à l'échelle micro et macroscopique

L'évaluation de la non-linéarité (paramètre β), mesure de la distorsion, peut se faire par propagation d'onde (Figure 5). Considérons un milieu non linéaire d'ordre deux en déformation. Pour simplifier le problème, considérons ici la mise en résonance locale du milieu. Deux sources S_1 et S_2, aux fréquences ω_1 et ω_2 sont présentes dans le milieu. La contrainte résultante en un point donné peut se décomposer en une partie linéaire (σ_L) et une partie non linéaire (σ_{NL}). La partie linéaire est la superposition des deux ondes sources (S_1+S_2), se traduisant par la présence des deux raies spectrales ω_1 et ω_2 sur le spectre.

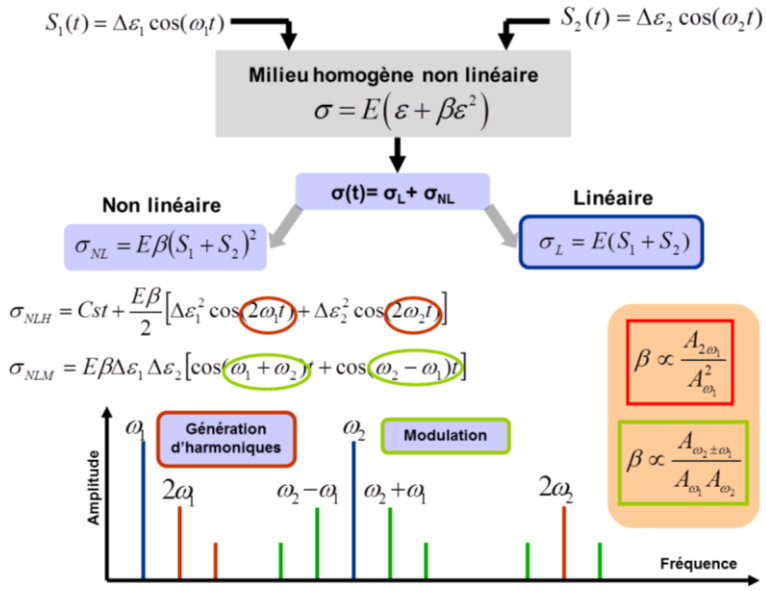

Figure 5 : Quantification de la non-linéarité

La partie non linéaire est le carré de la somme des deux sources. En développant cette expression apparait la somme des carrés (σ_{NLH}), qui par relations trigonométriques fait apparaitre des termes aux fréquences $2\omega_1$ et $2\omega_2$. Ces fréquences doubles, appelées harmoniques, permettent par un rapport d'amplitude, de remonter à une grandeur proportionnelle au paramètre β. Enfin, le double produit issu du développement (σ_{NLM}), fait quant à lui, apparaître les fréquences dites sommes et différences $\omega_2+\omega_1$ et $\omega_2-\omega_1$. C'est un phénomène de modulation d'amplitude. De même, un rapport d'amplitude permet de remonter à une grandeur proportionnelle au paramètre β.

Il a été montré dans les années 1990 que dans les milieux dont la microstructure n'est pas homogène (roches, bétons…), la théorie dite « classique » de Landau et Lifshitz [LAN86], ne suffit pas à décrire les phénomènes non linéaires observés (Figure 6). Les auteurs rapportent des phénomènes non linéaires inattendus, des phénomènes d'hystérésis et de mémoire discrète sous chargement quasi statique et sous sollicitation dynamique [MCC94, GUY95, GUY99, JOH05]. Dans un tel milieu soumis à une onde de forte amplitude (de l'ordre de 10^{-6} en déformation), est observé une chute rapide (~µs) des propriétés élastiques. Ce phénomène est appelé dynamique rapide. Lorsque la sollicitation est stoppée, le matériau recouvre lentement (~h) ses propriétés élastiques initiales. Ce phénomène est appelé dynamique lente. Les observations expérimentales ne suivant pas la théorie « classique » de la non-linéarité décrite ci-dessus, les auteurs ont introduit une loi de comportement phénoménologique permettant de décrire et de quantifier les théories « classique » et « non classique » (Figure 7).

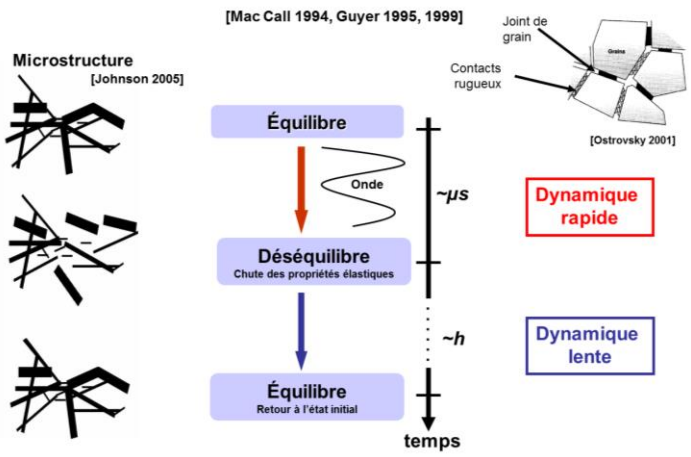

Figure 6 : Phénomènes « non classiques »

Cette loi de comportement prend en compte les phénomènes non linéaires à l'échelle atomique avec le paramètre β introduit ci-dessus, ainsi que les phénomènes non classiques à l'échelle de la microstructure, dite échelle mésoscopique [GUY09] avec le paramètre dit non classique α. La physique liée à ces phénomènes n'est à ce jour pas encore entièrement connue, mais son origine vient d'un ensemble de phénomènes à l'échelle des joints de grains, des potentiels contacts entre ces grains, de la présence de micro fissures… Il est important de souligner que dans les matériaux fortement inhomogènes (typiquement le béton), le paramètre de non-linéarité non classique α domine le comportement non linéaire global. Notons que Johnson *et al.* en 2005 et 2006 [JOH05,JOH06] précisent que bien que la physique ne soit pas encore établie, cette équation est une estimation pratique des phénomènes, spécialement pour les applications en CND.

$$\sigma = M(\epsilon + \beta\epsilon^2 + \cdots) + \hat{\alpha}[\epsilon, \mathrm{sign}(\dot{\epsilon})],$$

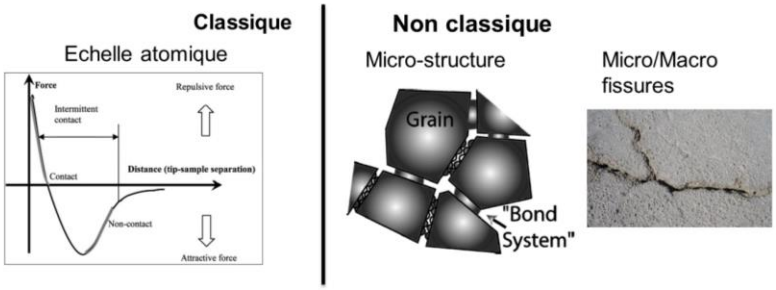

[Johnson, 2005, 2006] : " A specific form of α should follow from the material physics,not yet established." / " This equation is a practical estimate of the dynamics, especially for NDE applications,…"

Figure 7 : Loi de comportement phénoménologique

3. Estimation de la non-linéarité « classique »

Plusieurs méthodes permettent d'estimer la non-linéarité. Nous nous attarderons ici sur la génération d'harmoniques (Figure 5) afin de montrer que beaucoup de paramètres physiques et expérimentaux sont à prendre en considération avant de pouvoir conclure quant à la sensibilité, même relative, de ces paramètres.

L'approche simplifiée détaillée Figure 5 n'est pas valide pour des ondes propagatives. C'est pourtant toujours le cas dans un contexte de CND. Supposons ici un milieu non linéaire « classique ». Le dispositif standard employé pour la mesure d'harmoniques est présenté Figure 8. Un train d'ondes de quelques périodes (fréquence f) est généré par un générateur de fonction, amplifié et transmis au matériau par l'émetteur couplé par du gel couplant ou collé. Ce train d'ondes se propage sur une distance d et est réceptionné par un capteur récepteur (couplé ou collé) de fréquence centrale 2f afin d'être plus sensible aux harmoniques.

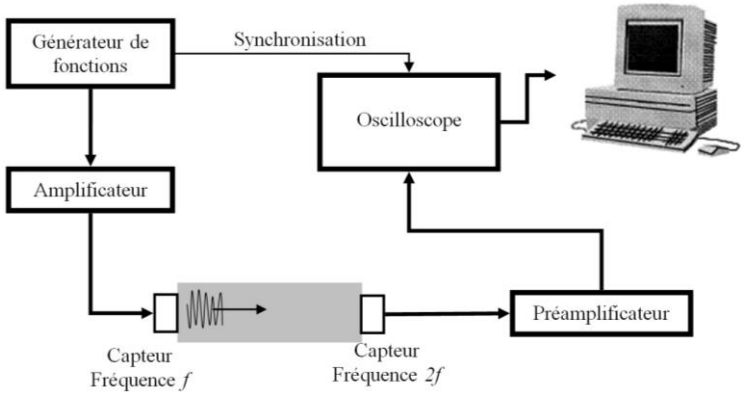

Figure 8 : Dispositif expérimental pour la mesure d'harmoniques

Dans ce cas de figure, en supposant un milieu 1D infini, une onde propagative monochromatique, le paramètre non linéaire β est donné par :

$$\beta = \frac{8c^2}{\omega^2 d}\frac{A_2}{A_1^2}, \quad (1)$$

où c est la célérité dans le milieu, d la distance entre émetteur et récepteur, ω la pulsation, A_1 et A_2 sont respectivement l'amplitude du déplacement particulaire du fondamental et de l'harmonique enregistrés par le récepteur.

Dans beaucoup de publications relatives au CND, la non-linéarité est estimée simplement par le rapport d'amplitude de l'harmonique et du carré du fondamental. Même pour une étude qualitative s'intéressant à une évolution relative du matériau, tous les autres paramètres restant inchangés, cette approche ingnore l'effet de la variation de vitesse entre les deux états. L'ensemble des paramètres à prendre en compte sont :

-Absence d'ondes stationnaires : L'approche développée ici n'est valide que pour une onde propagative en milieu infini. Il est donc nécessaire de choisir le nombre de cycle du train d'onde de manière à s'assurer qu'aucune réflexion n'interfère avec l'onde mesurée. Il faut par ailleurs un train d'onde le plus long possible pour s'approcher au mieux de l'hypothèse d'ondes monochromatiques.

-Taille de l'échantillon : Dans le cas d'une comparaison entre plusieurs éprouvettes, il est important corriger l'effet de la distance de propagation, la non-linéarité étant cumulative sur le parcours de l'onde.

-Paramètre linéaire : La mesure de vitesse pour chaque échantillon n'est pas à négliger, surtout que l'équipement permettant la mesure d'harmonique permet également une mesure de la vitesse.

-Linéarité du dispositif : Dans la mesure du possible, il est important de tester le dispositif expérimental sur un matériau de référence bien connu. Les sources de non-linéarités autres que celles induites par le matériau sont nombreuses et peuvent venir de l'électronique (amplificateur, pré-amplificateur…), des capteurs piézoélectriques ainsi que du couplage de ces derniers à la surface de l'éprouvette.

-Mesure du déplacement : Pour des mesures relatives, les auteurs postulent souvent que la tension sortie du récepteur est proportionnelle au déplacement. Cette hypothèse est acceptable mais il faut être vigilant quant au fait qu'un récepteur de type piézoélectrique, un vélocimètre laser (souvent employé) ou un accéléromètre ne mesurent pas les mêmes grandeurs physiques.

-Dispersion, atténuation : Il est important de noter que cette approche ignore l'atténuation qui a tendance à limiter les effets non linéaires. Par ailleurs, l'expression proposée n'est pas valide pour les ondes dispersives telles les ondes guidées.

4. Estimation de la non-linéarité « non classique »

Une méthode très employée pour l'estimation de la non-linéarité non classique est la résonance non linéaire. Le principe consiste à mettre en résonance une éprouvette de géométrie donnée en faisant varier le niveau de sollicitation (Figure 9). Le phénomène de dynamique rapide (Figure 6) fait que la fréquence de résonance décroit linéairement avec l'amplitude de la déformation. Sous l'approximation 1D, la pente de cette droite (Figure 9) donne le paramètre α [JOH05].

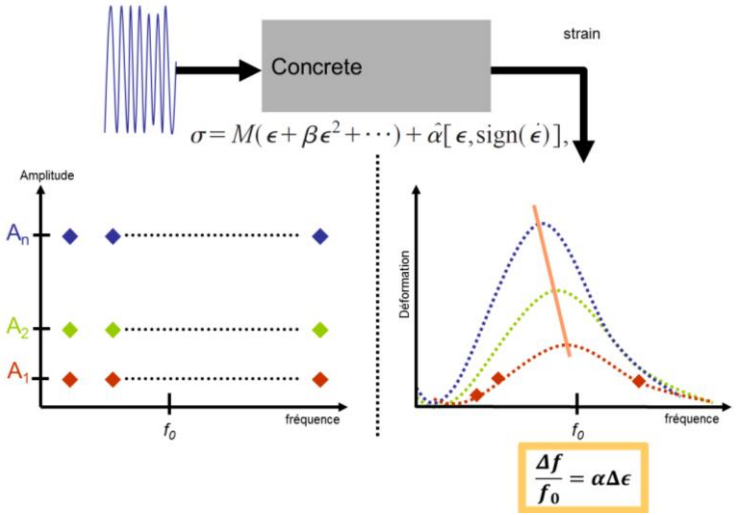

Figure 9 : Principe de la mesure de résonance non linéaire

La problématique est résumée Figure 10. Pour une barre 1D, configuration pour laquelle la loi phénoménologique a été introduite, la déformation correspond au déplacement enregistré par le récepteur divisé par la longueur (en conditions libre/libre). Pour une géométrie 3D, beaucoup plus de modes propres sont présents. Dans ce cas, à partir d'une mesure en un point donné, il n'est pas possible d'estimer la déformation. Pour pallier cette limitation, une méthode originale est présentée dans la suite.

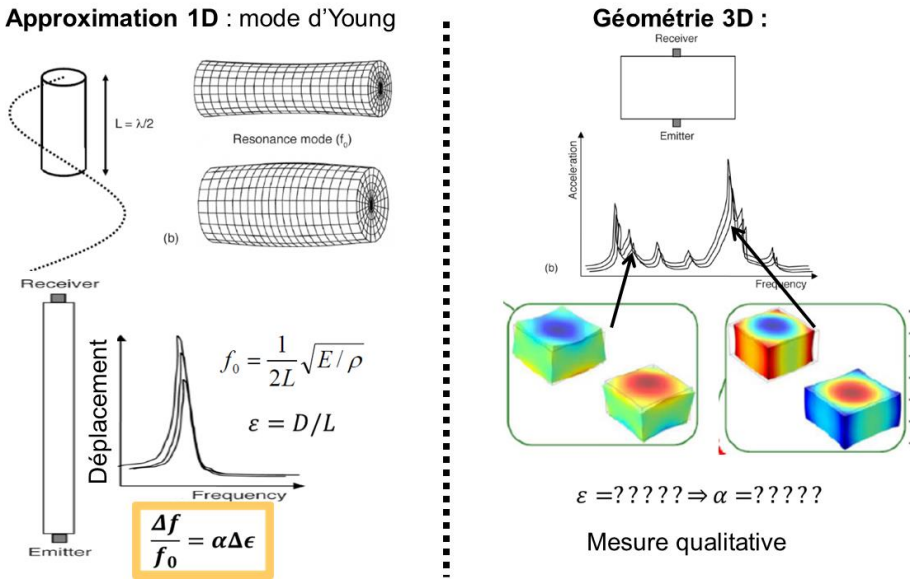

Figure 10 : Influence de la géométrie sur la déformation

5. CND du béton par acoustique non linéaire : limitations

Depuis les années 2000, de nombreuses études montrent le potentiel des paramètres non linéaires pour le CND du béton. Plusieurs types de mesures ont été employées pour caractériser l'endommagement ou les pathologies du béton. Citons ici les méthodes de modulation sensibles à l'endommagement thermique [YIM12], à la fissuration [ZAR10], l'ASR (Alcali Silica Reaction) [KOD09], à la teneur en eau [PAY10]. La génération d'harmoniques [SHA10] ou SSM (Scaling Subtracting Method) [ANT10] sensibles à l'endommagement mécanique. Cette méthode sera détaillée au dernier chapitre. Les méthodes de résonances, détaillées dans la suite, se sont montrées sensibles à la carbonatation [BOU11], l'endommagement mécanique [ABE00a, BEN06], l'endommagement thermique [PAY07] et l'ASR [LES11]. Le point déterminant pour ce type de mesures est l'estimation de la déformation, gérant les effets non linéaires (Figure 7). Une compilation de résultats est fournie Figure 11, ils sont loin d'être exhaustifs, beaucoup d'autres ont été publiés depuis, mais les conclusions sont toujours sensiblement les mêmes. Au vu de ces résultats, la première conclusion qui interpelle est la sensibilité du paramètre mesuré face à l'état du béton avec des évolutions relatives supérieures à 100% ce qui en fait un bon indicateur en vue d'application en CND.

Cependant, il est important de noter que tous ces résultats sont des valeurs relatives ou variations relatives obtenues avec diverses configurations expérimentales. Aucun des travaux publiés jusqu'alors ne fournit de valeur absolue du paramètre non linéaire mesuré pour la simple raison que la déformation n'est pas évaluée. Il n'est pas évident dans tous les cas d'évaluer la déformation. Pour une série d'échantillons donnée qui sont endommagés graduellement, avec une géométrie et une configuration expérimentale déterminée et inchangée, il est possible de comparer les mesures. Cependant, si la configuration expérimentale change (espacement entre les transducteurs, type de transducteurs, signal transmis, générateur….) les mesures ne sont pas comparables.

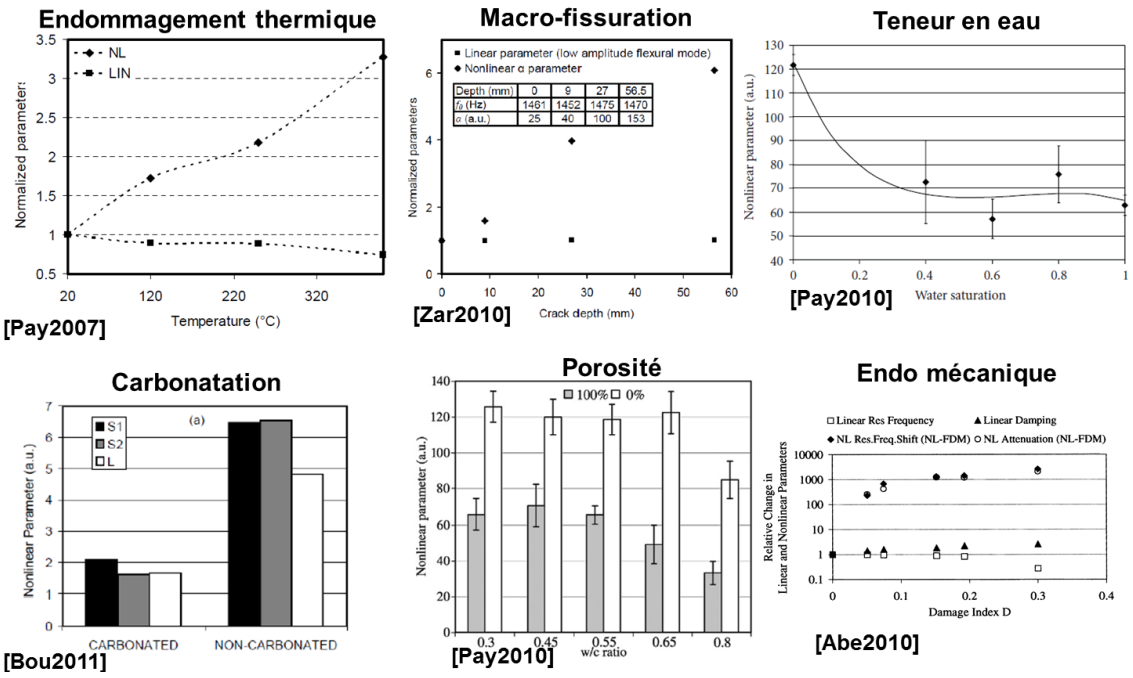

Figure 11 : Evolution de la non-linéarité pour différents états du béton.

Une méthode universelle permettant la mesure absolue du paramètre α permettrait d'avancer dans la compréhension des phénomènes physiques à l'origine du comportement « non classiques ». Il n'y a que quatre publications [Abe02], [Abe00b], [Joh02], [Hau11] qui proposent des mesures absolues du paramètre α. Nous proposons dans la partie suivante une méthode absolue permettant d'identifier l'origine possible du comportement non linéaire.

6. Mesure quantitative globale par résonance non linéaire

Le principe développé ici est schématisé Figure 12. La géométrie de l'échantillon ainsi que sa masse volumique servent d'entrée au processus. L'analyse de toutes les fréquences de résonance de l'échantillon permet d'obtenir le tenseur élastique linéaire complet via la méthode non destructive RUS (Resonant Ultrasound Spectroscopy). Le lecteur peut se référer à [MIG97] pour plus de détails. En corolaire à cette méthode linéaire, les auteurs [JOH00] ont appelé la méthode de résonance non linéaire NRUS (Nonlinear Resonant Ultrasound Spectroscopy). Connaissant alors la géométrie, la masse volumique et le tenseur élastique, ces données servent d'entrées dans une simulation par éléments finis fournissant l'ensemble des modes propres. Un mode est alors sélectionné. Ici, de manière à comparer les résultats avec les données de la littérature issue du mode d'Young (1D), le mode « battant » est sélectionné. La position de l'émetteur et du récepteur sont incluses dans la simulation. Cela permet alors de relier la quantité mesurée par le récepteur (vitesse ou accélération en un point) à l'état de déformation du matériau (ici déformation volumique). Connaissant la décroissance de la fréquence de résonance en fonction de l'amplitude de la déformation, le paramètre α est obtenu quantitativement.

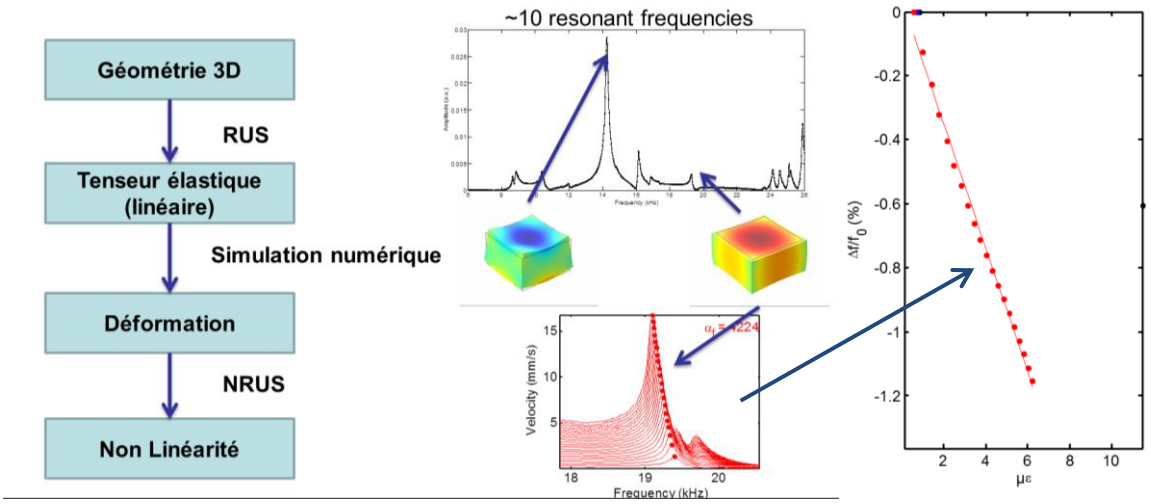

Figure 12 : Schéma de principe de la mesure quantitative

Face à un endommagement thermique progressif, la méthode quantitative est appliquée pour des éprouvettes de mortier, béton haute performance et béton ordinaire (Figure 13). L'endommagement thermique agissant principalement à l'interface ciments/granulats, le mortier est moins non linéaire que le béton. La linéarité des mesures de résonances a été calibrée par une mesure sur un échantillon linéaire de plexiglass pour lequel α=6, soit plusieurs ordres de grandeurs en-dessous des présents résultats. L'ensemble des analyses de la microstructure et les validations associées sont détaillées dans [PAY14a], disponible au chapitre VIII, et constituent les premières valeurs quantitatives relatées pour une géométrie complexe et pour le béton. La méthode proposée et validée peut s'étendre à tout type de matériaux.

Sample	α
High Performance Concrete	
HPC 20	566
HPC 120	966
HPC 250	1941
HPC 400	8125
Ordinary Concrete	
OC 20	1457
OC 120	1204
OC 250	4224
OC 400	14502
Mortar	
M 20	49
M 120	138
M 250	161
M 400	414

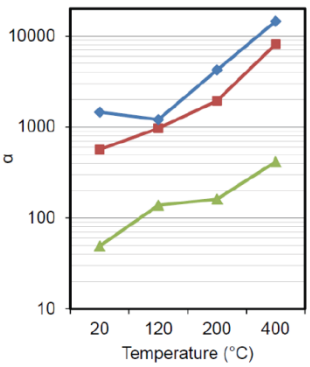

Figure 13 : Compilation des résultats face à un endommagement thermique et corrélation avec la microstructure.

Il est également démontré dans [PAY14a] que la taille des granulats est corrélée quantitativement avec la non-linéarité et son évolution face à l'endommagement thermique. L'aire de contact entre les granulats et la matrice est déterminée connaissant la composition du béton et du mortier. Le rapport entre ces aires pour le béton et le mortier (qui contient de beaucoup plus petits agrégats) correspond au rapport des non-linéarités respectives. Une étude sur le plâtre a également été menée en utilisant cette même méthode. Un des avantages du plâtre est qu'il n'est composé que de cristaux de gypse. En fonction du mode de fabrication, plusieurs tailles de cristaux peuvent être obtenues. La Figure 14 montre la corrélation entre la

taille des cristaux (aire moyenne de contact entre deux cristaux de gypse) obtenue par des images de microscopie électronique à balayage.

Il est ici démontré que la mesure quantitative permet de trouver des corrélations entre la microstructure des matériaux non classiques et la non-linéarité. La multiplication des données pourraient permettre une avancée dans la compréhension des phénomènes physiques. Nous reviendrons en fin de mémoire sur les pistes de recherche à suivre pour atteindre l'objectif.

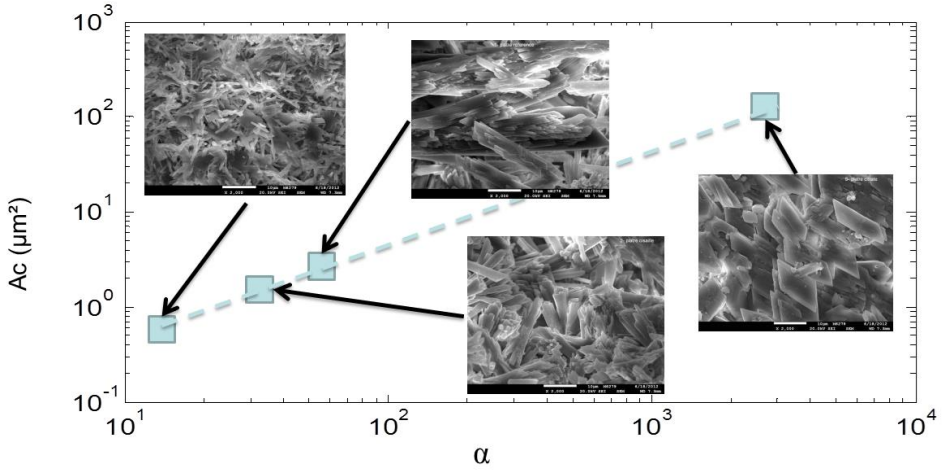

Figure 14 : Corrélation entre la non-linéarité et l'aire moyenne de contact entre deux cristaux de gypse.

7. Mesure locale par retournement temporel

La mesure locale de non-linéarité est un enjeu majeur pour le développement des applications pratiques. La résonance n'est pas applicable à l'échelle d'une structure. Les mesures par propagation d'ondes de forte amplitude (nécessaire pour mesurer la non-linéarité) accumulent les informations non linéaires sur l'ensemble de leurs parcours, interdisant la localisation précise de sources non linéaires. Par ailleurs, le couplage entre l'émetteur et la surface de l'objet à tester peut lui-même induire des non-linéarités.

Le principe physique du retournement temporel repose sur l'invariance de l'équation d'onde par renversement du temps ($t \rightarrow -t$). Il a été largement employé et développé par M. Fink depuis les années 90 [FIN92] avec des applications médicales dans les liquides ou les tissus biologiques. Son application au CND des solides, à la géophysique et l'idée d'utiliser la focalisation de l'énergie pour extraire des informations sur la non-linéarité a été développée au LANL. Le lecteur peut se référer à [AND08] pour une revue détaillée du retournement temporel et de son application.

Un avantage notable de cette méthode est que le régime non linéaire (forte amplitude) n'est atteint qu'à l'instant et à l'endroit précis de la focalisation (Figure 15). La réception étant réalisée sans contact par un vibromètre laser à balayage, le point de mesure peut être déplacé n'importe où. Il est donc possible de focaliser de l'énergie ultrasonore à n'importe quel endroit à la surface de l'échantillon, la taille de la tache focale en profondeur et à la

surface dépendant de la longueur d'onde employée (Figure 15). En effet, en profondeur, la taille de la tache focale correspond à la longueur d'onde des ondes de compression divisée par deux. En changeant les fréquences, la longueur d'onde varie donc la taille de la tache focale évolue également, permettant d'inspecter à différentes profondeurs. Par ailleurs, du fait que 90% de l'énergie est localisé en temps et en espace au niveau de la focalisation, la non-linéarité potentielle due au couplage des émetteurs est négligeable. En faisant varier l'amplitude de la focalisation, il est alors possible d'obtenir des informations relatives à la non-linéarité. Pour plus de détails sur le dispositif expérimental et le traitement des données, on peut se référer à [ULR12a,ULR12b,ULR13] accessibles gratuitement en ligne. Conceptuellement, il est donc possible de déplacer cette tache focale et de choisir sa taille à l'endroit désiré, celui que pointe le laser. L'utilisation d'un laser à balayage automatique permet d'imager la non-linéarité en tout point et à différentes profondeurs d'auscultation.

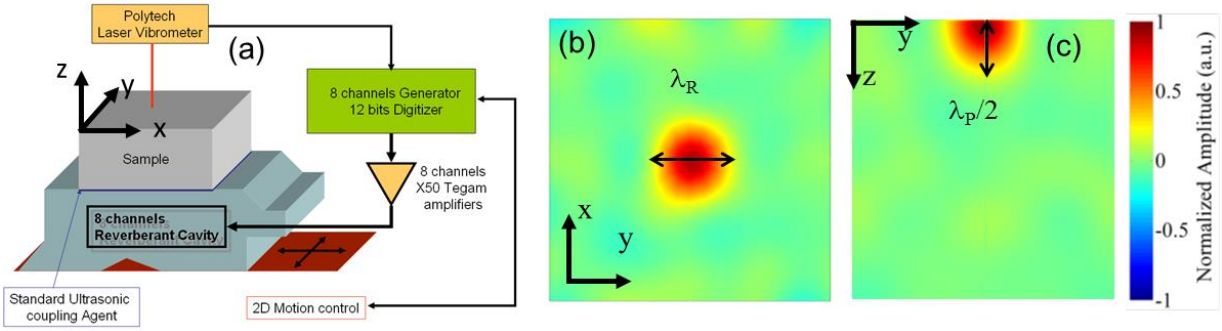

Figure 15 : (a) Schéma de principe expérimental (b) Exemple numérique de focalisation en surface. (c) Forme de la tache focale dans le volume au moment de la focalisation (simulation numérique)

Ce concept a été employé lors de mon séjour au LANL en 2011 et lors de l'accueil de Pierre-Yves Le Bas (LANL) en 2013. Quelques résultats appliqués à la corrosion ainsi qu'à la carbonatation sont fournis Figure 16. L'image Figure 16(a) représente l'image en surface de l'amplitude relative de la non-linéarité, à une fréquence donnée, donc à une profondeur d'auscultation fixe. La barre en acier corrodée est à 1cm de profondeur par rapport à la surface. La Figure 16(b) représente le gradient de non-linéarité mesuré à différentes profondeurs d'auscultation pour des éprouvettes en béton carbonatées à différentes profondeurs (0, 1, 2 et 4 cm). Le fait que le gradient augmente à 4cm vient de la géométrie finie des éprouvettes. Les longueurs d'ondes à employer pour mesurer un tel gradient sont supérieures à 10cm. L'épaisseur de l'éprouvette étant de 12cm, des modes propres seront inévitablement excités, faussant la mesure.

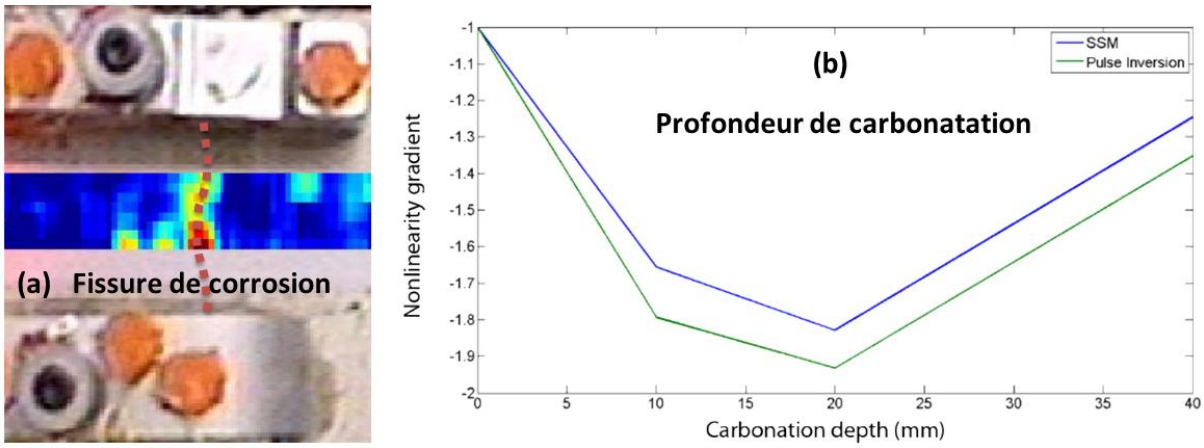

Figure 16 : Evolution de la non-linéarité en présence de (a) une fissure provoquée par corrosion et (b) carbonatation à différentes profondeurs.

Pour revenir maintenant à la mesure absolue, une adaptation de la méthode a été développée de manière à fournir des valeurs quantitatives du paramètre α. Lors de la focalisation des ondes, le matériau est localement conditionné. Comme dans les mesures de résonance durant lesquelles la fréquence de résonance décroit avec l'amplitude, la vitesse des ondes (c) est localement diminuée (Figure 17). Le principe est expérimenté sur les éprouvettes endommagées thermiquement de la partie précédente à 20°C (référence), 120, 250 et 400 °C. Une éprouvette en plexiglass sert de référence linéaire. Cinq fréquences sont employées sur chaque éprouvette afin de mesurer la non-linéarité à cinq profondeurs. Les résultats sont fournis Figure 18. La non-linéarité est donnée en fonction de la profondeur de pénétration et la mesure est calibrée sur un échantillon linéaire de plexiglass. La non-linéarité est obtenue par $\Delta c/c_0=\alpha\Delta\varepsilon$ (pente des droites Figure 17). La déformation est approximée par $\Delta\varepsilon=\Delta v_{zz}/c_0$ où Δv_{zz} est la vitesse particulaire hors plan enregistrée en surface par le laser et c_0 la vitesse des ondes à faible amplitude. Les détails du traitement et les approximations associées sont précisés dans [PAY14b]. Toutes les éprouvettes de béton montrent une non-linéarité constante en fonction de la profondeur, exceptée l'éprouvette endommagée à 400°C. Cette dernière éprouvette a été inspectée par tomographie X à l'EMPA à Zurich. Le traitement des images confirme que dans le volume, le premier centimètre de béton est le plus fissuré. Par ailleurs, la moyenne des non-linéarités mesurées (traits pleins Figure 18 à gauche) est comparée à celle mesurés précédemment par résonance (Figure 18 en bas à droite). Le bon accord entre les deux évolutions est notable.

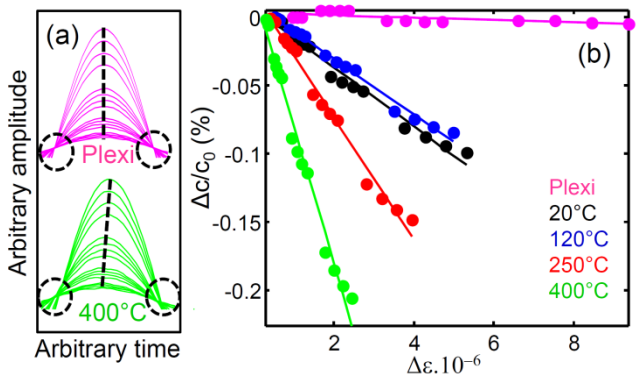

Figure 17 : (a) Focalisation de plus en plus tardive en fonction de l'amplitude dans du béton endommagé à 400°C. (b) Variation relative de vitesse en fonction de l'amplitude pour quatre éprouvettes de béton endommagées thermiquement.

Le fait que la mesure par retournement temporel soit inférieure à celle par résonance est due au fait que l'approximation $\Delta\varepsilon=\Delta v_{zz}/c_0$ a pour conséquence de surestimer la déformation. En effet cette approximation n'est valide qu'en 1D en supposant des ondes monochromatiques stationnaires, ce qui n'est pas le cas ici.

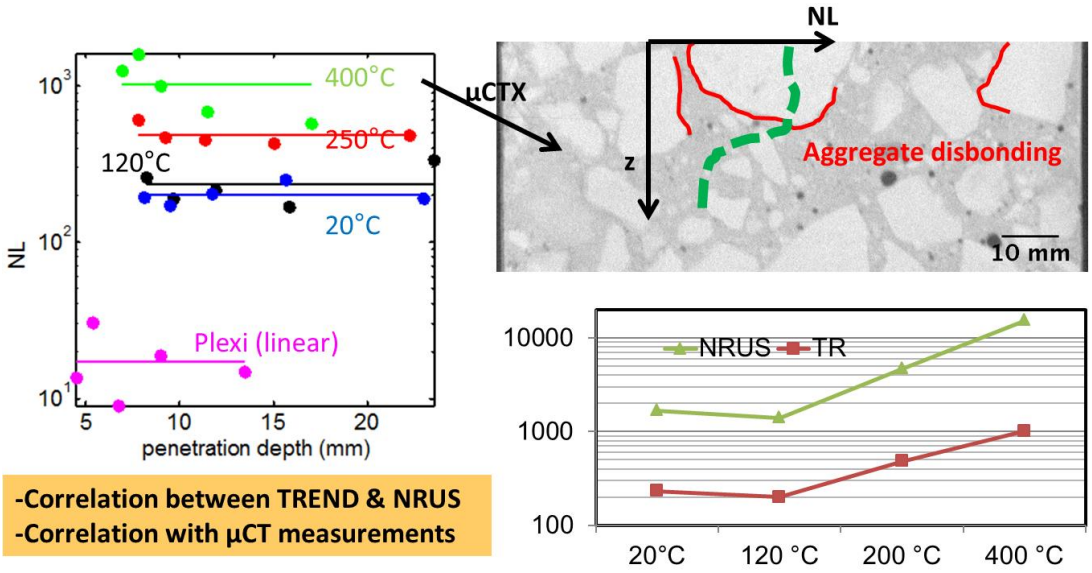

Figure 18 : Paramètre non linéaire α en fonction de la profondeur de pénétration pour le jeu complet d'éprouvette. En haut à droite, image issue de mesure de tomographie X de l'éprouvette 400°C, confirmant la présence de fissures (rouge) à l'interface granulat/ciment localisées dans le premier centimètre de profondeur. En vert, schématisation de la non-linéarité mesurée en profondeur. En bas à droite, comparaison de la mesure absolue par retournement temporel avec les mesures quantitatives de résonance. TR = retournement temporel, NRUS = résonance.

Les travaux en cours en simulation numérique permettront de relier quantitativement la valeur mesurée par le laser en un point à la déformation locale à l'instant de la focalisation [REM15]. Rappelons que cette méthode est une bonne candidate pour les applications pratiques car elle n'est pas sensible au couplage entre les capteurs et la surface du béton, la forte amplitude n'étant atteinte qu'à l'endroit et à l'instant de la focalisation.

8. Conclusion

La thématique de l'élasticité non linéaire appliquée au génie civil est en plein essor soutenu par le contexte économique et politique lié à l'énergie nucléaire et la sécurité. Depuis 2000, la publication d'articles scientifiques sur le sujet croit exponentiellement. Devant la complexité du matériau, les difficultés expérimentales inhérentes et la problématique globale, beaucoup d'entre eux, et j'y ai contribué, se limitent à étudier la non-linéarité avec une configuration de mesure donnée face à un endommagement donné. Tous relatent des évolutions relatives de la non-linéarité qui sont très sensibles à la problématique étudiée, mais il est cependant impossible de comparer quantitativement, donc de valider, tous ces résultats. La grandeur clé est la déformation. A défaut de pouvoir l'estimer, il ne faut pas l'ignorer. Ce

point crucial cause et a causé beaucoup d'erreurs d'interprétations dans les articles scientifiques. Elle est souvent dite proportionnelle à la tension donnée par le récepteur, qui lui est sensible au déplacement. Proportionnelle oui, mais suivant la configuration et le matériau, le facteur de proportionnalité change, pouvant générer des erreurs d'interprétation. Par ailleurs, cette approximation est fausse dans les cas de résonances d'objets non 1D et des modes guidés. Elle est cependant souvent employée pouvant alors mener à des conclusions erronées. Les approches proposées dans ce chapitre sont une voie possible, d'autres seront détaillées dans le dernier chapitre. Le leitmotiv des recherches entreprises et détaillées dans ce chapitre est la compréhension et la prise en compte de la physique des phénomènes. Retenons la Figure 19 imaginée avec Jean Salin (Ingénieur Sénior, EDF R&D), représentant un schéma global du principe de mesure physique. Ce principe général résume les points clés amenant l'industriel jusqu'au diagnostic (but de toutes les méthodes CND). L'analyse des signaux ne peut se faire qu'au regard de la physique pour pouvoir conclure. Même si dans le cas présent, la physique n'est pas encore complètement établie, le paramètre non linéaire α est une estimation pratique des phénomènes non classiques. A défaut donc, l'estimation de la déformation permettant des mesures absolues est un passage obligé pour envisager des applications pratiques dans l'avenir.

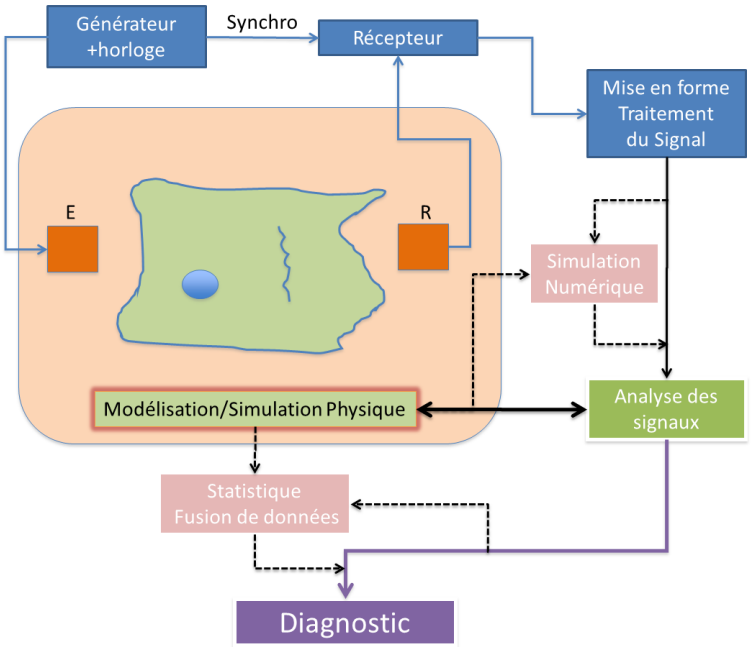

Figure 19 : Développement Mesures Physiques

III. Ultrasons diffus : tirer parti du « bruit »

Collaborations:
Laboratoire : A. Quiviger, V. Garnier, J.F. Chaix
ISTERRE Grenoble : E. Larose
Laboratoire Matériaux et Durabilité des Constructions (LMDC, Toulouse) : J.P. Balayssac
EDF R&D : J. Salin, G. Moreau, A. Girard, G. Durso
Projets/contrats associés : [P1,2,3,7]/[C4,10]
Publications internationales associées : [2,10,13,14]

1. Motivation : CND du béton par méthodes acoustiques

Le CND du béton par méthodes acoustiques est standardisé [ISO04, AST09]. Les recommandations précisent les gammes de fréquences à employer. Ces fréquences sont généralement basses du point de vue des « ultrasonistes ». Elles sont dans la majorité des cas de 24kHz ou 54kHz, ces deux fréquences étant celles employées par les équipements commerciaux standards. A ces fréquences, considérant la vitesse des ondes moyennes dans le béton de l'ordre de 3500m/s, les longueurs d'ondes sont respectivement de 14,6 et 6,5 cm. A cette échelle, la détection de défauts de l'ordre ou inférieurs au centimètre est impossible. Afin d'augmenter la résolution des mesures, les fréquences peuvent être augmentées. Cependant, dans la gamme de fréquence supérieure (100kHz-1MHz), les longueurs d'ondes (3,5cm – 3,5mm) correspondent à la taille moyenne des agrégats et de leur espacement. Il en résulte un phénomène de diffusion multiple marqué qui se traduit par l'apparition d'une « coda » (Figure 20). Ce terme a été introduit en géophysique par K. Aki [AKI69] pour décrire la fin des sismogrammes enregistrés lors de tremblement de terre, référence à la fin des pièces musicales.

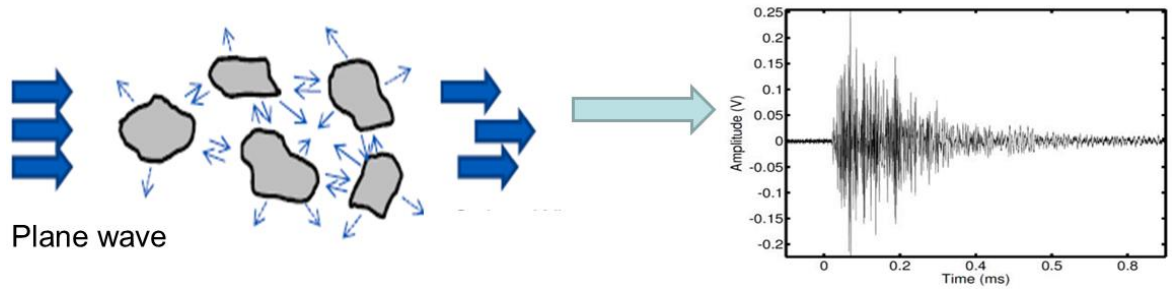

Figure 20 : Diffusion multiple des ondes dans le béton

L'étude de la multidiffusion dans le béton est un thème de recherche au laboratoire. Des méthodes d'homogénéisation [CHA03, CHA12] ont été étudiées et validées décrivant la propagation des ondes cohérentes (résistant au moyennage spatial) dans le béton. L'idée complémentaire proposée ici est d'étudier les ondes incohérentes porteuses d'information sur le milieu de propagation. Ce thème a commencé au laboratoire [PAY09] avec l'étude d'une méthode, Coda Wave Interferometry (CWI), issue de la géophysique [SNI02] pour déterminer les constantes élastiques non linaires du béton. L'étude de la CWI s'est poursuivie, appliquée à la caractérisation de l'endommagement thermique [LAR13]. La CWI ne sera pas détaillée dans ce manuscrit, pour plus de détails, se référer à [PAY09] section VIII.

2. Les ultrasons diffus pour le CND du béton

La partie incohérente du signal peut être décrite par une approximation de régime de diffusion, décrivant l'évolution temporelle de la densité d'énergie du signal reçu. Cette notion de diffusion de l'énergie ultrasonore est décrite et validée par Weaver [WEA98] sur des mousses d'aluminium à porosité variables. Concernant le béton, Anugonda et al. [ANU01], détermine les paramètres de diffusion avec une fréquence centrale d'émission de 500 kHz, soit bien supérieures aux fréquences usuelles dans ce type de matériau. Ils laissent ainsi entrevoir un grand nombre de possibilités de caractérisation non destructive d'endommagements microstructuraux du béton. Becker et al. [BEK03] étudie l'évolution des paramètres de diffusion en fonction des diamètres et de la fraction volumique des granulats, représentés par des billes de verre. Punurai et al. [PUN07] caractérise cette évolution dans du ciment en fonction de la quantité d'air occlus dans le système. L'influence d'un endommagement diffus est démontrée [DER10]. Les ultrasons diffus sont également utilisés pour imager et localiser l'apparition de variations (défaut) par rapport à un état de référence [LAR09, LAR10].

L'équation de diffusion exprime la variation spatio-temporelle, dépendant de la fréquence, de l'énergie E pour une source impulsionelle P [WEA98]:

$$\frac{\partial\langle E(x,t,f)\rangle}{\partial t} - D\Delta\langle E(x,t,f)\rangle + \sigma\langle E(x,t,f)\rangle = P(x,t,f), \tag{2}$$

où x est la position, t le temps, f la fréquence, D la diffusivité et σ la dissipation. La diffusivité est caractéristique de la microstructure du matériau. Elle dépend de la densité d'agrégats, de leur géométrie et de leur espacement moyen [ANU01]. La dissipation reflète les propriétés viscoélastiques du milieu qui dans le cas du béton est essentiellement liée aux propriétés de la pâte de ciment [ANU01].

La solution de l'équation 1 peut être décrite en 1D [ANU01], 2D [RAM04] ou 3D [DER10]. En l'absence quantitative sur la morphologie de fissures dans le volume du matériau (cf. paragraphe suivant), nous nous intéressons dans la suite à la solution 2D qui sous forme logarithmique s'écrit :

$$\log\left(\langle E(r,t,f)\rangle\right) = C_0 - \log(Dt) - \frac{r^2}{4Dt} - \sigma t\,, \tag{3}$$

où r est la distance à la source et C_0 une constante dépendant de l'énergie injectée par la source.

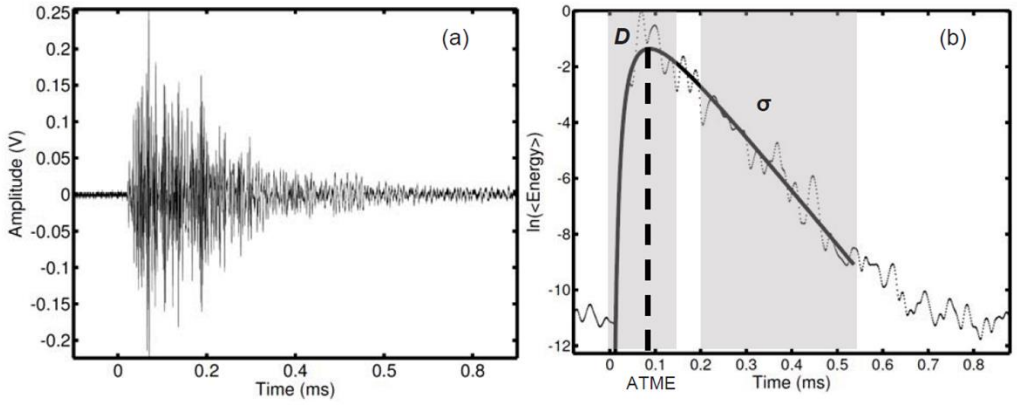

Figure 21 : (a) Signal ultrasonore diffus. (b) Représentation de la densité spectrale d'énergie en fonction du temps (courbe en pointillés) et la solution lissée (trait plein) selon l'Equation(2)

La Figure 21(a) montre un signal ultrasonore diffus typique dans du béton. La Figure 21(b) représente l'évolution de l'énergie au cours du temps (pointillés) et l'ajustement de ces données (trait plein) avec la solution de l'équation 2D. Notons qu'un paramètre supplémentaire est étudié : le *Arrival Time of the Maximum Energy* (ATME Figure 21(b)) qui est un indicateur étudié par [RAM04] et qui fera l'objet de la suite de ce chapitre. Un point important à souligner est que l'estimation des paramètres de diffusion ne dépend pas du couplage entre les transducteurs et la surface du béton. En effet, la constante C_0, traduisant l'amplitude du signal, n'est pas influente sur ces derniers.

Dans la suite, l'application de cette méthode est employée pour la caractérisation de fissures réelles dans le béton.

3. Caractérisation de fissures réelles

La fissuration est un problème majeur au regard de l'intégrité des ouvrages en béton du génie civil. En effet, ces derniers tiennent principalement leurs propriétés mécaniques des armatures d'acier qu'ils contiennent. Généralement, la première nappe de ferraillage ne se situe qu'à quelques centimètres de la surface, protégée par le béton d'enrobage. Le rôle de ce dernier est principalement d'assurer la protection des aciers contre les agents agressifs présents naturellement dans l'environnement d'un ouvrage : l'eau, le CO_2 contenu dans l'air (causant une diminution du pH), … Une mauvaise étanchéité de ce béton entraîne une corrosion des armatures, engendrant une macro-fissuration qui a pour conséquence d'accélérer le processus de dégradation de la structure. Il est donc particulièrement important de pouvoir caractériser une fissure présente dans le béton d'enrobage, afin de prévenir au plus tôt tout endommagement de la structure. L'objectif de ces travaux est donc de parvenir in fine à une détection, une localisation ainsi qu'à une caractérisation de macro-fissures présentes dans le béton d'enrobage.

Suivant le thème de recherche du laboratoire concernant le CND des matériaux et structures réels, la fissure n'est pas considérée comme une simple entaille. Les fissures étudiées ici sont des fissures fermées (invisibles à l'œil nu), dont la morphologie est complexe. Les éprouvettes ont été confectionnées par le Laboratoire Matériaux et Durabilité des Constructions (LMDC).

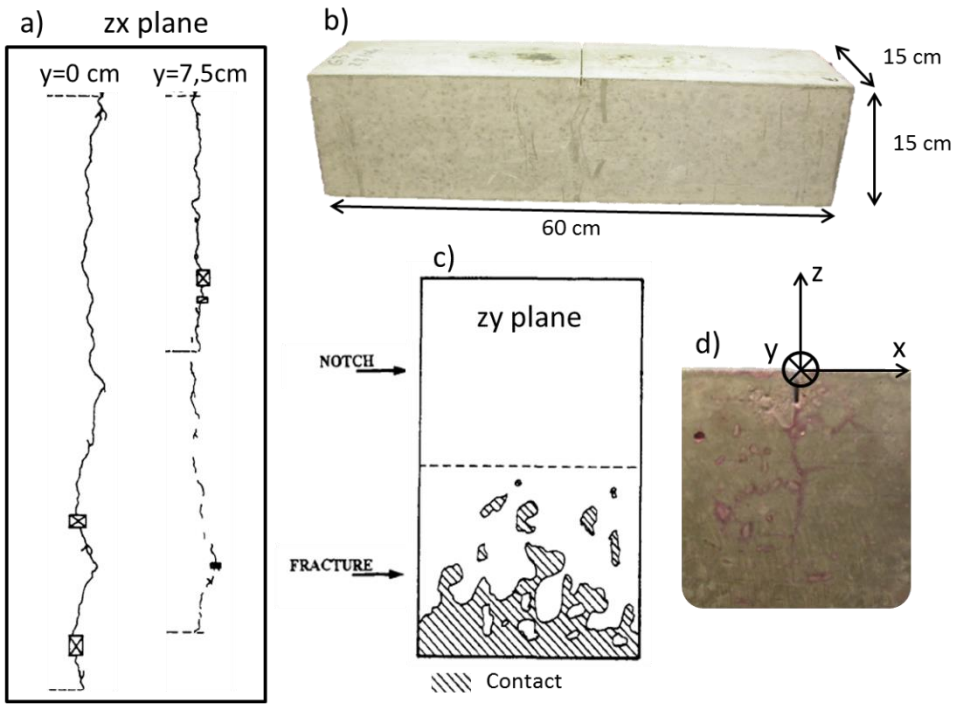

Figure 22 : D'après [TUR96]. Cartographie de la fissure. a) surface latérale de l'éprouvette, b) éprouvette de béton de l'étude c) plan longitudinal central, d) géométrie latérale de la fissure, obtenue par ressuage.

La morphologie de la fissure débouchante en surface dans du béton est décrite Figure 22. La fissure est composée de deux parties : La première est la partie ouverte de la fissure. Elle est localisée sur la partie supérieure de la fissure, au niveau de la surface. La seconde, pour laquelle les deux lèvres sont partiellement ou totalement en contact, est considérée comme fermée. La particularité d'une fissure réelle fermée réside dans le nombre et la nature de points ou zones de contact qui existent entre les lèvres. La Figure 22 montre une disparité dans le profil d'une fissure. Elle ne présente pas la même morphologie suivant la profondeur à laquelle elle se situe dans l'éprouvette. La Figure 22 met en évidence la présence de discontinuités dans le profil de la fissure située dans le plan médian d'une éprouvette de béton et observée en surface (Figure 22 a et c). La fissure n'est pas unique, mais peut être représentée dans cette zone par une succession de zones partiellement ouvertes le long d'une même ligne directrice.

Jusqu'à présent, les seules données issues de la littérature concernent les entailles [RAM04]. La méthode proposée est donc validée sur des éprouvettes entaillées (courbe rouge Figure 23). Pour plus de détails concernant les conditions expérimentales et les validations, le lecteur peut se référer à [QUI12] section VIII. Dans le cas de fissures réelles (courbe bleue Figure 23), la faible augmentation observée sur ce paramètre n'est pas suffisante pour caractériser la profondeur. Cependant, il est important de noter que de faibles variations sont observées sur l'ATME pour les éprouvettes fissurées. Cela est sans doute dues au zones partiellement ouvertes le long de la fissure, conformément à la morphologie décrite Figure 22.

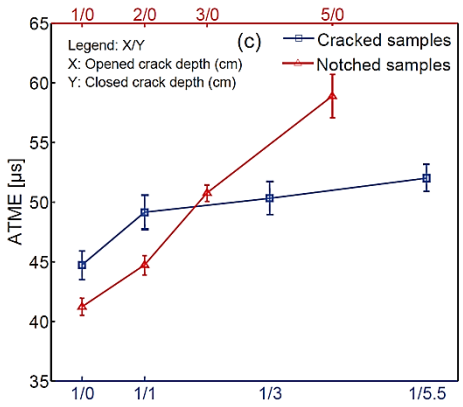

Figure 23 : Evolution de l'ATME en fonction de la profondeur d'une entaille (rouge) et d'une fissure réelle (bleu)

Ces variations, même faibles, devraient être porteuses d'informations quant à la morphologie de la fissure et les zones partiellement ouvertes/fermées. Pour mieux comprendre ces phénomènes, une simulation numérique de la diffusion est présentée dans la partie suivante.

4. Simulation numérique de la diffusion

La propagation d'ondes en régime multidiffusant dans le béton est complexe à simuler car il faut considérer chaque agrégat, sa taille, sa position… En considérant le béton comme un milieu diffusif, le problème se ramène à la résolution de l'équation de diffusion dans un milieu homogène, simplifiant grandement la résolution.

Le code de calcul développé par A. Girard (EDF R&D) est basé sur une méthode des différences finies en 2D. Tous les détails relatifs à ce code sont disponibles dans [QUI13] section VIII. Le choix de cette méthode est principalement justifié par la symétrie du problème. Le béton, dans lequel l'onde diffuse se propage, possède des valeurs de dissipation et de diffusivité fixes (entrées du code). La géométrie, la position des émetteurs et récepteurs ainsi que les conditions aux limites du modèle sont fixées également afin de correspondre aux conditions de l'expérience. Le maillage utilisé dans l'étude suivante est un maillage rectangulaire, de résolution horizontale 2 mm et de résolution verticale 1 mm. Les conditions aux limites du modèle sont donc choisies en conséquence : des conditions d'énergie nulle sur les bords, des conditions de Neumann à l'interface béton-air (partie supérieure). L'atténuation dans le béton est en particulier suffisamment importante pour ne pas avoir à considérer de couches absorbantes (PML = Perfectly Matched Layer) pour éviter les réflexions.

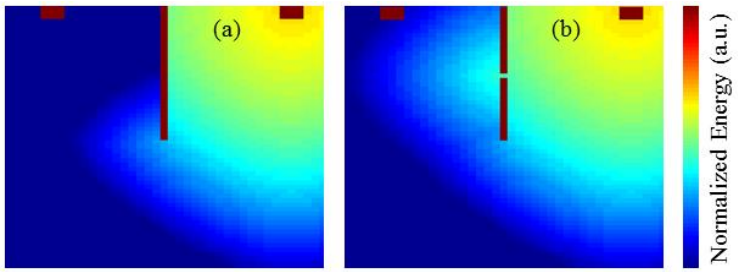

Figure 24 : Image à un instant donné de l'énergie diffuse dans le béton. (a) Fissure ouverte. (b) Même fissure avec un point de contact entre les lèvres.

Plusieurs cas sont étudiés. L'influence du nombre de points de contact, l'influence de la position d'un point de contact le long de la fissure et enfin, les données expérimentales sur fissures réelles et la morphologie, servent de base à l'optimisation du modèle.

- *Nombre de points de contacts*

Les résultats de la Figure 25 montrent que l'ATME diminue en fonction du nombre de points de contacts. La présence d'un seul point de contact situé à mi-hauteur de la fissure induit une variation de l'ATME de 5 µs soit environ 10% de la valeur originale. Le temps de transit de l'énergie décroit, tendant vers le temps de trajet direct

- *Position d'un point de contact*

La Figure 26 montre que plus le point de contact est éloigné de la surface, plus le temps d'arrivée du maximum de l'énergie est grand. Ainsi, pour une profondeur donnée, la position d'un point unique de contact peut engendrer une variation de l'ATME de l'ordre de 10 µs, ce qui représente 25% de variation pour la fissure considérée.

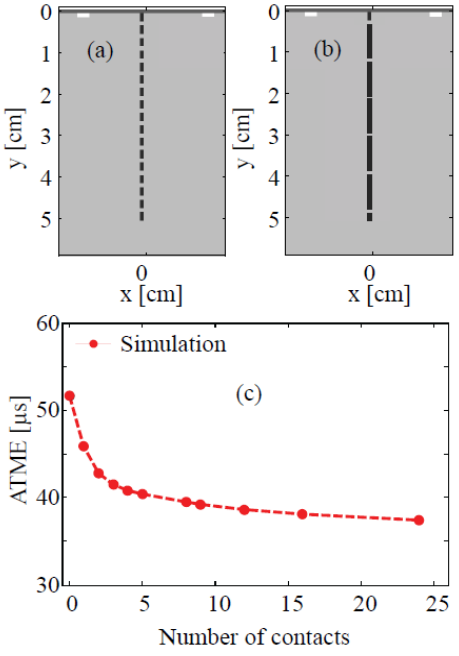

Figure 25 : Distribution spatiale des contacts le long de la fissure, et évolution de l'ATME en fonction du nombre de points de contact distribués linéairement sur une hauteur totale de fissure de 5 cm

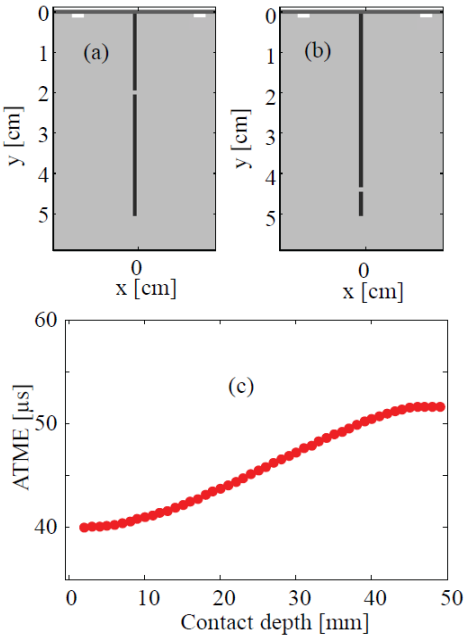

Figure 26 : Variation de l'ATME en fonction de la distance à la surface d'un contact de 1 mm de longueur entre les lèvres de fissure.

- *Optimisation*

Les fissures simulées, identiques à celles analysées expérimentalement dans la section précédente (1, 3 et 5.5 cm), sont représentées sous la forme d'une répartition de points de contact linéaire le long de la fissure (Figure 27). Cette distribution est cohérente avec celle décrite dans la section précédente. La densité linéique des contacts est le paramètre d'optimisation du modèle numérique.

Le Temps d'Arrivée du Maximum de l'Energie est déterminé pour différentes densités de contact le long de la fissure. Un processus d'itération permet de modifier cette densité de contact afin d'optimiser la morphologie de la fissure numérique par rapport aux résultats expérimentaux. Les résultats sont présentés Figure 28.

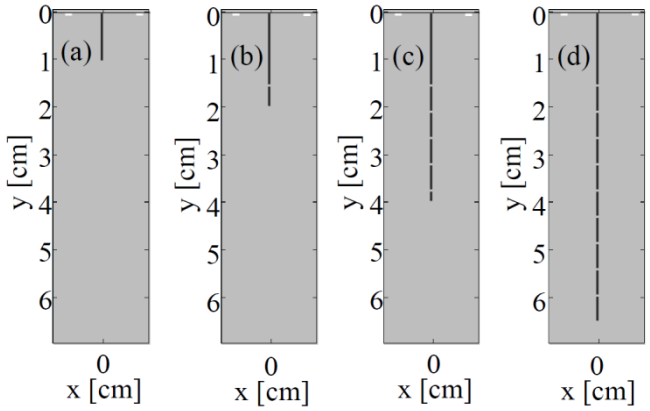

Figure 27 : Simulation numérique des fissures exploitées lors des expériences (0, 1, 3 et 5.5 cm).

Les résultats de la simulation numérique montrent que les évolutions des résultats simulés et expérimentaux sont en accord pour une configuration de la fissure fermée où 6.5% de la fissure correspond à des points de contact, par lesquels l'énergie peut transiter. Notons que les résultats numériques de l'ATME passent par un maximum pour une profondeur de 4 cm pour décroître ensuite pour la profondeur de 6.5 cm alors que les résultats expérimentaux montrent une croissance continue. Toutefois les évolutions numériques restent dans le domaine d'incertitude des résultats expérimentaux. Cette différence peut trouver son origine dans la description du modèle, incluant la distribution des points de contact, mais aussi de la description numérique 2D alors que l'expérience est en 3D avec notamment la présence des bords de l'éprouvette.

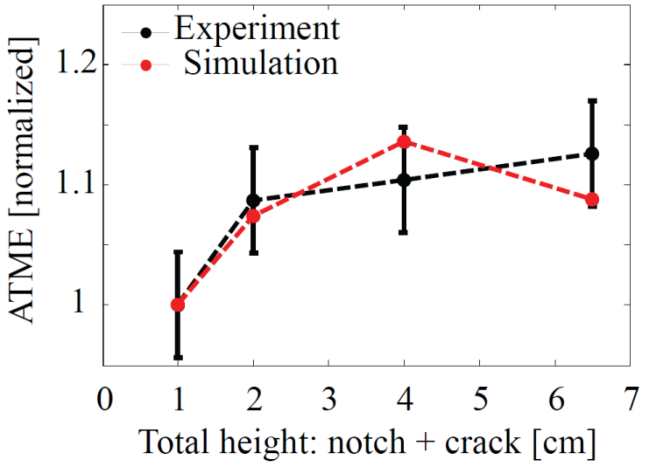

Figure 28 : Variation de l'ATME en fonction de la hauteur de fissure pour une densité de contacts optimisée, comparaison aux résultats expérimentaux.

L'outil de simulation développé et la description numérique d'une fissure permet de mieux comprendre les interactions des ondes diffuses avec une fissure réelle. Les simulations montrent l'influence du nombre de contacts ainsi que de leur répartition spatiale sur l'ATME

mesurée. Une morphologie de fissure réaliste est décrite numériquement. Elle permet d'optimiser le modèle et montre qu'une densité linéique de contact de 6.5% explique les évolutions expérimentales de l'ATME pour des fissures variant de 1 à 5.5cm de profondeur.

La Figure 22 montre le caractère 3D de la fissure avec des densités de contact qui évoluent entre les bords et le centre de l'éprouvette. Il est cependant important de noter que Turatsinze et al. [TUR96] imagent la fissure par découpage en tranches fines d'éprouvettes. Cela a pour effet de relâcher les contraintes, pouvant provoquer des ouvertures qui n'existent pas dans le volume. L'observation non destructive de la morphologie de ce type de fissure dans le volume est un élément à considérer dans les futures études par micro tomographie X par exemple. L'intégration de la géométrie de la fissure à une extension 3D de ce modèle pourrait ouvrir la voie à une inversion de la morphologie de la fissure à partir des données expérimentales.

Il est ici démontré que les ultrasons diffus sont sensibles aux zones partiellement ouvertes le long de la fissure. Afin de caractériser complètement la fissure et obtenir des informations quant aux zones fermées, les ultrasons diffus sont couplés à un chargement dynamique qui ouvre et ferme alternativement la fissure. Ce thème est l'objet de la partie suivante.

5. Ultrasons diffus sous chargement dynamique

L'idée d'employer un chargement dynamique vient de la littérature. Guillaume Renaud développe une méthode nommé DAET (Dynamic AcoustoElastic Testing) consistant à mesurer la vitesse et l'atténuation des ondes à travers un milieu sous chargement dynamique pour en extraire des paramètres non linéaires. Cette méthode, initialement développée pour les applications biomédicales [REN09] a évoluée à l'étude des solides complexes comme les roches [REN12]. Nous reviendrons à la fin de ce manuscrit sur le potentiel de cette méthode. Comme pour le DAET, il est ici proposé de réaliser un chargement dynamique en flexion de nos éprouvettes (Figure 29). Se référer à [PAY13] chapitre VIII pour plus de détails sur cette méthode. Durant ce chargement, le protocole expérimental réalisée en partie 2 est réalisée de manière à pouvoir extraire l'ATME, à partir des signaux bleus Figure 29(c), à différents niveaux de sollicitation enregistrés via un accéléromètre, à partir des signaux rouges Figure 29(c).

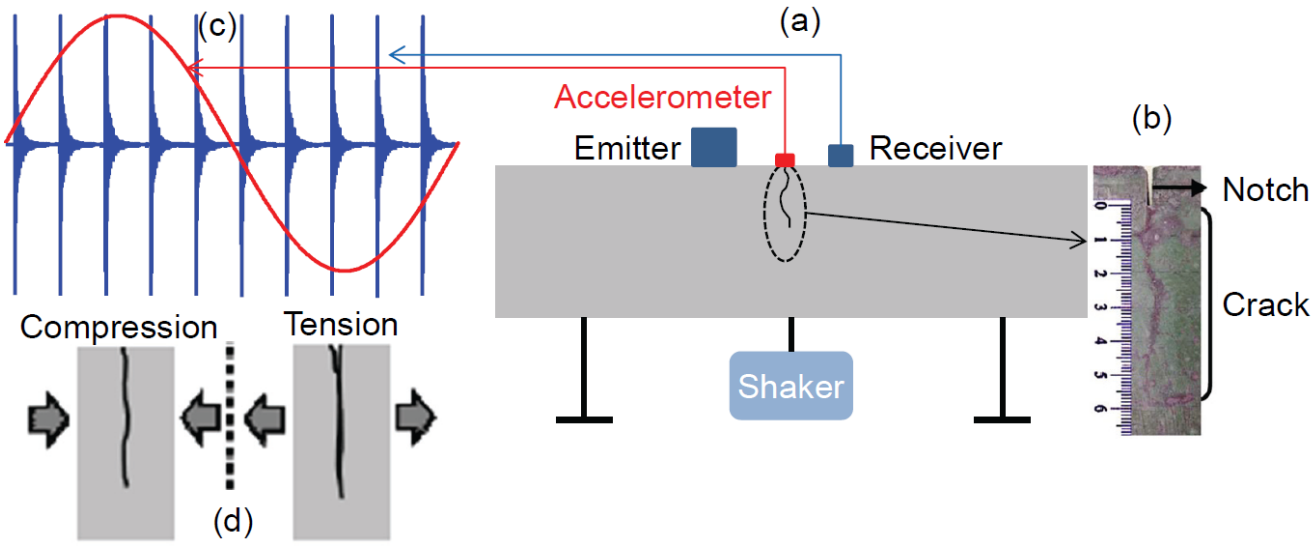

Figure 29 : (a) Dispositif expérimental. (b) Zoom sur la fissure. (c) Schéma de principe de l'acquisition. (d) comportement de la fissure en traction et compression

L'important pour ce type de mesure est de pouvoir considérer l'état de l'éprouvette comme stable pendant le temps de propagation des ondes diffuses (Figure 30). Cela permet d'associer une amplitude à une valeur d'ATME (Figure 30b). Ceci répété sur des centaines de cycles permet de tracer l'évolution de l'ATME en fonction de l'amplitude de la basse fréquence (Figure 31).

La grandeur mesurée ici par l'accéléromètre est le déplacement vertical au niveau de la fissure (Figure 29). Il est en effet impossible de déterminer la déformation tel que suggéré dans le premier chapitre. En présence d'une fissure, la répartition des contraintes dynamiques peut être estimée dans un matériau homogène. Cependant au vu de la morphologie des fissures dans le béton, avec des zones partiellement en contact, il est difficile d'avancer des valeurs.

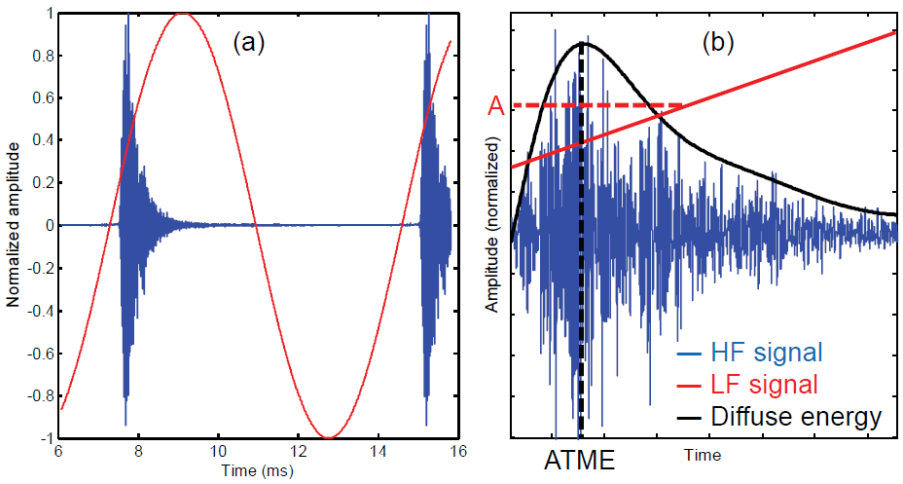

Figure 30 : (a) Signaux expérimentaux. En bleu, les ondes diffuses. En rouge, la basse fréquence. (b) Zoom sur un signal. Estimation de l'ATME et de l'amplitude de la basse fréquence A.

Pour chacun des résultats présentés Figure 31, l'ATME diminue dans les phases de compression de la fissure, et augmente dans les phases de traction. Cette évolution est en accord avec les résultats expérimentaux et la simulations numériques (parties 2 et 3) qui indiquent que l'ATME augmente lorsque le nombre de points de contact diminue.

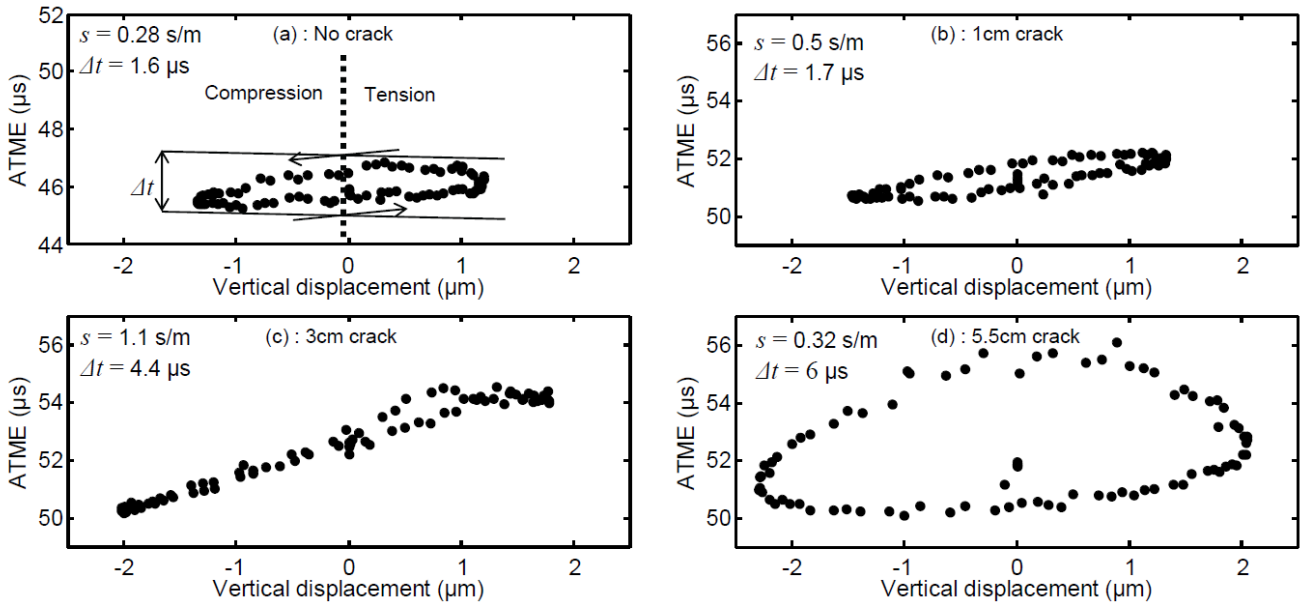

Figure 31 : Compilation des résultats pour toutes les éprouvettes. (a) non fissurée. (b) fissure 1cm, (c) 3cm et (d) 5,5cm. Les flèches indiquent le sens de déplacement dynamique qui est le même pour toutes les figures. s est la pente des évolutions. Δt est l'excursion maximale de l'ATME durant un cycle.

Plusieurs observations peuvent être faites :

- *L'hystérésis :* Physiquement, l'hystérésis est due à la nature viscoélastique du ciment mais également aux phénomènes d'ouverture/fermeture des fissures. Elle est présente dans chaque cas, moins pour l'éprouvette avec une fissure de 3cm, sans doute en raison de la morphologie particulière permettant aux contacts de s'ouvrir et se fermer pour le même déplacement. L'éprouvette à fissure de 5,5cm montre un comportement très particulier. Son comportement hystérétique marqué est sans doute dû à une redistribution des contacts le long de la fissure sous chargement dynamique.
- *La pente s :* Physiquement, cette pente est liée à la non-linéarité. La première éprouvette, non fissurée, représente la non-linéarité intrinsèque du béton. Elle croit en fonction de la taille des fissures sauf pour l'éprouvette la plus fissurée pour laquelle l'approximation à une droite n'a que peu de sens physique.
- *L'excursion maximale Δt :* Elle augmente de façon régulière avec la taille de la fissure. Pour rappel, la partie 3 (Figure 23) montre qu'une entaille de 5 cm induit une variation de l'ATME de 15µs. Etant donné la présence de contact partiels, il n'est pas surprenant que les présentes valeurs restent inférieures à 10µs.

Pour comparaison, les résultats de l'évolution de Δt (Figure 32) sont confrontés à ceux obtenus sur les mêmes éprouvettes (Figure 33) par méthode de modulation non linéaire quelques années auparavant. Un signal continu transite à travers la fissure. Un impact excite

le même premier mode de flexion. Le récepteur enregistre la modulation d'amplitude qui en résulte. Pour plus de détails sur cette étude, se référer à [ZAR10] fourni au chapitre VIII. La comparaison est frappante, les deux méthodes fournissant les mêmes tendances. Cette similitude est due au fait que physiquement, les mêmes phénomènes sont mesurés. La modulation d'amplitude Figure 33 est provoquée par l'ouverture et la fermeture des zones partiellement fermées le long de la fissure sous chargement dynamique. Ceci a pour conséquences de moduler l'amplitude du signal se propageant à travers cette dernière.

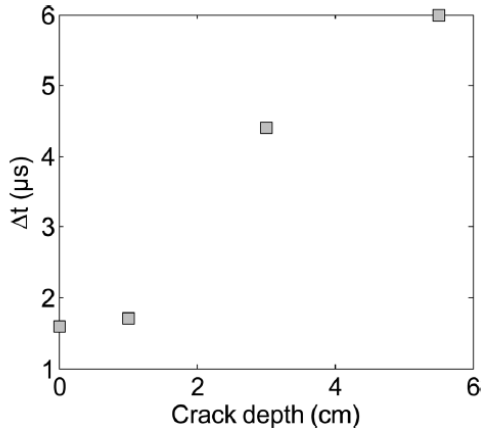

Figure 32 : Evolution de l'excursion maximale de l'ATME en fonction de la profondeur des fissures

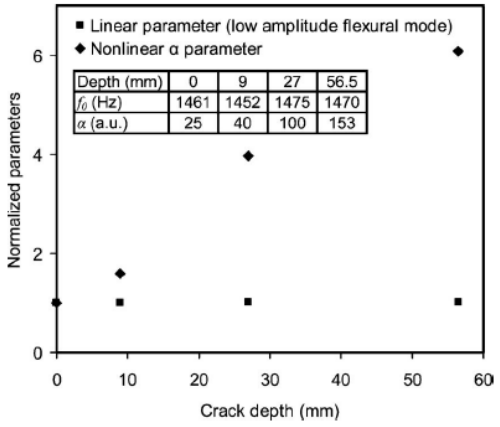

Figure 33 : Evolution de la non-linéarité mesurée par modulation sur les mêmes éprouvettes en fonction de la profondeur des fissures

6. Conclusion

Dès les années 1980, les contrôleurs CND s'interrogeaient sur la signification physique du bruit dans les matériaux métalliques à gros grains, que les méthodes de traitements de signal à l'époque avaient pour vocation de supprimer. Il est montré dans ce chapitre que la « coda » est bien porteuse d'informations. La méthodologie proposée permet de s'affranchir des problèmes théoriques de diffraction par un obstacle (pas simple car les agrégats peuvent être de toute taille et toute forme), d'homogénéisation (pas simple car ces méthodes ne sont valides que dans certaines gammes de concentration de diffuseurs) ou de simulations numériques de propagation couteuses (pas simple pour des raisons de maillage des frontières de diffuseurs). Le régime de diffusion permet de rendre compte de la réalité du matériau dans toute sa complexité par seulement deux constantes de diffusion. L'analogie peut être faite avec le CND par ultrason standardisé des matériaux homogènes métalliques avec les deux paramètres que sont la vitesse et l'atténuation des ondes. Des études systématiques sur plusieurs natures de béton, plusieurs types d'endommagements permettraient de fournir des grandeurs caractéristiques applicables à la réalité du CND en génie civil. Dans le domaine du CND des matériaux métalliques, le même type d'approche est à l'étude concernant les aciers à gros grains [BAD12, SHA13] au CEA et chez EDF, même si la physique est différente car les diffuseurs ne sont plus aléatoirement répartis due à la croissance épitaxiale des grains.

IV. Extensions thématiques

Collaborations:
Laboratoire : M. Cavaro, D. Fouan, A. Baudot, C. La Rocca, Y. Achaoui, J. Moysan, S. Mensah, E. Debieu, E. Franceschini
IMP Lyon : J. Gally, N. Coullaud
CEA Cadarache : F. Baque, J.P. Jeannot
Safran : S. Maillard, A. Baillard
Projets/contrats associés : [P5,8]/[C6,2]
Publications internationales/Brevets associées : [B1,B2,B3, B4, 8,16, 21]

1. Introduction

Ce chapitre regroupe les études concernant d'autres thèmes que le CND du béton. Les compétences physiques et expérimentales acquises au fil des années sur la thématique de l'acoustique/élasticité non linéaire font que je me suis impliqué dans d'autres voies. Cette ouverture m'a permis d'acquérir et de pouvoir apporter une vision nouvelle sur des thèmes qui peuvent sembler éloignés.

D'abord les bulles. C'est l'objet rêvé pour l'expérimentateur qui bataille des jours et des semaines avant de voir un harmonique apparaitre. Le comportement non linéaire de ces microbulles est impressionnant comparativement aux solides que j'ai pu avoir à tester. Une méthode « standard » en acoustique non linéaire a porté ses fruits pour déterminer l'histogramme des rayons d'un nuage de microbulles [CAV11a]. Avisé du comportement « non classique » des roches et des bétons en résonance, le NRUS a été appliqué à un résonateur rempli de microbulles, méthode utilisée pour déterminer le taux de vide qui a fait l'objet d'un brevet [CAV11b]. Toujours avisé des méthodes employées pour caractériser le comportement des milieux solides « non classiques », une méthode dérivée du DAET a été appliquée avec succès, permettant la mesure absolue du rayon d'une bulle (ou d'une inclusion) hors résonance [FOU15]. Cette méthode a également fait l'objet d'un brevet [FOU13]. Suite à des discussions avec Younes Achaoui, Serge Mensah et Eric Debieu au laboratoire, me remémorant des cours d'asservissement de classe préparatoire, une idée simple a permis de mettre au point un dispositif de génération de microbulles calibrées et contrôlées en temps réel (ce point ne sera pas abordé dans ce manuscrit pour des raisons de confidentialités : de brevet en cours de dépôt [ACH14]).

Historiquement, le laboratoire a surtout travaillé sur des thématiques liées au nucléaire. Cependant, des travaux sur la problématique du collage structural ont été initiés avec un stage de master en 2010. Depuis, les collaborations avec l'industrie aéronautique ont débuté et un projet ANR porté par Joseph Moysan a été accepté. Le thème de la caractérisation de l'adhésion est abordé dans cette partie. Comme le dirait justement Gilles Corneloup, la difficulté pour mettre au point une méthode de CND est la fabrication d'éprouvettes étalons représentatives du défaut que l'on cherche à contrôler. Les exemples sont nombreux au laboratoire. Par exemple, si nous savions fabriquer des éprouvettes à « mauvaise » adhésion, le process serait maîtrisé, donc nous serions en mesure de fabriquer des éprouvettes à adhésion optimale. Et pour aller jusqu'au bout du raisonnement, nous n'aurions plus besoin de

CND. Ce thème de recherche à cheval entre la physico-chimie, la mécanique et le CND fera l'objet d'une partie de ce chapitre.

Intégré au LMA en janvier 2012, je découvre le thème des ultrasons médicaux. Suite à l'achat d'un échographe de recherche dans l'équipe, j'assiste à formation organisée par le fabricant. Me rendant compte que l'on pouvait jouer sur l'amplitude des ondes, j'ai rapidement proposé de participer à une action de recherche pour tester des méthodes non linéaires. Ce fut le cas avec une application à la mort cellulaire en collaboration avec Emilie Franceschini qui travaille sur des méthodes de BSC (Back Scattering Coeficient) afin de remonter au rayon et à la densité des cellules. Les cellules, soumises à un agent chimique radioactif (chimiothérapie), se fragmentent. Il y a là une analogie avec les fissures dans les solides détectables par les méthodes d'acoustique non linéaire. Les résultats préliminaires montrent que tout se passe comme pour une fissure. Lors de l'appartition de la fissure (début de la fragmentation) la réponse non linéaire croit. Puis, une fois fragmentées (plus de phénomènes d'ouverture/fermeture), la réponse non linéaire décroit.

2. Les bulles : Engazement du sodium liquide

a. Motivation

L'étude des microbulles est initiée au laboratoire dans le contexte du contrôle de l'engazement du sodium liquide des réacteurs à neutrons rapides de quatrième génération. La présence de microbulles d'argon est continue et normale. Elle provient essentiellement de l'entrainement de l'argon situé au-dessus du sodium et des nucléation provenant des phénomènes de dissolution du gaz. Les autorités de sureté nucléaires demandent un contrôle continu de l'engazement du sodium afin de prévenir le risque d'accumulation de poches de gaz. Le sodium est un métal liquide opaque, empêchant tout contrôle optique. Les ultrasons ont donc été identifiés comme potentiel candidat à la caractérisation des microbulles. Par caractérisation, nous entendons ici fournir un taux de vide et un histogramme des rayons de bulles. Avec comme retour d'expérience les réacteurs Phénix et Superphénix, la taille des bulles à caractériser est de l'ordre de 10µm pour un taux de vide de 10^{-6}.

Les méthodes acoustiques basées sur la propagation d'ondes linéaire comme la vitesse ou l'atténuation requièrent un a priori sur la taille, ce qui n'est pas acceptable du point de vue des exigences de sureté. En effet, une bulle résonante peut être confondue avec une bulle non résonante beaucoup plus grosse et les mesures de vitesses requièrent d'être en régime basse fréquence, dépendant du rayon des bulles en présence. Les méthodes issues de l'acoustique non linéaire se sont donc imposées car le comportement des bulles est fortement non linéaire et une bulle peut être détectée et caractérisée sans ambigüité.

Il existe beaucoup de modèle décrivant la dynamique d'évolution du rayon d'un bulle soumise à une onde acoustique. Retenons ici l'équation de Rayleigh modifiée [LAU76]:

$$\rho R\ddot{R} + \frac{3}{2}\rho\dot{R}^2 = \left(p_0 + \frac{2\sigma}{R_0} - p_v\right)\left(\frac{R}{R_0}\right)^{3\gamma} - \frac{2\sigma}{R_0} - \frac{4\mu}{R}\dot{R} + p_v - p_0 - P(t) \quad (3)$$

Où R est le rayon instantané, R_0 le rayon à l'équilibre, le point ($\dot{}$) désigne la dérivée temporelle, ρ la densité du liquide, γ le coeficient polytropique, µ la viscosité dynamique du

liquide, σ la tension de surface, p_v la pression de vapeur saturante, p_0 la pression statique, P(t) le champ de pression acoustique. La linéarisation de cette équation permet d'exprimer la fréquence de résonance, dites fréquence de Minnaert [MIN33], d'une bulle en fonction de son rayon :

$$f_{\text{res}} = \frac{1}{2\pi R_0}\sqrt{\frac{3\gamma p_0}{\rho}}. \tag{4}$$

Le couple sodium/argon ayant les mêmes caractéristiques que le couple eau/air, pour des raisons de facilité expérimentale, les campagnes d'essais sont réalisées dans l'eau. La génération de bulles est ici réalisée par aéroflottation, technique basée sur l'établissement d'un état de sursaturation en gaz dissous menant à un phénomène de nucléation de bulles. Afin de valider les mesures ultrasonores, un dispositif optique immergé contrôle le nuage de bulle ainsi généré (Figure 34). Un algorithme de traitement d'image permet de reconstruire l'histogramme optique des rayons de bulles (Figure 36). Les détails concernant la génération de bulles et le traitement d'image sont rapportés dans [CAV10].

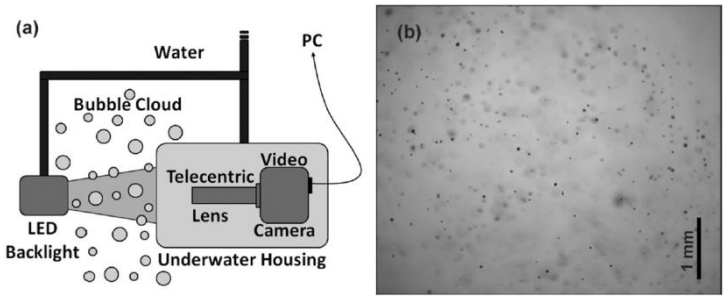

Figure 34 : Dispositif de contrôle optique du nuage de microbulles

b. Méthode bifréquences

L'excitation d'une bulle à sa fréquence de résonance (f_1) conduit à l'apparition de fréquences multiples et sous-multiples telles que ses harmoniques ($n.f_1$). Dans le cas d'une excitation bifréquentielle ($f_1<f_2$), si f_1 correspond à la fréquence de résonance de la bulle, le mixage des différentes fréquences conduit en plus à l'apparition de fréquences sommes et différences ($f_2 \pm nf_1$). L'estimation de la taille se fait par la mesure de ces fréquences sommes et différences. La Figure 35(a) montre le dispositif expérimental employé avec une haute fréquence continue à 2,25 MHz, et une basse fréquence balayant entre 10 et 500kHz. Un récepteur centré à 2,25MHz enregistre les signaux réfléchis dont des exemples de spectres sont fournis Figure 35(b).

L'algorithme employé pour construire un histogramme acoustique (Figure 36) est simple. Un seuil est défini sur le spectre fréquentiel au dessus du niveau de bruit. Dès qu'une composante apparaît dans l'intervalle [ωi-500kHz,ωi[∩]ωi+500kHz], la position du maximum dans cette zone donne la fréquence de résonance de la bulle.

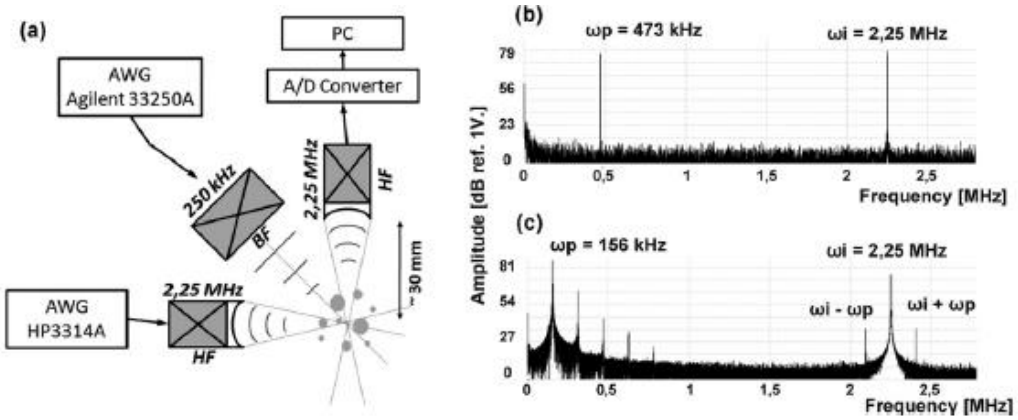

Figure 35 : (a) Dispositif expérimental. (b) exemple de spectre avec (en bas) et sans (en haut) présence de bulle résonante.

L'équation 4 permet alors de calculer le rayon par R=3,3/ωp (pour le couple air/eau), et l'histogramme des rayons est alors incrémenté. L'analyse d'environ 2000 séquences acoustiques de 5 ms a ainsi permis de reconstruire l'histogramme présenté Figure 36. Pour comparaison, l'histogramme obtenu optiquement est également présenté.

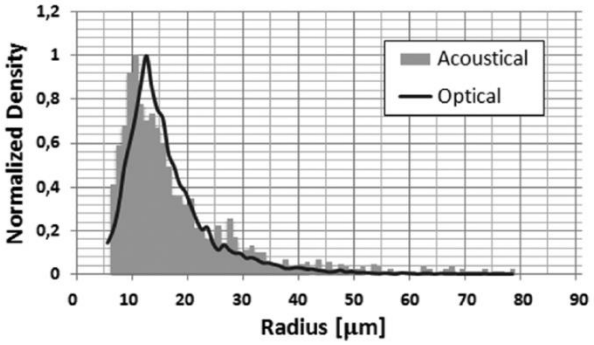

Figure 36 : Comparaison des histogrammes optiques et acoustiques

La littérature sur le sujet de la mesure de rayon de bulle par méthodes bi fréquences est riche depuis les années 1970 [ZAB73, NEW84, CHA85, KOL92, SUT98, BUC05]. Cependant, les histogrammes obtenus par méthodes optiques et acoustiques présentent ici une concordance qui n'a jamais été atteinte. Contrairement à la plupart des travaux antérieurs, nous avions fait le choix de ne pas travailler sur les amplitudes des fréquences sommes et différences mais sur leurs apparitions seulement. Ceci a simplifié le traitement des signaux, qui associée à l'absence d'amplificateurs (générateurs de non-linéarités) et à une électronique 12 bits permet d'obtenir des résultats concluants.

c. Résonateur de Helmholtz « bulleux » linéaire

La méthode précédente permet d'obtenir un histogramme des rayons d'un nuage de microbulles. Cependant, l'incertitude sur la zone d'interaction des ultrasons [CAV10] ne permet pas de déterminer le taux de vide. Le taux de vide peut être obtenu par mesures de vitesses basses fréquences, basse fréquence impliquant de se trouver loin de la fréquence de résonance des bulles, donc d'avoir un a priori sur leurs tailles. Afin de remédier à cette

limitation, la mesure de célérité dans le nuage de bulles est effectuée non pas par propagation d'ondes, mais via la fréquence de résonance d'un résonateur de Helmholtz [HEL85]. Pour une géométrie de résonateur donnée (section et longueur du col A et L, volume V) la fréquence de résonance s'écrit en fonction de la célérité dans le milieu $f=c/2\pi\sqrt{(A/VL)}$. Le résonateur employé (Figure 37(a)) pour les validations expérimentales est un magnum de champagne, dont les parois sont suffisamment rigides pour supporter la pression.

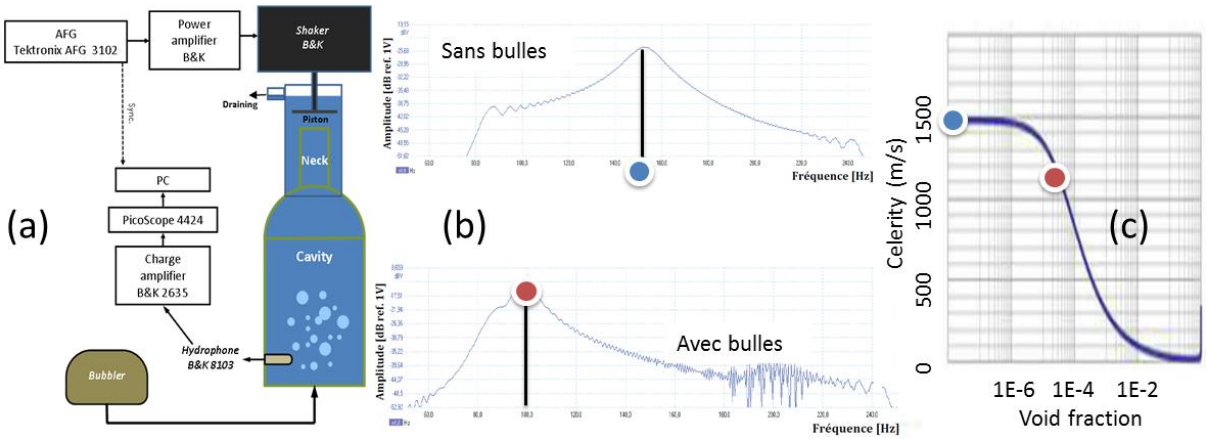

Figure 37 : (a) Résonateur de Helmholtz employé. (b) Spectre fréquentiel donnant la fréquence de résonance avec (dessous) et sans bulle (dessus). (c) Détermination du taux de vide par le modèle de Wood.

La mesure de cette fréquence de résonance (Figure 37(b)) permet d'obtenir la célérité. Par ailleurs, une loi de mélange (modèle de Wood) permet de relier la célérité au taux de vide dans le milieu [WOO41] en fonction des propriétés du gaz et du liquide (Figure 37(c)). Le taux de vide déterminé ici est de 6.10^{-6}, correspondant aux mesures optiques réalisées dans la partie précédente.

d. Résonateur de Helmholtz « bulleux » non linéaire

Dans cette partie la transposition des méthodes de résonances non linéaires appliquées dans les solides (Chapitre II) est étudiée. La fréquence de résonance est déterminée en augmentant l'amplitude des oscillations du piston, donc la pression. Afin de remonter à des informations physiques, un modèle de résonateur diphasique non linéaire a été imaginé par Serge Mensah. Ce modèle est résumé Figure 38. La description détaillée du modèle est disponible dans [CAV10, CAV12].

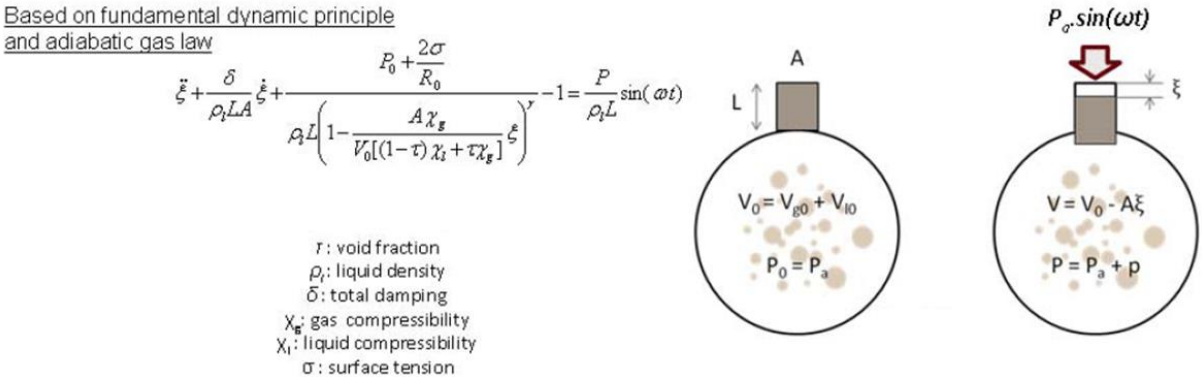

Figure 38 : Description du modèle de résonateur diphasique

Le résonateur est simulé numériquement (Figure 39). La similitude avec la courbe de résonance non linéaire d'une roche issue de la littérature [TEN98] est frappante, montrant que les mêmes phénomènes physiques régissent le comportement de ces deux milieux. Le comportement non linéaire des microbulles dans ce résonateur joue le rôle des micro- fissures présentent dans les roches. Macroscopiquement (à l'échelle du résonateur entier) les mêmes phénomènes, comme l'hystérésis (non montré ici), les instabilités, le décalage de la fréquence de résonance avec l'amplitude, sont observés.

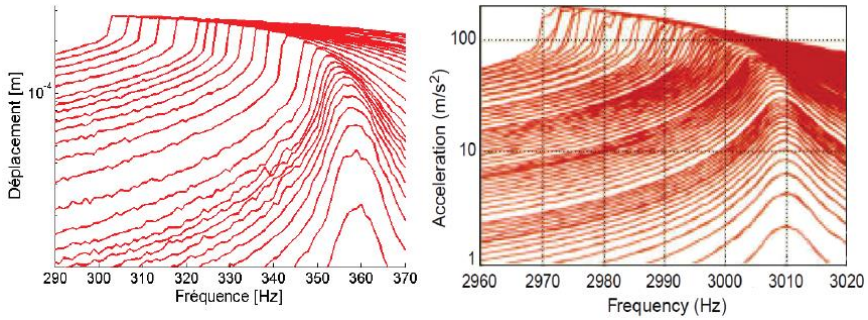

Figure 39 : Courbes de résonances à différentes amplitudes obtenues numériquement sur un nuage de bulles à basse fréquence (à gauche) et expérimentalement sur du grès [Ten98] (à droite)

Expérimentalement, des décalages de fréquences de résonances en fonction de l'amplitude ont été observés pour différents taux de vides (Figure 40). Les taux de vides sont obtenus par le modèle de Wood, via la fréquence de résonance à faible amplitude (régime linéaire).

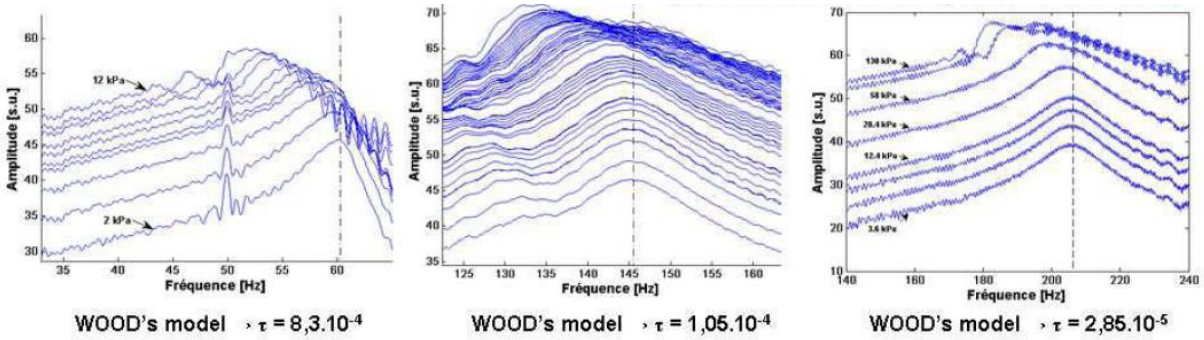

Figure 40 : Courbes de résonances non linéaires pour différents taux de vide obtenus par la fréquence de résonance à faible amplitude (régime linéaire)

Les travaux sont toujours en cours sur ce thème en collaboration avec Matthieu Cavaro et Serge Mensah. Expérimentalement, des problèmes liés à la présence de bulles de cavitation millimétriques dans le résonateur ont été observés. La première courbe liant qualitativement la non-linéarité au taux de vide a été obtenue [CAV12]. Reste à vérifier si ce comportement est confirmé par la simulation numérique en incluant des données quantitatives du nuage de bulle dans le résonateur.

3. Les bulles : mesure absolue de rayon hors résonance

Le contexte de cette étude est la thèse de Damien Fouan, thèse CIFRE en partenariat avec la société BF systèmes. L'objectif concerne la prévention des accidents de désaturation chez les plongeurs par estimation du nombre et de la taille des bulles de gaz présentes dans le sang in situ (pendant les paliers de décompression ou en surface). Le retour d'expérience montre que les bulles à mesurer sont dans la gamme 1-200µm. Ce contexte implique un cahier des charges précis :

- Une mesure rapide (<20ms) car les bulles étant circulantes, elles ne passeront dans la zone d'interaction acoustique que pendant une durée limitée.
- Un index mécanique MI <0,3 (MI = pression acoustique / √fréquence) signifiant que l'amplitude des ondes doit évidemment être sans conséquences pour le plongeur.
- Une mesure simple car l'objectif est la mesure in situ, pendant la plongée, réalisée par la plongeur lui-même.

Arrivé en 2012 au LMA, ce partenariat était déjà en cours, Damien Fouan avait déjà commencé sa thèse sous la direction de Serge Mensah. C'est fin 2012 que j'ai commencé à collaborer avec Damien et Serge sur cette thématique suite à la publication d'un article de Guillaume Renaud [REN12b] qui appliquait une méthode originale (issue du DAET) pour mesurer des variations relatives de rayons d'agents de contrastes. Au fait de ce type d'approche du point de vue de la mesure de non-linéarité dans les solides, au fait du comportement dynamique des bulles, je me suis naturellement impliqué dans cette thématique.

Le principe de cette estimation de taille est fondé sur une double modulation (temps de vol et amplitude) d'une haute fréquence par une basse fréquence. En immersion, une bulle est accrochée à un fil de 80µm de diamètre (Figure 41(a)). Soumise à une basse fréquence, la bulle vibre et oscille autour de son rayon nominal R_0 (Figure 41(c)). Durant ses oscillations, une impulsion ultrasonore haute fréquence se réfléchit sur la bulle (Figure 41(b)). L'amplitude et le temps de vol de l'onde sont modulés en fonction du rayon instantané de la bulle.

Dans cette configuration, la modulation d'amplitude est sensible aux variations de sections de la bulle dans le plan yz (Figure 41(a)). Supposant une vibration sur son mode 0 (mode respirant), la variation relative de rayon est donnée par $\Delta R/R_0 = \Delta A/A_0$. La modulation de temps de vol est sensible quant à elle aux variations dans la direction x (Figure 41(a)).

Sous les mêmes hypothèses, la variation absolue de rayon est donnée par $\Delta R = - \Delta t\, c / (2\cos\theta)$ où c est la célérité dans le milieu et θ l'angle d'incidence de l'onde. En combinant les deux équations (première divisée par la seconde) il est possible de déterminer le rayon de la bulle à l'équilibre $R_0 = - 2\, \Delta A \cos\theta / [A_0\, \Delta t\, c]$.

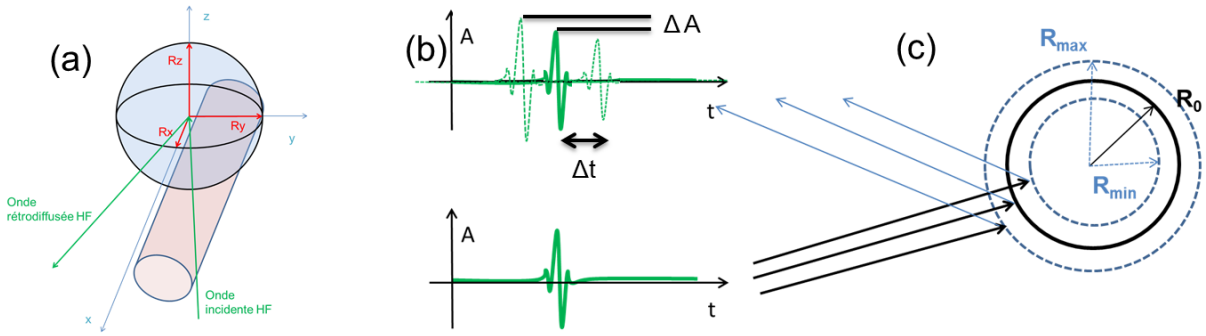

Figure 41 : (a) Bulle accrochée à un fil. (b) Modulations de temps de vol et d'amplitude des impulsions ultrasonores en fonction de la variation de rayon (c) de la bulle.

Il apparaît donc possible de déterminer acoustiquement le rayon d'une bulle même si cette dernière ne résonne pas. Rappelons le contexte qui impose que la caractérisation doit être réalisée dans un intervalle de 20 ms. Cette contrainte entraine que la fréquence de répétition des ondes hautes fréquences doit être élevée. A cette contrainte, s'ajoute celle du moyennage des signaux nécessaire pour obtenir un bon rapport signal à bruit. Par ailleurs, un prototype basé sur la méthode doppler a été développé par la société BF Systèmes. De manière à réaliser un appareillage unique, il convient d'utiliser les mêmes sondes hautes fréquences centrées à 1MHz. Toutes ces contraintes mises bout à bout entrainent qu'il est impossible d'employer telle quelle la méthode proposée ci-dessus.

Dans le but donc de réduire le temps de mesure, la même approche est appliquée à des signaux haute fréquence continus à 1MHz. Le principe est résumé Figure 42. L'amplitude de la haute fréquence est estimée dans le domaine fréquentiel sur le spectre en amplitude. Un signal continu à 1MHz est construit numériquement. Le déphasage $\Delta\Phi$ entre le signal expérimental et le signal idéal construit numériquement est estimé à 1MHz sur le spectre de phase. Le décalage temporel correspondant est obtenu par $\Delta t = \Delta\Phi / (2\pi 10^6)$. Un filtre passe haut est appliqué pour corriger le mouvement éventuel de la bulle pendant la mesure.

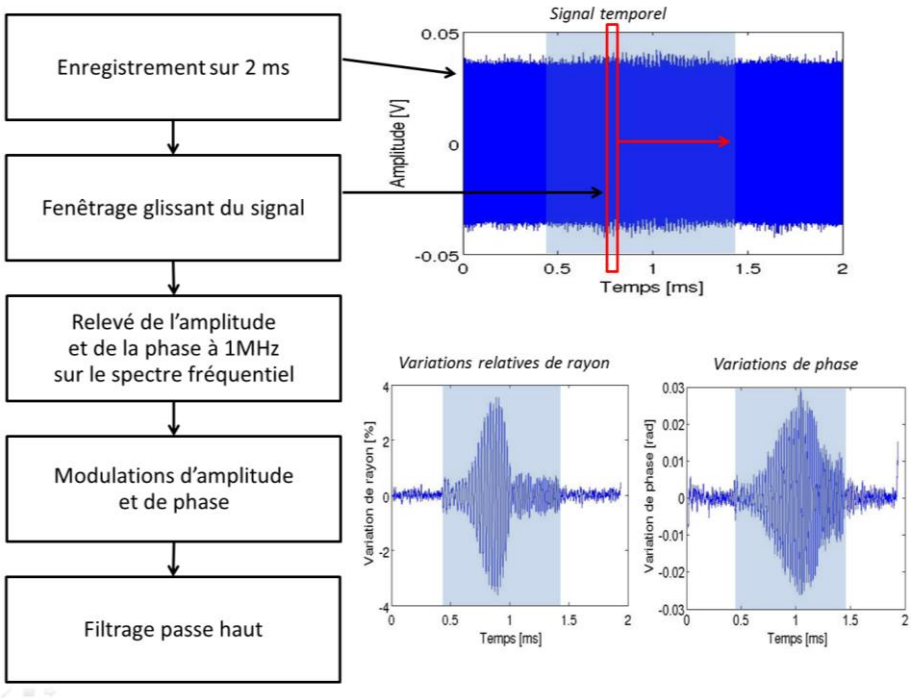

Figure 42 : Principe de la mesure absolue de rayon en mode continu. En transparence le temps pendant lequel la basse fréquence fait vibrer la bulle.

A ce stade, ayant estimé $\Delta R/R_0$ par modulation d'amplitude et ΔR par modulation de phase, le rapport entre les enveloppes des deux courbes obtenues donne le rayon à l'équilibre R_0 (Figure 43).

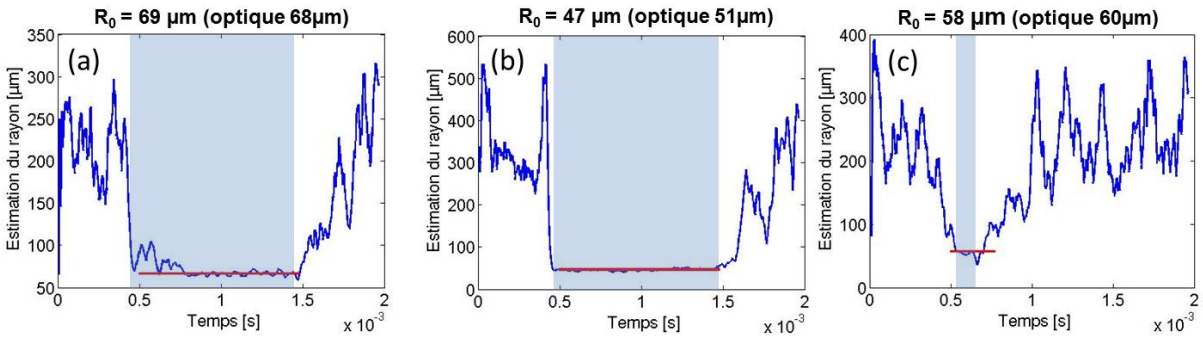

Figure 43 : Rapport des enveloppes et détermination du rayon pour une basse fréquence en mode (a) balayage en fréquence 30kHz-60kHz, (b) continue 60kHz et (c) impulsionnelle. En transparence le temps pendant lequel la basse fréquence est en marche. Pour comparaison, une mesure optique du rayon de la bulle est également effectuée.

Trois types de basses fréquences sont employés. Tout d'abord une basse fréquence d'une durée de 1 ms qui balaye les fréquences entre 30kHz et 60 kHz (Figure 43(a)), passant par la fréquence de résonance de la bulle ; puis un train d'onde basse fréquence de 1ms à 60kHz, hors de la résonance de la bulle (Figure 43(b)) ; enfin, une impulsion basse fréquence large bande (Figure 43(c)). Pour comparaison et validation, le rayon de la bulle est également déterminé optiquement. La concordance entre les deux est très bonne. Il est démontré que le rayon de la bulle peut bien être déterminé hors de la fréquence de résonance.

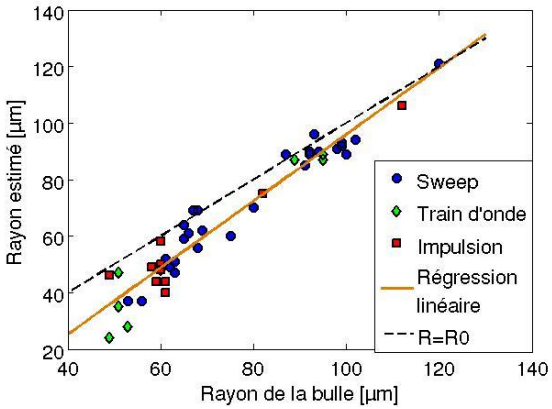

Figure 44 : Comparaisons entre les mesures de rayon de bulles acoustiques et optiques pour différents types de basses fréquences.

L'ensemble des mesures réalisées suivant cette méthode est synthétisé Figure 44 avec différents types de basse fréquence. Les rayons estimés sont systématiquement en bon accord avec le rayon mesuré optiquement. Cependant, il est remarquable que les mesures s'éloignent de la courbe idéale ($R=R_0$) en se rapprochant des faibles rayons. Ceci est sans doute dû à l'interaction entre le fil et la bulle qui y est accrochée. Accrochée au fil, la bulle n'est pas parfaitement sphérique, induisant de surcroit des vibrations non symétriques, hypothèse de base permettant de déterminer le rayon de la bulle. Cette interaction est d'autant plus importante que la bulle est petite.

4. Caractérisation de l'adhésion

a. Contexte

La thématique présentée ici est abordée du point de vue de l'industrie aéronautique, même si les champs d'applications potentiels sont bien plus vastes et s'étendent du génie civil (réparation par collage de plaques composites), l'énergie (pales d'éoliennes), l'industrie navale… Lorsqu'un assemblage est réalisé par collage, les exigences en termes de certifications imposent des procédures drastiques pour valider la qualité de ce dernier. A ce jour aucune méthode de CND ne le permet. La solution est soit d'ajouter des rivets, soit réaliser une gamme d'éprouvette suiveuses pour chaque produit dont une partie est conservée et l'autre testée mécaniquement. Ces éprouvettes permettent de valider un niveau mécanique minimal mais ne répondent pas au problème initial qui est de qualifier le niveau d'adhésion. De plus ce procédé est long (fabrication des éprouvettes, réalisation des essais mécaniques et analyses des résultats) et coûteux. Trouver une méthode permettant de contrôler le niveau d'adhésion, permettrait de diminuer le nombre d'éprouvettes et donc le coût.

Le problématique est résumée Figure 45(b). Sur 10 éprouvettes confectionnées en même temps, suivant rigoureusement le même mode opératoire (préparation de surface, type de colle, séchage…), huit présentent les caractéristiques mécaniques escomptées, alors que deux cassent à un niveau plus faible. Ce comportement peut être dû à des défauts dans le joint de colle (Figure 45(a)). Tous les défauts ici présentés sont détectables par méthodes de CND excepté les zones de cohésion faibles et les zones de faible adhérence. Une gamme de

formulation maitrisée et un cycle de polymérisation optimal limitent ce dernier problème. Mais à ce jour, la problématique de la caractérisation de l'adhésion reste entière.

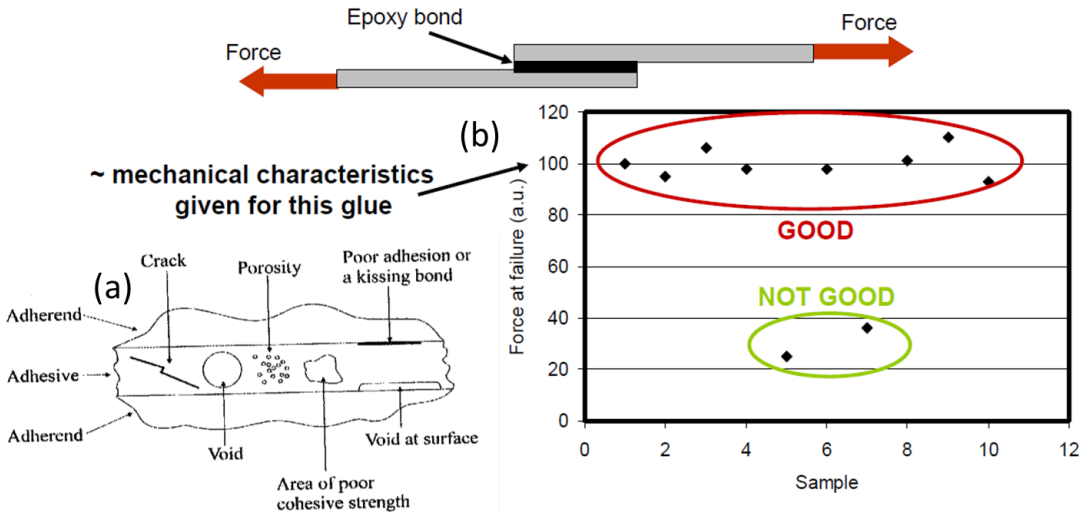

Figure 45 : (a) [ADA99] différentes type de défauts dans un joint de colle. (b) Définition d'un bon et mauvais collage

b. Premières analyses

Cette thématique débute en 2010 au laboratoire avec un stage de master. L'objectif étant dans un premier temps d'étudier le potentiel des ultrasons non linéaires pour discriminer des défauts de type adhésifs ou cohésifs (Figure 46).

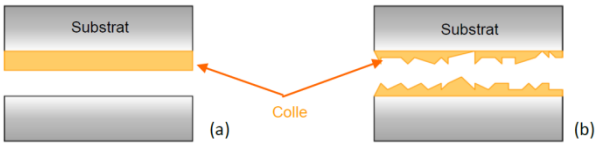

Figure 46 : (a) Rupture adhésive. (b) Rupture cohésive.

La méthode employée consisté à étudier l'évolution du coefficient de transmission à l'interface en fonction de l'amplitude d'une sollicitation dynamique appliquée. L'approche est similaire à celle présentée au chapitre III, partie 5. Un pot vibrant excite une poutre d'aluminium en flexion (Figure 47(a)). Un patch est collé près de l'encastrement, endroit où les contraintes sont maximales. Un transducteur ultrasonore à 5MHz en mode écho sonde l'interface durant la sollicitation. L'énergie En du signal réfléchi (Figure 47(b)) est déterminée et associée à l'amplitude du déplacement (A). L'ensemble des données permet de tracer l'évolution de l'énergie réfléchie en fonction du niveau de sollicitation dynamique (Figure 47(c)) et d'en extraire une information quant à la non-linéarité. Le détail du protocole expérimental est disponible dans [ROC10], accessible gratuitement en ligne.

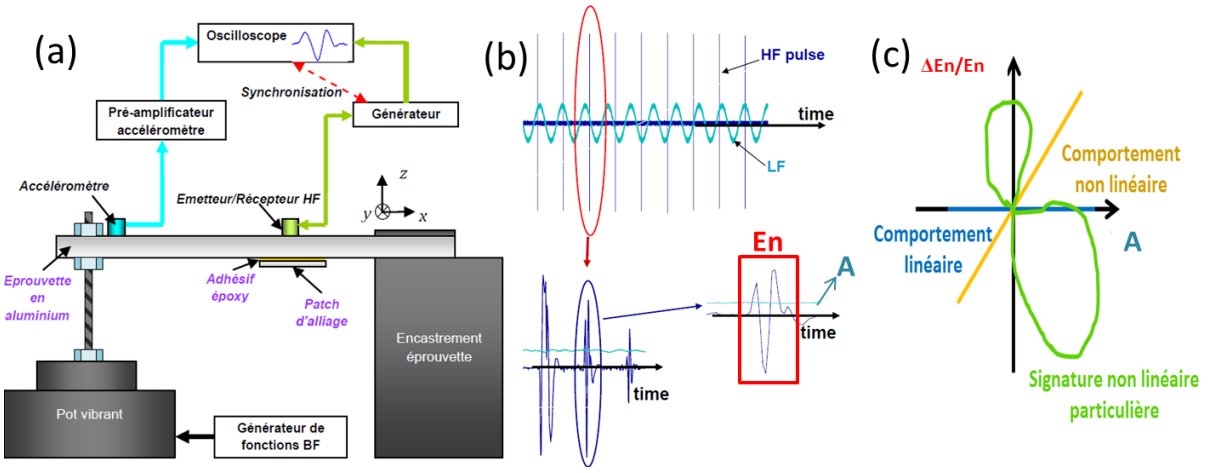

Figure 47 : (a) Dispositif expérimental. (b) Traitement des signaux. (c) Exemple de signatures non linéaires

Des éprouvettes avec traitement de surface et polymérisation optimale (référence), sans traitement de surface et polymérisation optimale (défaut d'adhésion) et avec traitement de surface et polymérisation dégradée (défaut de cohésion) sont confectionnées. Les résultats sont fournis Figure 48.

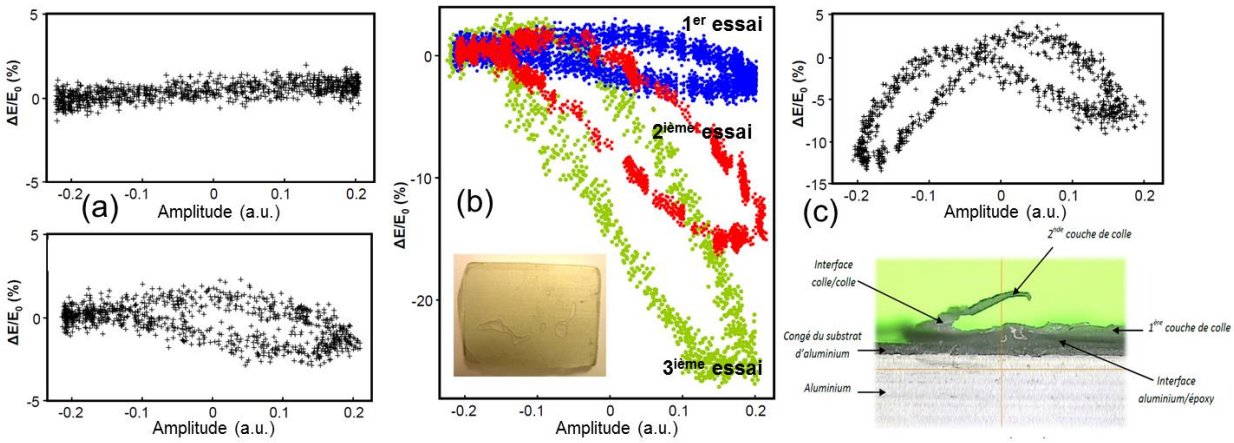

Figure 48 : Signatures non linéaires pour les éprouvettes (a) de référence, (b) avec défaut d'adhésion et (c) défaut de cohésion.

Les deux éprouvettes de référence montrent un comportement quasi linéaire (Figure 48(a)), avec pour la seconde une légère hystérésis. Une éprouvette avec défaut d'adhésion montre un comportement hystérétique et non linéaire (Figure 48(b)). La pente des tendances, donc la non-linéarité, croit jusqu'à la rupture. Le type de rupture est bien de type adhésif, le joint de colle se trouvant après rupture côté patch uniquement. L'éprouvette avec défaut de cohésion (Figure 48(c)) montre quant à elle une signature particulière avec une forme en « 8 ». Cette éprouvette a bien un défaut de cohésion car après rupture, le joint de colle se trouve en partie sur l'éprouvette et en partie sur le patch.

L'objectif initial est atteint, c'est-à-dire, identifier une signature non linéaire propre au comportement de type cohésif ou adhésif. Cependant, il est important de souligner que ces résultats ne sont que qualitatifs. En effet, à 5MHz, la longueur d'onde est telle qu'il est impossible de discriminer l'écho provenant de l'entrée et celui provenant de la sortie du joint

de colle. Par ailleurs, le comportement cohésif n'est pas significatif des besoins actuels car les procédures de collage industrielles permettent de maîtriser ce problème. Ces résultats donc, bien qu'encourageants, ne permettent pas de quantifier le niveau d'adhésion. C'est l'objet de la section suivante.

c. Caractérisation des paramètres critiques de l'adhésion

Cette étude est entamée en 2012 avec la thèse CIFRE d'Alice Baudot avec Safran. Dans le cadre d'un contrat de collaboration avec le Laboratoire d'Ingénierie des Matériaux Polymères (IMP, UMR CNRS 5223), une ingénieure est en charge de la réalisation d'assemblages collés de niveaux d'adhésion variable et contrôlée. Ces assemblages sont de type aluminium / adhésif époxy / aluminium, de type éprouvette de cisaillement simple selon la norme NF EN 2243-1. Les éprouvettes sont de dimension 25x100x1,6 mm^3. La zone de recouvrement est de 12,5x25 mm. Le niveau d'adhésion est déterminé par essai mécanique standardisé en cisaillement simple, réalisé à l'IMP. La contrainte à la rupture étant évaluée, selon la norme, par la force à la rupture divisé par la surface de recouvrement. Après rupture, le faciès de rupture est analysé afin de vérifier si la rupture a bien été de type adhésive, comme escompté.

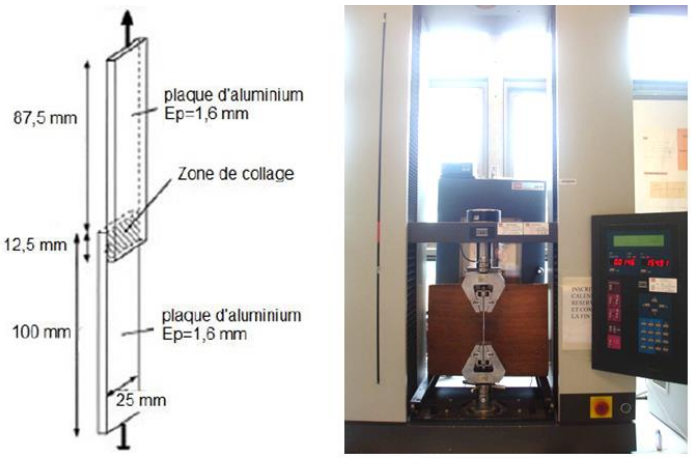

Figure 49 : Eprouvettes réalisée selon la norme NF EN 2243-1

Un protocole de fabrication précis est élaboré, incluant l'optimisation de la découpe des éprouvettes, d'un moule sur mesure, d'une formulation de l'époxy, de la quantité de colle, du traitement de surface, d'un cycle de temps/température/pression de polymérisation, de la viscosité par ajout de particules… Les détails des traitements et validations physico chimiques sont fournis dans [BAU14] disponible au chapitre VIII. Il est rapidement apparu que ce ne serait pas simple de réaliser des lots d'éprouvettes homogènes, à épaisseur calibrées et à adhésion variables (comme indiqué en début de chapitre). Les premiers travaux en CND ont donc porté sur le soutien à l'élaboration du protocole de fabrication, en collaboration étroite avec l'IMP.

L'objet des CND est ici de vérifier l'homogénéité des joints de colle. Pour cela, une série de Cscans ultrasonores hautes fréquence en immersion est réalisé. Les transducteurs employés sont hautes fréquences (~20MHz) et focalisés afin de réaliser des images bien résolues des joints de colles (Figure 50(a)). La taille de la tache focale à -6dB est de 0,3mm, le pas de

déplacement est de 0,2mm. Les images ultrasonores obtenues Figure 50(b) représentent l'amplitude transmise. Les points 1, 2, 3 et 4 correspondent respectivement aux signaux 1, 2, 3 et 4 Figure 50(a). Une fois les Cscans réalisés, les éprouvettes sont retournées à l'IMP pour déterminer le niveau d'adhésion correspondant et analyser le faciès de rupture (Figure 50(c)). Les résultats montrent une bonne corrélation entre les faciès de ruptures et les images ultrasonores. Ces derniers confirment bien une rupture de type adhésive car sur les deux faciès présentent systématiquement de la colle d'un côté et le substrat de l'autre (Figure 50(c)). Il n'a jamais été observé d'époxy des deux côtés. La zone identifiée Al-Al correspond à un trou (manque de colle).

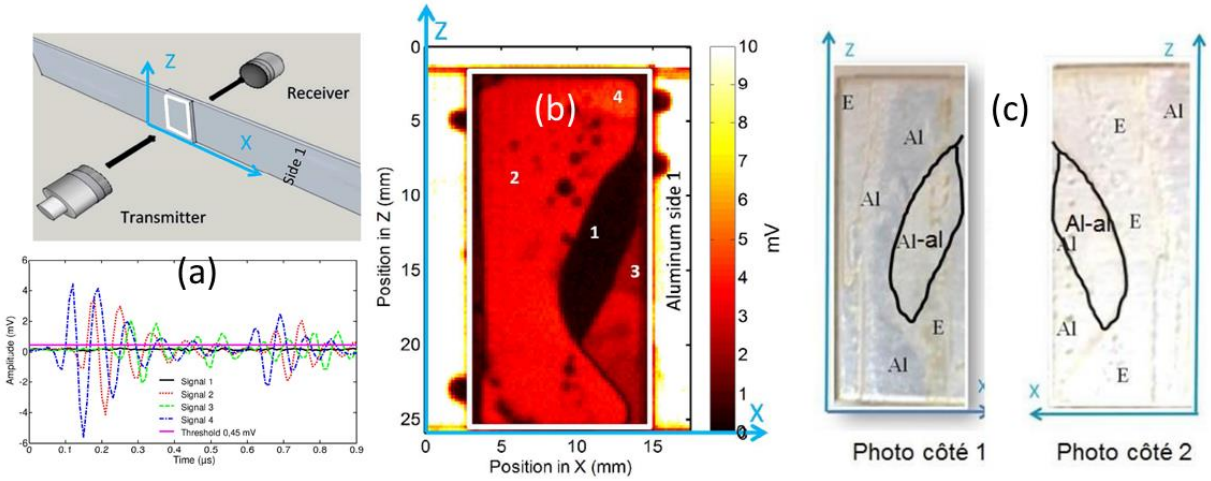

Figure 50 : (a) Configuration expérimentale et exemple de signaux transmis. (b) Image Cscan ultrasonore correspondante. (c) Faciès de rupture (Al = aluminium, E= Epoxy)

Par ailleurs, le dimensionnement des défauts via un traitement d'image par seuillage permet de déterminer l'aire de collage effective, permettant de corriger les valeurs de contraintes à la rupture (Figure 51). L'exemple fourni Figure 51 montre que les deux lots considérés, sans correction de la surface effective, pouvaient être considérés comme présentant deux niveaux d'adhésion distincts. L'ensemble des méthodes et traitements sont détaillés dans [BAU14] disponible au chapitre VIII.

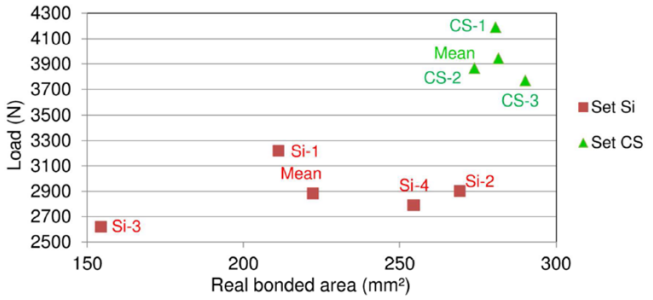

Final Sets	Surface treatment	Average/std σ (MPa) / std Uncorrected	Average/std Bonded area (mm²)	Average/std σ (MPa) / std Corrected	Number of samples
AA-Si	Silanization	9.2 / 0.7	222.3 / 51.5	13 / 3.1	4
AA-SC	Chromic-sulfuric	12.6 / 0.7	281.5 / 8.20	14.0 / 1	3

Figure 51 : Exemple de surfaces collées corrigées pour deux lots et correction de la contrainte à la rupture.

Ces études ultrasonores de qualification des lots d'éprouvettes se sont révélés concluantes car elles ont permis de mettre à jour des défauts qui n'étaient pas visibles, ni prévisibles. Elles ont également permis de proposer de nouvelles formulations d'époxy pour améliorer la viscosité de la colle. Grace à ces échanges, à ce jour, des éprouvettes à adhésion variables ont bien été obtenues. Un protocole d'imagerie ultrasonore sous sollicitation a été

développé dans le cadre de la thèse d'Alice Baudot afin de combiner les approches présentées dans cette partie et dans la précédente. Un brevet SAFRAN/LMA [BAU15] est en cours de traitement, les résultats ne seront donc pas présentés dans ce manuscrit.

5. Le suivi de la mort cellulaire

Dans le domaine de l'imagerie ultrasonore pour le biomédical, la majeure partie des études traitant de la non-linéarité acoustique concerne les agents de contrastes [BOR03]. Les agents de contrastes sont des microbulles encapsulées dans un milieu visqueux, injectées dans le sang, conçues pour améliorer le contraste des images échographiques. Concernant les tissus, la possibilité d'imager la non-linéarité peut constituer un moyen d'identification et de caractérisation. Plusieurs méthodes permettent d'extraire une information relative à la non-linéarité des milieux dont la plus utilisée est la génération d'harmoniques (cf chapitre II) qui permet d'extraire le paramètre β. Cependant cette méthode nécessite des sondes larges bandes (capables de générer le fondamental et détecter le fondamental et le deuxième harmonique) et le problème majeur est le découplage de la non-linéarité physique de la non-linéarité électronique intrinsèque à l'équipement utilisé. Une nouvelle méthode basée sur la transmission d'ondes à plusieurs amplitudes est assez prometteuse. Développée par Scalerandi et al. [SCA10], la Scaling Substraction Method (SSM) permet d'extraire la non-linéarité des milieux même avec des sondes dont la bande passante est limitée. Le principe est simple : une onde avec une amplitude A_1 est transmise à travers le milieu, la réponse enregistrée par le récepteur est notée s_1. L'amplitude est augmentée d'un facteur 2 ($A_2=2A_1$), le signal reçu est noté s_2. Si le milieu est linéaire, le signal noté ssm = (s_2 - A_2/A_1 x s_1) est nul. Si le milieu est non linéaire, l'énergie du signal ssm est évaluée à plusieurs amplitudes, permettant de déterminer la non-linéarité globale du milieu. Cette méthode de traitement globale permet une estimation qualitative de la non-linéarité. En effet, tous les types de non-linéarité sont inclus dans ce traitement, aussi bien l'atténuation non linéaire que les harmoniques potentielles ou tout autre phénomène non linéaire. Outre son utilisation pour le CND des solides, les méthodes de non-linéarités sont également employées pour des tissus osseux [MUL06] permettant de détecter des micro fissurations ou micro endommagements.

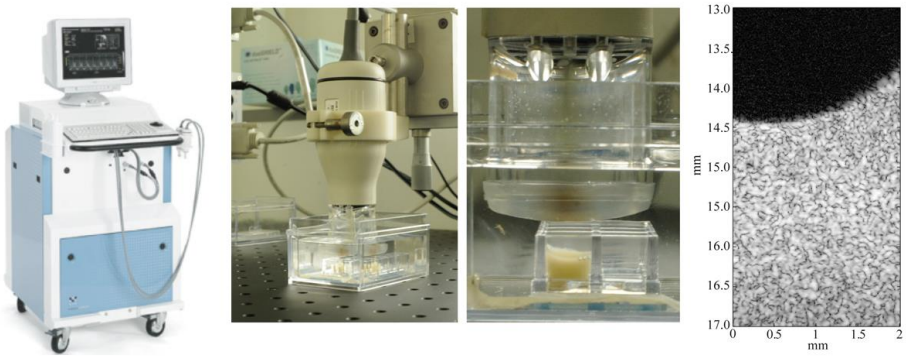

Figure 52 : Echographe Visulasonics Vevo 770 (à gauche). Image de la sonde employée et des chambres de culture remplies de cellules (au milieu). Exemple d'image échographique obtenue (à droite).

A notre connaissance, aucune étude n'a été menée avec ces techniques pour le suivi d'un processus apoptotique. Pourtant, le processus par lequel une cellule déclenche son auto-destruction est similaire à des processus d'endommagement des solides : le cytoplasme se condense, le noyau se décompose et l'ADN s'émiette, puis le noyau se fragmente formant plusieurs corps apoptotiques.

Une expérience préliminaire a été mise en place pour évaluer le potentiel de la technique ultrasonore de non-linéarité pour quantifier la mort cellulaire (apoptose). Un échographe de recherche Visulasonics Vevo 770 est utilisé (Figure 52). Des cellules K562 (lignée cellulaire de leucémie humaine) sont placées dans des chambres de culture et immergées pour réaliser l'image échographie (Figure 52). La même image est réalisée pour plusieurs niveaux d'amplitudes pour employer la méthode SSM. Le paramètre non linéaire évalué Figure 53 est la non-linéarité globale moyennée sur tous signaux ultrasonores issus de l'image échographique. Ces cellules sont traitées avec un agent chimiothérapeutique cisplatinum à 10 µg/mL provoquant l'apoptose des cellules. Au temps 0h, les cellules sont traitées avec cette drogue durant 6, 12, 24 et 48h. Avant l'acquisition ultrasonore, les cellules sont traitées (lavage et centrifugation) de manière à simuler l'entassement des cellules dans les tissus. Les mesures ultrasonores sont réalisées dans l'heure suivant le traitement. Les premiers résultats obtenus (Figure 53) montrent que la technique SSM (Scaling Substraction Method) permet de détecter les phases de condensation et de fragmentation de l'ADN (aux temps 6 et 12 heures). En effet, le paramètre de non-linéarité augmente de façon significative au temps 6 et 12 heures lors des phases de condensation et de fragmentation de l'ADN, puis le paramètre de non-linéarité est à nouveau proche de sa valeur initiale au temps 24 et 48 heures lorsque les noyaux/cellules se fragmentent pour former des corps apoptotiques.

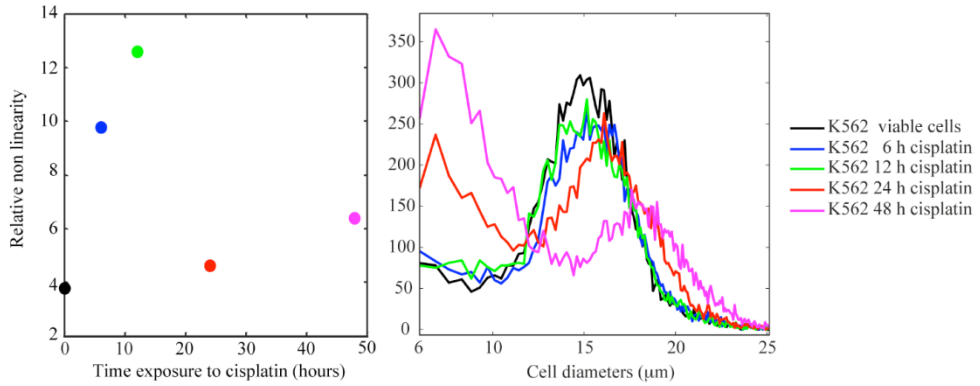

Figure 53 : (A gauche) Paramètre de non-linéarité en fonction de différents temps d'exposition à l'agent chimiothérapeutique cisplatinum (0, 6, 12, 24 et 48 heures). (A droite) Histogrammes de tailles des cellules mesurés avec un compteur de cellules pour différents temps d'exposition à l'agent chimiothérapeutique.

Ces résultats sont encourageants, cette voie sera poursuivie. Nous nous intéresserons à l'évaluation locale de la non-linéarité par la méthode SSM. Un effort particulier sera apporté au traitement des données permettant l'estimation quantitative de la non-linéarité. Nous explorerons plusieurs possibilités de normalisation des signaux ssm et de traitement dans le domaine temporel ou fréquentiel. L'objectif étant in fine de trouver une méthode

d'exploitation transposable à tous les types de conditions expérimentales et plus particulièrement in vivo.

6. Conclusion

Ce chapitre aborde beaucoup de thématiques différentes dans lesquelles je me suis impliqué au fil des années. Ces études ne sont pas le fruit d'un projet de recherche élaboré sur le long terme, mais le fruit d'échanges scientifiques avec des collègues qui n'étaient pas à première vue de mon champ d'applications original. La curiosité scientifique des uns et des autres a permis, à un moment donné, la coalescence d'idées isolée en une réflexion aboutie. Cette ouverture me permet aujourd'hui d'élargir mon domaine d'expertise à des champs d'applications nouveaux. L'intégration du LCND au LMA y est pour beaucoup. Travaillant régulièrement sur le site de Joseph Aiguier, c'est assez naturellement que des voies nouvelles se sont ouvertes. Cependant, le point central reste la caractérisation non destructive et les méthodes issues de l'acoustique non linéaire.

Les pistes qui seront suivies à propos des bulles concernent l'extension de la méthode proposée en partie 3 à la caractérisation d'un milieu connaissant l'inclusion. La mesure absolue de son rayon et de ses variations permettrait de remonter à des paramètres physiques du milieu hôte. Par ailleurs, cette méthode permettra à terme de se substituer à une caméra ultra-rapide. En effet, une couronne multiéléments permettrait d'imager les vibrations d'une inclusion en 3D.

La perspective du CND du collage qui est en cours concerne l'imagerie du champ de déformation sous chargement. Une méthode dérivée de l'acoustoélasticité associée à l'imagerie haute fréquence permet de déterminer le champ de déformation. Un défaut d'adhésion sera détecté, localisé et dimensionné par une non informité de ce champ au voisinage du défaut.

Les pistes dans le domaine du suivi de la mort cellulaire concerne l'imagerie et les tests in vivo. La méthode proposée sera prochainement testée sur le petit animal dans le cadre de projets en cours.

D'autres collaborations en cours concernent la modélisation et la simulation de la physique des milieux non linéaires. Les résultats sont trop préliminaires pour faire l'objet d'une partie de ce manuscrit, ils sont néanmoins décrits dans les perspectives.

V. Synthèse, Conclusion et perspectives

1. Synthèse

Le thème du contrôle ou de la caractérisation non destructive est en plein essor dans le milieu scientifique. J'ai assisté à l'émergence de cette thématique au fil des années. Arrivé en thèse en 2004, le CND n'était pas (ou peu) considéré comme une discipline scientifique à part entière. Un virage est en train de s'opérer depuis quelques années. Le laboratoire est impliqué dans des actions de « rétro-CND » consistant à expertiser la conception de nouveaux composants mécaniques, et éventuellement proposer une modification, en fonction de la contrôlabilité de ces derniers. Par ailleurs, comme évoqué en introduction, les compétences requises pour répondre à des besoins en CND, impliquant donc des matériaux réels, vont au-delà des connaissances académiques en acoustique (ou électromagnétisme, radiographie…). Des connaissances sur la réalité des matériaux inspectés, les évolutions de sa microstructure en fonction des procédés de fabrication, de l'endommagement, de son environnement, sont autant de paramètres à ne pas négliger. Dans ce contexte, considérant les évolutions des besoins en termes de certification lié à la sécurité et la sureté dans l'industrie, avec des problématiques de plus en plus complexes, le CND s'impose aujourd'hui comme discipline scientifique. C'est d'ailleurs un thème de recherche fort affiché au LMA avec une vingtaine de permanent et non permanents.

Dans le cadre de cette thématique de CND des matériaux réels, appliqué au génie civil, la recherche d'indicateurs d'endommagement sensibles a été une des pistes abordées. Les méthodes issues de l'acoustique non linéaires se sont imposées comme candidates potentielles. La physique des phénomènes n'est à ce jour pas encore complètement comprise. A ce jour, seule une loi phénoménologique permet de quantifier les effets non linéaires observés dans le béton. La sensibilité de ses méthodes à l'endommagement est relatée dans beaucoup de publications sur le sujet depuis début 2000. Pour démontrer le potentiel de ces méthodes, les auteurs, dont je fais partie, se sont focalisés sur la sensibilité de ces paramètres avec des conclusions concernent la comparaison « non linéaire versus linéaire » (mesure de vitesse essentiellement) dont la sensibilité à l'endommagement est inférieure d'un ou plusieurs ordres de grandeur. Le potentiel est maintenant largement démontré, la majorité des pathologies, des méthodes de mesures, des types d'endommagement ont été étudiés. Cependant, aucune de ces études ne sont comparables de façon quantitative par omission d'une grandeur essentielle : la déformation. La loi de comportement utilisée, à défaut de fondements physiques, indique que c'est cette grandeur qui gère les effets non linéaires. Il convient donc de la quantifier de manière à proposer des valeurs quantitatives de non-linéarité qui permettraient à terme, de progresser sur la compréhension des phénomènes physiques mis en jeu. La méthodologie proposée au premier chapitre, utilisant la simulation numérique, est une voie possible, il y en a d'autres qui seront évoquées en perspectives. Cette prise en compte de la déformation a permis de mettre en évidence l'influence de la microstructure et son évolution face à l'endommagement, validée par des analyses d'images de tomographie X. Ce chapitre montre également que le retournement temporel peut être utilisé pour une mesure quantitative locale de la non-linéarité.

La propagation d'ondes dans le béton a également été abordée suivant un axe en développement en CND ultrasonore des matériaux dont les échelles des hétérogénéités microstructurales sont de l'ordre de grandeur de la longueur d'onde employée. Dans ce cas, les méthodes standardisées de CND ultrasonores ne sont pas applicables car les signaux enregistrés sont « perturbés » par des phénomènes de diffusion multiple. Un axe de recherche au laboratoire concerne la modélisation de la multidiffusion dans le but de comprendre la propagation d'onde dans le béton. L'axe de recherche complémentaire développé au second chapitre consiste à tirer parti du « bruit » porté par les signaux ultrasonores, semblables aux sismogrammes rencontrés en géophysique. La propagation complexe des ondes dans les milieux multiplement diffusants peut être simplifiée par une équation semblable à celle de la chaleur, décrivant la diffusion de l'énergie ultrasonore au cours du temps. Deux paramètres suffisent pour décrire toute la complexité du problème. La validité de l'approche est démontrée pour la caractérisation de fissures fermées dans le béton. L'originalité est ici que les fissures considérées ne sont pas simplifiées par des entailles dont les bords ne sont pas en contacts mais sont bien réelles. Elles présentent une morphologie complexe avec des zones d'ouverture partielle dans le volume. Un outil de simulation numérique de la diffusion est développé et permet de remonter à des informations quantitatives sur la morphologie de ces fissures. La mise en flexion dynamique associée à la diffusion permet enfin d'extraire des informations complémentaires sur les zones de la fissure partiellement fermées. Les perspectives de ces travaux abordées dans la suite concernent l'imagerie du champ diffus dans le béton enregistré depuis la surface, permettant de caractériser en profondeur grâce à l'extension 3D du modèle numérique proposé.

L'extension thématique des méthodes et principes physiques mis en jeu dans les deux premiers chapitres est présentée. L'application à la caractérisation des microbulles est un axe de recherche investigué dans des cadres très différents. Le premier concerne la caractérisation de l'engazement du sodium liquide dans les réacteurs nucléaires, le second la prévention des accidents de désaturation chez les plongeurs. La forte non-linéarité du comportement dynamique des bulles à la résonance est mis à profit pour déterminer sans ambiguïté l'histogramme des rayons de bulles validé par méthode optique. Une approche originale brevetée, dérivée de la résonance non linéaire dans les solides, est employée pour obtenir des informations sur les bulles présentes dans un résonateur de Helmholtz. Une autre approche originale brevetée concerne la détermination des rayons de bulles par double modulation de phase et d'amplitude d'une haute fréquence par une basse fréquence. L'avantage majeur de cette méthode est que le rayon des bulles est déterminé hors résonance. L'extension des méthodes non linéaires employées dans le béton est également appliquée à l'imagerie haute fréquence des joints de colles avec des applications dans l'aéronautique pour la détection des défauts d'adhésion. Enfin, dans le domaine de l'imagerie médicale ultrasonore non linéaire, les méthodes développées dans les solides se montrent prometteuses pour le suivi de la mort cellulaire avec pour application l'optimisation des traitements radiothérapies et chimiothérapiques pour le traitement du cancer.

L'ensemble de ces travaux permettent d'entrevoir des perspectives et de proposer des pistes de recherches afin de répondre à des questions encore ouvertes aujourd'hui : Quelle est l'origine physique de la non-linéarité observée dans les solides complexes comme les roches

et les bétons ? Est-il envisageable de proposer un modèle unifié permettant de décrire l'ensemble des phénomènes non linéaires dits classiques et non classiques ? En quoi la technologie permet d'envisager des applications pratiques à l'échelle d'un ouvrage d'art ? Ces questions sont traitées dans les perspectives suivantes.

2. Conclusion

Mes recherches ont été initiées dans la thématique CND pour laquelle le matériau et sa microstructure est un point central. Les collaborations nationales et internationales suivies depuis des années m'ont permis une ouverture scientifique et des compétences en physique non linéaire. L'intégration au LMA en 2012 m'a permis une ouverture thématique et d'autres champs d'applications. Les apports scientifiques présentés dans ce manuscrit s'articulent suivant un triptyque entre l'expérimentation, le matériau et la physique non linéaire (Figure 54). C'est ce qui en fait l'originalité.

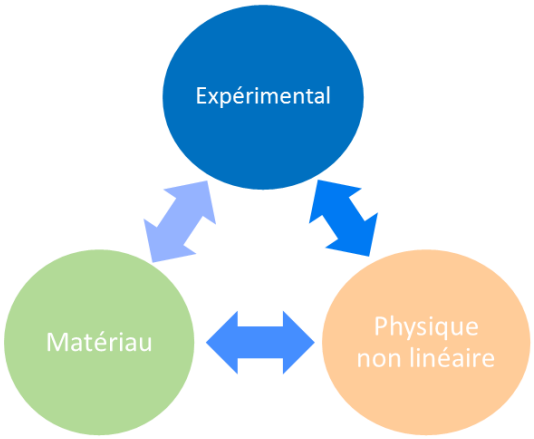

Figure 54 : Triptyque des apports scientifiques développés dans ce manuscrit

3. Perspectives

Chacune des perspectives énoncées ci-dessous est imaginée comme un sujet de thèse à part entière.

a. Origine physique de la non-linéarité non classique

Selon les résultats présentés dans ce manuscrit, la taille des inclusions à l'échelle de la microstructure semble corrélée avec la non-linéarité mesurée. Cette constatation a été faite dans deux matériaux très différents : le béton (taille des agrégats) et le plâtre (taille des cristaux de gypse). Les collaborations avec Michele Griffa (EMPA, Zurich, Suisse) se poursuivent. Ses activités de recherches sont partagées entre le centre d'imagerie X et le département de génie civil de son laboratoire. Deux projets sont en cours avec lui. Le premier consiste à imager le transport de l'eau dans le béton qui pourrait avoir un impact sur le comportement non linéaire. Un projet est en cours à l'ERSF (European Synchrotron Radiation Facility) de Grenoble avec pour but de comprendre l'influence du séchage du béton sur les phénomènes de micro fissurations qui ont lieu dans la matrice de ciment. Le second est la réponse à un appel à projet du collège doctoral de l'Université d'Aix Marseille visant à

promouvoir les échanges avec les « meilleures » université internationales, dont l'Institut Polytechnique Fédéral de Zurich (ETHZ) fait partie. Cette promotion se fait par l'intermédiaire de financement de bourses de thèses en co-direction. Faute de candidats éligibles, nous n'avons pas soumis le projet mais le sujet de thèse reste d'actualité. L'idée est de remplacer des granulats par des billes de verres dont la taille est calibrée. Les mesures de résonances quantitatives proposées dans ce manuscrit seront appliquées. Par ailleurs, les éprouvettes seront imagées en 3D au centre d'imagerie de l'EMPA afin d'examiner si des corrélations peuvent être faites entre la taille des inclusions, le degré de fissuration et la non-linéarité mesurée. La fabrication de tels échantillons est maîtrisée à l'EMPA (Figure 55). Ce projet plus fondamental qu'appliqué vient en soutien de projets en cours au LMA (ANR ENDE) et à l'EMPA (Nanocem core project).

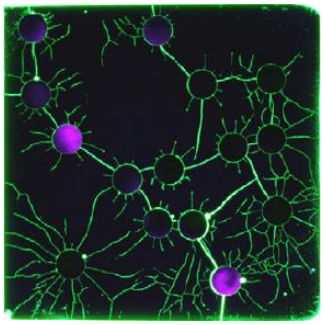

Figure 55 : [Michele Griffa] Photographie d'une section de béton « modèle » avec des billes de verre comme aggrégats.

Par ailleurs, la méthodologie développée au premier chapitre sera étendue au cas 3D. Ce projet de thèse est également soutenu par le Los Alamos National Laboratory avec qui nous progressons. Ces travaux consistent à étendre la méthode RUS linéaire, permettant l'estimation du tenseur d'élasticité, à la détermination du tenseur d'élasticité non linéaire non classique. En effet, la méthode NRUS appliquée à différents modes de résonances permet, via simulation numérique, d'estimer toutes les composantes du tenseur des déformations donnant accès à la non-linéarité absolue (Figure 56). Ainsi, il sera possible d'identifier et de quantifier un endommagement isotrope ou anisotrope. Les fondements de cette théorie 3D sont en cours de formalisation [ULR14].

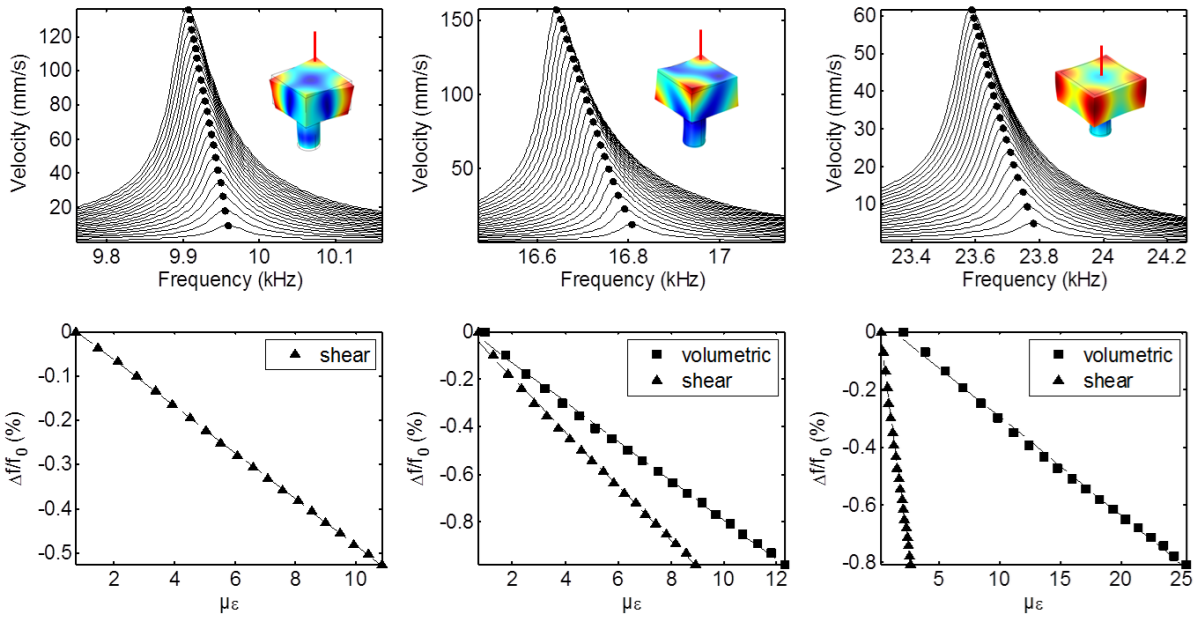

Figure 56 : Résonance non linéaire pour plusieurs modes de résonance d'un même échantillon et estimation de la déformation volumique et de cisaillement associée.

b. Traitement unifié des phénomènes non linéaires classiques et non classiques

Pendant ma thèse j'ai été amené à étudier le seul modèle non phénoménologique permettant de décrire les phénomènes classiques et non classiques. Ce modèle a été introduit par Vakhnenko et al. [VAK04, VAK05]. Le principe repose sur une loi de comportement élastique non linéaire classique du même type que celle présentée Figure 4. L'originalité repose sur l'interaction d'un sous-système élastique « rapide » et un sous-système élastique « lent » en référence à la dynamique rapide et la dynamique lente. En plus de l'élasticité non linéaire classique, cette interaction joue sur le module élastique du matériau via une équation différentielle du premier ordre de couplage. Sans entrer dans les détails, ce modèle permet de décrire l'ensemble des phénomènes non linéaires non classiques tels la dynamique rapide, le conditionnement et la dynamique lente. En 2004, les phénomènes étaient essentiellement observés par des expériences de résonance non linéaires, correctement transcrite par le modèle proposé (Figure 57). La dynamique lente, lent retour à l'équilibre du module élastique, est également correctement modélisé par le modèle de Vakhnenko (Figure 57).

Cependant, dans les deux articles cités précédemment, le couplage entre les deux sous-systèmes élastiques, originalité du modèle, est rompu afin de trouver des solutions analytiques. Les phénomènes en résonance, donc en régime entretenu, sont stables dans le temps et permettent de ne considérer que le système rapide. La relaxation quant à elle correspond au retour à l'équilibre lorsque la sollicitation dynamique est stoppée, le sous-système rapide ne joue plus aucun rôle.

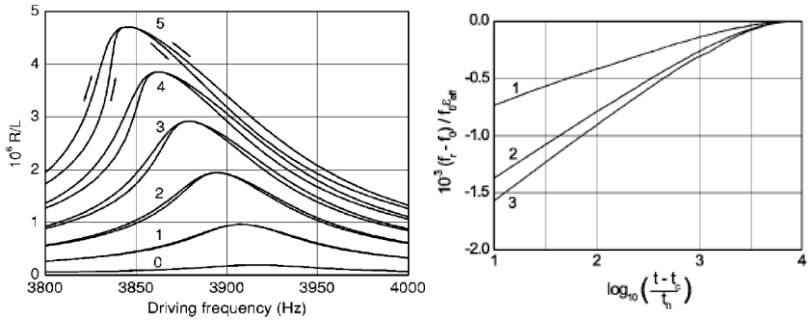

Figure 57 : [VAK05]. A gauche : Mise en évidence du décalage de la fréquence de résonance et de phénomènes d'hystérésis. A droite : retour à l'équilibre après différentes sollicitations.

Depuis quelques années, la méthode d'acoutoélasticité dynamique introduite par G. Renaud et al. [REN09,REN12,REN13] a permis une observation fine des phénomènes non linéaires en étudiant la variation de vitesse des ondes pendant que le matériau est en résonance (Figure 58(a)). La variation de vitesse ΔV pendant la sollicitation dynamique (Figure 58(b)) permet d'estimer la variation du module élastique M par $\Delta M/M_0 = 2\ \Delta V/V_0$ au cours du temps pendant, et après la mise en résonance (Figure 58(c)).

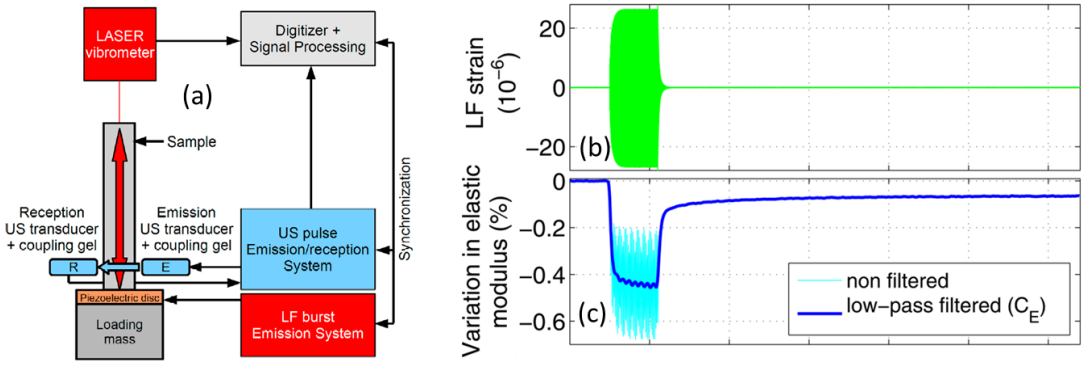

Figure 58 : [REN13] (a) Mise en résonance d'un échantillon et mesure simultanée de la vitesse de propagation. (b) Basse fréquence. (c) Evolution du module élastique obtenu à partir des mesures de vitesses avant, pendant, et après la mise en résonance.

Aucun modèle ne permet à ce jour de décrire l'ensemble de ces phénomènes : (i) dynamique rapide : chute rapide du module élastique en début de sollicitation, (ii) conditionnement : stabilisation de la moyenne (données filtrées) et oscillations autour de la moyenne et (iii) dynamique lente : lent retour à l'équilibre du module élastique. Le modèle de Vakhnenko le permettrait mais le découplage des sous-systèmes élastiques le rend impossible.

Une collaboration avec Bruno Lombard (LMA) et Nicolas Favrie (IUSTI) a été initiée avec pour objectif de simuler numériquement les effets non linéaires. Après avoir présenté sans enthousiasme le modèle phénoménologique usuellement utilisé, j'ai proposé le modèle de Vakhnenko. A l'unanimité, pour ses propriétés physiques, c'est celui qui a été retenu. Sans entrer dans les détails, nous l'avons fait évoluer en conservant le couplage mutuel entre les deux sous-systèmes élastiques et en ajoutant une atténuation non linéaire. Les résultats obtenus à ce jours sont très prometteurs (Figure 59). Cette figure est à mettre en parallèle à la Figure 58(c). La chute rapide du module élastique, le conditionnement, les oscillations autour de la valeur moyenne et la dynamique lente sont présents et sont quantitativement corrélés

avec l'expérience de G. Renaud. L'extension de ce modèle au 2 puis 3D est envisagé à court terme. Un article dans Wave Motion est accepté [FAV14], un autre pour Physical Review Letters est en cours de réalisation. En parallèles des études des expériences sont en cours dans le but d'obtenir une base de résultats pour développer le modèle 3D.

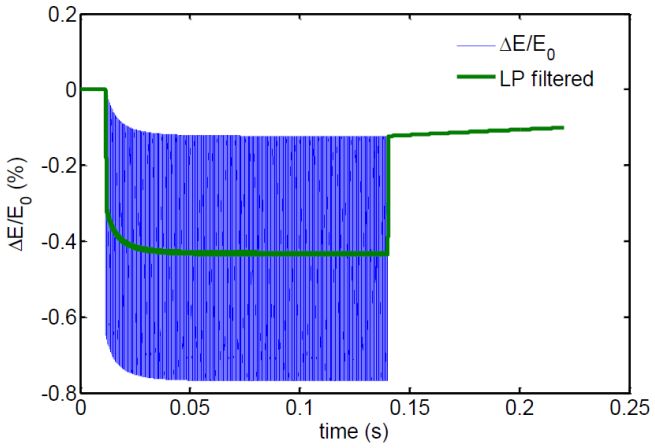

Figure 59 : Résultats de la simulation numérique obtenus avec les paramètres physiques issus de [REN13]

c. Perspectives industrielle

A ce jour, malgré de nombreuses études académiques, aucune application à l'échelle industrielle n'a abouti. La collaboration avec Saint Gobin recherche continue. Ils travaillent en interne à l'application des méthodes de résonances non linéaires initiées avec nous pour déterminer la taille des cristaux dans le plâtre industriel (en se passant de SEM ou micro tomographie) ou encore le contrôle qualité de composants industriels. La méthode NRUS quantitative pourrait également être appliquée à des carottages en génie civil. Considérons une carotte standard de diamètre 10 cm et 20 cm de long. Un gradient de propriété en profondeur n'est pas détectable par méthode standard qui donnera une valeur moyenne sur les 20cm. La méthode proposée étant adaptée à tout type de géométrie, les carottes peuvent être découpées en tranches. Les propriétés linéaires et non linéaires pourraient ainsi être déterminées en fonction de la profondeur.

Les applications à plus grande échelle, en génie civil par exemple, ne sont à ce jour toujours pas prêtes pour les raisons invoquées dans ce manuscrit concernant l'estimation de la déformation qui permet d'estimer une valeur absolue de la non-linéarité. Une fois que la physique des phénomènes sera comprise et correctement décrite, les applications pratiques pourront débuter. Nous avons cité comme piste la simulation numérique pour obtenir la déformation en résonance. Il existe aujourd'hui sur le marché, des vibromètres laser à balayage qui permettent d'imager les trois composantes du déplacement et de fournir une cartographie de la déformation. Ceci permettrait de se passer de l'étape de simulation numérique et de mesurer directement toutes les grandeurs physiques en jeu pour l'estimation quantitative de la non-linéarité.

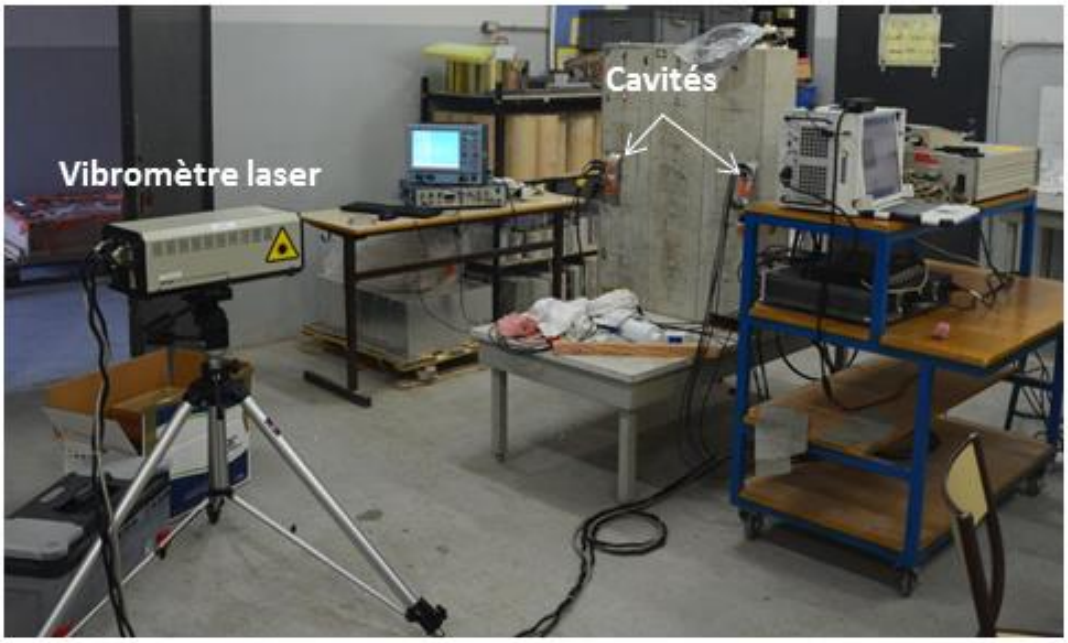

Figure 60 : Application du retournement temporel à l'échelle d'un mur.

Il existe sur le marché un laser capable de fonctionner à 300m de distance de l'objet à inspecter. Une application de la diffusion ultrasonore présentée au chapitre III de ce manuscrit peut être envisagée à grande échelle. L'emploi simultané d'un laser de puissance pour générer des impulsions ultrasonores permettrait la mesure locale, sans contact et à distance des propriétés diffusives du béton. Les méthodes issues du retournement temporel pourraient également être appliquées in situ avec des cavités positionnées sur un mur, comme pour des essais préliminaires réalisés à Toulouse avec un vibromètre laser à balayage (Figure 60).

VI. Bibliographie

[ABE00a] K. Van Den Abeele and J. De Visscher, “Damage assessment in reinforced concrete using spectral and temporal nonlinear vibration techniques,” *Cement Concrete Res.* 30(9), 1453-1464 (2000)

[ABE00b] K. Van Den Abeele, J. Carmeliet, J.A. TenCate, and P.A. Johnson, “Nonlinear Elastic Wave Spectroscopy (NEWS) techniques to discern material damage. Part II: Single mode nonlinear resonance acoustic spectroscopy,” Res. Nondestruct. Eval. 12, 31-43 (2000).

[ABE02] K. Van Den Abeele, J. Carmeliet, P.A. Johnson, and B. Zinzsner, “The influence of water saturation on the nonlinear mesoscopic response of earth materials, and the implications to the mechanism of nonlinearity,” J. Geophys. Res. 107(B6), 10, 2121 (2002).

[ACH14] Y. Achaoui, S. Mensah, C. Payan, E. Debieu, Z. Hammadi, R. Morin, Contrôle et stabilisation de procédés de génération de bulles, En cours de traitement par la SATT

[ADA99] R. Adams, B. Drinkwater, "Non-Destructive testing of adhesively-bonded joint," Journal of Materials and Product Technology 14, 385-398 (1999)

[AKI69] K. Aki, "Analysis of the Seismic Coda of Local Earthquakes as Scattered Waves," J. Geophys. Res. 74, 615-631 (1969)

[AND08] B. Anderson, M. Griffa, C. Larmat, T.J. Ulrich, and P.A. Johnson, “Time reversal,” Acoust. Today, 4 (1), 5-16 (2008)

[ANT10] P. Antonaci, C L E Bruno, A S Gliozzi, M Scalerandi, Monitoring evolution of compressive damage in concrete with linear and nonlinear ultrasonic methods, Cem. Concr. Res. 40 (7), 1106-1113 (2010)

[ANU01] P. Anugonda, J. Wiehn and J. Turner, "Diffusion of ultrasound in concrete," Ultrasonics 39(6),429-435 (2001)

[AST09] ASTM C597-09, Standard Test Method for Pulse Velocity Through Concrete

[BAU14] A Baudot, J. Moysan, C. Payan, N. Ylla, J. Galy, B. Verneret, A. Baillard, "Improving adhesion strength analysis by the combination of ultrasonic and mechanical tests on single lap joints," The Journal of Adhesion (in press, 2014)

[BAU15] A. Baudot, C. Payan, J. Moysan, "Procédé de détection et caractérisation de défauts d’adhésion dans les assemblages collés," Brevet déposé, n° de dépôt : 15/50432 (février 2015)

[BED12] T. BEDETTI, Étude de la diffusion multiple des ultrasons en vue de la modélisation du bruit de structure et de la caractérisation des aciers moulés inoxydables à gros grains, Thèse de doctorat, Paris 7 (2012)

[BEK03] J. Becker, L. Jacobs and J. Qu, "Characterization of Cement-Based Materials Using Diffuse Ultrasound," Journal of Engineering Mechanics 129 (12),1478-1484 (2003)

[BEN06] M. Bentahar, H. El Aqra, R. El Guerjouma, M. Griffa, and M. Scalerandi, “Hysteretic elasticity in damaged concrete: Quantitative analysis of slow and fast dynamics,” Phys. Rev. B 73, 014116 (2006)

[BOR03] JM Borsboom, Jerome M.G., Chien Ting Chin, De Jong N., “Nonlinear coded excitation method for ultrasound contrast imaging”, Ultrasound Med Biol 29, 277–284 (2003)

[BOU11] F. Bouchaala, C. Payan, V. Garnier and J.P. Balayssac, "Carbonation Assessment in Concrete by Nonlinear Ultrasound," Cement and Concrete Research 41, 557–559 (2011)

[BUC05] J.C. Buckey, D.A Knaus, D.L. Alvarenga, M.A. Kenton, P.J. Magari, "Dual-frequency ultrasound for detecting and sizing bubbles," Acta Astronautica 56, 1041-1047 (2005)

[CAV10] M. Cavaro, Apport de l'accoustique non linéraire à la caractérisation de l'engagement du sodium liquide : application aux réacteurs nucléaires de quatrième génération, thèse de doctorat, Université de la Méditerranée (2010)

[CAV11a] M. Cavaro, C. Payan, J. Moysan and F. Baqué, "Microbubble cloud characterisation by nonlinear frequency mixing," Journal of the Acoustical Society of America 129 (5), EL179-EL183 (2011)

[CAV11b] Cavaro, C. Payan, Method Of Determining Void Rate By Nonlinear Acoustic Resonance Spectrometry In A Biphase Medium And Application In A Nuclear Reactor, Brevet WO/2011/141370

[CAV12] M. Cavaro, C. Payan, S. Mensah, J. Moysan, and J.-P. Jeannot, Linear and nonlinear resonant acoustic spectroscopy of micro bubble clouds, 17th ICNEM, July 1-7th, Cefalu, Italy. POMA 16, 045003 (2012)

[CHA06] J.F.Chaix, Garnier V, Corneloup G. Ultrasonic wave propagation in heterogeneous solid media: Theoretical analysis and experimental validation. Ultrasonics 44, 200-210 (2006)

[CHA12] J.F. Chaix, M. Rossat, V. Garnier and G. Corneloup, "An experimental evaluation of two effective medium theories for ultrasonic wave propagation in concrete," Journal of the Acoustical Society of America, 131, 4481-4490 (2012)

[CHA85] J.Y. Chapelon, P.M. Shankar, V.L. Newhouse, "Ultrasonic measurement of bubble cloud size profiles," J. Acoust. Soc. Am. 78(1),196-201 (1985)

[DER10] F. Deroo,J. Kim,J. Qu,K. Sabra,L. Jacobs, "Detection of damage in concrete using diffuse ultrasound," J Acoust Soc Am. 127(6), 3315-3318 (2010)

[FIN92] M. Fink, "Time Reversal of Ultrasonic Fields-Part I: Basic Principles," IEEE Trans. Ultrason. Ferroelectr. Freq. Control. 39(5), 555 (1992).

[FOU13] D. Fouan, S. Mensha, C. Payan, C. Quinsac, Acoustical determination of the average radius of an inclusion in a medium, Brevet Soumis, n° de dépôt : 1354609

[FOU15] D. Fouan, Y. Achaoui, C. Payan, S. Mensah, "Microbubble dynamics monitoring using a dual modulation method," J. Acoust. Soc. Am. 137 (2), EL144-EL150 (2015)

[GUY09] Guyer, R.A.& Johnson, P.A., Nonlinear Mescopic Elasticity, Wiley-VCH 1st edition (2009)

[GUY95] R.A. Guyer, K.R. McCall, and G.N. Boitnott, "Hysteresis, discrete memory and nonlinear wave propagation in rock: A new paradigm," Phys. Rev. Lett. 74(17), 3491-3494 (1995).

[GUY97] R.A. Guyer, K.R. McCall, G.N. Boitnott, L.B. Hilbert Jr., and T.J. Plona, "Quantitative implementation of Preisach-Mayergoyz space to find static and dynamic elastic moduli in rock," J. Geophys. Res. 102(B3), 5281-5293 (1997).

[GUY99] Guyer, R.A., and P.A. Johnson, "Nonlinear mesoscopic elasticity: Evidence for a new class of materials," Phys. Today 52, 30-35 (1999)

[HAU11] S. Haupert, G. Renaud, J. Rivière, M. Talmant, P.A. Johnson, and P. Laugier, "High-accuracy acoustic detection of non-classical component of material nonlinearity," J. Acoust. Soc. Am. 130(5), 2654-2661 (2011).

[HEL85] H. Von Helmholtz – On the sensations of tone – 1885 – Dover ed. 1954 ré-ed.

[ISO04] ISO 1920-7:2004, Testing of concrete, Part 7: Non-destructive tests on hardened concrete.

[JOH00] P. Johnson, J. TenCate, R. Guyer, K. Van Den Abeele, "Resonant nonlinear ultrasound spectroscopy," patent WO 2000034750 A1 (2000)

[JOH05] P. Johnson, and A. Sutin, "Slow dynamics and anomalous nonlinear fast dynamics in diverse solids," J. Acoust. Soc. Am. 117(1), 124-130 (2005)

[JOH06] P. Johnson, "Nonequilibrium nonlinear-dynamics in solids: State of the art," The Universality of Nonclassical Nonlinearity with Applications to NonDestructive Evaluations and Ultrasonics, Delsanto, P.P., Ed., Springer, New York, 49-67 (2006)

[KOD09] A. Kodjo et al., Evaluation of damages due to alkali-silica reaction with nonlinear acoustics techniques, POMA 7, 045003 (2009)

[KOL92] D. Koller, Y. Li, M. Shankar, V.L. Newhouse, "High-Speed Bubble Sizing Using the Double Frequency Technique for Oceanographic Applications," IEEE Journal of Oceanic Engineering 17(3) (1992)

[LAN86] D. Landau and E. M. Lifschitz, Theory of Elasticity (Pergamon, New York, 1986), 3rd (revised) English ed.

[LAR09] Localisation d'apparition de défaut par ultrasons dans le béton, Brevet FR0950612

[LAR10] E. larose, T. Planes, V. Rossetto and L. Margerin : Locating a small change in a multiple scattering environment, Appl. Phys. Lett. 96 (2010).

[LAR13] E. Larose, N. Tremblay, C. Payan, V. Garnier, and V. Rossetto, "Ultrasonic slow dynamics to probe concrete aging and damage," 39th QNDE, 15-20 July 2012, Denver, USA, AIP Conf. Proc. 1511, 1317-1324 (2013)

[LAU76] W. Lauterborn, "Numerical investigation of nonlinear oscillations of gas bubbles in liquids," J. Acoust. Soc. Am. 59(2), 283–293 (1976).

[LES11] K.J. Lesnicki, J.-Y. Kim, K.E. Kurtis, and L.J. Jacobs, Characterization of ASR Damage in Concrete using Nonlinear Impact Resonance Acoustic Spectroscopy Technique, NDT&E Int. 44, 721-727 (2011)

[MCC96] K.R McCall and R.A. Guyer, "Equation of state and wave propagation in hysteretic nonlinear elastic material," J. Geophys. Res. 99, 23887-23897 (1994).

[MIG97] A. Migliori, J.L. Sarrao, Resonant ultrasound spectroscopy: applications to physics, materials measurements, and nondestructive evaluation, Wiley, 1997

[MIN33] M. Minnaert, "On musical air bubbles and the sound of running water," Philos.Mag. 16(7), 235–248 (1933).

[MUL06] M. Muller, Guyer R., Laugier P. and Johnson P. A., "Non linear resonant, ultrasound spectroscopy applied to damage assessment in bone", J. Acoust. Soc. Am. 188, 3946-3952 (2006)

[NAG98] P. Nagy, "Fatigue damage assessment by nonlinear ultrasonic materials characterization," Ultrasonics 36(1), 375-381 (1998).

[NEW84] V.L. Newhouse, P.M. Shankar, "Bubble sizing using the nonlinear mixing of two frequencies," J. Acoust. Soc. Am. 75(5), 1473-1477 (1984)

[OST01] L. Ostrovsky, and P.A. Johnson, "Dynamic nonlinear elasticity in geomaterials," Rivista del Nuovo Cimento 24(7), 1-46 (2001)

[PAY07] C. Payan, V. Garnier, J. Moysan and P. A. Johnson, "Applying nonlinear resonant ultrasound spectroscopy to improving thermal damage assessment in concrete," J. Acoust. Soc. Am. 121 (4), EL125-EL130 (2007)

[PAY09] C. Payan, V. Garnier, J. Moysan and P.A. Johnson, "Determination of third order elastic constants in a complex solid applying coda wave interferometry," Applied Physics Letters 94, 011904 (2009)

[PAY10] C. Payan, V. Garnier and J. Moysan, "Effect of water saturation and porosity on the nonlinear elastic response of concrete," Cement and Concrete Research 40, 473–476 (2010)

[PAY13] C. Payan, A. Quiviger, V. Garnier, J.F. Chaix, J. Salin, "Applying diffuse ultrasound under dynamic loading to improve closed crack characterization in concrete," Journal of the Acoustical Society of America 134 (2), EL211-EL216 (2013)

[PUN07] W. Punuraia, J. Jarzynskib, J. Qu, K. Kurtisa and L. Jacobs, "Characterization of dissipation losses in cement paste with diffuse ultrasound," Mech. Res. Com. 34 (3), 289-294 (2007)

[QUI12] A. Quiviger, C. Payan, J.F. Chaix, V. Ganier and J. Salin, "Effect of the presence and size of a real macro-crack on diffuse ultrasound in concrete," NDT & E International 45 (1), 128-132 (2012)

[QUI13] A. Quiviger, A. Girard, C. Payan, J.F. Chaix, V. Garnier, J. Salin, "Influence of the depth and morphology of real cracks on diffuse ultrasound in concrete: a simulation study," NDT & E International 60, 11-16 (2013)

[RAM04] S. Ramamoorthy, Y. Kane and J. Turner, "Ultrasound diffusion for crack depth determination in concrete," J. Acoust. Soc. Am. 115 (2), 523-529 (2004)

[REM15] M.C. Remillieux, B.E. Anderson, T.J. Ulrich, P.Y. Le Bas, C. Payan, "Depth profile of a time-reversal focus in an elastic solid," Ultrasonics 58, 60–66 (2015)

[REN09] G. Renaud, S. Calle, M. Defontaine, "Remote dynamic acoustoelastic testing: Elastic and dissipative acoustic nonlinearities measured under hydrostatic tension and compression,"

Applied Physics Letters 94 (1), 011905 (2009)

[REN12] G. Renaud, P.-Y. Le Bas, and P.A. Johnson, “Dynamic measures of elastic nonlinear (anelastic) behavior: Dynamic acousto-elasticity testing (DAET),” J. Geophys. Res. 117, B06202 (2012).

[REN12b] G. Renaud, J. G. Bosch, A.F.W. van der Steen and N. Jong, "acoustical camera" for in vitro characterization of contrast agent microbubble vibrations. Applied Physics Letters 100 (10), 101911 (2012)

[REN13] G. Renaud, J. Rivière, S. Haupert, and P. Laugier, "Anisotropy of dynamic acoustoelasticity in limestone, influence of conditioning, and comparison with nonlinear resonance spectroscopy," J. Acoust. Soc. Am. 133 (6), 3706 (2013)

[ROC10] C. La Rocca, C. Payan and J. Moysan, "Evaluation of epoxy bonded joint quality using nonlinear acoustics," XV ICNEM Otranto, Italy, 4 - 10 July 2010, POMA 10, 045001 (2010)

[SCA10] M. Scalerandi, Gliozzi A. S., Bruno, C. L. E. and Antonaci, P., “Nonequilibrium and hysteresis in solids: Disentangling conditioning from nonlinear elasticity”, Phys. Rev. B 81, 104114 (2010)

[SHA10] A. A. Shah and S. Hirose, Nonlinear Ultrasonic Investigation of Concrete Damaged under Uniaxial Compression Step Loading, J. Mater. Civ. Eng. 22, 476 (2010)

[SHA13] S. SHAHJAHAN, Étude expérimentale et numérique d’un procédé de détection de défauts fondé sur la théorie des matrices aléatoires : application au contrôle de matériaux polycristallins multiplement diffuseurs par un réseau de transducteurs ultrasonores, Thèse de doctorat, Paris 7 (2013)

[SNI02] R.Snieder, A. Grêt, H. Douma, and J. Scales, “Coda wave interferometry for estimating nonlinear behavior in seismic velocity,” Science 295, 2253-2255 (2002).

[STE12] P. Stephan, J. Salin, "Ageing management of concrete structure: Assessment of EDF methodology in comparison with SHM and AIEA guides," Construction and Building Materials 37, 924-933 (2012)

[SUT98] A.M. Sutin, S.W. Yoon, E.J. Kim, I.N. Didenkulov, "Nonlinear acoustic method for bubble density measurements in water," J. Acoust. Soc. Am. 103(5), 2377-2384 (1998)

[TEN98] J.A. TenCate and T.J. Shankland, "Slow Dynamics and Nonlinear Response at Low Strains in Berea Sandstone," Proceedings of the 16th International Congress on Acoustics 3, P.A. Kuhl and L.A. Crum, Eds, AIP, New York, 1565-1566 (1998)

[TUR96] A. Turatsinze, and A. Bascoul, “Restrained Crack Widening in Mode I Crack Propagation for Mortar and Concrete.” Advanced Cement Based Materials 4, 77–92 (1996)

[ULR12a] T.J. Ulrich, C. Payan, "Nondestructive Evaluation: Nonlinear Ultrasound to Evaluate the Integrity of Thermally Damaged Concrete," EPRI, Palo Alto, CA: 2012. 1026501. (2012)

[ULR12b] T.J. Ulrich, C. Payan, P. Roberts, "Addressing Facility Needs for Concrete Assessment Using Ultrasonic Testing: Mid-year Report," LA-UR-12-20274 (2012)

[ULR13] T.J. Ulrich, B.E. Anderson, P.Y. Le Bas, C. Payan, B. Reichman, "Experimental Investigations–End of Year Technical Report," LA-UR-13-27010 (2013)

[VAK04] O.O. Vakhnenko, V.O. Vakhnenko, T.J. Shankland, and J.A. TenCate, “Strain-induced kinetics of intergrain defects as the mechanism of slow dynamics in the nonlinear resonant response of humid sandstone bars,” *Phys. Rev. E* 70, 015602 (2004)

[VAK05] O.O. Vakhnenko, V.O. Vakhnenko, and T.J. Shankland, “Soft-ratchet modeling of end-point memory in the nonlinear resonant response of sedimentary rocks,” *Phys. Rev.* B 71, 174103 (2005).

[WEA98] R. Weaver, "Ultrasonics in an aluminum foam," Ultrasonics 36, 435-442 (1998)

[WOO41] A.B. Wood – A textbook of sound – Macmillan, New York, 1941

[YIM12] H.J. Yim et al., "Characterization of thermally damaged concrete using a nonlinear ultrasonic method," Cem. Concr. Res. 42, 1438-1446 (2012)

[ZAB73] E.A. Zabolotskaya, S.I. Soluyan, "Emission of harmonic and combination frequency waves by air bubbles," Soviets Physics – Acoustics 18(3), 396-398 (1973)

[ZAR10] J.-P. Zardan , C. Payan, V. Garnier and J. Salin, "Effect of the presence and size of a localized nonlinear source in concrete," Journal of the Acoustical Society of America 128 (1), EL38-EL42 (2010)

VII. Curriculum Vitae

Formation, Diplômes

2007: Doctorat en Mécanique, Université de la Méditerranée, Mention très honorable.
2004 : CAPLP Génie Mécanique option Construction
2001: DEA d'Acoustique, Université de la Méditerranée
2000 : Maîtrise de Technologie Mécanique, Université de la Méditerranée, Mention AB
1999 : Licence de Technologie Mécanique, Université de la Méditerranée
1995-1998 : CPGE Physique/Technologie
1995 : Baccalauréats S (SI), Mention AB

Expérience

Professionnelles

2011 - 2012 : séjour invité au Los Alamos National Laboratory, EES 17 (USA) – En position de Congés pour Recherche ou Conversion Thématique
Depuis 2008: Maître de Conférences, Aix Marseille Université, IUT Aix en Provence, Département HSE
2007-2008: ATER, Aix Marseille Université, IUT Aix en Provence, Département HSE
2005-2007: ATER, Aix Marseille Université, IUT Aix en Provence, Département GMP
2004-2005: PLP Génie Mécanique Construction, Lycée Jean Moulin (Port de Bouc)
2002-2004: Aide éducateur, Maintenance Informatique, Lycée du rempart, Marseille

Thématiques de Recherche (mots clés)

Physique, Acoustique, Elasticité non linéaire, Contrôle Non Destructif, Traitement de signal.
Investigation expérimentale des phénomènes non linéaires, retournement temporel, résonance non linéaire, ondes diffuses.
Application au CND dans le domaine de l'Energie Nucléaire et Génie Civil (béton, sodium liquide), l'Aéronautique (collage structural), l'industrie (plâtre).

Expertises pour les journaux internationaux/organismes

Journal of Applied Physics
Journal of the Acoustical Society of America,
International Journal of Solids and Structures,
International Journal of Non-Linear Mechanics,
Mechanics Research Communications,
Ultrasonics,
NDT & E International,
Cement and Concrete Research,
Construction & Building Materials,
Mechanical Systems and Signal Processing,
Materials and Structures,
Journal of Geophysics and Engineering,
Journal of ASTM International,
Fatigue and Fracture of Engineering Materials and Structures.

Expertises de projets :
Natural Sciences and Engineering Research Council of Canada (NSERC)
Association Nationale de la Recherche et de la Technologie (ANRT)

Membre de l'Acoustical Society of America et de la Société Française d'Acoustique.

Responsabilités – Membre de conseils

- 2015… : Responsable de l'équipe Ondes et Imagerie LMA (CNRS UPR 7051)
- 2013… : Membre de la Commission Recherche de l'IUT d'Aix Marseille
- 2013… : Responsable des projets tuteurés 1ère et 2ième année IUT HSE
- 2012… : Membre de la Commission Scientifique du LMA (CNRS UPR 7051)
- 2007… : Responsable de la gestion et de l'administration du réseau et du parc informatique (IUT HSE La Ciotat).
- 2007… : Administration du site web du département HSE

Animation scientifique

- XIX International Conference on Nonlinear Elasticity in Materials : June 22-27th 2014, Fréjus, France. Comités scientifique et d'organisation
- Organisation du GDRE « Nonlinear Acoustics », Aix en Provence, France, 9-10 janvier 2014.
- XIII International Conference on Nonlinear Elasticity in Materials : June 22-27th 2008, Aix en Provence. Comités scientifique et d'organisation
- Diagnobéton 2007 : May 10-11th 2007, Aix en Provence. Commité d'organisation

Enseignement

Cours Magistraux, Travaux Dirigés et Travaux Pratiques :

- Nuisances sonores, Vibrations corporelles, Mécanique, Résistance des Matériaux, Electricité, Thermodynamique, Ultrasons : IUT Aix département HSE
- CAO, DAO, Construction Mécanique, Résistance des Matériaux : IUT Aix GMP
- CND ultrasons appliqué au génie civil : INSA CAST, Polytech Marseille Génie Civil

Participation à des jurys/comités de sélection

- Thèse M. Cavaro (co-directeur), Aix Marseille Univ., novembre 2010
- Thèse A. Quiviger (co-directeur), Aix Marseille Univ., 2012
- Thèse Y. Baccouche (examinateur), LAUM, avril 2013
- Thèse C. Trarieux (examinateur), Université François Rabelais, décembre 2014
- Thèse A. Baudot (co-directeur), Aix Marseille Univ., janvier 2015
- Comité de Sélection poste MCF 0737 Aix Marseille Université, avril 2011.
- Jury concours de recrutement Technicien Supérieur Hospitalier, Hôpital Edouard Toulouse, avril 2015.
- Participations régulières (président de jury) depuis 2008 aux jurys VAE du lycée professionnel de l'Estaque (Marseille) pour attribution du BAC PRO Sécurité-Prévention.

Directions de thèses

- Matthieu Cavaro (LCND/CEA): Octobre 2007 - Novembre 2010

Apport de l'acoustique non linéaire à la caractérisation de l'engazement du sodium liquide. Application aux réacteurs nucléaires de quatrième génération
Université de la Méditerranée, ED353, Co directeur : J. Moysan 50%
Devenir en 2015 : CDI Ingénieur de Recherche CEA

- Audrey Quiviger (LCND/EDF) : novembre 2009 – novembre 2012

Ultrasons diffus pour la caractérisation d'une fissure dans le béton : Approche linéaire et non linéaire
Aix Marseille Université, ED353, Co directeur : V. Garnier 40%, J.F. Chaix 30%
Devenir en 2015 : CDI Ingénieur Comex Nucléaire

- Alice Baudot (LMA/Safran composites) : janvier 2012- janvier 2015

Mesures non destructives pour la caractérisation des paramètres critiques de l'adhésion sur structures collées
Aix Marseille Université, ED353, Co directeur : J. Moysan 50%
Devenir en 2015 : CDI Ingénieur Areva

- Martin Lott (LMA) : juin 2014- juin 2017

Apport du retournement temporel non linéaire pour la caractérisation de fissures dans le béton
Aix Marseille Université, ED353, Co directeur : V. Garnier 50%

Participations aux thèses

- Damien Fouan (LMA/BF Système) : septembre 2010- novembre 2013

Détection et caractérisation d'embolies gazeuses : application à la prévention des accidents de décompression.
Aix Marseille Université, ED353, Directeur : S. Mensah 100%
Devenir en 2015 : Post Doc à Tours

- Emmanuelle Lefevre (ISM / INSERM UMR 1033) : septembre 2012- novembre 2015

Propriétés mécaniques et biologiques de l'os en croissance
Aix Marseille Université, Directeur : M. Pithioux 50% - H. Follet 50%

- Quang Vu (LMA) : septembre 2012- novembre 2015

Ondes de surfaces non linéaires pour la caractérisation du béton
Aix Marseille Université, ED353, Directeur : V. Garnier 50% - J.F. Chaix 50%

Autres activités d'encadrement scientifique

- Jean Phillipe Zardan: mars 2009 – septembre 2009 : MasterII

Application de l'acoustique non linéaire pour le CND du béton
Devenir en 2015 : CDI ingénieur SNCF

- Christine La Rocca : avril 2010 – juillet 2010 : MasterII

Evaluation non destructive des joints époxy par acoustique non linéaire
Devenir en 2015 : CDI Ingénieur Eurocopter

- Fathe Bouchaala : septembre 2009 – juillet 2010 : ATER

Caractérisation de la carbonatation du béton par ultrasons non linéaires
Devenir en 2015 : Chercheur permanent au Petroleum Institute (Emirats Arabes)

- Alice Baudot : mars 2011 – juillet 2011 : MasterII

Caractérisation non destructives de bulles de gaz en milieu visqueux représentatif du verre en fusion
Devenir en 2015 : CDI Ingénieur Areva

- Hery Ramanasse : juillet 2012 – décembre 2012 : MasterII

Influence de la microstructure du plâtre sur sa réponse non linéaire
Devenir en 2015 : CDI Ingénieur MCA Ingénierie

Distinctions

- Titulaire de la Prime d'Excellence Scientifique (PES) d'Aix Marseille Université depuis 2011.
- Thèse M. Cavaro:

- Prix Claude BIRAC 2011 délivré par la COFREND (Confédération Française pour les Essais Non Destructifs)
- Prix Jean Bourgeois 2011 délivré par la SFEN (Société Française d'Énergie Nucléaire)

- 2nd prix du concours University Challenge pour un TP réalisé pour l'IUT d'Aix, département HSE.
F. Falco & C. Payan, *Evaluation des Risques, Nuisances Sonores, Vibration Corporelles*, Journée faites de la mesure, Mennecy, France (2009)

- 3ième prix du concours University Challenge pour un TP fait pour les étudiants de MasterII concernant le CND du béton par ultrasons.
C. Payan, JF Chaix, F. Falco, *Contrôle de l'état de santé des structures en béton par méthodes acoustiques et vibratoires*, Colloque vibrations, chocs et bruits, June 15-17th , Lyon, France (2010)

Contrats, Projets nationaux et internationaux

Projets académiques nationaux, internationaux

[P11] Analyse multiéchelle de la croissance osseuse chez l'enfant : une approche conjointe par imagerie ultrasonore et une modélisation biomécanique (MALICE)
Financement : Agence Nationale pour la Recherche (2012-2016)
Porteur P. Lasaygues (LMA)

[P10] Novel Ultrasonics Biomarkers (NOVUSBIO)
Financement : AMidex, Interdisciplinarité PR2I (2014-2016)
Porteur E. Franceschini (LMA)

[P9] Exploiting edge illumination dark-field imaging to assess the water distribution in porous building materials
Financement : ESRF Synhrotron project MA2396

Porteur M. Griffa (EMPA-ETH, Zurich, Suisse)

[P8] Evaluation ultrasonore des effets d'irradiation forte dose lors d'un accident de contamination externe ou interne : étude in vivo sur le petit animal
Financement : EDF – Conseil de radioprotection (2013-2015)
Responsable « Techniques ultrasonores de non-linéarité tissulaire »
Porteur E. Franceschini (LMA)

[P7] Evaluation Non Destructive des Enceintes de confinement des centrales nucléaires (ENDE)
Financement : Projet d'Investissement d'Avenir (2014-2018)
Responsable tâche 3 « Evolution de la Fissuration »
Porteur V. Garnier (LMA)

[P6] Used Fuel Campaign, Experimental Investigations
Financement : U.S. Department of Energy (2013)
TJ Ulrich (LANL)

[P5] Innovating for Structural Adhesive Bonding Evaluation and Analysis with Ultrasounds (ISABEAU)
Financement : Agence Nationale pour la Recherche (2012-2016)
J. Moysan (LMA)

[P4] Addressing Facility Needs for Concrete Assessment Using Ultrasonic Testing
Financement : US Department Of Energy (2012)
TJ Ulrich (LANL, USA)

[P3] Evaluation non destructive pour la prédiction de la Dégradation des structures et l'Optimisation de leur Suivi (EVADEOS)
Financement : Agence Nationale pour la Recherche (2011-2014)
J.P. Balayssac (LMDC, Toulouse)

[P2] Auscultation des Câbles Tendus Non Accessibles (ACTENA)
Financement : Agence Nationale pour la Recherche (2005-2008)
J.L. Chazelas (IFSTAR, Nantes)

[P1] Stratégie d'Evaluation Non destructive pour la Surveillance des Ouvrages en béton (SENSO)
Financement : Agence Nationale pour la Recherche (2006-2009)
J.P. Balayssac (LMDC, Toulouse)

Contrats industriels

[C10] JF. Chaix, E. Larose, C. Payan, F. Mazerolle, I. Lillamand, V. Garnier, G. Moreau
Caractérisation ultrasonore de fissures dans le béton.
EDF R&D (2013)

[C9] V. Garnier, C. Payan
Influence de la microstructure du plâtre sur sa réponse dynamique non linéaire. [Master H. Ramanasse]
Saint Gobain Recherche (2012)

[C8] C. Payan, I. Lillamand, G. Corneloup
Mesure non invasive de vide dans un tube
CEA Valduc (2011-2012)

[C7] T.J. Ulrich, C. Payan
Non-linear ultrasound to evaluate the integrity of concrete
US Electrical Power Research Institute (2011)

[C6] J. Moysan, C. Payan
Mesures non destructives pour la caractérisation des paramètres critiques de l'adhésion sur structures collées [Thèse A. Baudot]
Safran (2012-2015)

[C5] C. Payan
Caractérisation des bulles dans le verre fondu [Master A. Baudot]
Saint Gobain Recherche (2011)

[C4] V. Garnier, C. Payan, JF Chaix
Ultrasons diffus pour la caractérisation d'une fissure dans le béton. : approche linéaire et non linéaire. [Thèse A. Quiviger]
EDF R&D (2009-2012)

[C3] C. Payan, G. Corneloup
Faisabilité de la mesure non invasive de vide dans un tube
CEA Valduc (2010)

[C2] J. Moysan, C. Payan
Apport de l'acoustique non linéaire à la caractérisation de l'engagement du sodium liquide : application aux réacteurs nucléaires de quatrième génération [Thèse M. Cavaro]
CEA Cadarache (2007-2010)

[C1] C. Payan, V. Garnier
Détection de fissure dans le béton par acoustique non linéaire [Master J.P. Zardan]
EDF R&D (2009)

VIII. Liste des publications

Publications internationales

[24] M. Remillieux, TJ Ulrich , C. Payan , J. Rivière , C. Lake , P.-Y. Le Bas
Resonant ultrasound spectroscopy for materials with high damping and samples of arbitrary geometry
Journal of Geophysical Research: SolidEarth (In press)

[23] J.N. Eiras, Q.A. Vu, M. Lott, J. Payá, V. Garnier, C. Payan
Evaluation of material nonlinearity under transient solicitation
Ultrasonics (Under review, 2015)

[22] E. Lefèvre, P. Lasaygues, C. Baron, C. Payan, F. Launay, H. Follet, M. Pithioux
Analyzing the anisotropic Hooke's law for children's cortical bone
Journal of the Mechanical Behavior of Biomedical Materials (In press, 2015)

[21] D. Fouan, Y. Achaoui, C. Payan and S. Mensah
Monitoring microbubbles' dynamics using a dual modulation method
Journal of the Acoustical Society of America 137(2), EL144-EL150 (2015)

[20] M.C. Remillieux, B.E. Anderson, T.J. Ulrich, P.Y. Le Bas, C. Payan
Depth profile of a time-reversal focus in an elastic solid
Ultrasonics 58, 60-66 (2015)

[19] T.J. Ulrich, C. Payan, P.Y. Le Bas, M. Griffa, T. Saleh
Nonlinear Elastic Constants determination by Nonlinear Resonance Ultrasound Spectroscopy
Physical Review Letters (In preparation)

[18] N. Favrie, B. Lombard, C. Payan
Fast and slow dynamics in a nonlinear viscoelastic bar excited by longitudinal vibrations
Wave Motion 56, 221–238 (2015)

[17] C. Payan, T.J. Ulrich, P.Y. Le Bas, M. Griffa, P. Schuetz, M.C. Remillieux, T.A. Saleh
Probing material nonlinearity at various depths by the use of time reversal mirror
Applied Physics Letters 104, 144102 (2014)

[16] A Baudot, J. Moysan, C. Payan, N. Ylla, J. Galy, B. Verneret, A. Baillard
Improving adhesion strength analysis by the combination of ultrasonic and mechanical tests on single lap joints.
The Journal of Adhesion 90 (5-6), 555-568 (2014)

[15] C. Payan, T.J. Ulrich, P.Y. Le Bas, T.A. Saleh, M. Guimaraes
Quantitative Linear and Nonlinear Resonance Inspection Techniques and Analysis for material characterization: Application to concrete thermal damage.
Journal of the Acoustical Society of America 136 (2), 537-546 (2014)

[14] C. Payan, A. Quiviger, V. Garnier, J.F. Chaix, J. Salin
Applying diffuse ultrasound under dynamic loading to improve closed crack characterization in concrete
Journal of the Acoustical Society of America 134 (2), EL211-EL216 (2013)

[13] A. Quiviger, A. Girard, C. Payan, J.F. Chaix, V. Garnier, J. Salin
Influence of the depth and morphology of real cracks on diffuse ultrasound in concrete: a simulation study
NDT & E International 60, 11-16 (2013)

[12] V. Garnier, B. Piwakowski, O. Abraham, G. Villain, C. Payan, J.F. Chaix
Acoustical techniques for concrete evaluation: Improvements, comparisons and consistencies
Construction and Building Materials 43, 598–613 (2013)

[11] Z.M. Sbartaï, S. Laurens, S.M. Elachachi, C. Payan
Concrete Evaluation by Statistical Fusion of NDT Techniques,
Construction and Building Materials 37, 943-950 (2012)

[10] A. Quiviger, C. Payan, J.F. Chaix, V. Ganier and J. Salin
Effect of the presence and size of a real macro-crack on diffuse ultrasound in concrete
NDT & E International 45 (1), 128-132 (2012)

[9] C. Payan, V. Garnier and J. Moysan
Determination of nonlinear constants and stress monitoring in concrete by coda waves analysis
European Journal of Environmental and Civil Engineering 15 (4), 519-531 (2011)

[8] M. Cavaro, C. Payan, J. Moysan and F. Baqué
Microbubble cloud characterisation by nonlinear frequency mixing
Journal of the Acoustical Society of America 129 (5), EL179-EL183 (2011)

[7] F. Bouchaala, C. Payan, V. Garnier and J.P. Balayssac
Carbonation Assessment in Concrete by Nonlinear Ultrasound
Cement and Concrete Research 41, 557–559 (2011)

[6] J.-P. Zardan , C. Payan, V. Garnier and J. Salin
Effect of the presence and size of a localized nonlinear source in concrete
Journal of the Acoustical Society of America 128 (1), EL38-EL42 (2010)

[5] C. Payan, V. Garnier and J. Moysan
Potential of nonlinear ultrasonic indicators for NonDestructive Testing of concrete
Advances in Civil Engineering 2010, 238472 (2010)

[4] C. Payan, V. Garnier and J. Moysan
Effect of water saturation and porosity on the nonlinear elastic response of concrete
Cement and Concrete Research 40, 473–476 (2010)

[3] V. Garnier, J.F. Chaix, M. Rossat, C. Payan and G. Corneloup
Nondestructive characterisation of concretes by ultrasonic wave's propagation
Mécanique & Industries 10, 299-303 (2009)

[2] C. Payan, V. Garnier, J. Moysan and P.A. Johnson
Determination of third order elastic constants in a complex solid applying coda wave interferometry
Applied Physics Letters 94, 011904 (2009)

[1] C. Payan, V. Garnier, J. Moysan and P. A. Johnson
Applying nonlinear resonant ultrasound spectroscopy to improving thermal damage assessment in concrete
Journal of the Acoustical Society of America 121 (4), EL125-EL130 (2007)

Publications nationales

[N2] C. Payan, P.Y. Le Bas, V. Garnier, T.J. Ulrich, M. Griffa
Caractérisation non destructive du comportement élastique non linéaire du béton : Potentiel, limitations et perspectives

Annales du Bâtiment et des Travaux Publics, Janvier-Mars, 77-82 (2014)

[N1] J.F. Chaix, C. Payan, V. Garnier, A. Quiviger
Diffusion des ondes ultrasonores appliquée à la caractérisation d'endommagement de béton
Annales du Bâtiment et des Travaux Publics, Janvier-Mars, 41-46 (2014)

Brevets

[B4] A. Baudot, C. Payan, J. Moysan
Procédé de détection et caractérisation de défauts d'adhésion dans les assemblages collés
Brevet déposé, n° de dépôt : 15/50432 (février 2015)

[B3] Y. Achaoui, S. Mensah, C. Payan, E. Debieu, Z. Hammadi, R. Morin
Procédé de contrôle d'au moins une bulle de gaz produite de manière localisée
Brevet déposé, n° de dépôt : 1459127 (septembre 2014)

[B2] D. Fouan, S. Mensha, C. Payan, C. Quinsac
Acoustical determination of the average radius of an inclusion in a medium.
FR3006054

[B1] M. Cavaro, C. Payan
Method Of Determining Void Rate By Nonlinear Acoustic Resonance Spectrometry In A Biphase Medium And Application In A Nuclear Reactor
WO/2011/141370

Séminaires/conférences invités

[T8] *T.J. Ulrich*, C. Payan
Nonlinear UT to Characterize Thermally Damaged Concrete
EPRI Symposium on Concrete Structures, Liner Barriers and Tanks, May 6-8 2014, Charlotte NC, USA

[T7] *J. Moysan*, V. Garnier, C. Payan
NDT and NDE for Mechanics and Materials
NDE Workshop, Saint Gobain CREE, December 10th 2014, Cavaillon, France

[T6] C. Payan
Diffuse ultrasound & quantitative nonlinear resonance techniques for concrete NDE
EMPA, Zurich, Switzerland, October 24th (2013)

[T5] *M. Cavaro*, C. Payan and J.P. Jeannot
Towards the bubble presence characterization within the SFR liquid sodium
ANIMMA International Conference, Marseille, France, 23-27 June 2013

[T4] C. Payan
Influence of the microstructure and damage on the nonlinear elastic behaviour of heterogeneous materials: Application to NDE.
Pôle Européen de la Céramique, Cavaillon, France, April 10th 2013

[T3] C. Payan
Quantification du comportement élastique non linéaire et sa relation avec la microstructure : Application à la caractérisation non destructive du béton
Laboratoire d'Imagerie Paramétrique, Paris, France, 7 novembre 2012

[T2] C. Payan
Nonlinear acoustics for damage detection in industrial materials.
Saint Gobain Recherche, Paris, France, October 25th (2012)

[T1] C. Payan
Quantitative linear and nonlinear resonant inspection techniques for characterizing thermal damage in concrete
European GDR-Workshop on Nonlinearities in Acoustics, Nice, France, March 22-23rd (2012)

Conférences nationales/internationales (sélection). [En italique l'orateur]

[IC33] *Q.A. Vu*, V. Garnier, *C. Payan*, J.-F. Chaix, M. Lott
Nonlinear ultrasonic testing by Rayleigh waves on control of concrete cover – Application in thermal damage evaluation
20th International Symposium on Nonlinear Acoustics, June 29th - July 3rd 2015, Lyon, France

[IC32] *M. Remillieux*, T.J. Ulrich, C. Lake, C. Payan, P.-Y. Le Bas
Multimode Nonlinear Resonant Ultrasound Spectroscopy (NRUS): From the 1D to 3D Characterization of the Elastic Nonlinearity
20th International Symposium on Nonlinear Acoustics, June 29th - July 3rd 2015, Lyon, France

[IC31] *B. Lombard*, C. Payan and N. Favrie
Nonlinear elasticity and slow dynamics: physical and numerical modeling
2015 International Congress on Ultrasonics, May 11-14 2015, Metz, France

[IC30] *D. Fouan*, Y. Achaoui, C. Payan and S. Mensah
Experimental Method for Microbubbles Dynamics Monitoring and Radius Sizing
2015 International Congress on Ultrasonics, May 11-14 2015, Metz, France

[IC29] *E. Lefèvre*, C. Payan, C. Baron, F. Launay, P. Lasaygues, H. Follet, M. Pithioux
Anisotropic properties of children's cortical bone measured by ultrasonic method
27th European Conference on Biomaterials, 30 August - 3 September 2015, Kraków, Poland

[IC28] *C. Payan*
NDE of concrete by nonlinear ultrasound : potential, limitations and prospects
19th International Conference on Nonlinear Elasticity in Materials, 22-27 July 2014, Frejus, France

[IC27] C. Payan, P.Y. Le Bas, *V. Garnier*, T.J. Ulrich, M. Griffa
Caractérisation non destructive du comportement élastique non linéaire du béton : Potentiel, limitations et perspectives
Diagnobéton 2014, 19-20 mars 2014 Toulouse (France)

[IC26] *J.F. Chaix*, C. Payan, V. Garnier, A. Quiviger
Diffusion des ondes ultrasonores appliquée à la caractérisation d'endommagement de béton
Diagnobéton 2014, 19-20 mars 2014 Toulouse (France)

[IC25] C Payan, *V Garnier*, JF Chaix, A Quiviger
Probing Macro Cracks in Concrete Using Diffuse Ultrasound
EWSHM-7th European Workshop on Structural Health Monitoring, July 8-11 2014, Nantes, France

[IC24] *P.Y. Le Bas*, C. Payan, T.J. Ulrich, V. Garnier
Evaluation of concrete carbonation using time reversal and nonlinear acoustics

166th ASA meeting, San Francisco, CA, USA, 2-6 December (2013), The Journal of the Acoustical Society of America 134 (5), 4033 (2013)

[IC23] *M. Cavaro*, C. Payan and J.P. Jeannot
Towards the bubble presence characterization within the SFR liquid sodium
ANIMMA International Conference, Marseille, France, 23-27 June, doi: 10.1109/ANIMMA.2013.6727947 (2013)

[IC22] *M. Cavaro*, C. Payan
Microbubble histogram reconstruction by nonlinear frequency mixing
International Congress on Acoustics, June 1-7th, Montreal, Canada, POMA 19, 030111 (2013)

[IC21] *E. Larose*, N. Tremblay, C. Payan, V. Garnier, and V. Rossetto
Ultrasonic slow dynamics to probe concrete aging and damage
39th QNDE, 15-20 July 2012, Denver, USA, AIP Conf. Proc. 1511, 1317-1324 (2013)

[IC20] *T.J. Ulrich*, B. Anderson, PY Le Bas, C. Payan, J. Douma, R. Snieder
Improving Time Reversal Focusing Through Deconvolution: 20 questions
17th ICNEM, July 1-7th, Cefalu, Italy (2012). POMA 16, 045015 (2012)

[IC19] *M. Cavaro*, C. Payan, S. Mensah, J. Moysan, and J.-P. Jeannot
Linear and nonlinear resonant acoustic spectroscopy of micro bubble clouds
17th ICNEM, July 1-7th, Cefalu, Italy. POMA 16, 045003 (2012)

[IC18] *C. Payan*, T.J. Ulrich, P.Y. Le Bas, T. Saleh, M. Guimaraes
Probing materials damage at various depths by use of Time Reversal Elastic Nonlinearity Diagnostic: Application to concrete.
17th ICNEM, July 1-7th, Cefalu, Italy (2012). POMA 16, 045013 (2012)

[IC17] A. Quiviger, *C. Payan*, J-.F. Chaix, V. Garnier, J. Salin
Macro-crack characterization in concrete by diffuse ultrasound under low frequency dynamic loading
17th ICNEM, July 1-7th, Cefalu, Italy (2012). POMA 16, 045016 (2012)

[IC16] *V. Garnier*, A Quiviger, C. Payan, Jean-François Chaix, J Salin
Non Linear Acoustic Applied to the Concrete Study
Acoustics 2012, April 23-27, Nantes, France, HAL 00811375 (2012)

[IC15] *C. Payan*, T.J. Ulrich, P.-Y. Le Bas and M. Guimaraes,
Probing materials damage at various depths by use of Time Reversal Elastic Nonlinearity Diagnostic: Application to concrete
Acoustics 2012, April 23-27, Nantes, France, HAL 00810940 (2012)

[IC14] *C. Payan*, T.J. Ulrich, P.-Y. Le Bas and M. Guimaraes,
Quantitative linear and nonlinear resonant inspection techniques for characterizing thermal damage in concrete
Acoustics 2012, April 23-27, Nantes, France, HAL 00810938 (2012)

[IC13] C. La Rocca, *J. Moysan* and C. Payan
Characterization of an epoxy bonded aluminum alloy sample applying dynamic acousto elastic testing
REVIEW OF PROGRESS IN QUANTITATIVE NONDESTRUCTIVE EVALUATION: Volume 31. AIP Conference Proceedings, Volume 1430, pp. 1261-1267 (2012).

[IC12] *A. Quiviger*, C. Payan, J.-F. Chaix, V. Garnier, J.-P. Zardan, J. Salin
Non Destructive characterization of cracks in concrete by ultrasonic auscultation of civil engineering structures

7th SFEN International Symposium, paper n°A121-T10, Fontevraud, 26-30 septembre 2010

[IC11] C. La Rocca, *C. Payan* and J. Moysan
Evaluation of epoxy bonded joint quality using nonlinear acoustics
XV ICNEM Otranto, Italy, 4 - 10 July 2010, Proceedings of Meetings on Acoustics 10, 045001 (2010)

[IC10] A. Quiviger, J.P. Zardan, *C. Payan*, J.F. Chaix, V. Garnier, J. Moysan and J. Salin
Macro crack characterization by linear and nonlinear ultrasound in concrete
XV ICNEM Otranto, Italy, 4 - 10 July 2010, Proceedings of Meetings on Acoustics 10, 045003(2010)

[IC9] F. Bouchaala, *C. Payan* and V. Garnier
Effect of carbonation on the nonlinear response of concrete
XV ICNEM Otranto, Italy, 4 - 10 July 2010, Proceedings of Meetings on Acoustics 10, 045002 (2010)

[IC8] *M. Cavaro*, J. Moysan, G. Corneloup, C. Gueudre, C. Payan, F. Baque, G. Prele, J. Sibilo
Towards in-service acoustic characterization of gaseous microbubbles applied to liquid sodium
ANIMMA International Conference, Marseille, France, 7-10 June 2009. http://dx.doi.org/10.1109/ANIMMA.2009.5503768

[IC7] *C. Payan*, V. Garnier, J. Moysan and P. Johnson
Determination of nonlinear elastic constants and stress monitoring in concrete by coda waves analysis
NDTCE'09, Non-Destructive Testing in Civil Engineering, Nantes, France, June 30th – July 3rd, 2009

[IC6] *V. Garnier*, J.F. Chaix, C. Payan
Improvement of new wave propagation techniques to characterize concrete
NDTCE'09, Non-Destructive Testing in Civil Engineering, Nantes, France, June 30th – July 3rd, 2009

[IC5] *M. Cavaro*, J. Moysan, C. Payan, C. Gueudré, G. Corneloup, and F. Baqué
Towards nonlinear ultrasonic characterization of air microbubbles in water
XIV ICNEM, 1 - 5 June 2009, Lisbon, Portugal. Full paper : POMA 7, 045005 (2009).

[IC4] *V. Garnier*, M. Stéphane, J.F. Chaix, C. Payan, and G. Corneloup,
Analysis of the backscattered waves in an heterogeneous material: Application on concretes
J. Acoust. Soc. Am. 123, 3848 (2008), Acoustics 2008, July 2008, Paris. Full paper : POMA 4, 045015 (2008).

[IC3] *C. Payan*, V. Garnier, and J. Moysan
Effect of Water Saturation on the Nonlinear Elastic Response of Concrete
J. Acoust. Soc. Am. 123, 3399 (2008), Acoustics 2008, July 2008, Paris. Full paper : POMA 4, 045013 (2008).

[IC2] *C. Payan*, V. Garnier, J. Moysan, and P. Johnson,
Determination of nonlinear elastic constants and stress monitoring in concrete by coda waves analysis,
XIII ICNEM, June 2008, Aix en Provence. Full paper : POMA 3, 045002 (2008).

[IC1] *C. Payan*, V. Garnier, G. Corneloup, J. Moysan
Potential of nonlinear ultrasound spectroscopy to monitor thermal damage in concrete
Proceedings GDR 2501, pp. 225-230, INRIA Editions - ISBN 2-7261-1282-x, Giens, 15-19 May 2006.

Rapports

[R12] JF. Chaix, E. Larose, C. Payan, F. Mazerolle, I. Lillamand, V. Garnier, G. Moreau
Caractérisation ultrasonore de fissures dans le béton.

Rapport final EDF R&D (2014)

[R11] T.J. Ulrich, B.E. Anderson, P.Y. Le Bas, C. Payan, B. Reichman
Experimental Investigations–End of Year Technical Report
LA-UR-13-27010 (2013)

[R10] T.J. Ulrich, B.E. Anderson, P.-Y. Le Bas, J. Riviere, J.C. Tokash, S. Haupert, C. Payan and Y. Ohara
Storage Experimentation: Midyear Progress Report
LA-UR-13-23383, May 2013

[R9] C. Payan, I. Lillamand, E. Taviot, G. Corneloup
Mesure non invasive de vide dans un tube
Rapport final contrat CEA VAlduc (2012)

[R8] T.J. Ulrich, C. Payan, P. Roberts
Addressing Facility Needs for Concrete Assessment Using Ultrasonic Testing: Mid-year Report
LA-UR-12-20274, March 2012

[R7] C. Payan, T.J. Ulrich
Nondestructive Evaluation: Nonlinear Ultrasound to Evaluate the Integrity of Thermally Damaged Concrete.
EPRI, Palo Alto, CA: 2012. 1026501. (2012)

[R6] C. Payan,
Caractérisation des bulles dans le verre fondu
Rapport final contrat Saint Gobain Recherche (2011)

[R5] C. Payan, G. Corneloup
Faisabilité de la mesure non invasive de vide dans un tube
Rapport final contrat CEA Valduc (2010)

[R4] J.F. Chaix, G. Corneloup, V. Garnier, I. Lillamand, M.A. Ploix, C. Payan
Mesure de contrainte dans les structures béton par ultrason
Rapport final pour le projet ANR ACTENA (2008)

[R3] V. Garnier, M.A. Ploix, C. Payan, J.F. Chaix, J. Moysan
Potential of backscattered waves for concrete NDE
Rapport pour le projet ANR SENSO (2008)

[R2] C. Payan
Caractérisation non destructive du béton : étude du potentiel de l'acoustique non linéaire
Thèse de doctorat, Aix Marseille Univ, (2007)

[R1] C. Payan
Système anti vibratoire auto-adaptatif
Rapport de DEA, Aix Marseille Univ (2001)

IX. Sélection d'articles internationaux publiés

[REM15] M.C. Remillieux, B.E. Anderson, T.J. Ulrich, P.Y. Le Bas, C. Payan,
Depth profile of a time-reversal focus in an elastic solid.
Ultrasonics 58, 60–66 (2015)

[FOU15] D. Fouan, Y. Achaoui, C. Payan, S. Mensah,
Microbubble dynamics monitoring using a dual modulation method
Journal of the Acoustical Society of America 137 (2), EL144-EL150 (2015)

[PAY14a] C. Payan, T.J. Ulrich, P.Y. Le Bas, T.A. Saleh, M. Guimaraes
Quantitative Linear and Nonlinear Resonance Inspection Techniques and Analysis for material characterization: Application to concrete thermal damage.
Journal of the Acoustical Society of America 136 (2), 537-546 (2014)

[PAY14b] C. Payan, T.J. Ulrich, P.Y. Le Bas, M. Griffa, P. Schuetz, M.C. Remillieux, T.A. Saleh
Probing material nonlinearity at various depths by time reversal mirrors
Applied Physics Letters 104, 144102 (2014)

[BAU14] A Baudot, J. Moysan, C. Payan, N. Ylla, J. Galy, B. Verneret, A. Baillard
Improving adhesion strength analysis by the combination of ultrasonic and mechanical tests on single lap joints.
The Journal of Adhesion 90 (5-6), 555-568 (2014)

[PAY13] C. Payan, A. Quiviger, V. Garnier, J.F. Chaix, J. Salin
Applying diffuse ultrasound under dynamic loading to improve closed crack characterization in concrete
Journal of the Acoustical Society of America 134 (2), EL211-EL216 (2013)

[QUI13] A. Quiviger, A. Girard, C. Payan, J.F. Chaix, V. Garnier, J. Salin
Influence of the depth and morphology of real cracks on diffuse ultrasound in concrete: a simulation study
NDT & E International 60, 11-16 (2013)

[QUI12] A. Quiviger, C. Payan, J.F. Chaix, V. Ganier and J. Salin
Effect of the presence and size of a real macro-crack on diffuse ultrasound in concrete
NDT & E International 45 (1), 128-132 (2012)

[CAV11] M. Cavaro, C. Payan, J. Moysan and F. Baqué
Microbubble cloud characterisation by nonlinear frequency mixing
Journal of the Acoustical Society of America 129 (5), EL179-EL183 (2011)

[BOU11] F. Bouchaala, C. Payan, V. Garnier and J.P. Balayssac
Carbonation Assessment in Concrete by Nonlinear Ultrasound
Cement and Concrete Research 41, 557–559 (2011)

[ZAR10] J.-P. Zardan , C. Payan, V. Garnier and J. Salin
Effect of the presence and size of a localized nonlinear source in concrete
Journal of the Acoustical Society of America 128 (1), EL38-EL42 (2010)

[PAY10] C. Payan, V. Garnier and J. Moysan
Effect of water saturation and porosity on the nonlinear elastic response of concrete
Cement and Concrete Research 40, 473–476 (2010)

[PAY09] C. Payan, V. Garnier, J. Moysan and P.A. Johnson
Determination of third order elastic constants in a complex solid applying coda wave interferometry
Applied Physics Letters 94, 011904 (2009)

[PAY07] C. Payan, V. Garnier, J. Moysan and P. A. Johnson
Applying nonlinear resonant ultrasound spectroscopy to improving thermal damage assessment in concrete
Journal of the Acoustical Society of America 121 (4), EL125-EL130 (2007)

Ultrasonics 58 (2015) 60–66

Contents lists available at ScienceDirect

Ultrasonics

journal homepage: www.elsevier.com/locate/ultras

Depth profile of a time-reversal focus in an elastic solid

Marcel C. Remillieux [a,*], Brian E. Anderson [a], T.J. Ulrich [a], Pierre-Yves Le Bas [a], Cedric Payan [b]

[a] Geophysics Group (EES-17), MS D446, Los Alamos National Laboratory, Los Alamos, NM 87545, United States
[b] Aix Marseille Université, Laboratory of Mechanics and Acoustics, LMA CNRS UPR 7051, 31 chemin Joseph-Aiguier, 13402 Marseille CEDEX 20, France

ARTICLE INFO

Article history:
Received 26 August 2014
Received in revised form 12 December 2014
Accepted 13 December 2014
Available online 24 December 2014

Keywords:
Time-reversal
Elastodynamics
Lamb's problem

ABSTRACT

The out-of-plane velocity component is focused on the flat surface of an isotropic solid sample using the principle of time reversal. This experiment is often reproduced in the context of nondestructive testing for imaging features near the surface of the sample. However, it is not clear how deep the focus extends into the bulk of the sample and what its profile is. In this paper, this question is answered using both numerical simulations and experimental data. The profiles of the foci are expressed in terms of the wavelengths of the dominant waves, based on the interpretation of the Lamb's problem and the use of the diffraction limit.

Published by Elsevier B.V.

1. Introduction

Over the last decade, a number of sophisticated imaging techniques have emerged that combine the properties of nonlinear elasticity observed in a damaged material and the principle of time reversal (TR) [1–7]. A TR mirror (TRM) allows focusing narrowly energy in space and time. If energy is focused near a damaged region (e.g. crack, delamination), the relatively large amplitude of the wave field at that location will activate a nonlinear elastic response in the test sample, which can then be exploited for imaging applications.

A standard TR experiment in a reverberant elastic medium is a two-step process [8]. In the first step, or *forward* propagation, a known signal is emitted from a transducer (source) at a point *A* on the surface of the sample while another transducer (receiver) records the response at a point *B* on the surface. The received signal is the convolution of the source signal with the impulse response between the source transducer at *A* and receiver transducer at *B*. This impulse response is rather complex due to the multiple paths (e.g. reflections) that the waves may follow within the bounded medium. In the second step, or *backward* propagation, the received signal is reversed in time and emitted from the transducer at point *B*. As a result of the invariance of the TR operator in a lossless medium [9], the elastic wave field focuses on point *A* and reconstructs the original source signal. There are some imperfections in this reconstruction process, mainly because the directional information of the energy received in the *forward* signals is typically not used, attenuation that exists in a realistic system, and because a limited (as opposed to infinite) acquisition time of the *forward* propagation signal is available. An alternative to standard TR is reciprocal TR (R-TR) [10–12]. In R-TR, the reversed signal is emitted from the original source position *A* and the elastic wave field focuses at the original receiver position *B*. It is possible to interchange the source and receiver positions thanks to the principle of spatial reciprocity [13].

In the context of a TR experiment, a reverberant medium offers a number of advantages over an unbounded one. In an unbounded homogeneous medium, the TRM ideally forms a closed surface around the source [14]. In practice, however, the TRM often has a small aperture and does not capture the full wave field propagating away from the source, which leads to an imperfect reconstruction of the focused signal [15]. In contrast, the multiple reflections of the waves on the boundaries of a medium with a finite size act as virtual sources that improve the quality of the TR focusing. Therefore, if the modal density within the finite medium is sufficiently large and damping is relatively small, the TRM can be reduced to a single element. Following this idea, a number of TR experiments have been conducted using *chaotic cavities* [16–18], where one emitter is used within a cavity of arbitrary shape. Such devices will enhance wave scattering and break any symmetry that could potentially exist in the problem. In this paper, the cavity has the shape of a rectangular parallelepiped, so multiple transducers must be used to break the symmetry of the problem.

TR of elastic waves in a solid is a more complex problem than TR of acoustic waves in a fluid because the wave field is no longer scalar but vectorial. Consequently, different types of wave motions

* Corresponding author.
E-mail address: mcr1@lanl.gov (M.C. Remillieux).

http://dx.doi.org/10.1016/j.ultras.2014.12.003
0041-624X/Published by Elsevier B.V.

may coexist in a solid: e.g. shear (S), compressional (P), and Rayleigh (R) waves. Draeger et al. [19] delineated theoretically the mechanisms involved in the focusing of P and S waves in a solid half-space using a TRM. A point source in the solid generated P and S waves, which propagated to a TRM placed in a fluid surrounding the solid. In the far-field, the P and S waves separate because of their different propagation speeds and reach the TRM at different times. This property may be used to focus the P and S waves in the solid, almost independently from one another. It was shown that when the signals from both waves are emitted by the TRM into the fluid, each wave generates a P and an S wave in the solid, thus leading to a total of four waves propagating in the solid. Two of these waves will focus properly, while the other two will not and simply generate some "low-level noise". In experiments, Draeger et al. [20] related the size of the focal spot to the type of wave used in the TR process and validated their theoretical analysis. Sutin et al. [12] designed a TR experiments in a reverberant solid sample using only one transducer. They successfully focused elastic energy on the surface of the sample using the out-of-plane velocity component at the selected focal point where the receiver was placed. They reported that the width of the focal spot at -3 dB was equal to a factor $\times$ 0.44 of the shear wavelength at the center frequency of the pulse for a doped-glass block, which is a weakly dissipative medium. In fact, if the reference wave is taken as the Rayleigh wave, then they reach exactly the diffraction limit. Ulrich et al. [21] showed in a series of R-TR experiments and simulations that a scalar source (or a source whose radiation characteristics are not known) may be used to focus selectively vector components of the motion (either individual components or some combinations of them) on the surface of a sample. For instance, if energy is focused at a point on the surface of the sample using the out-of-plane velocity component, the in-plane components of the velocity vector will exhibit amplitude levels that are similar to the temporal side lobes of the reconstructed pulse, i.e. "low-level noise". However, in their study, they did not relate the size of the focal spot to the types of waves propagating in the medium. In most TR experiments it is not possible to probe the elastic wave field in the bulk of the sample. Numerical simulations are an alternative to experiments when the wave propagation needs to be characterized within the bulk of the sample. Some recent work involving simulations of TR experiments in solids have been carried out but were limited to 2D systems [22,23], thus possibly missing some features that could be observed in a realistic 3D system.

In this paper, the out-of-plane velocity component is focused on the surface of a 3D aluminum sample using R-TR. The focal spot has a finite size related to the types of waves propagating within the medium and to the center frequency of the focused signal (e.g. pulse). The focal spot observed in experiments on the surface of a sample also extends into the bulk of the sample with an unknown depth profile. In this context, the objective of this paper is to characterize the depth profile of the TR focal spot for various conditions (e.g. center frequencies and material properties). In the context of nondestructive testing (NDT), this profile relates to the portion of a sample that will be probed around the focal time of a TR experiment and consequently to the nonlinear signature that will be recorded. Since depth profiles of the TR foci cannot be measured experimentally, the analysis is supported mainly by numerical simulations, within the framework of linear elasticity. Experimental data are used mainly to validate the numerical model. The paper is organized at follows. Section II validates the numerical model used in the rest of the analysis against experimental data for the case where elastic energy is focused near an edge of an aluminum block. Section III examines the depth profiles of the TR foci on a surface of a block for various material properties and center frequencies of the focused signal. Section IV concludes.

2. Experimental validation of the numerical model

2.1. Experiments

Experiments were conducted on an aluminum sample with a rectangular shape and dimensions of $10 \times 10 \times 19$ cm^3. Fig. 1 is a photograph of the experimental setup. Elastic energy was transmitted into the sample using eight identical piezoelectric disks (type PZT-5, diameter of 12.7 mm, and thickness of 2 mm) that were glued onto three surfaces, at locations far from the desired focal point to allow diffusion of the elastic energy into the sample. The velocity wave field was measured on the surface of the sample using single point laser Doppler vibrometers (LDV) from Polytec Inc. The normal component of the velocity was measured with the OFV 303 (3001 controller, VD-02, 5 mm/s/V) and the in-plane components with the OFV 552 (5000 controller, VD-02, 5 mm/s/V) fiber-optic differential laser vibrometer. The angle of $\pm 30^\circ$ between the fiber-optic laser heads and the surface normal is used to eliminate the normal component of the velocity vector through subtraction and provide the in-plane component [24]. A rotation stage is incorporated to allow measurements in the two orthogonal in-plane directions of motion when the fiber-optic laser heads are rotated 90 degrees. Source signals were generated with an 8-channel, 12-bit A/D Gage CompuGen 8150 card and received signals were digitized with a 2-channel, 14-bit D/A Gage CompuScope 14,200 cards using a sampling rate of 10 MHz per channel. Source signals were amplified 50 times with Tegam 2350 power amplifiers. A scanning system was developed that allows the laser vibrometer to record the motion of the sample at various locations within a region of interest with a system consisting of a Newport ESP300 positioning controller and two Newport ILS250MVTP linear-axis translation stages that move the laser and pause during the measurement at each scan point location. The experiment was setup on a floating, vibration isolation table (Newport LW3048B).

The R-TR method [8] is used to create a focus of the vertical, in-plane component of motion centered at the location of the laser spot in Fig. 1 (point B). First, impulse responses (IRs) are determined between the PZT transducers and point B. For this purpose, a linear chirp signal with appropriate frequency bandwidth is emitted from a single PZT transducer while the vertical, in-plane velocity component is measured with the LDV at point B. This operation is repeated for all PZT transducers. Then, the IRs are determined from a cross correlation of the input chirp signal with the measured response, reversed in time, scaled in amplitude to maximize the amplifier output, and all reversed signals are broadcast simultaneously from the corresponding PZT transducers. This creates a TR focus of the vertical, in-plane velocity component (v_z). The in-plane velocity component (v_x) and the out-of-plane velocity component (v_y), are also measured. Spatial scans of the TR focus in each component of motion are displayed in Fig. 2.

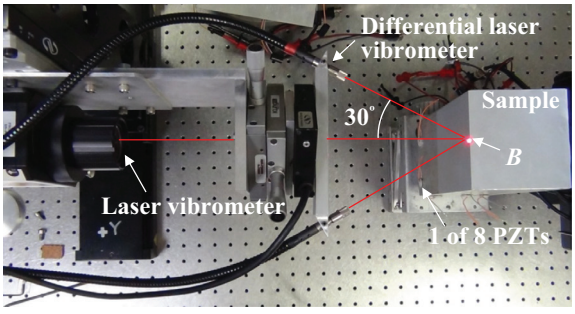

Fig. 1. Photograph of the experimental setup.

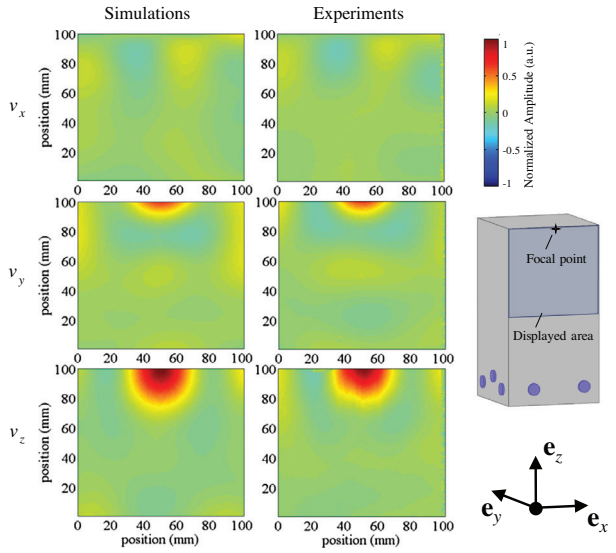

Fig. 2. Velocity components at the focal time. Focusing was achieved using the v_z component at the focal point. The drawing on the right-hand side indicates the location of the focal point and the area on the sample surface where results are displayed. Simulated (left column) and experimental (right column) results. For each column, data are normalized with respect to the peak amplitude of v_z. The v_z signal generated at the focal point (see Fig. 3) consists of a pulse centered at 52.8 kHz in simulations and at 54.7 kHz in experiments. As a result, the spot size of v_z is larger in simulations than in experiments. Witness the dipole motion around the focal point observed in v_x due to the Poisson effect. This motion has a much smaller amplitude than v_z at the focal point but is larger than the background.

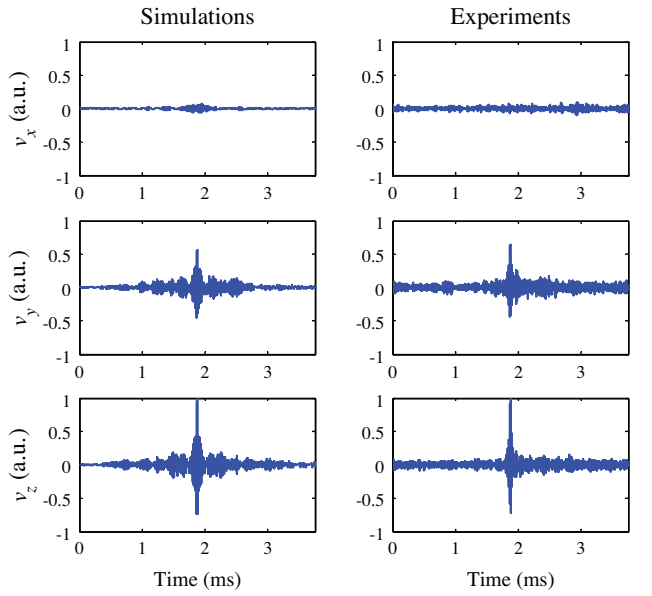

Fig. 3. Time histories of the velocity components at the focal point, for the problem settings described in Fig. 2. Simulated (left column) and experimental (right column) results. For each column, data are normalized with respect to the peak amplitude of v_z.

2.2. Numerical model

The above experiment is simulated using the "Solid Mechanics" module of the commercial finite-element software package COMSOL MULTIPHYSICS 4.3a. In the simulations, the aluminum has a mass density of 2700 kg m^{-3}, a Young's modulus of 70 GPa, and a Poisson's ratio of 0.33. The PZT transducers are not modeled. Instead, a normal surface load is applied at the location of the transducers. The time history of the surface load in the *forward*-propagation step consists of a 50 kHz tone-burst with a full bandwidth at half maximum (FBHM) of 10 kHz, similar to that observed in the experiments at the focal point. The computational domain is discretized into quadratic tetrahedral elements with a maximum size of 5 mm, which corresponds to 10 elements per smallest wavelength at 55 kHz (center frequency + half bandwidth of the pulse). The smallest wavelength is that of the Rayleigh wave and is equal to 52.9 mm, based on a propagation speed of 2910 m.s^{-1}. Transient simulations are carried out using a time step of 0.1 μs, which satisfies the Courant–Friedrichs–Lewy condition for a 3D problem of elastodynamics.

2.3. Discussion

Fig. 2 depicts snapshots of the three simulated and measured velocity components, v_x, v_y, and v_z, at the focal time of t = 1.876 ms. Results are displayed on a portion of the surface surrounding the focal point. Time histories of these velocity components at the focal point are shown in Fig. 3. The v_z component exhibits the largest peak amplitude at the focal time, which is expected since this is the component used in the TR process. A significant portion of the elastic energy is also contained in the y-component of the motion, as a result of focusing near an edge parallel to the x-axis. The asymmetry of the system in the y-direction (e.g. fluid or vacuum on one side of the focal point and solid on the other side) causes motion of the focal-point region in the y–z plane. Likewise, if the focal point was close to a corner of the sample, energy would be contained in all three components of the motion, regardless of the component used in the TR process, due to the asymmetry of the system in the three Cartesian directions. Last, it is interesting to observe the dipole structure of the v_x component around the focal point, due to the Poisson effect. This motion has much smaller amplitude than v_z at the focal point but is larger than the background.

The numerical model captures successfully the main features of the elastic response observed in experiments, including the dipole structure of the v_x component and the focal spots for the v_y and v_z components in Fig. 2. Note that the size of the focal spot for the v_z component is larger in simulations than in experiments. As discussed in the introduction, the size of the focal spot is related to the center frequency of the focused signal at the focal point. The signal of the v_z component at the focal point consists of a pulse centered at 52.8 kHz in simulations and 54.7 kHz in experiments, which implies a smaller size of the focal spot in experiments. It is also worth mentioning that, in Fig. 3, the ratios between the peak amplitudes of the v_y and v_z components at the focal point are 57% in simulations and 63% in experiments. The close qualitative and quantitative agreements between experiments and simulations are remarkable given the different approaches used to create the TR signals.

3. Focusing elastic energy at the center of a flat surface

The out-of-plane velocity component (now v_z) is focused numerically at the center of the top surface of the aluminum sample described in Section 2. A Ricker wavelet is used in the forward-propagation step of the TR simulation. This pulse has a wider bandwidth than that described in Section 2.2, and thus will lead to a focusing of better quality. For instance, a Ricker pulse centered at 50 kHz has a FBHM of nearly 58 kHz. Besides, the fact that Ricker wavelets are commonly used in the field of elastodynamics makes the study more general than using a narrowband pulse mimicking a particular experiment. The computational domain is discretized with at least 6 quadratic tetrahedral elements per smallest wave-

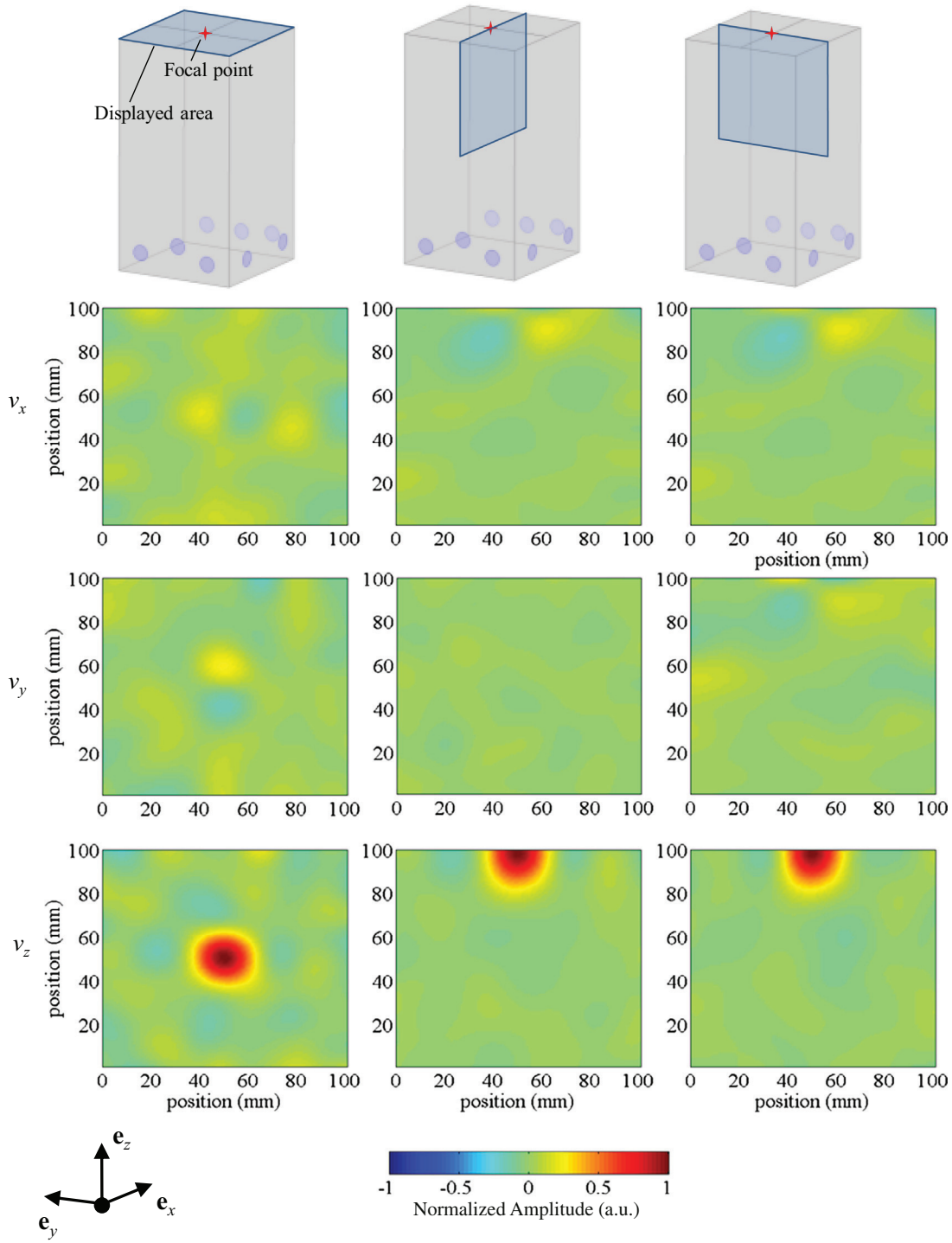

Fig. 4. Simulated velocity components at the focal time. Focusing was achieved using the v_z component. The drawings on the bottom row indicate the location of the focal point and the area where results are displayed. Data are normalized with respect to the peak amplitude of v_z. The v_z signal generated at the focal point consists of a pulse centered at 79.2 kHz.

length. For a Ricker wavelet centered at 50 kHz, the maximum element size is set to 5 mm (the same mesh is used in Section 2.2).

Snapshots of the three simulated velocity components at the focal time are depicted in Fig. 4, for a pulse centered at 79.2 kHz. Results are displayed on the top surface (x–y plane) and within the depth of the sample (x–z and y–z planes). As expected, the largest amplitude is observed for the v_z component while the in-plane components, v_x and v_y, exhibit the Poisson effect (dipole structure) discussed in Section II. The focus has the shape of a half prolate spheroid, elongated along the z-axis. It is not perfectly symmetric with respect to the z-axis, indicating an imperfect reconstruction of the original source. The normalized surface and depth profiles of the focus are shown in Fig. 5. Their respective size can be analyzed in connection with Lamb's problem described below.

Fig. 6 shows snapshots of the v_x and v_z components in the x–z plane due to a normal point load on the surface of a larger aluminum sample with dimensions of $0.4 \times 0.2 \times 0.2$ m^3. This is a *forward*-propagation problem that does not involve TR. The load

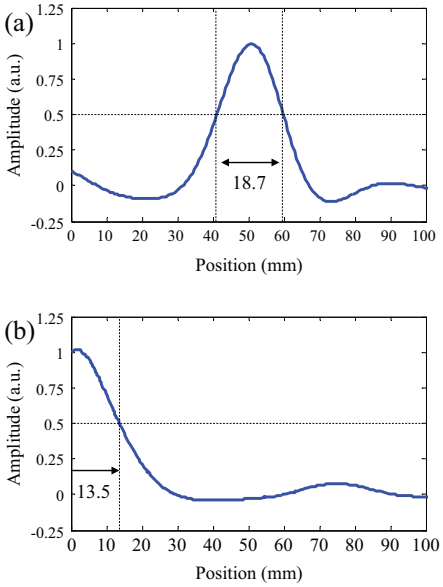

Fig. 5. Simulated surface and depth profiles of v_z at the focal time. The v_z signal generated at the focal point consists of a pulse centered at 79.2 kHz.

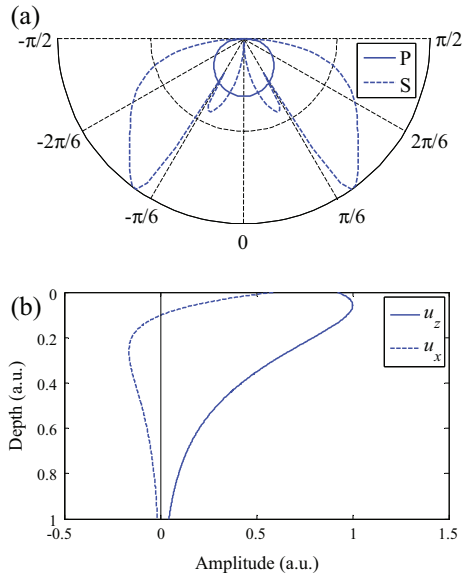

Fig. 7. Analytical far-field radiation patterns in an elastic half space for Lamb's normal point load problem in 3D. (a) *P* and *S* waves. (b) Vertical and horizontal motion components of the *R* wave. Note that the peak amplitude of the Rayleigh wave is found beneath the surface, which is consistent with the depth profile of the TR focus in Fig. 5.

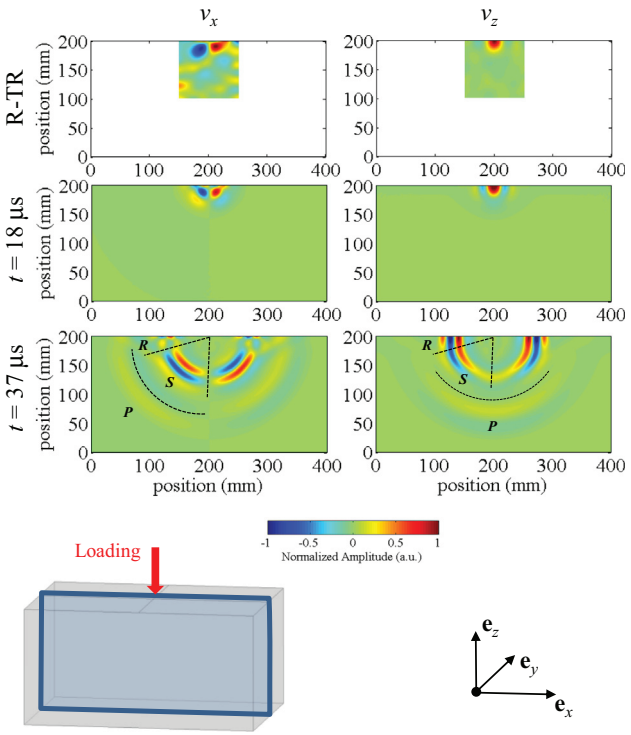

Fig. 6. Simulated velocity components in the near and mid fields due to a normal point load applied on the surface of the sample (*forward*-propagation problem). The two plots on the top row are the velocity components at the focal time of the corresponding R-TR problem, reproduced here for convenience. For each plot, data are normalized with respect to the peak amplitude of the corresponding velocity component. The time history of the load is a Ricker wavelet centered at 75 kHz.

signal consists of a Ricker wavelet centered at 75 kHz. Results are displayed at times $t = 17$ µs (near-field radiation) and 37 µs (mid-field radiation). For convenience, the v_x and v_z components at the focal time of the R-TR simulation (see center column in Fig. 4) are scaled appropriately and reproduced in this figure (top row).

This *forward*-propagation problem would be equivalent to Lamb's normal point load problem [25] if the medium was an elastic half space. Analytical solutions have been derived for this problem but are mostly limited to the far-field radiation [26,27], as shown in Fig. 7 for a harmonic, point-load (3D) configuration. Most of the features of the far-field radiation can also be observed in the mid-field: (i) *S* waves dominate the elastic wave field in the bulk of the sample, with their amplitude being the largest between the angles of $\pi/6$ and $2\pi/6$ with respect to the vertical axis; (ii) the vertical component of the *R* wave reaches a maximum beneath the surface while its horizontal component experiences a phase change along the depth. The *R*-wave features are also observed in the vertical and horizontal components of the velocity field at the focal time of the TR simulation indicating that *R* waves dominate the propagation in the vicinity of the surface in a TR experiment. This would explain why the peak amplitude of the focal spot in Fig. 5 is not found exactly on the surface (where the velocity component is focused) but beneath it. Last, it is interesting to observe that the R-TR process recreates an approximate snapshot of the near-field *forward* radiation. The size of the virtual source is controlled by the diffraction limit, thus preventing the reconstruction of details smaller than the wavelength(s) of the wave(s) involved in the propagation.

In a perfect TR experiment, the diameter of a focal spot measured at the half maximum value is equal to one half of the dominant wavelength, as a consequence of the diffraction limit. On the surface of the sample, the propagation is dominated by the *R* waves. Therefore, the diameter of the focal spot in the *x*–*y* plane can be expressed as,

$$w^{\text{emp}} = \lambda_R/2, \tag{1}$$

where the superscript "emp" refers to empirical. Along the *z*-axis, the propagation is dominated by *R* waves close to the surface and *S* waves in the bulk of the sample. As a result, the focal spot in a vertical plane of the sample has the shape of a half ellipse. Although two types of waves dominate the propagation, their wavelengths

Table 1
Measured and simulated sizes (width and depth) of the focal spot during the TR focusing of the out-of-plane motion component (v_z) for various materials and center frequencies of the focused signals.

Data type	Material	E (GPa)	ν	ρ (kg m^{-3})	f_c (kHz)	λ_P (mm)	λ_S (mm)	λ_R (mm)	w^{obs} (mm)	w^{emp} (mm)	d^{obs} (mm)	d^{emp} (mm)
Num	Aluminum	70	0.33	2700	53.4	116.1	58.5	54.5	28	27.3 (−2.5%)	19.2	19 (−1%)
Num	Aluminum	70	0.33	2700	79.2	78.3	39.4	36.7	18.7	18.4 (−1.6%)	13.5	12.8 (−5.2%)
Num	Undefined	70	0.15	2700	59.2	88.4	56.7	51.2	26	25.6 (−1.5%)	19.2	18.4 (−4.2%)
Num	Undefined	70	0.2	2700	59.4	90.4	55.3	50.4	25.6	25.2 (−1.6%)	18.8	18 (−4.3%)
Num	Undefined	70	0.45	2700	55	180	54.4	51.5	26	25.8 (−0.8%)	17.8	17.7 (−0.6%)
Exp	Aluminum	/	/	2705	75	83.4	42	39.2	20.1	19.6 (−2.5%)	/	/
Exp	Aluminum	/	/	2705	123	50.9	25.6	23.9	12.3	12 (−2.4%)	/	/
Exp	Aluminum	/	/	2705	152	41.2	20.7	19.3	10.2	9.7 (−4.9%)	/	/
Exp	Aluminum	/	/	2705	169	37	18.7	17.4	8.9	8.7 (−2.2%)	/	/

are proportional to one another so that the depth of the focus can be expressed in terms of one wavelength only as,

$$d^{emp} = 1.3\lambda_S/4, \quad (2)$$

where the factor 1/4 is assumed because the diffraction-limit theory is applied to a half focal spot and the factor 1.3 is found by inspecting the radii of the focal spots in the z-direction for all the numerical simulations.

Results from simulations and experiments for various material properties and center frequencies of the focused signals are summarized in Table 1. Material properties were those of aluminum but with a Poisson's ratio varied from 0.15 to 0.45. Center frequencies were varied from 53 to 169 kHz. There is a fair agreement between the observed and predicted sizes of the focal spots, with differences mostly within 5% for all cases considered. Besides the use of an empirical expression, variations of the results can be attributed to the imperfect reconstruction of the source in the R-TR process. Note that an expression of d^{emp} involving λ_P would not be robust to changes of the Poisson's ratio. This is another indication that in the bulk of the sample, the diffuse wave field is mostly dominated by S waves.

Before closing this section, some important differences between 2D and 3D modeling are outlined in the context of TR near the surface of an elastic solid. The volumetric strain is chosen for the analysis since it has been used in previous numerical work related to imaging applications where the principle of TR is combined with the properties of nonlinear elasticity [23]. The volumetric strain is an eigenvector of the elasticity tensor and thus can be used to apply scalar nonlinearity laws in which, for instance, the volumetric stiffness is a power series of the volumetric strain. The volumetric strains obtained at the focal time of a TR experiment simulated with 2D and 3D models are shown in Fig. 8. In both simulations, a Ricker wavelet centered at 75 kHz was used in the *forward*-propagation problem and the out-of-plane velocity component was focused. In 2D, the volumetric strain has a pear-like shape, which was also predicted by Janssen and Van Den Abeele [23]. It reaches two local maxima, one close to the surface where the R waves dominate and one in the bulk of the sample where the P and S waves dominate. In 3D, the volumetric strain field has the shape of a half ellipse with only one local maximum obtained on the surface of the sample and a penetration depth of only 5.3 mm, for the case of a pulse centered at 75 kHz. In this case, the depth profile of the volumetric strain seems to be dominated by the R waves only, which decay exponentially with depth.

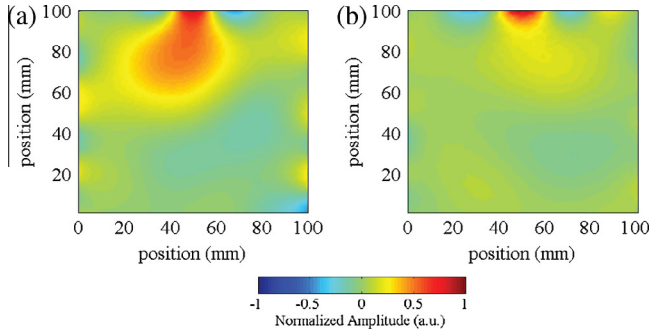

Fig. 8. Simulated volumetric strain fields at the focal time with (a) 2D and (b) 3D models. In 3D, a slice of the data is extracted in the x–z plane, following the cut depicted in Fig. 4. Due to symmetry, identical results are obtained in the y–z plane. Focusing was achieved using the v_z component. A Ricker wavelet centered at 75 kHz was used in the *forward*-propagation problem.

4. Conclusion

This paper investigated the problem of focusing the out-of-plane velocity component on the surface of an isotropic solid sample. The numerical model used in the analysis was first validated against experimental data. Subsequently, empirical expressions for the width and depth of the focal spot (that of the out-of-plane velocity component) were found based on (i) an interpretation of Lamb's problem to determine which waves dominate the propagation in the regions of interest (surface and bulk) and (ii) the use of the diffraction limit. In these expressions: the width of the focal spot depends only on the wavelength of the Rayleigh wave and the depth on the wavelength of the shear wave, at the center frequency of the focused pulse. The empirical expressions were found to be robust to changes of the center frequency of the focused pulse and of the Poisson's ratio of the material. The problem studied in this paper is of interest in a number of NDT applications. In the experiments conducted recently by the authors [7], it is now sufficient to measure the size of the TR focal spot on the surface of the sample to infer how deep the sample is probed.

Acknowledgment

We gratefully acknowledge the institutional support of the Los Alamos National Laboratory (LDRD program).

References

[1] T.J. Ulrich, P.A. Johnson, R.A. Guyer, Interaction dynamics of elastic waves with a complex nonlinear scatterer through the use of a time reversal mirror, Phys. Rev. Lett. 98 (2007) 104301.
[2] T.J. Ulrich, A.M. Sutin, T. Claytor, P. Papin, P.-Y. Le Bas, J.A. Ten Cate, The time reversed elastic nonlinearity diagnostic applied to evaluation of diffusion bonds, Appl. Phys. Lett. 93 (2008) 151914.
[3] T.J. Ulrich, A.M. Sutin, R.A. Guyer, P.A. Johnson, Time reversal and non-linear elastic wave spectroscopy (TR NEWS) techniques, Int. J. Non-Linear Mech. 43 (2008) 209–216.
[4] O. Bou Matar, S. Dos Santos, J. Fortineau, T. Goursolle, L. Haumesser, and F. Vander Meulen, Pseudo spectral simulations of elastic waves propagation in heterogeneous nonlinear hysteretic medium, in: Proceedings of the 17th International Symposium of Nonlinear Acoustics, State College, PA, 2005, pp. 95–98.

[5] G. Zumpano, M. Meo, A new nonlinear elastic time reversal acoustic method for the identification and localisation of stress corrosion cracking in welded plate-like structures – a simulation study, Int. J. Solids Struct. 44 (2007) 3666–3684.
[6] T. Goursolle, S. Callé, S. Dos Santos, O. Bou Matar, A two-dimensional pseudospectral model for time reversal and nonlinear elastic wave spectroscopy, J. Acoust. Soc. Am. 122 (2007) 3220–3229.
[7] C. Payan, T.J. Ulrich, P.Y. Le Bas, M. Griffa, P. Schuetz, M.C. Remillieux, T.A. Saleh, Probing material nonlinearity at various depths by time reversal mirrors, Appl. Phys. Lett. 104 (2014) 144102.
[8] B.E. Anderson, M. Griffa, C. Larmat, T.J. Ulrich, P.A. Johnson, Time reversal, Acoust. Today 4 (2008) 5–16.
[9] M. Fink, Time reversal of ultrasonic fields – Part I: basic principles, IEEE Trans. Ultrason. Ferroelectr. Freq. Contr. 39 (1992) 555–566.
[10] A. Parvulescu, C.S. Clay, Reproducibility of signal transmission in the ocean, Radio Electr. Eng. 29 (1965) 223–228.
[11] C. Draeger, J.-C. Aime, M. Fink, One-channel time-reversal in chaotic cavities: experimental results, J. Acoust. Soc. Am. 105 (1999) 618–625.
[12] A. Sutin, J.A. TenCate, P.A. Johnson, Single-channel time reversal in elastic solids, J. Acoust. Soc. Am. 116 (2004) 2779–2784.
[13] J.D. Achenbach, Reciprocity in Elastodynamics, Cambridge University Press, Cambridge, UK, 2003.
[14] D. Cassereau, M. Fink, Time-reversal of ultrasonic fields. Part III: theory of the closed time-reversal cavity, IEEE Trans. Ultrason. Ferroelectr. Freq. Contr. 39 (1992) 579–592.
[15] A. Derode, P. Roux, M. Fink, Robust acoustic time reversal with high-order multiple scattering, Phys. Rev. Lett. 75 (1995) 4206–4209.
[16] C. Draeger, M. Fink, One-channel time-reversal in chaotic cavities: theoretical limits, J. Acoust. Soc. Am. 105 (1999) 611–617.
[17] C. Draeger, J.-C. Aime, M. Fink, One-channel time reversal in chaotic cavities: experimental results, J. Acoust. Soc. Am. 105 (1999) 618–625.
[18] O. Bou Matar, Y.F. Li, K. Van Den Abeele, On the use of a chaotic cavity transducer in nonlinear elastic imaging, Appl. Phys. Lett. 95 (2009) 141913.
[19] C. Draeger, D. Cassereau, M. Fink, Theory of the time-reversal process in solids, J. Acoust. Soc. Am. 102 (1997) 1289–1295.
[20] C. Draeger, D. Cassereau, M. Fink, Acoustic time reversal with mode conversion at a solid–fluid interface, Appl. Phys. Lett. 72 (1998) 1567–1569.
[21] T.J. Ulrich, K. Van Den Abeele, P.-Y. Le Bas, M. Griffa, B.E. Anderson, R.A. Guyer, Three component time reversal: focusing vector components using a scalar source, J. Appl. Phys. 106 (2009) 113504.
[22] T. Goursolle, S. Dos Santos, O. Bou Matar, S. Calle, A two-dimensional pseudospectral model for time reversal and nonlinear elastic wave spectroscopy, J. Acoust. Soc. Am. 122 (2007) 3220–3229.
[23] E.N. Jansen, K. Van Den Abeele, Dual energy time reversed elastic wave propagation and nonlinear signal processing for localisation and depth-profiling of near-surface defects: a simulation study, Ultrasonics 51 (2011) 1036–1043.
[24] F. Simonetti, P. Cawley, A guided wave technique for the characterization of highly attenuative viscoelastic materials, J. Acoust. Soc. Am. 114 (1) (2003) 158–165.
[25] H. Lamb, On the propagation of tremors over the surface of an elastic solid, Philos. Trans. R. Soc. Lond. A203 (1904) 1–42.
[26] G.F. Miller, H. Pursey, The field and radiation impedance of mechanical radiatiors on the free surface of a semi-infinite isotropic solid, Philos. Trans. R. Soc. Lond. A233 (1944) 521–541.
[27] J.D. Achenbach, Wave Propagation in Elastic Solids, Elsevier Science, Amsterdam, 1973.

Microbubble dynamics monitoring using a dual modulation method

Damien Fouan
BF SYSTEMES, Technopôle de la Mer, 229, chemin de la Farlède, 83500 La Seyne-sur-Mer, France
damien.fouan@gmail.com

Younes Achaoui, Cédric Payan, and Serge Mensah
Laboratoire de Mécanique et d'Acoustique, Université d'Aix-Marseille, CNRS, 31 chemin Joseph Aiguier, 13420 Marseille, France
younes.achaoui@fresnel.fr, cedric.payan@univ-amu.fr, mensah@lma.cnrs-mrs.fr

Abstract: An experimental method for characterizing microbubbles' oscillations is presented. With a Dual Frequency ultrasound excitation method, both relative and absolute microbubble size variations can be measured. Using the same experimental setup, a simple signal processing step applied to both the amplitude and the frequency modulations yields a two-fold picture of microbubbles' dynamics. In addition, assuming the occurrence of small radial oscillations, the equilibrium radius of the microbubbles can be accurately estimated.

[MH]
Date Received: September 25, 2014 **Date Accepted:** December 30, 2014

1. Introduction

Ultrasonic detection and sizing of microbubbles circulating in blood is of particular interest in the context of divers' desaturation accident prevention. These measurements should be performed *in situ* by the divers themselves in order to optimize the decompression stages, taking several parameters into account. (1) All microbubbles ranging from 20 to 200 μm circulating in the acoustical measurement zone have to be detected and sized. (2) The measurements have to be performed very quickly (within less than 20 ms) in order to avoid miscounting circulating bubbles. (3) Low acoustical pressures [Mechanical Index (MI) < 0.3] are required to ensure the safety of the measurements, especially at low frequencies (between 10 and 200 kHz).

There exist very few efficient experimental methods of detecting and characterizing microbubbles. In the prevention of decompression sickness, the quantities of micro-emboli present in the blood flow (Eftedal, 2007) are generally assessed by physicians on the basis of the heart sound signals delivered by Doppler systems. Doppler approaches, which can be used only for detection (but not sizing) purposes, often give rise to wrong audio interpretations because of the noise resulting from the cardiac activity. It is necessary to focus on the microbubbles' acoustic characteristics in order to ensure accurate detection and sizing. Other methods involving the use of ultrasound contrast agents (UCA) such as harmonic imaging (Frinking *et al.*, 2000) and subharmonic imaging methods (Overvelde *et al.*, 2010) focus on the nonlinearity of the bubbles. But when dealing with natural microbubbles of various sizes, the resonance frequency is not known. Non-linear techniques with which the excitation has to be selected near the resonance frequency and a high MI is required are therefore unsuitable. Bi-frequency methods are also based on the detection of microbubble resonances (Newhouse and Shankar 1984). The latter methods make it possible to detect the presence of microbubbles and calculate their radius. However, none of these methods based on the resonance of the bubbles under investigation entirely meet the requirements: It is impossible to ensure that all the bubbles in the range of radii of interest

will be detected within less than 20 ms because the driving frequency needs to exactly match the resonant frequency of the bubble present during this time. In addition, classical transducers are not compatible with the wide range of excitation frequencies corresponding to microbubble radii ranging from 20 to 200 μm (frequencies of about 16 to 160 kHz). Some improvements have been proposed using non-linear excitations (Fouan *et al.*, 2014), but they do not suffice to completely overcome these limitations. In addition, bubbles' radii can be determined with these methods but they yield no information about the microbubbles' dynamic responses.

Optical methods have been presented for measuring microbubbles' responses. In view of the frequencies used in medical ultrasound investigations, only very fast optical cameras would be suitable for this purpose. The idea of probing the bubbles' dynamics was developed at Erasmus MC (Rotterdam, NL) using the Brandaris ultrafast optical camera. In order to improve the UCA detection, the use of an acoustical camera was suggested (Renaud *et al.*, 2012a). The acoustical camera based on the use of bi-frequency methods (Newhouse and Shankar, 1984; Chapelon *et al.*, 1985) is able to measure the changes in the relative radius of a microbubble subjected to an acoustical field (Renaud *et al.*, 2012a). It is therefore possible to identify single bubbles' "buckling state" behavior and nonlinear behavior (Renaud *et al.*, 2014). However, the latter authors (Renaud *et al.*, 2012b) observed that this method has two main limitations: It cannot be used to measure the equilibrium radius or the absolute changes in the bubble radius. The simple approach presented in the present paper may help to provide this complementary information.

The aim of the present study is therefore to produce an acoustical camera for measuring the absolute changes in bubbles' radii. In addition to the amplitude modulation method used by Renaud *et al.*, we also study the information carried by the phase of the HF wave reflected by an oscillating microbubble. By combining these two measurements, it is possible to directly and reliably calculate the equilibrium radius without any need to sweep the whole resonance frequency domain (which can be defined by the full width at half maximum, FWHM).

To deal with the problem of detecting and sizing microbubbles during the decompression phase, the acoustic power transmitted has to be as low as possible in order to prevent newly developing microbubbles cavitating in saturated tissues and the resulting biological damage. In addition, as explained by Renaud *et al.* (2012a), the amplitude of the probing wave must be low enough to maintain the (quasi-)linear regime. In this set-up, the acoustic pressure of the High Frequency (HF) wave is therefore set at 10 kPa and the acoustic pressure of the Low Frequency (LF) wave is restricted to 5 kPa. The duration of the measurements used for the data acquisition is less than 2 ms, including the 1-ms excitation time. With the "acoustical camera" method, only the variations induced by the LF excitation in the cross-section orthogonal to the direction of propagation of the HF wave are detected. The relative change in the amplitude of the backscattered HF wave ($\Delta A/A_0$) can be simply expressed as follows:

$$\frac{\Delta A}{A_0} = \frac{\Delta R}{R_0}, \tag{1}$$

where R_0 is the equilibrium radius of the bubble and ΔR is the variation of the radius. In the approximation for the radial motion, whenever the wall of the microbubble moves, a Doppler effect will occur and a frequency modulation will be induced. The radial velocity of the bubble's wall (ν) is associated with a shift in the frequency (Δf), and the radius variation ΔR is therefore correlated with both the phase shift $\Delta\varphi$ and the incident angle θ of the HF wave, since

$$\nu = \frac{c}{2f\cos\theta}\Delta f \tag{2}$$

and

$$\Delta R = \frac{c}{4\pi f \cos\theta}\Delta\varphi. \quad (3)$$

2. Experimental tests on the absolute and relative bubble sizing performances

Experiments are performed in a $2\,\text{m} \times 3\,\text{m} \times 0.5\,\text{m}$ water tank in order to reduce the effects of any standing waves resulting from the multiple reflections at the boundaries. A hydrojet (Braun OralB) is used to generate microbubbles (with radii ranging from 20 to 200 μm). A thin wire is placed on the path of the rising bubbles, and measurements are performed on a single tethered bubble. Using this simple method, several measurements are carried out under identical conditions and compared. A microbubble's radius is assumed to be constant during the 2-ms measurement period (Church, 1988; Fyrillas, 2006). The acoustically characterized bubbles are monitored optically at the same time with a CCD camera. The acoustic measurements are performed using three confocused transducers. The first transducer radiates the LF pumping wave (Ultran, GMP 50 kHz, Hoboken, NJ) and the other two are used for the transmission and reception of the imaging wave (Imasonic, 1 MHz; f = 90 mm, Besançon, France). The two emitting transducers are connected to an arbitrary waveform generator (LeCroy, ArbStudio 1104, four channels, Thousand Oaks, CA). The receiving transducer is connected to a bandpass filter (Krohn-Hite, 3940, dual channel filter, Brockton, MA) and an oscilloscope (Agilent Technologies, Infini-iVision DSO5014A, 100 MHz, Santa Clara, CA). The experimental setup is shown in Fig. 1.

In order to perform both phase and amplitude estimations, as suggested by Renaud *et al.* (2012a), short sliding time windows are applied to the backscattered HF signals. In each time window, the amplitude of the 1-MHz component is assessed in the frequency domain. At each time-point, the change in the relative radius is determined using Eq. (1). The phase is estimated using the known values of the HF frequency and the angle between the two HF transducers, and ΔR is then calculated using Eq. (3). The time windows must be set between the LF and the HF periods. A 6-μs window duration was adopted for this purpose and a 0.2-μs step is applied between two consecutive windows. These parameters give a final sampling rate of 5 MHz for the measurement of the changes in the bubbles' radius.

For the sake of comparison, two different studies are performed on the two different microbubbles (with radii of 69 and 45 μm) presented in Fig. 2. In Figs. 2(a) and 2(c), the low frequency excitation is a 1-ms chirp with a frequency increasing from 30 to 60 kHz. These frequencies correspond to the resonances of microbubble radii

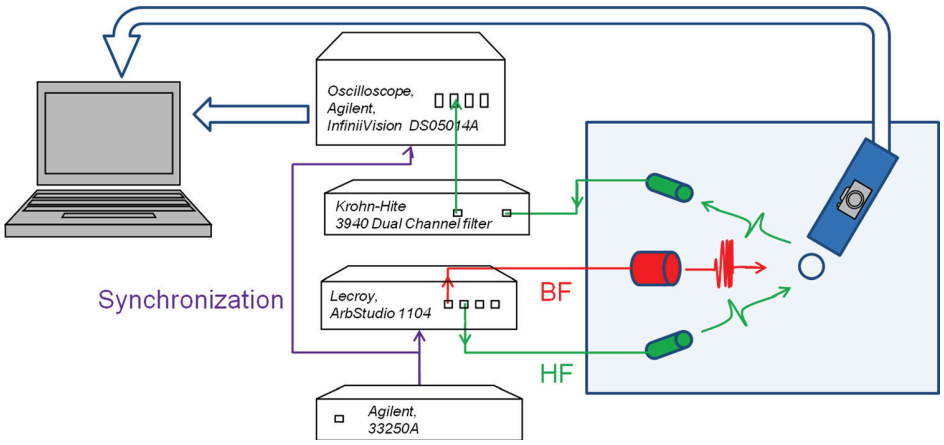

Fig. 1. (Color online) Experimental setup for microbubble detection and characterization.

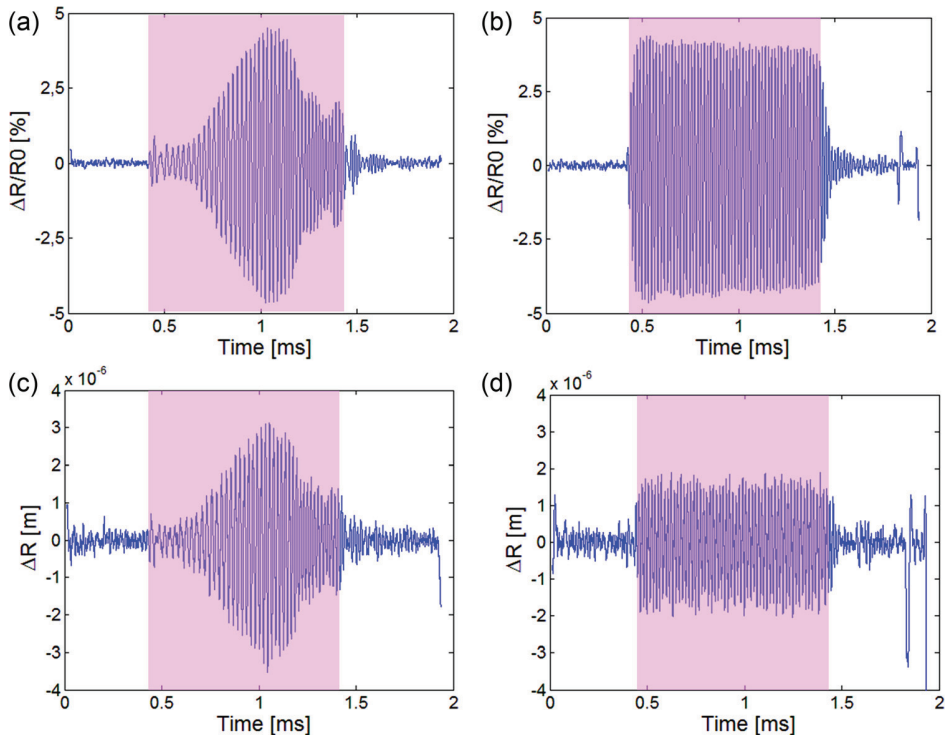

Fig. 2. (Color online) Changes with time in a microbubble's radius under acoustic excitation. The highlighted portions show the time during which the LF was switched on. (a) and (b) correspond to the relative measurements based on the amplitude modulation, and (c) and (d) correspond to the absolute measurements based on the frequency modulation. In (a) and (c), the excitation was a 1-ms sweep from 30 to 60 kHz applied to a 69-μm bubble. In (b) and (d), the excitation was a 1-ms burst at 60 kHz applied to a 45-μm bubble.

ranging between 50 and 100 μm. In the cases presented in Figs. 2(b) and 2(d), the frequency is constant (60 kHz) and differs from the bubble's resonance frequency (71 kHz). The two excitations are tested on 2 different bubbles, which are measured optically at 69 and 45 μm. Unsurprisingly, the phase modulation recording is noisier than the amplitude modulation recording. This noise level (see the region before and after the excitation in Fig. 2) depends on both the HF and the changes in the bubble amplitude. If these parameters are constant (which was the case in our measurements), the noise level affecting each curve depends on the microbubble's equilibrium radius. The larger the bubble becomes, the greater the absolute variations and hence, the greater the change in the phase will be.

As described above, similar changes in the microbubble's radius are observed with both excitations. In most previous models predicting microbubbles' behavior in response to acoustic excitation, only changes of volume have been taken into account. In other words, the direction of the excitation wave has never been taken into account so far. This is especially true in the case of this method, where the acoustic powers involved are very low (Ainslie and Leighton, 2011). The changes in the radius can therefore be assumed to be equal in both directions. In order to prevent any phase shifts due for example, to the presence of the wire, only the modulus of the change in the radius is assumed to be constant. Under this assumption, it is possible to calculate the equilibrium radius R_0 from the amplitude and phase measurements, using Eqs. (1) and (3). For this purpose, the envelopes of both curves are extracted using a Hilbert

transform. The ratios between the absolute and relative envelopes observed in the present experiments with both excitations (pulse and sweep) are shown in Fig. 3.

3. Results and discussion

The results presented in Fig. 3 can be interpreted in several ways. The three phases in the excitation scheme are visible. First, when the power is off, the ratio is insignificant because the bubble is not oscillating. Second, when the excitation is applied to the bubble, the ratio becomes almost constant. Last, after the offset of the excitation, the ratio again becomes insignificant. The average ratio during the acoustic excitation time amounted to 67.2 and 39.7 μm with the chirp and burst excitations, respectively. These values are very similar to the equilibrium radii measured with the camera (69 and 45 μm). Unlike the classical Dual Frequency Method, this approach does not require the excitation to encompass the microbubble's resonance frequency. A broadband source covering all the resonance frequencies of the microbubbles present in blood is therefore no longer required. In the case of the present method, one only needs to activate the microbubble in order to detect it and assess the equilibrium radius. The estimation of single microbubbles' equilibrium radii in response to excitations of several kinds is plotted in Fig. 4, which shows that a wide range of radii were obtained.

The values obtained fall very near the first bisector defining the spread between the true (optically measured) and measured absolute radii. It is worth noting that the accuracy depends greatly on the bubble's radius: the larger the bubble, the more accurate the sizing becomes. In particular, a maximum error of 10% was obtained with microbubbles larger than 80 μm. The fact that greater accuracy is achieved with the largest bubbles matches the present needs, since in diver's blood, these bubbles are also the most dangerous ones. There are several possible reasons for the discrepancies observed between the true and measured radii in the case of smaller bubbles. As mentioned above, it is more difficult to detect frequency modulations in small microbubbles. In addition, the impact of the HF wave on the microbubble may become less negligible as we approach the microbubble's resonance domain. However, the most plausible reason may be that the wire starts to have a real impact on the oscillations of smaller microbubbles. When the microbubble is small in comparison with the wire, its size variations may not be the same in all directions. Further measurements using a modified setup (without any wire) would certainly lead to a better understanding of these differences.

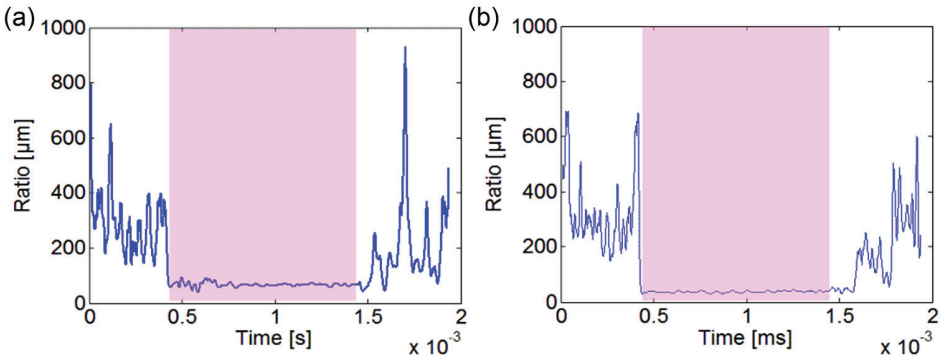

Fig. 3. (Color online) Ratio between the changes in the absolute radius and the relative radius versus the excitation time. The highlighted portions correspond to the time during which the LF was switched on. (a) In response to the sweep excitation (frequency 30 to 60 kHz, duration 1 ms) shown in Figs. 2(a) and 2(c), and (b) in response to the burst excitation (60 kHz, 1 ms) shown in Figs. 2(b) and 2(d).

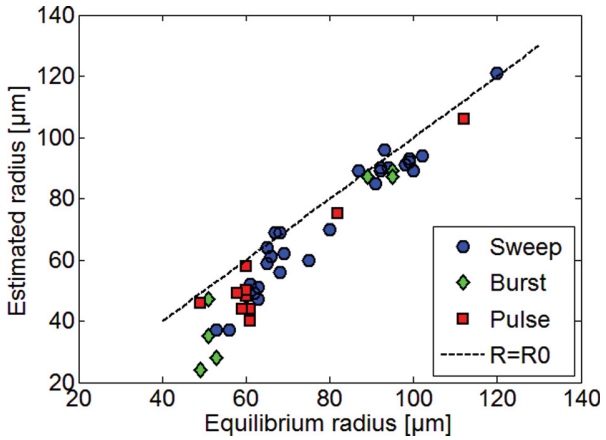

Fig. 4. (Color online) Estimation of a microbubble's radius expressed as the average ratio between the amplitude and phase variations recorded in response to sweep, burst and pulse excitations.

4. Conclusion

The dual modulation method presented in this paper is a considerable improvement in the field of microbubble sizing, since the frequency band of the pumping wave does not have to encompass the resonance frequency of the bubble. Excitations of all kinds which make these bubbles oscillate could presumably be used, especially pulse excitations, which last for a very short time and have a wide frequency range. The results obtained here using an *in vitro* setup show that a fairly small LF amplitude (<5 kPa) suffices to be able to detect changes in the amplitude and frequency, and hence to accurately determine the equilibrium radius of the microbubble under investigation. Now that the power and duration requirements have been successfully met, we are developing an adapted version of an existing 2-MHz Doppler system with a carefully chosen excitation for *in vivo* experiments. The last point worth mentioning is that methods based on both frequency and amplitude modulations would certainly shed useful light on the behavior of microbubbles subjected to acoustic excitations. The use of this dual approach would result in a tremendous improvement in the performances of acoustical cameras, since it would provide them with the means of giving quantitative information. This would make it possible to compare the changes of radius occurring in several directions and to study various modes of microbubble vibration using a multi-channel ultrasonic system.

Acknowledgments

This work was partly supported by the French Research Ministry under the Smart U.S. project, Ref. ANR-10-BLAN-0311, the Provence-Alpes-Côte-D'Azur Council, in the framework of the Comedies project, the Canceropôle PACA and by the French Ministry of Defense under the BORA project.

References and links

Ainslie, M. A., and Leighton, T. G. (**2011**). "Review of scattering and extinction cross-sections, damping factors, and resonance frequencies of a spherical gas bubble," J. Acoust. Soc. Am. **130**(5), 3184–3208.

Chapelon, J. Y., Shankar, P. M., and Newhouse, V. L. (**1985**). "Ultrasonic measurement of bubble cloud size profiles," J. Acoust. Soc. Am. **78**(1), 196–201.

Church, C. (**1988**). "Prediction of rectified diffusion during nonlinear bubble pulsations at biomedical frequencies," J. Acoust. Soc. Am. **83**, 2210–2222.

Eftedal, O. S. (**2007**). "Ultrasonic detection of decompression induced vascular microbubbles," Ph.D. thesis, Norwegian University of Science and Technology, Trondheim, Norway.

Fouan, D., Achaoui, Y., and Mensah, S. (**2014**). "Improvement of micro-bubble sizing using multi-harmonic excitations under the transducer bandwidth constraint," Appl. Phys. Lett. **104**, 114102.

Frinking, P. J. A., Bouakaz, A., Kirkhorn, J., Ten Cate, F. J., and de Jong, N. (**2000**). "Ultrasound contrast imaging: Current and new potential methods," Ultrasound Med. Biol. **26**(6), 965–975.
Fyrillas, M. (**2006**). "Dissolution or growth of soluble spherical oscillating bubbles," Ph.D. thesis, University of California, Irvine, CA.
Newhouse, V. L., and Shankar, P. M. (**1984**). "Bubble size measurements using the nonlinear mixing of two frequencies," J. Acoust. Soc. Am. **75**(5), 1473–1477.
Overvelde, M., Garbin, V., Sijl, J., Dollet, B., de Jong, N., Lohse, D., and Versluis, M. (**2010**). "Nonlinear shell behavior of phospholipid-coated microbubbles," Ultrasound Med. Biol. **36**(12), 2080–2092.
Renaud, G., Bosch, J. G., Van der Steen, A. F. W., and de Jong, N. (**2012a**). "An 'acoustical camera' for in vitrocharacterization of contrast agent microbubble vibrations," Appl. Phys. Lett. **100**(10), 101911.
Renaud, G., Bosch, J. G., Van der Steen, A. F. W., and de Jong, N. (**2012b**). "Chirp resonance spectroscopy of single lipidcoated microbubbles using an 'acoustical camera'," J. Acoust. Soc. Am. **132**(6), EL470–EL475.
Renaud, G., Bosch, J. G., Van der Steen, A. F. W., and de Jong, N. (**2014**). "Low-amplitude non-linear volume vibrations of single microbubbles measured with an 'acoustical camera,'" Ultrasound Med. Biol. **40**(6), 1282–1295.

Quantitative linear and nonlinear resonance inspection techniques and analysis for material characterization: Application to concrete thermal damage

C. Payan[a)]
Aix Marseille University, LMA UPR CNRS 7051, Marseille France

T. J. Ulrich and P. Y. Le Bas
Los Alamos National Laboratory, EES-17, Los Alamos, New Mexico 87545

T. Saleh
Los Alamos National Laboratory, MST-16, Los Alamos, New Mexico 87545

M. Guimaraes
Electrical Power Research Institute, Charlotte, North Carolina 28262

(Received 21 March 2013; revised 13 November 2013; accepted 17 June 2014)

Developed in the late 1980s, Nonlinear Resonant Ultrasound Spectroscopy (NRUS) has been widely employed in the field of material characterization. Most of the studies assume the measured amplitude to be proportional to the strain amplitude which drives nonlinear phenomena. In 1D resonant bar experiments, the configuration for which NRUS was initially developed, this assumption holds. However, it is not true for samples of general shape which exhibit several resonance mode shapes. This paper proposes a methodology based on linear resonant ultrasound spectroscopy, numerical simulations and nonlinear resonant ultrasound spectroscopy to provide quantitative values of nonlinear elastic moduli taking into account the 3D nature of the samples. In the context of license renewal in the field of nuclear energy, this study aims at providing some quantitative information related to the degree of micro-cracking of concrete and cement based materials in the presence of thermal damage. The resonance based method is validated as regard with concrete microstructure evolution during thermal exposure.
 [http://dx.doi.org/10.1121/1.4887451]

PACS number(s): 43.25.Ba, 43.25.Gf [ROC] Pages: 537–546

I. INTRODUCTION

Many Non-Destructive Evaluation (NDE) methods such as thermography, radiography, electrical resistivity, radar, etc. provide information about the state of the concrete, but the only one which is directly related to concrete mechanical characteristics is acoustics. Standard methods such as ISO 1920-7 and ASTM C597-09, founded on low frequency ($<$100 kHz = wavelength $>$ 4 cm) pulse wave velocity, cannot provide information about the presence of a localized defect at the centimeter scale. Developments in the field of concrete NDE show that the information obtained from the nonlinear elastic wave propagation can increase the sensitivity by a factor 10 or more in homogeneous materials[1] and in concrete and cement based materials.[2]

In the context of license renewal in the field of nuclear energy, maintaining in service concrete structures for the period of long-term operations is challenging. For ecologic, economic and societal reasons, replacing a structure is often complicated. Subjected to radiation and medium temperature ($<$500 °C) for a long period of time, the integrity of concrete in the pedestal and biological shield wall in nuclear plants and the overpack of storage casks remains unknown. Thus, increasing the safety and anticipating concrete degradation through the use of a powerful tool, with the capability to characterize concrete mechanical quality as its main function, should be welcome. The purpose of this study is to provide quantitative information about the amount of damage in concrete subjected to thermal damage.

A. Thermal damage of concrete

Chemical reaction occurring with thermal damage process of concrete is known. Above 105 °C, all the free and a part of adsorbed water are released. From 180 to 300 °C, hydrated silicates decompose by tearing water molecules, which evaporate. Above 450 °C, the portlandite breaks down and releases water: $Ca(OH)_2 \rightarrow CaO + H_2O$. The first aggregate transformation (α to β quartz transition) appears at 600 °C. Other transformations occur up to the aggregates/cement paste fusion at about 1300 °C. This process results in an increase of porosity and micro-cracking.

This study focuses on temperatures encountered in nuclear facilities so up to 400 °C. In this range, three sets of four samples (about 6 cm × 10 cm × 10 cm) were manufactured by Centre Scientifique et Technique du Bâtiment[3] (CSTB), France. Their compositions are given in Table I. For each set, one sample is kept as a reference, the second one is damaged at 120 °C, the third one at 250 °C, the last at 400 °C (refer to the codification in Table I). Thermal damage is achieved by heating the sample at the desired temperature with an increase of 0.5 °C/min, holding a constant

a)Author to whom correspondence should be addressed. Electronic mail: cedric.payan@univ-amu.fr

TABLE I. Concrete samples composition and codification.

Composition (kg/m^3)	High Performance Mortar (M) w/c = 0.3	High Performance Concrete (HPC) w/c = 0.3	Ordinary Concrete (OC) w/c = 0.5
Codification	M 20-120-250-400	HPC 20-120-250-400	OC 20-120-250-400
Limestone 12.5-20	0	579	514
Limestone 5-12.5	0	465	514
Limestone 0-5	739	442	401
Seine 0-4	727	435	401
Silica fume	37	22	0
CPA 52.5 cement	602	0	0
CEM I 52.5 cement	0	360	0
CEM I 32.5 cement	0	0	350
Water	219	136	181
GT Super plasticizer	10	12	0

temperature for 3 h, then decreasing by 0.5 °C/min. The thermal damage protocol was designed to avoid any undesired mechanical damage induced by thermal gradients, thus internal stresses, during heating. In concrete the most brittle zone is the interface between aggregates and cement paste. This zone, namely Interfacial Transition Zone (ITZ), is the most porous and crystallized region.

The average Coefficient of Thermal Expansion (CTE) of aggregates (mainly limestone in this study) ranges between $5.5 \times 10^{-6} < \mathrm{CTE_A} < 11.8 \times 10^{-6}\,^{\circ}\mathrm{C}^{-1}$ (Ref. 3). The average hardened cement paste CTE ranges between $11 \times 10^{-6} < \mathrm{CTEP} < 20 \times 10^{-6}\,^{\circ}\mathrm{C}^{-1}$ (Ref. 4). Considering a single inclusion in a matrix, numerical simulation[5] shows that in such a case ($\mathrm{CTE_A} < \mathrm{CTE_P}$), most of the damage will occur at the ITZ. Considering the spatial distribution of aggregates, numerical simulation[6] shows that depending on the spatial arrangement, on the shape and on the size distribution of aggregates, a complex thermo mechanical interplay between them occurs. As $\mathrm{CTE_A} < \mathrm{CTE_P}$, the most affected region will also be the ITZ.

In concrete, both $\mathrm{CTE_A}$ and $\mathrm{CTE_P}$ are temperature dependent. $\mathrm{CTE_A}$ increases with temperature up to 17×10^{-6}. When increasing temperature[3] above 150 °C, the cement paste starts shrinking while the aggregates are still expanding. In such a case radial cracks (cracks connection between two neighbor aggregates) should also appear in the cement paste. Taking into account the fact that the ITZ is the most brittle zone, it is reasonable to assume that most of the damage will occur in this region with some additional cracks inside the matrix. The nature of thermal damage also allows considering a homogeneous and isotropic damage.

B. Nonlinear mesoscopic behavior of concrete

The nonlinear elastic behavior of homogeneous material is described by the Landau and Lifshitz[7] elasticity theory. In the 1990s, authors[8] report the so called "non-classical" nonlinear behavior of complex materials such as rocks and concrete which do not follow the former theory. Phenomena, such as large and unexpected nonlinearity, hysteresis and endpoint-memory effects are reported whether under quasi-static or dynamic loading.[8] To describe this complex behavior, authors introduce a 1D phenomenological nonlinear and hysteretic modulus[9]

$$K = K_0\left[1 - \beta\varepsilon - \delta\varepsilon^2 - \cdots - \alpha(\Delta\varepsilon, \dot{\varepsilon})\right], \quad (1)$$

where K_0 is the elastic modulus, β and δ are the Landau type nonlinear elastic terms, α is the phenomenological nonlinear hysteretic parameter, the dot indicates the time derivative, $\Delta\varepsilon$ is the strain amplitude. Physically, the first nonlinear terms relate the nonlinearity of the force/displacement relationship at the atomic scale. The physical origin of the last one arises at the mesoscopic scale. Phenomena such as opening/closing of microcracks, break/recovery of cohesive grain bonds properties, friction, contacts, capillary effects in porosities, etc., are expected to be responsible of the complex behavior of this nonlinear mesoscopic class of materials into which concrete falls. Even if there is still not any universal theory allowing to physically describing this class of materials, the nonlinear α parameter can nevertheless be employed to quantify the nonlinearity and thus used for nondestructive evaluation. Several methods were used to evaluate the nonlinearity. In concrete, among others, one can cite Nonlinear Resonant Ultrasound Spectroscopy (NRUS) which is employed by Abeele *et al.*[10] and Bentahar *et al.*[11] to study the effect of mechanical damage on the measured nonlinearity. Bouchaala *et al.*[12] reports the sensitivity of the nonlinear parameter to carbonation. Lesnicki *et al.*[13] studies the influence of Alkali Silicate Reaction (ASR). Payan *et al.*[2] qualitatively shows the effect of thermal damage on the nonlinearity using pressure and shear transducers. These studies were conducted with various resonance modes but all of them only provide qualitative variation of the nonlinearity with increasing the amount of damage. These qualitative data do not allow comparisons to be done among a large variety of material and applications.

While the physical mechanisms responsible of the nonlinear behavior are still not understood, the aim of this paper is to propose a nonlinear resonance based method able to provide quantitative information, and thus, to allow proper comparisons and expectation of possible mechanisms to be done.

II. RESONANCE INSPECTION TECHNIQUES AND ANALYSIS

A. Introduction to the methodology

NRUS consists of conducting resonance frequency measurements at various driving amplitudes (as will be

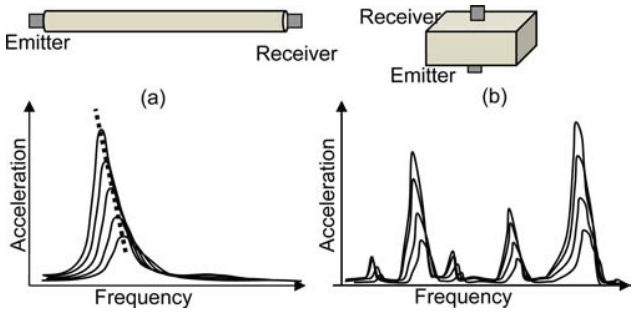

FIG. 1. (Color online) NRUS curves for (a) optimal and (b) more complex geometry.

shown in Fig. 2). For a given resonance mode, a linear material maintains a constant resonance frequency while a nonlinear mesoscopic material softens with increasing drive amplitudes (i.e., dynamic strain). Following Eq. (1), this softening results in a decrease of the resonant frequency as a function of the strain amplitude ($\Delta\varepsilon$). The nonlinear α parameter is obtained by the linear decrease of the resonance frequency indicating that the non-classical phenomenon dominates the global nonlinear behavior[14]

$$\Delta f/f_0 = \alpha\Delta\varepsilon, \tag{2}$$

where f_0 is the low amplitude linear resonance frequency and $\Delta f = f - f_0$ (f is the resonance frequency for increasing drive amplitudes).

This method quantitatively applies to samples with appropriate 1D geometry (cylinder with large aspect ratio), as the longitudinal vibration mode is very easy to detect, the measured vibration amplitude of the sample is proportional to the strain amplitude [Fig. 1(a)]. However, for more complex geometry [Fig. 1(b)], this assumption is no longer valid because of the complexity of mode shapes. That point is underlined by Johnson and Sutin,[15] who were unable to evaluate the nonlinear parameter for a parallelepiped type sample using NRUS.

To overcome this difficulty, in order to evaluate the strain amplitude for a given mode shape, a methodology based on Resonant Ultrasound Spectroscopy (RUS) and numerical simulation is developed. The steps of the method consist of the following:

(1) The geometry and the density of the sample serve as input for a linear resonance method which provides the linear elastic tensor.

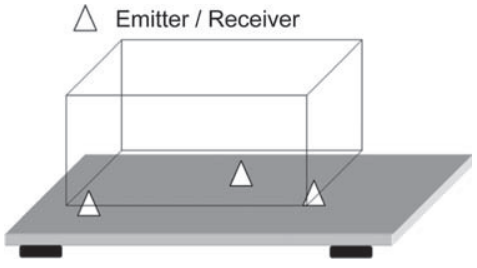

FIG. 2. Schematic of rectangular concrete block sample sitting on the conical transducer stand.

(2) The elastic tensor serves as an input for a numerical simulation which allows the experiment, including the effect of the emitters and receivers mass, to be modeled. This step allows linking the quantity measured by the receiver to the strain amplitude inside the sample, as well as identifying the mode shape under study.
(3) The mode shape selected and the strain determined, the NRUS experiment provides an absolute value of the nonlinearity.

This method is detailed in the following.

B. Resonant Ultrasound Spectroscopy

Adapted to complex 3D geometries, resonance inspection techniques are known and have been employed for years.[16] Resonant Ultrasound Spectroscopy (RUS) allows the material elastic properties to be determined accurately by non-destructive means. The input values are the sample geometry and the density. By exciting the sample over a large frequency range, one can extract the resonance peaks (experimentally measured values) corresponding to various eigenmodes. Then, by combining experimental and input values, an inversion algorithm provides the full elastic tensor of the sample. This can apply to any elastic material type (isotropic or anisotropic). RUS has been employed in various homogeneous materials and more recently in inhomogeneous ones such as rocks[17] and cement.[18] Here the application of RUS is extended to various forms of concrete materials.

The procedure for performing a RUS measurement and obtaining the full elastic tensor from such a measurement is well defined in general,[16] with specifics for dealing with inhomogeneous earth materials having been specified by Ulrich *et al.*[17] and recently for anisotropic and highly damped material such as bone.[19] As such, the reader is refereed to these publications for details of the method. Here the experimental system and an example spectrum are briefly presented before focusing on the results as a function of thermal damage.

Traditional RUS requires free boundary conditions in order to invert the measured frequencies to find the elastic moduli using the Visscher RUS algorithm.[16] To approximate this, the sample is placed upon a stand containing three conically shaped transducers (Fig. 2). Dry contact is used, however, use of an ultrasonic coupling gel may also be applied to the transducer/sample contact area without adverse effects. Two of the available transducers are used during the measurement: One as an emitter and one as a receiver. The order/placement of these transducers has minimal importance as resonance frequencies will not change with the location of the source/receiver, however, the amplitude of the resonance frequencies will change. As the amplitude is not used in the inversion for elastic moduli, this is unimportant as long as each resonance frequency is large enough to be measured. Positioning transducers near corners of the sample and/or avoiding points of symmetry is sufficient to avoid nodal locations for the low lying modes.

After placement onto the stand, the sample is excited (here using a National Instrument PXI- 5406 function generator) in a constant amplitude stepped sine fashion and the

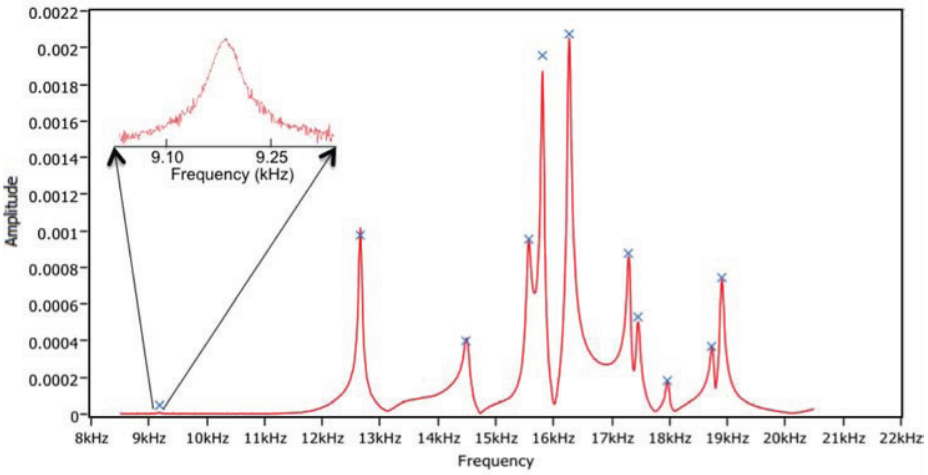

FIG. 3. (Color online) Resonance spectrum taken from sample OC-120. "×" indicates peak values used in RUS inversion.

resulting amplitude recorded at each frequency is recorded by the receiver and digitized (here using a National Instrument PXI-5122 A/D high speed digitizer). Both generation and acquisition lines are managed by the RITA© (Resonance Inspection Techniques and Analysis) software, designed and implemented by the LANL Geophysics group's Wave Physics team (Ulrich and Le Bas). An example spectrum is shown in Fig. 3 as measured from the OC-120 sample.

Note the ×'s indicating the frequency values used in the RUS inversion for this sample. Once a sufficient number of resonance peaks have been identified and measured, the inversion can be performed to extract the elastic moduli. For all samples herein 11 resonance peaks were measured and an inversion was performed using an isotropic assumption. This resulted in the inversion being performed to better than 1% RMS error (deviation between experimental and computed resonance frequencies) for all samples with the exception of HPC 250 whose inversion was obtained to only 3% RMS error. This increased RMS error may be due to either overwhelming inhomogeneity over this scale or an incorrect assumption in the elastic tensor symmetry (i.e., sample may be anisotropic).

C. Nonlinear Resonant Ultrasound Spectroscopy and numerical simulation

The goal of the proposed method is to identify a mode similar to the Young's mode for a cylinder and so for which Eq. (2) applies. Here we have chosen a bulk/breathing mode. The experimental scheme is presented in Fig. 4. Generation and acquisition are ensured by the same equipment than for RUS section. The generation is coupled to a voltage amplifier TEGAM 2350. Both generation and acquisition lines are also managed by the RITA© software, NRUS module. For NRUS studies, a transducer able to drive the sample at high amplitude is needed. An ultrasonic cleaning transducer (Ultrasonics World, DE, USA) is driven by the amplifier up to a peak to peak voltage of 400 V. To minimize the influence of this big transducer on the bulk resonance mode, it is glued at the sample center. A Polytec laser vibrometer (OFV 5000, 1.5 MHz bandwidth) records the out of plane particle velocity at the same location on the side opposite. This arrangement is chosen in order to favor the measurement of the bulk mode and limit the sensitivity to flexural/shear modes.

To perform quantitative NRUS, the protocol is as follows:

Step 1. Experimental resonance spectrum: The sample is excited at low amplitude over a large frequency band in order to identify the resonance modes of the sample. An example of resonance curves is given in Fig. 5 for the M samples.

The peaks around 15 kHz present the most energetic modes in this configuration, i.e., generation with the

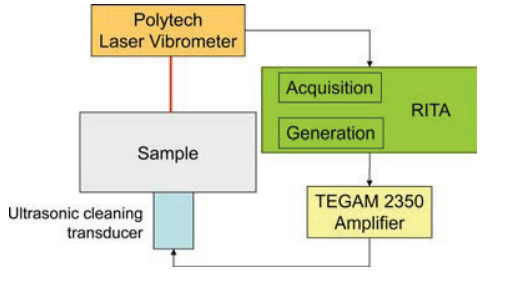

FIG. 4. (Color online) NRUS experimental scheme.

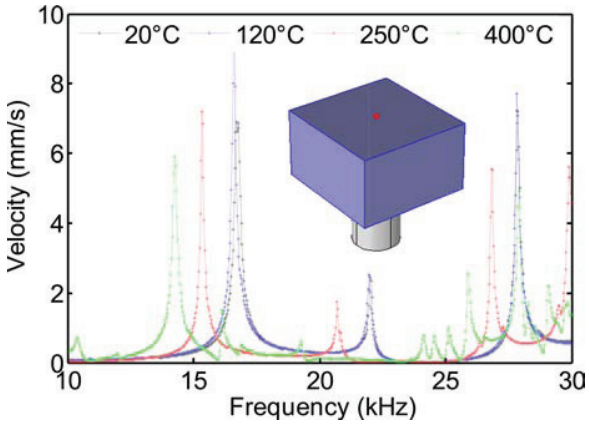

FIG. 5. (Color online) Resonance modes of the Mortar samples set. The sample is also shown, including the transducer and the laser spot location (spot at the sample center).

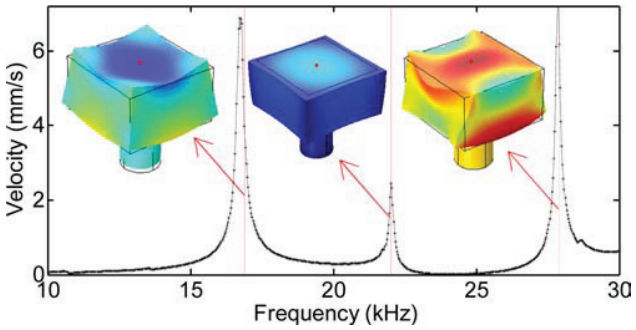

FIG. 6. (Color online) Experimental and simulated resonance modes for M20 sample. The curve is the experimental spectrum, the vertical lines are the simulated resonant frequencies (limited to the most three energetic ones). The corresponding mode shapes are also shown.

transducer at the sample center, acquisition at the side opposite center (Fig. 5). To link the measured particle velocity to the strain inside the sample, the experiment is modeled by finite element numerical simulation.

Step 2. Identification of resonance modes: The linear elastic characteristics of the samples are used as input in the numerical simulation using Comsol®, Solid Mechanics module assuming homogeneous and isotropic material. An example for the M20 sample is given in Fig. 6 in the 10–30 kHz frequency range. In this range, numerical simulation provides the resonance modes corresponding to the experiments, i.e., including the ultrasonic cleaning transducer attached to the sample. The bulk mode is identified around 22 kHz (Fig. 6). For the latter, one can link the measured velocity amplitude Δv_{laser} to the volumetric strain amplitude $\Delta\varepsilon$ by

$$\Delta\varepsilon = C\Delta v_{laser}, \tag{3}$$

where C is a constant depending on the linear elastic properties of the sample. This constant is evaluated at the resonance frequency by the average volumetric strain amplitude in the sample divided by the out of plane velocity amplitude at the laser spot. This quantity has been checked to be amplitude independent in simulations; meaning that in experiments, multiplying the velocity amplitude (laser measurement) by this constant provides the volumetric strain amplitude. For each sample, the bulk mode is identified and the C constant is determined. The data summary is presented in Table II.

Table II shows that the accuracy of the method decreases with increasing damage. This can be explained by the decrease of linear elastic properties which effects the position of the resonance peaks whereby the bulk mode is influenced more by nearby resonances.

Step 3. Performing NRUS: With the bulk mode determined, the sample is driven around the corresponding frequency. The NRUS resonance curves are obtained by sending tone-burst series to the transducer starting from f_1 to f_n (Fig. 7), with a constant Δf step, at a constant amplitude A_1. For each tone-burst, the received amplitude is determined from a heterodyne Fourier analysis at the driving frequency of the received signal. The driving amplitude is increased by a constant step ΔA from A_1 to A_n then the tone

TABLE II. Comparison of numerical and experimental data and values of the C constant.

T (°C)	Experiments f_0 (kHz)	Simulation f_0 (kHz)	Error (%)	C.10-3 (s/m)
		High performance concrete		
20	24.41	24.29	0.481	0.269
120	23.78	23.56	0.921	0.34
250	22.3	22.55	1.115	0.291
400	17.45	16.9	3.152	2.1
		Ordinary concrete		
20	22.14	21.76	1.738	0.374
120	21.72	21.31	1.881	0.469
250	19.4	18.73	3.444	1.17
400	15.43	14.08	8.745	11.5
		Mortar		
20	22.15	22.1	0.224	0.506
120	22.2	22.33	0.566	0.464
250	21	20.87	0.587	0.745
400	19.34	18.28	5.478	1.77

burst series starts again. The number of driving periods of the tone-burst is determined so as to exceed the quality factor Q of the sample in order to ensure steady state conditions. The highest quality factor over the full set of the sample was set to ensure steady state conditions for every sample (about 200 for present samples). The quality factor is defined as the resonance frequency divided by the resonance peak width evaluated at the half maximum amplitude for a given mode.

The slope of the line in Fig. 7 is proportional to the nonlinearity. The absolute nonlinear α parameter is evaluated by the combination of Eq. (2) and Eq. (3). The linearity of the experimental system is checked by applying NRUS to a known linear material (Plexiglas) (Fig. 8) with the same geometry as the concrete samples and thus exhibiting the same resonance mode shapes.

III. RESULTS AND DISCUSSION

A. RUS

The results for all samples are shown in Fig. 9. These results highlight the global decrease of the Young modulus and Poisson ratio with increasing thermal damage. Because of the presence of adjuvant in HPC, The Young's modulus

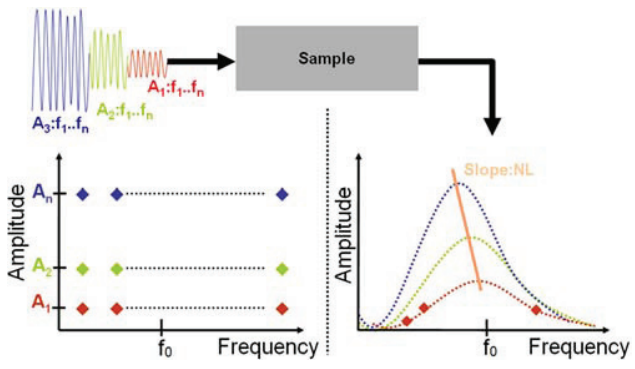

FIG. 7. (Color online) Data acquisition procedure. (left) Generation. (right) Reception.

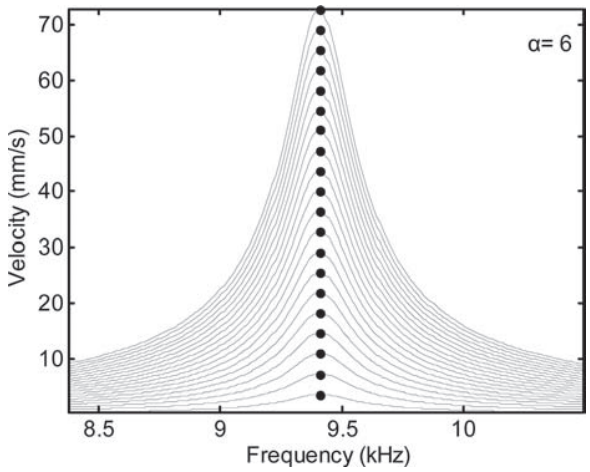

FIG. 8. Plexiglas sample NRUS results.

of HPC is greater than OC. The residual Young's modulus is about 50% at 400 °C for both HPC and OC. These values are in agreement with the literature[20,21] with the same kind of damage protocol (slow increase and decrease of temperature) and limestone type aggregates. The M samples are less affected than HPC and OC ones with a 71% residual Young's modulus at 400 °C. The Poisson ratio decreases with temperature by an amount in agreement with literature.[22]

B. Quantitative NRUS

The methodology is applied to each sample. Figures 10–12 present the full set of results for HPC, OC, and M samples, respectively.

The compilation is provided in Fig. 13.

Several interpretations and comments arise from these data.

1. Comparison with other materials

This quantitative measure allows to compare the actual absolute nonlinear parameter to the literature. These results range in the absolute values reported in rocks[23,24] under various conditions. In the undamaged state, the M nonlinearity is comparable to alumina, quartzite, and cracked pirex.[15] It is worth noticing that except for undamaged mortar, present values are an order of magnitude higher than materials such as aluminum or bone.[25] These four references are the only ones providing absolute values of the nonlinear parameter. It is thus anticipated that we can draw general conclusions about possible mechanisms responsible of the nonlinear hysteretic behavior.

2. Correlation with the microstructure

From the thermo-mechanical properties of concrete presented Sec. I A, the ITZ is identified as an important contributor to the thermal damage process. From the composition of present samples (Table I), a rough estimate of the ITZ area can be achieved assuming aggregates as spheres with diameters corresponding to the average aggregate size weighted by the quantity of each class. For M samples, the average ITZ area is $A_M = 16$ mm^2. For HPC, which contains also plasticizer and presents the same w/c ratio than M samples, the ITZ area is $A_{HPC} = 203$ mm^2. The ratio of both quantities provides $A_{HPC}/A_M = 12.7$. On the other hand, the ratio of the nonlinearity for these two samples is $\alpha_{HPC}/\alpha_M = 11.5$. This ratio is more or less constant over full the damage process (Fig. 13). This rough estimate underlines that the ITZ can be one of the main nonlinearity source in concrete subjected to thermal damage. Because of different composition, the same assumption qualitatively holds for OC samples compared to M ones.

It is important to notice that taking into account the volumetric density of ITZ, the results are opposite to what is expected. Because of the small diameters of inclusions, M samples exhibit a density of ITZ considerably higher than HPC. Recent results in plaster[26] and in concrete[27] show that the sizes of inclusions (respectively gypsum crystals and aggregates) play a key role on the nonlinear behavior.

The presence of plasticizer in HPC makes the spatial arrangement of aggregates homogeneously distributed. Silica fume allows a better adherence between aggregates and cement paste. Regarding the thermal damage process of concrete described Sec. I A, these two observations may explain their lower nonlinearity compared to OC ones.

3. Correlation with linear elastic properties

The nonlinear parameter is not correlated with the Young's modulus. Over the full damage process, M exhibits

Sample	E (Gpa)	ν
High Performance Concrete		
HPC 20	48.9	0.21
HPC 120	45.3	0.19
HPC 250	39.4	0.2
HPC 400	24.8	0.1
Ordinary Concrete		
OC 20	36.9	0.2
OC 120	35.5	0.18
OC 250	28.6	0.13
OC 400	16.4	0.08
Mortar		
M 20	37.1	0.17
M 120	38.4	0.17
M 250	33.6	0.14
M 400	26.5	0.09

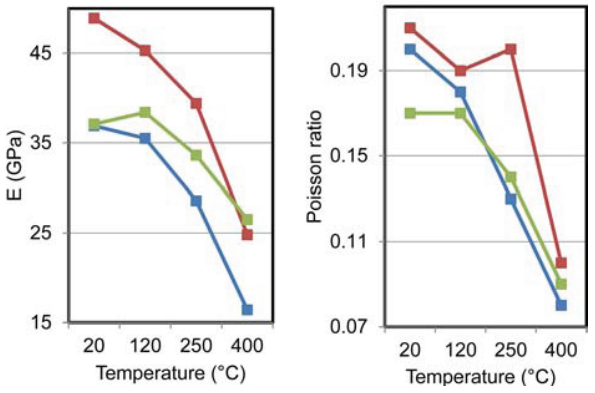

FIG. 9. (Color online) Evolution of elastic properties for the full set of sample as a function of thermal damage.

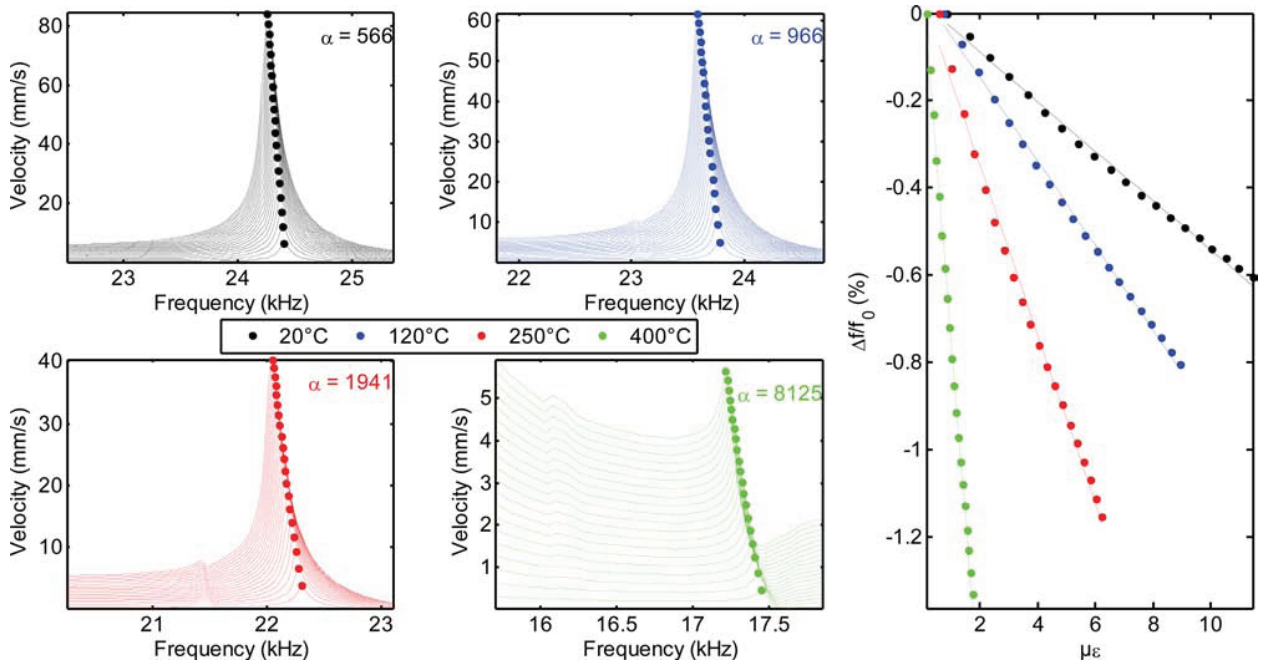

FIG. 10. (Color online) High Performance Concrete NRUS curves.

a low nonlinearity compared with ordinary and HPC while its linear elastic properties range between the latters (Fig. 9). The nonlinear parameter is supposed to be physically driven by nonlinear and hysteretic phenomena such as contact, friction, opening/closing of micro cracks at mesoscopic scale. The linear elastic properties are affected by the composition as well as any kind of porosities (crack type or air voids).

4. Other physical mechanisms in play

It is worth noticing that actual experiments were performed under ambient laboratory conditions (air conditioning at 20 °C), meaning that the influence of water saturation and temperature during experiments is not taken into account here. Water saturation is known to have an influence on the nonlinear response of mesoscopic materials.[24] Temperature changes during experiments are known to be a source of uncertainties for weekly nonlinear materials[25] (which is not the case here except for M20 sample). This effect can be reduced using an experimental protocol developed by Haupert *et al.*[25]

A sensitivity study is provided in Fig. 14. For comparison purposes, the sensitivity of the compressional wave velocity estimated from time of flight measurement is also

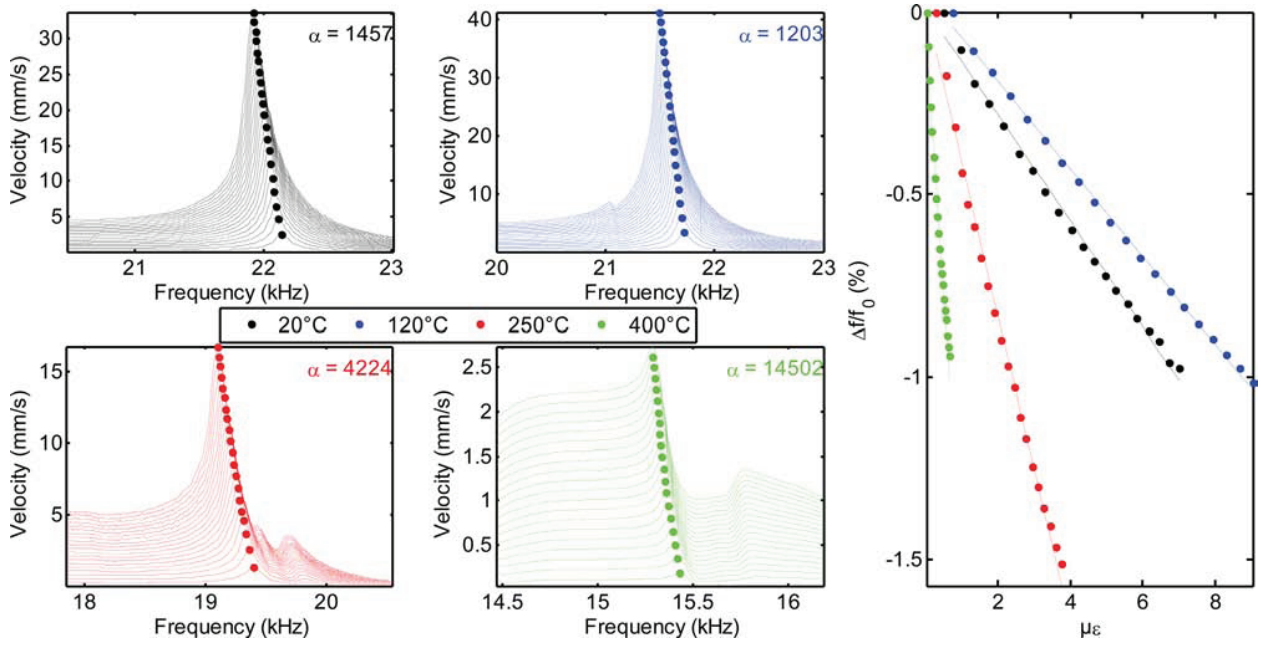

FIG. 11. (Color online) Ordinary Concrete NRUS curves.

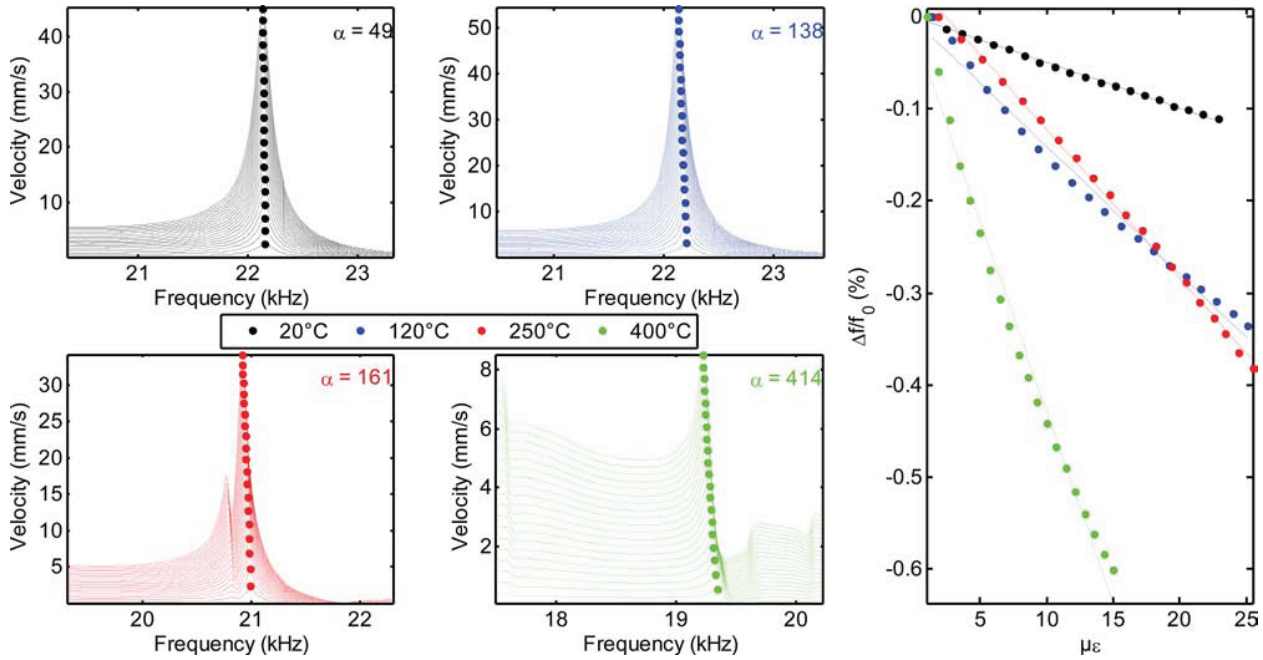

FIG. 12. (Color online) Mortar NRUS curves.

shown. The nonlinear parameter globally increases by 1000% while the speed of sound reaches only 25%. The equivalent nonlinearity values found for intact and 120 °C damaged OC samples are not explainable except by the sample variability at manufacturing or an unexpected change in temperature or humidity during the OC20 experiment. Here, the supposed intact sample is suspected to be too nonlinear, making the relative sensitivity of OC samples a little bit lower than the HPC samples. Physically, due to the ITZ effect comparable for both OC and HPC, this sensitivity should be comparable (about 1300%).

Because of the global fall of elastic properties, one can observe from Fig. 10 to Fig. 12 that the mode density increases around the selected mode for most damaged samples (250 and 400 °C). It may become problematic with highly damaged samples for which modes could overlap making impossible the evaluation of the strain amplitude, however, with a different choice of the sample geometry (if possible) one can alleviate this problem. It is observed that the intact state deviation between M, HPC, and OC samples remains more or less constant over the full damage process. For lower frequencies, the accuracy would probably have been better but the aim of this paper is to study the bulk mode nonlinearity and highlight the importance of the knowledge of mode shape to properly evaluate the strain amplitude, thus the nonlinearity.

Sample	α
High Performance Concrete	
HPC 20	566
HPC 120	966
HPC 250	1941
HPC 400	8125
Ordinary Concrete	
OC 20	1457
OC 120	1204
OC 250	4224
OC 400	14502
Mortar	
M 20	49
M 120	138
M 250	161
M 400	414

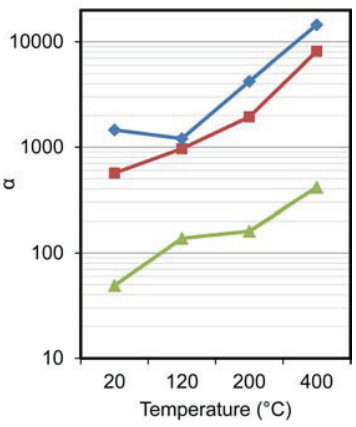

FIG. 13. (Color online) Result's compilation of nonlinear parameters.

With increasing damage, as widely reported in the literature, the sensitivity of the nonlinear parameter is more than one order magnitude greater than linear ones. It is important to notice that without taking into account the "true" strain inside the sample, the net effect appears larger or does not really reflect the physics. A typical evaluation of strain amplitude is v_{laser}/c, with c being the speed of sound. This assumption is only valid in free space as it provides the strain component perpendicular to the surface and does not hold for modal analysis. As an example, the speed of sound decreases with damage by 25% for most damaged samples which implies a 33% increase of strain for a given particle velocity level. Table II shows that the C constant can increase by more than a factor of 10 which implies a 10 times increase of strain amplitude for a given particle velocity level. That means that with the previous approximation, being the slope of the trend in Eq. (2), the nonlinearity is over estimated making the apparent sensitivity too high. Then, applying this assumption for modal analysis may lead to erroneous interpretations in case of non-symmetric mode shapes such as shown in Fig. 6.

IV. CONCLUSION AND PROSPECTS

In this paper, the combination of linear measurements (RUS) with numerical simulation and nonlinear measurements

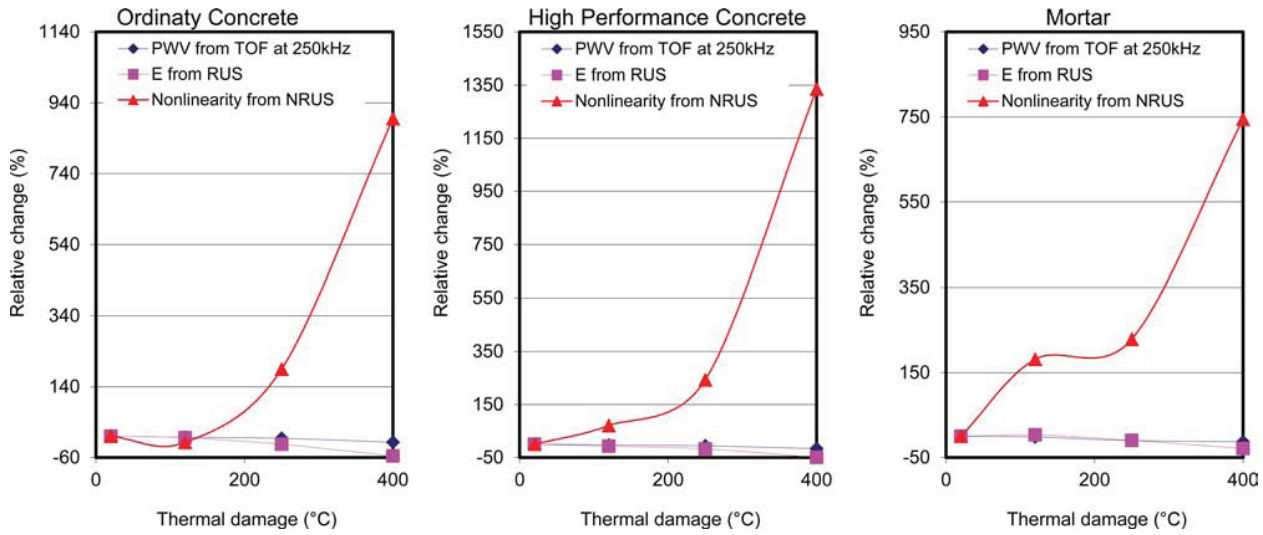

FIG. 14. (Color online) Sensitivity study. PWV is the Pulse Wave Velocity evaluated from time of flight measurements.

(NRUS) is proposed in order to quantitatively evaluate the nonlinear behavior of materials. This paper highlights the importance of the mode shape to quantitatively evaluate the nonlinearity. It is applied to study the effect of thermal damage in concrete with results correlated to the evolution of the microstructure. The evolution of the Young's modulus and Poisson ratio evaluated from RUS are in agreement with the literature. The cement/aggregate interface (ITZ) is identified as the main source of nonlinearity for thermal damage regarding the thermo mechanical properties of concrete. The large sensitivity of the nonlinear parameter is shown with a sensitivity 2 orders of magnitude higher than a standard ultrasonic nondestructive indicator such as pulse wave velocity.

At the present time, many studies emphasize the nonlinear α parameter to be highly sensitive to damage, which is true. However, due to the lack of the "true" strain in the sample, most of them are not comparable to each other, thus making the proper validation of the data impossible. The presented methodology is one of the possible ways to extend the literature with quantitative values that are comparable from one material to another by providing absolute values of α, rather than simply relative changes.

The assessment of gradual damage in depth is one of the main problems in Nuclear Energy concrete structures that are subject to both radiation and elevated temperature. It is important to underline that this procedure applies for any kind of geometry (cores or parallelepiped) with any aspect ratio. So, by considering core extraction from a concrete structure, one can cut these cores into slices corresponding to various depths and apply the present methodology to evaluate the depth and the amount of damage. In contrast, standard mechanical tests (e.g., stress-strain testing) that only apply to standard cores (i.e., specific dimensions) make it impossible to get the evolution in depth of linear and nonlinear properties in that case.

Studies in progress are aimed at going one step beyond these quantitative nonlinearity values in order to nondestructively provide the evolution of elastic properties with strain amplitude, i.e., being able to provide the evolution of the Young's modulus and Poisson ratio as a function of strain amplitude.

ACKNOWLEDGMENTS

The authors thank the U.S. DOE Used Fuel Disposition (Storage) campaign and the Electrical Power Research Institute for supporting this study and C.P.'s visit to LANL, and CSTB for manufacturing the samples. C.P. was also supported by Aix Marseille University. The authors would also like to thank James Ten Cate, Paul Johnson, and Robert Guyer for useful discussion during the course of this work.

[1]P. Nagy, "Fatigue damage assessment by nonlinear ultrasonic materials characterization," Ultrasonics **36**, 375–381 (1998).
[2]C. Payan, V. Garnier, J. Moysan, and P. A. Johnson, "Applying nonlinear resonant ultrasound spectroscopy to improving thermal damage assessment in concrete," J. Acoust. Soc. Am. **121**(4), EL125–EL130 (2007).
[3]A. Menou, "Thermal and mechanical behavior of concrete, a Multi-Scale Approach to Thermal Damage: Applications to Concrete at High Temperature," Ph.D. thesis, University Pau et Pays de l'Adour, France, 2004 (in French).
[4]A. M. Neville, *Properties of Concrete*, 3rd ed. (Longman Scientific and Technical, Essex, UK, 1981), 779 pp.
[5]Y. F. Fu, Y. L. Wong, C. A. Tang, and C. S. Poon, "Thermal induced stress and associated cracking in cement-based composite at elevated temperatures—Part I: Thermal cracking around single inclusion," Cement Concrete Compos. **26**(2), 99–111 (2004).
[6]Y. F. Fu, Y. L. Wong, C. A. Tang, and C. S. Poon, "Thermal induced stress and associated cracking in cement-based composite at elevated temperatures—Part II: Thermal cracking around multiple inclusions," Cement Concrete Compos. **26**(2), 113–126 (2004).
[7]D. Landau and E. M. Lifshitz, *Theory of Elasticity*, 3rd ed. (Pergamon, New York, 1986), 187 pp.
[8]R. Guyer and P. A. Johnson, "Nonlinear mesoscopic elasticity: Evidence for a new class of materials," Phys. Today **52**, 30–35 (1999).
[9]K. Van Den Abeele, P. A. Johnson, and A. Sutin, "Nonlinear Elastic Wave Spectroscopy (NEWS) techniques to discern material damage. Part I: Nonlinear Wave Modulation Spectroscopy (NWMS)," Res. Nondestruct. Eval. **12**, 17–30 (2000).
[10]K. Van Den Abeele and J. De Visscher, "Damage assessment in reinforced concrete using spectral and temporal nonlinear vibration techniques," Cem. Concr. Res. **30**, 1453–1464 (2000).
[11]M. Bentahar, H. El Aqra, R. El Guerjouma, M. Griffa, and M. Scalerandi, "Hysteretic elasticity in damaged concrete: Quantitative analysis of slow and fast dynamics," Phys. Rev. B **73**, 014116 (2006).

[12]F. Bouchaala, C. Payan, V. Garnier, and J. P. Balayssac, "Carbonation assessment in concrete by nonlinear ultrasound," Cem. Concr. Res. **41**, 557–559 (2011).
[13]K. J. Lesnicki, J.-Y. Kim, K. E. Kurtis, and L. J. Jacobs, "Characterization of ASR damage in concrete using nonlinear impact resonance acoustic spectroscopy technique," NDT&E Int. **44**, 721–727 (2011).
[14]K. Van Den Abeele, J. Carmeliet, J. A. TenCate, and P. A. Johnson, "Nonlinear Elastic Wave Spectroscopy (NEWS) techniques to discern material damage. Part II: Single mode nonlinear resonance acoustic spectroscopy," Res. Nondestruct. Eval. **12**, 31–43 (2000).
[15]P. Johnson and A. Sutin, "Slow dynamics and anomalous nonlinear fast dynamics in diverse solids," J. Acoust. Soc. Am. **117**, 124–130 (2005).
[16]A. Migliori and J. L. Sarrao, *Resonant Ultrasound Spectroscopy: Applications to Physics, Materials Measurements, and Nondestructive Evaluation* (Wiley, New York, 1997).
[17]T. J. Ulrich, K. R. McCall, and R. Guyer, "Determination of elastic moduli of rock samples using resonant ultrasound spectroscopy," J. Acoust. Soc. Am. **111**(4), 1667–1674 (2002).
[18]W. Wu, A. Al-Ostaz, J. Gladden, A. H. D. Cheng, and G. Li, "Measurement of mechanical properties of hydrated cement paste using resonant ultrasound spectroscopy," J. ASTM Int. **7**(5), JAI102657 (2010).
[19]S. Bernard, Q. Grimal, and P. Laugier, "Accurate measurement of cortical bone elasticity tensor with resonant ultrasound spectroscopy," J. Mech. Behav. Biomed. Mater. **18**, 12–19 (2013).
[20]J. Xiao and G. König, "Study of concrete at high temperature in China—An overview," Fire Saf. J. **39**, 89–103 (2004).
[21]U. Schneider, C. Diererichs, and C. Ehm, "Effect of temperature on steel and concrete for PCRV's," Nucl. Eng. Design **67**, 245–258 (1982).
[22]J. C. Maréchal, "Variations of the modulus of elasticity and Poisson's ratio with temperature," Concrete Nucl. Reactors **1**(SP-34), 495–503 (1972).
[23]P. A. Johnson, B. Zinszner, P. Rasolofosaon, F. Cohen-Tenoudji, and K. Van Den Abeele, "Dynamic measurements of the nonlinear elastic parameter in rock under varying conditions," J. Geophys. Res. **109**, B02202, doi:10.1029/2002JB002038 (2004).
[24]K. Van Den Abeele, J. Carmeliet, P. A. Johnson, and B. Zinzsner, "The influence of water saturation on the nonlinear mesoscopic response of earth materials, and the implications to the mechanism of nonlinearity," J. Geophys. Res. **107**(B6), 2121, doi:10.1029/2001JB000368 (2002).
[25]S. Haupert, G. Renaud, J. Rivière, M. Talmant, P. A. Johnson, and P. Laugier, "High accuracy acoustic detection of non-classical component of material nonlinearity," J. Acoust. Soc. Am. **130**(5), 2654–2661 (2011).
[26]H. Ramanasse, C. Payan, V. Garnier, N. Chaouch, B. Lombard, and N. Favrie, "Influence of the microstucture on the Nonlinear properties of plaster: Experimental evidence and numerical simulation," *18th International Conference on Nonlinear Elasticity in Materials*, Ascona, Switzerland, June 9–14th (2013).
[27]M. Scalerandi, M. Griffa, P. Antonaci, M. Wyrzykowski, and P. Lura, "Nonlinear elastic response of thermally damaged consolidated granular media," J. Appl. Phys. **113**, 154902 (2013).

Probing material nonlinearity at various depths by time reversal mirrors

C. Payan,[1] T. J. Ulrich,[2] P. Y. Le Bas,[2] M. Griffa,[3] P. Schuetz,[3] M. C. Remillieux,[2] and T. A. Saleh[4]
[1]*LMA UPR CNRS 7051, Aix Marseille Université, 31 Chemin Joseph Aiguier, 13402 Marseille, France*
[2]*Los Alamos National Laboratory, EES-17, Los Alamos, New Mexico 87545, USA*
[3]*Swiss Federal Laboratories for Materials Science and Technology (EMPA), Überlandstrasse 129, 8600 Dübendorf, Switzerland*
[4]*Los Alamos National Laboratory, MST-16, Los Alamos, New Mexico 87545, USA*

(Received 25 December 2013; accepted 31 March 2014; published online 9 April 2014)

In this Letter, the time reversal mirror is used to focus elastic energy at a prescribed location and to analyze the amplitude dependence of the focus signal, thus providing the nonlinearity of the medium. By varying the frequency content of the focused waveforms, the technique can be used to probe the surface, by penetrating to a depth defined by the wavelength of the focused waves. The validity of this concept is shown in the presence of gradual and distributed damage in concrete by comparing actual results with a reference nonlinear measurement and X ray tomography images. © *2014 AIP Publishing LLC*. [http://dx.doi.org/10.1063/1.4871094]

The principle of time reversal acoustics is based on a simple idea. In any medium, send a pulse from a source. That pulse propagates into the medium. The pulse is eventually reflected many times at the boundaries and by other scatterers. The resulting signal is recorded at a defined location by a receiver. If the recorded signal is time reversed and sent back from the receiver, the wave will play this propagation history backward (as a movie played backward). The wave energy will focus at the precise source location, at a given time (namely the focal time). Thanks to the reciprocity principle,[1] the same scenario can be achieved even if the time reversed signal is sent back from the initial source. In this case, the focus will occur at the receiver location. While this is true with a single emitter, using multiple emitters allows for a proportionately higher amplitude to be obtained at the focal time.

This physical principle has been under study for many years and has been largely developed by Fink[2] with most of the applications in liquids or biological tissues for the medical field. Applications to the field of nonlinear elasticity in solids were developed with the goal of using the high energy focus to extract some nonlinear properties of solids. It has been successfully applied to locate and image cracks in a metal component,[3] to evaluate the quality of diffusion bonds,[4] and to probe the interior of a solid.[5] To probe the nonlinearity of the medium with varying amplitude time reversal experiments, so far, most of the studies have employed the harmonic content[3] or a scaled subtraction method.[6,7] However, these methods are dedicated to locate or size a single or multiple nonlinear scatterer embedded in a linear medium. They proved very efficient for nonlinear source localization. Here, we explore the applicability to volumetrically distributed cracks in a nonlinear material.

The aim of this Letter is to propose a physics-based method to measure the nonlinearity of the medium and to evaluate the nonlinearity at various depths. To provide a reliable nonlinear parameter, we make use of concrete samples whose nonlinear elastic behavior was assessed by a quantitative Nonlinear Resonant Ultrasound Spectroscopy (NRUS) measurement. The same samples in this work are also inspected by X-ray tomography to search for evidence of damage, usually considered as the source of the nonlinear behavior.[8] The reader is invited to refer to Ref. 8 for details about samples and NRUS results. To probe the nonlinearity at various depths, the frequency content of the transmitted signals is modified. It results in a variable focal spot size which depends on the wavelength.

The experiments are conducted on four concrete samples of size $10 \times 10 \times 6$ cm^3. The first sample remains undamaged while the others are thermally damaged at 120, 250, and 400 °C, respectively. A plexiglass sample with the same geometry is also used as a linear elastic reference sample. The experimental protocol is based on reciprocal Time Reversal (abbreviated "TR" hereafter). The sample is placed onto a reverberant cavity which is a simple aluminum block with 8 piezoelectric discs (emitters) bonded to the surface at various locations. This cavity allows multiple reflections to occur, delaying the information available over time. It has been shown that both multiple reflections at the boundaries and multiple scattering improve the efficiency of the time reversal process.[9] A laser vibrometer records the out-of-plane particle velocity at the top of the sample. An 8-channel 14-bit generator/digitizer system is used for signal generation and acquisition. The generator is connected to an 8-channel amplifier, which drives the emitters up to a 100 Vpp voltage. A computer controls the TR experiments and allows moving the sample with a synchronized motion controller.

Five frequencies ($f = 100$, 150, 200, 250, and 300 kHz) corresponding to various wavelengths are selected. Note that the wavelength varies as a function of speed of sound c as $\lambda = c/f$. The size of the focus, i.e., the penetration depth, is known to correspond to $\lambda/2$.[1,6] Over the full set of samples and frequencies, the wavelengths range from 9 mm to 48 mm. A chirp signal (sinusoid with frequency varying in a given range) with a 50 kHz bandwidth is sent to one emitter. The signal is recorded by the laser vibrometer, cross-correlated with the initial chirp signal (this operation allows

obtaining the impulse response of the sample in the selected frequency range), and recorded by the system. The same chirp is emitted from another emitter and the corresponding propagated signal is recorded as well. This process is executed for each channel. When the 8 impulse responses are recorded, a signal containing 4 successive amplitudes (scaled by 1, 0.9, 0.8, and 0.7, respectively) is built for each channel. All of them are then time reversed and sent back from their initial emitters simultaneously. The laser then records the four resulting focused waves, repeated each 50 ms to average 64 times. This process is performed for 4 increasing voltages (12.5, 25, 50, and 100 Vpp, respectively) producing a total of 16 amplitudes. The full protocol is repeated at 2 other locations on the sample, 2 cm away from each other's, in order to average the nonlinearity over the surface.

In materials such as rocks and concrete, so called nonlinear mesoscopic elastic materials,[10] several nonlinear and non-equilibrium phenomena occur. The phenomenon of interest in this work is related to the material softening subjected to high strain waves ($\sim 10^{-6}$), also called fast dynamics. Figure 1(a) shows an example of a recorded retro focal time series zoomed at focal time. It is noticeable [refer to the dotted circles] that the zero crossing occurs at the same time for each amplitude in the linear Plexiglass sample while a time delay is clearly visible in the 400 °C sample. The focal time appears more delayed, due to the decreasing speed of sound with increasing amplitude, a signature of the material softening. This time shift refers to the relative resonance frequency shift measured in NRUS experiments.[8] The softening of the material is evaluated as the relative velocity change $\Delta c/c_0$ with c_0 being the low amplitude speed of sound. The time delay Δt between signals is estimated by the cross-correlation of the low amplitude signal with higher amplitudes ones, similarly to the methods used by Rivière *et al.*[11] and Tournat and Gusev,[12] for assessing nonlinearity. For more accuracy, the maximum position of the cross correlation is obtained by fitting the peak region with an oversampled second order polynomial function. The delay measured for the 400 °C sample [Fig. 1(a)] is 7 ns for the highest amplitude. Over all measurements, the delay ranges from 20 ps. to 140 ns.

As most of the energy is concentrated into a $\lambda/2$ region, the hypothesis is that the focused waves reach the softening nonlinear regime[13] only in this region. Assuming in first approximation that the retro-focused wave field as a standing wave in a volume extended in depth for a length of $\lambda/2$, the relative velocity change can be approximated as $\Delta c/c_0 = -\Delta t/t_0 \approx -2f\,\Delta t$, where f is the central frequency of the chirp source signal and t_0 the time of flight for a $\lambda/2$ path. Similar to NRUS experiments,[8] the nonlinearity parameter α is extracted from the slope of the relative velocity change versus the strain amplitude $\Delta c/c_0 = \alpha\ \Delta\varepsilon$ [solid lines Fig. 1(b)]. The relative velocity change is averaged over the three measurements points at the surface of the sample. As an approximation, the strain amplitude is evaluated as $\Delta\varepsilon_{zz} \approx \Delta v_{zz}/c_0$ where Δv_{zz} is the out-of-plane particle velocity amplitude recorded by the laser. Due to the dispersive nature of concrete, the speed of sound c_0 is measured by time of flight for each frequency. Figure 1(b) shows results at 150 kHz. As expected, the Plexiglass sample is less nonlinear than concrete ones and the nonlinearity increases with thermal damage in the concrete samples.

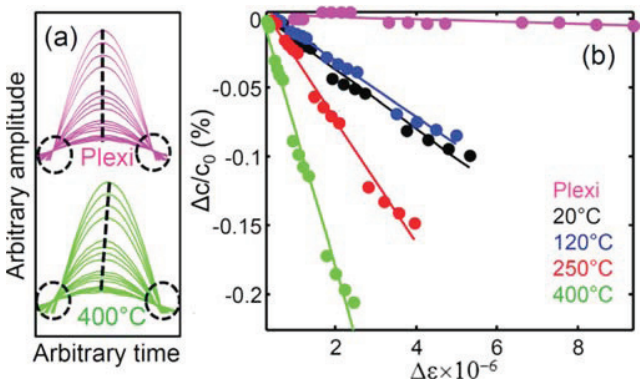

FIG. 1. (a) Zoom at focal time for the linear plexiglass sample and the most damaged sample at 150 kHz. For clarity, the time delay is magnified. (b) Relative velocity change at 150 kHz for the full set of sample.

Imperfections in the linear fit Fig. 1(b) are explained by experimental considerations associated with the coupling between nonlinearity and conditioning.[14] In each curve plotted in Fig. 1(b), considering a group of four points, the successive 4 amplitudes focused waves, averaged 64 times, make the material conditioned at the highest amplitude. Therefore, for the lower amplitudes, the material does not have time to entirely recover. Due to experimental conditions, the other groups of points are recorded about 1 min later, leaving time to the material to recover. By considering only the highest amplitude signals at each voltage (suppressing the cited effect), the results are affected by less than 2%. However, as for NRUS, time delay is evaluated under fully conditioned conditions. It is also noticeable that in some cases Fig. 1(b), the fit could also apply with a quadratic function. Over the entire data set, there is no general trend allowing to draw a conclusion. However, this nonlinear trend can be explained by the strain estimation which relates more the effect of pressure components here. The complex interplay of compressional and shear components at the focus is not accounted, thus depending on the orientation of the microcracks into the focal spot, it is likely that the nonlinearity could answer more to shear than pressure waves or inversely. The full set of results is presented and discussed in the next paragraph.

Fig. 2 relates the full set of results and validations. Figure 2(a) shows the nonlinearity as a function of penetration depth for the full set of samples. The linear reference, i.e., the plexiglass sample, is one order of magnitude less nonlinear than the concrete. It provides the Signal-to-Noise Ratio (SNR) of this experiment. The SNR is more important in this measurement than for the NRUS measurement performed on the same samples.[8] Due to the homogeneity of thermal damage in concrete,[15] the 20, 120, and 250 °C samples exhibit roughly constant nonlinearity. For the full set of concrete samples, the evolution of the average nonlinearity matches very well the reference NRUS measurements [See Ref. 8 and Fig. 2(c)]. The underestimation of the nonlinearity in the present study is due to the strain evaluation which is approximated by $\Delta\varepsilon_{zz}$ measured at the surface instead of the volumetric strain evaluated in Ref. 8. Janssen and Van Den Abeele[6] have shown that the focal shape looks like a pear shape with a maximum volumetric stress at the surface. Considering the

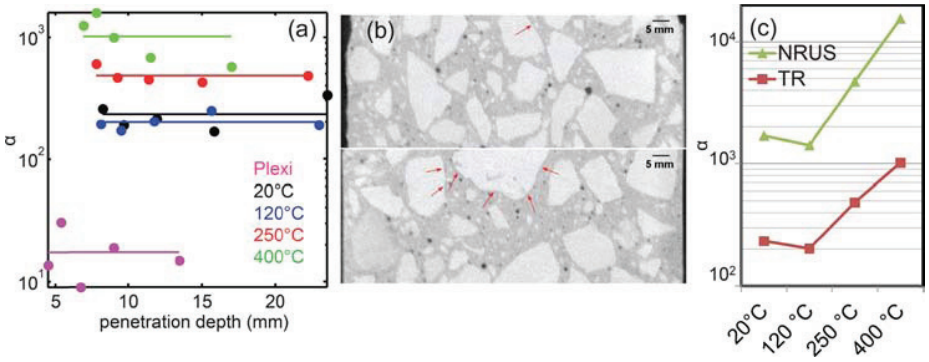

FIG. 2. (a) Compilation of the results. Solid lines are the average nonlinearity for each sample. (b) Xray CT images of the 20 °C sample (top) and the 400 °C sample (bottom). (c) Comparison of the average nonlinearity noted TR with NRUS data from Ref. 8.

interaction zone as the whole focal spot, the average strain amplitude should be lower than the one measured at the surface. This leads to an overestimation of the strain amplitude, which tends to decrease the nonlinear parameter.

Figure 2(a) shows that the 400 °C sample does not exhibit a constant nonlinearity with the depth of the material, with a clear increase of the nonlinearity in the near surface (∼1 cm). To understand this result, X-ray tomography measurements are performed on the reference concrete sample (20 °C) and on the 400 °C one. The details of such measurements are reported in the supplementary material.[15] During thermal loading of concrete, the main damage (thus nonlinearity) source consists of debonding at the interface between the cement paste and the aggregates.[8,16] Figure 2(b) shows two vertical, digital cross-sections extracted from two X-ray tomographic datasets, one dataset for the reference sample at 20 °C (top image), the other dataset for the sample thermally loaded at 400 °C (bottom image). The arrows overlaid on top of the two images point to regions of potential debonding between the aggregate and the cement paste. Despite the low spatial resolution (about 100 μm) compared with the debonding size, it is clear from the two sample images that such regions of potential debonding are more frequent and much more widespread in the thermally loaded sample. A semi-quantitative, 2D image analysis of such regions is presented in the supplementary material,[15] and it confirms that the thermally loaded sample is characterized by aggregate-to-cement paste boundary regions with more debonding features. The bottom image in Fig. 2(b) clearly shows that the debonding runs all along the boundaries between a large aggregate and the surrounding cement paste. Signs of debonding with such a spatial extension are present in other parts of the sample. However, their concentration is larger within the first centimeter from the surface. This is due to aggregate segregation by size, occurring during mixing, leading to a higher number of large aggregates closer to the surface than in depth. Larger aggregates correspond to smaller inter-aggregate distances, which then leads to larger, localized thermal stresses in the cement paste, thus more frequent debonding.[16] In addition, debonding at the aggregate-cement paste interface is also driven by drying shrinkage, which occurs more easily closer to the surface,[17] especially at elevated temperature such as 400 °C.

We show in this Letter the feasibility of using time reversal at various frequencies to probe the nonlinearity of materials at various depths. The correlation of the results with reference measurements from the literature, along with X-ray Computed Tomography images which explain the results for the 400 °C sample, validates the concept. The time delay observed in the experiments, a signature of nonlinear mesoscopic elasticity, suggests a physically based method to quantitatively evaluate the nonlinearity. This approach could be extended to the classical nonlinearity by monitoring the harmonic content with increasing amplitude or slow dynamics by looking at the slow recovery of initial focal time. A better estimation of strain amplitude is under study by further numerical simulations associated with three component laser measurements. It should ultimately allow precise and local nonlinearity measurements using a time reversal mirror, and it has the potential to be easily applied *in situ* for practical applications, such as inspection of concrete infrastructures.

The authors thank the US DOE Used Fuel Disposition (Storage) campaign and the Electrical Power Research Institute for supporting this study and Payan's visit to LANL. Payan was also supported by Aix Marseille Université. We would also like to thank James Ten Cate, Paul Johnson, and Robert Guyer for useful discussion during the course of this work.

[1]C. Draeger, J. C. Aime, and M. Fink, J. Acoust. Soc. Am. **105**(2), 618 (1999).
[2]M. Fink, IEEE Trans. Ultrason., Ferroelectr., Freq. Control. **39**(5), 555 (1992).
[3]T. J. Ulrich, P. A. Johnson, and R. A. Guyer, Phys. Rev. Lett. **98**, 104301 (2007).
[4]T. J. Ulrich, A. Sutin, T. Claytor, P. Papin, P. Y. Le Bas, and J. A. TenCate, Appl. Phys. Lett. **93**, 151914 (2008).
[5]P. Y. Le Bas, T. J. Ulrich, B. E. Anderson, R. A. Guyer, and P. A. Johnson, J. Acoust. Soc. Am. **130**(4), EL258 (2011).
[6]E. N. Janssen and K. Van Den Abeele, Ultrasonics **51**(8), 1036 (2011).
[7]M. Scalerandi, A. S. Gliozzi, C. L. E. Bruno, and K. Van Den Abeele, J. Phys. D: Appl. Phys. **41**, 215404 (2008).
[8]C. Payan, T. J. Ulrich, P. Y. Le Bas, T. A. Saleh, and M. Guimaraes, "Quantitative linear and nonlinear resonance inspection techniques and analysis for material characterization: Application to concrete thermal damage," J. Acoust. Soc. Am. (unpublished).
[9]A. Derode, P. Roux, and M. Fink, Phys. Rev. Lett. **75**, 4206 (1995).
[10]R. Guyer and P. A. Johnson, *Nonlinear Mesoscopic Elasticity* (Wiley-VCH, Berlin, 2009).
[11]J. Rivière, S. Haupert, P. Laugier, and P. A. Johnson, J. Acoust. Soc. Am. **132**(3), EL202 (2012).
[12]V. Tournat and V. E. Gusev, Phys. Rev. E **80**(1), 011306 (2009).
[13]J. A. TenCate, D. Pasqualini, S. Habib, K. Heitmann, D. Higdon, and P. A. Johnson, Phys. Rev. Lett. **93**(6), 065501 (2004).
[14]M. Scalerandi, A. S. Gliozzi, C. L. E. Bruno, and P. Antonaci, Phys. Rev. B **81**, 104114 (2010).
[15]See supplemental material at http://dx.doi.org/10.1063/1.4871094 for details about X-ray tomography measurements.
[16]M. Scalerandi, M. Griffa, P. Antonaci, M. Wyrzykowski, and P. Lura, J. Appl. Phys. **113**, 154902 (2013).
[17]J. Bisschop and J. G. M. van Mier, Mater. Struct. **35**, 453 (2002).

The Journal of Adhesion, 90:555–568, 2014

ISSN: 0021-8464 print/1545-5823 online
DOI: 10.1080/00218464.2013.868806

Improving Adhesion Strength Analysis by the Combination of Ultrasonic and Mechanical Tests on Single-Lap Joints

ALICE BAUDOT[1,2], JOSEPH MOYSAN[2], CÉDRIC PAYAN[2], NOËLLIE YLLA[3,4], JOCELYNE GALY[3,4], BLANDINE VERNERET[5], and ANDRÉ BAILLARD[1]

[1]*Safran Aircelle, Gonfreville l'Orcher, France*
[2]*Aix-Marseille Université, LMA UPR 7051 CNRS, Aix-en-Provence, France*
[3]*Université de Lyon, Lyon, France*
[4]*INSA Lyon, CNRS, UMR 5223, Ingénierie des Matériaux Polymères, Villeurbanne, France*
[5]*Safran Composite, Moissy-Cramayel, France*

The aim of this paper is to improve knowledge about adhesion strength in single-lap joints by the comparison of data from both nondestructive testing (NDT) and standard mechanical tests. This study presents a high-frequency ultrasonic imaging of aluminum–epoxy–aluminum joints that were carefully chemically prepared using two different surface treatments of the aluminum substrate: silanization and chromic–sulfuric etching. The surface energy of the treated substrate was measured. A complete set of ultrasonic data were obtained using high-frequency focused transducers. After ultrasonic inspection, single-lap shear tests were performed, and the mechanical strength of each joint was determined. The good correlations among the surface measurements, the mechanical tests, and the ultrasonic results are presented and discussed. The demonstration of a close correlation between the ultrasonic images obtained at high frequency and the fracture surface is promising.

KEYWORDS Adhesion; Epoxy; Lap shear; Ultrasonics

Received 22 July 2013; in final form 20 November 2013.

Address correspondence to Alice Baudot, Safran Aircelle, 76700 Gonfreville l'Orcher, France. E-mail: alice.baudot@univ-amu.fr

Color versions of one or more of the figures in the article can be found online at www.tandfonline.com/gadh.

1. INTRODUCTION

Structural bonding for the automotive industry, the naval industry, and aeronautics was one of the major industrial changes in the field of material assembly [1]. This major change was accompanied by the necessity of developing methodologies to assess the strength of a bonded assembly. Assessing this strength remained a real technological and scientific challenge for many years because of regular changes in the materials that were used, as well as changing standards. This challenge led to many interdisciplinary studies, as it involved both material science and mechanical science. The question of how an assembly should be mechanically tested has produced dozens of different mechanical tests. Concurrently, finite-element modeling offered new possibilities for understanding the effective mechanical strength of a structure and the impacts of many parameters (*e.g.*, thickness, roughness, and stress concentration) and for attempting to predict cohesive or adhesive rupture [2].

Structural bonding created specific challenges for NDT science, as well. As bonding assemblies were most of the time the result of an innovative process, material parts often possessed new mechanical properties and required the adaptation of NDT methods or the development of new ones [3]. The use of adhesive bonding in primary structures has been limited by the lack of nondestructive testing procedures capable of guaranteeing the reliability of the joint. To date, no reliable NDT test for the adhesion strength of a bond has been developed. At present, this problem is addressed by strict control of the adherend surface-preparation procedures [3]. In comparison with classical NDT methods previously developed for weld testing, the NDT testing of bonded assemblies presents new difficulties, as material parts can have very different thicknesses due to the finer thickness of the bond layer. Ultrasonic and acoustic methods are the approaches that have been most commonly pursued since the early stages of structural bonding applications [3].

The field of NDT applications is continuously expanding; they are used for assessing the initial manufacturing quality of the bonding process, for in-service testing, and for assessing the quality of bonding subject to aging degradation. Three classical defects are investigated [3,4]:

i. complete voids, disbands, or porosity
ii. poor adhesion (1-weak bond between the adhesive and one or both adherends)
iii. poor cohesive strength (1-weak adhesive layer)

Poor adhesion is a reduction in the strength of the bond between the adhesive and the adherend. It is extremely difficult to detect using classical ultrasonic techniques because the bond strength is governed by a layer thinner than a conventional ultrasonic wavelength. By preference, a high-frequency transducer should be used for signal analysis [5]. Severe cases

in which the poor adhesion tends to zero are commonly termed kissing bonds or, alternatively, zero-volume disbonds [6]. This form of poor adhesion stands between the pooradhesion case and the wholly disbonded case. Numerous ultrasonic testing solutions have been developed for this specific case including nonlinear acoustics [5,7–9] but also guided waves [10,11]. Alternative solutions are also in development, such as Digital Image Correlation [12].

One of the obstacles to the development and demonstration of an acoustic method capable of quantifying the adhesive strength of a bonded joint is the absence of reference samples with full knowledge of their assembly. Multiple solutions have been proposed in the past, and still are currently to create reference samples for NDT testing. Defects can be artificially created by adding a foreign part at the interface between two parts [13] or by modifying the bond itself by incorporating a release agent [14] or by incorporating particles [15,16]. To study the adhesion strength, the most appropriate approach would be to vary the surface preparation or the surface treatment [17]. Many parameters can modify the bond strength, so the true difficulty is to exactly reproduce the same preparation steps in the same environment [18]. More rarely, some studies use a chemical pollution to obtain imperfections similar to those created by pollution during industrial processes [19]. Another way to produce variable adhesion is to compress a bond; this case is representative of dry-contact kissing bonds [7].

The single-lap shearjoint is the most widely studied type of adhesive joint in the literature. The manufacture of this joint is relatively easy, and the corresponding test requires a classic tensile testing machine. Many corresponding standards have been developed in industry, such as the ASTM D1002, the popular standard test method for evaluating the apparent shear strength of single-lap joint adhesively bonded metal specimens by tension loading, or the European Standard EN 2243-1. Adhesive-lap-joint shear-strength tests do not create perfect shear solicitation, and other physical factors are uncertain, such as the overlap length and the bondline thickness [17]. Stress concentrations should also be taken into account for accurate mechanical analysis. The form of the adhesive edges greatly influences the shear-stress concentrations. Appropriate geometries were proposed to improve mechanical analysis by reducing edge effects [20]. This joint geometry is chosen for our study because it also enables a simple NDT evaluation using through-transmission ultrasonic testing.

This study presents samples of aluminum–epoxy–aluminum joints with two different surface treatments of the aluminum substrate: silanization and chromic–sulfuric etching. The samples surface energy was measured. After ultrasonic CSCAN imaging, mechanical tests were performed to determine the mechanical strength of each joint.

In the following, the experiments are described, and the results are presented and discussed in detail. Conclusions are proposed regarding the evaluation of variable adhesion on single-lap shear joints using high-frequency ultrasonic analysis.

2. EXPERIMENTAL METHODS

2.1. Materials

The adhesive formulation is based on a two-component epoxy system. Diglycidyl ether of bisphenol A (DGEBA, DER 332, Dow Chemicals, Paris Saint Denis, France) with an epoxy equivalent weight of 171–175 g/eq is cross-linked with a cycloaliphatic amine hardener, isophorone diamine (IPD, Aldrich,Saint-Quentin Fallavier, France). The epoxy and the amine are mixed at room temperature, at a stoichiometric ratio aminohydrogene/epoxy equal to 1; the mixture is degassed to avoid airbubble formation in the adhesive bond. γ-glycidoxypropyltrimethoxysilane (γ-GPS) is obtained from Aldrich (Saint-Quentin Fallavier, France).

The chemical structures of both components are given in Table 1.

The metallic substrate is an aluminum alloy, A2024, in the form of 1.6-mm thick sheets.

2.2. Sample Preparation

The aluminum sheets are cut to 100 mm × 25 mm, and their surfaces are cleaned and treated before bonding to eliminate surface contamination and to promote different adhesion strengths. The following two surface treatments are employed prior to the adhesive bonding of the lap-shear test samples:

- Silane treatment (Si). There are four steps in this treatment: (i) solvent degreasing with a tissue soaked in isopropanol; (ii) alkaline cleaning by immersing the specimens for 10 min in a Sococlean (Socomore, Vannes, France) A3431 solution (c = 10%) heated to 45°C followed by rinsing in water; (iii) alkaline etching by immersing the specimens for 2 min in

TABLE 1 Chemical Structure of Monomers

NAME	Chemical structure	Molar mass (g/mol)
DGEBA		348
IPD	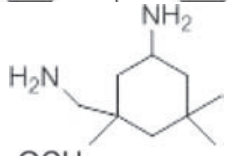	170
γ-GPS	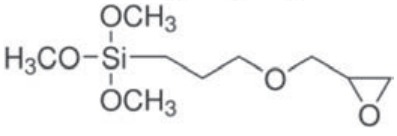	236

a solution of 40 g/l NaOH + 10 g/l sodium glucoheptonate heated to 40°C followed by rinsing in water; and (iv) silanization by immersing the specimens for 10 min in a 1 wt.% solution of GPS in distilled water; prior to immersion, the pH of the solution is adjusted to 5 using acetic acid, and the solution is stirred at room temperature for 1 h for the hydrolysis of the methoxy groups. The silane-treated specimens are heated for 1 h at 93°C in an oven to allow condensation reactions [21].

- Chromic–sulfuric acid treatment (CS). There are three steps in this treatment:(i) degreasing the specimens with acetone; (ii) immersing them in a water solution (∼300 g/l H2SO4, ∼30 g/l CrO3, ∼0.5 g Cu, ∼10 g Al) heated at 65°C for 15 min; and (iii) rinsing them in distilled water and drying them in an oven for 30 min at 60°C.

After the surface treatment, the aluminum pieces are assembled into single-lap shear joints with an overlap length of 12.5 mm. The lap-shear geometry is illustrated in Fig. 1. A specific metallic mold is designed to prepare the samples with a given thickness. This mold allows the simultaneous preparation of seven specimens. The mold is placed under a press, and a contact pressure of 2.2 bars is applied; then the samples are cured for 1 h at 80°C, followed by curing for 2 h at 180°C. This curing cycle fully cured the DGEBA–IPD adhesive.

2.3. Surface Energy

The surface energies of the aluminum substrate with and without surface treatment are determined from contact angles (CA) using a GBX Digidrop contact-angle goniometer following the Owens-Wendt method [22]. The average CAs are obtained by measuring the contact angles of at least six drops each for two probe liquids, water and diiodomethane.

2.4. Mechanical Testing

The samples are tested following EN 2243-1, using a universal testing machine (MTS, Eden Prairie, MN,USA) at a constant crosshead speed of 0.1 mm/min. The joint adhesive strength is calculated using the following formula:

$$\tau = \frac{P_{\max}}{A}, \tag{1}$$

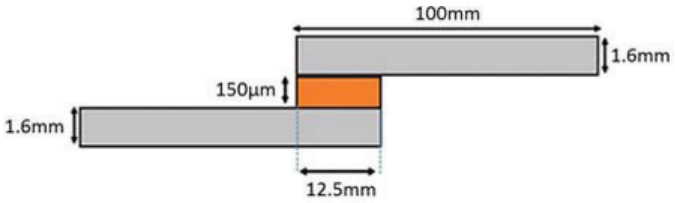

FIGURE 1 Geometry and dimensions of lap joint.

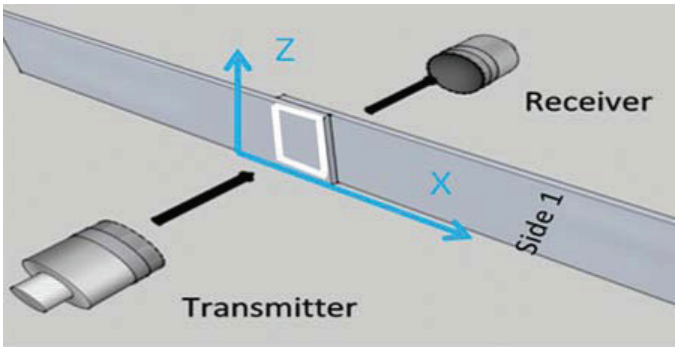

FIGURE 2 Normal-incidencetransmission experimental setup.

where τ is the adhesive strength in MPa, P_{max} is the maximum load at fracture in Newton, and A is the average cross-sectional area in mm^2. Lap-shear-strength data are obtained, and the corresponding standard deviations (std) are calculated.

2.5. NDT Characterization

Each sample is tested by the immersion technique using two focused Panametrics V376 (Olympus NDT, Waltham, MA, USA) transducers with a diameter of 12.7 mm and a focal distance of 31.75 mm. The experiment is performed in a water tank with two motorized arms. Each arm has five independent axes. The experimental setup is piloted by the software UTWIN (Mistras, Paris, France). Figure 2 presents the experimental setup for the normal-incidence transmission mode. The full bandwidth is very large (from 0 to 30 MHz), and as a consequence, we obtain short signals with a duration of two periods. This enables the separation of the two surface echoes, but the epoxy layer is too thin to create separated echoes (Figs. 3 and 4).

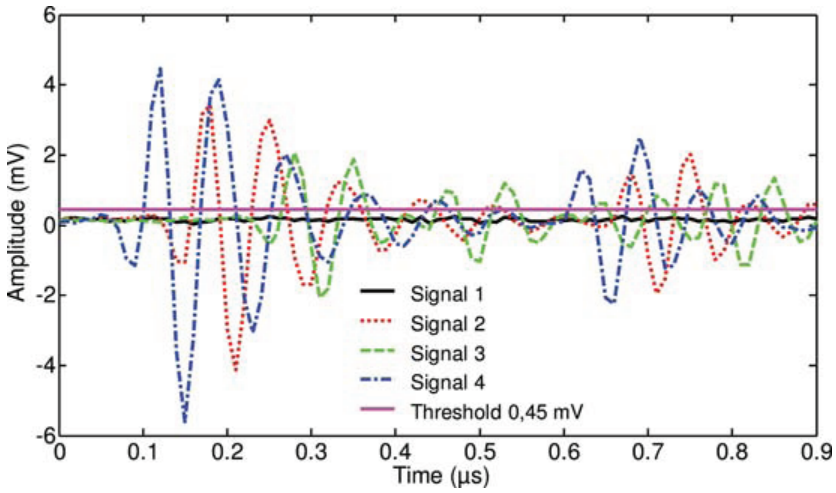

FIGURE 3 Sample Si-1: A-scan data from different areas.

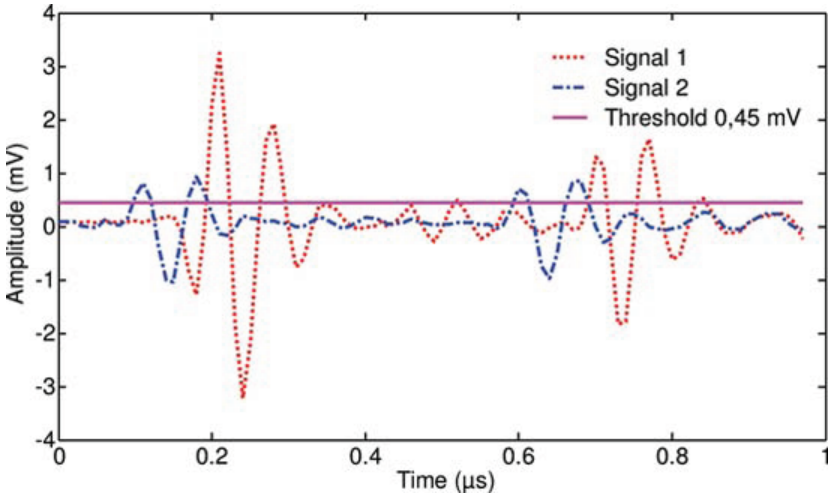

FIGURE 4 Sample CS-2: A-scan data from different areas.

A complete set of ultrasonic signals with both transmitted and reflected signals is obtained. The C-scan images (X, Z cartography) obtained in the transmission mode are the most informative for the discussion presented in Section 4. The displacement steps along both the X and Z axes for the C-scan are 0.2 mm, allowing the complete recovery of the focal width.

3. RESULTS AND DISCUSSION

3.1. Effect of the Surface Treatment on the Surface Energy of the Substrate

The contact angles and the calculated surface energies are reported in Table 2 for the as-received substrates as well as the silane-treated and sulfochromic-treated aluminum substrates. The surface energy of the as-received A2024 has been found to be equal to 50 mJ/m^2. This value is in agreement with the data published in the literature [23]. The surface energy of the GPS-silanized aluminum surface is similar to that of the as-received aluminum. Moreover, the polar and nonpolar contributions are the same. However, the surface is modified

TABLE 2 Surface Energy of the Substrates

		Contact angle θ (°)		Surface energy		
Samples	Surface treatment	Distilled water	CH_2I_2	Total surface energy (mJ/m^2)	Polar component (mJ/m^2)	Dispersive component (mJ/m^2)
Aluminum	AR	62 ± 7	43 ± 4	50 ± 5	12 ± 4	38 ± 2
Si	Silanization	63 ± 2	37 ± 1	51 ± 1	10 ± 1	41 ± 0
CS	Chromic–sulfuric	29 ± 6	28 ± 2	72 ± 2	27 ± 2	45 ± 1

because the protocol used in this work has proven to be effective in causing the condensation of silanol groups on the Al surface [24]. Finally, the sulfochromic treatment leads to a higher surface energy, equal to 72 mJ/m^2; this increase is mainly attributed to the increase of the polar component.

3.2. Adhesive Properties

Protocols for the two surface treatments and the preparation of the lap-shear specimens have been validated using preliminary tests. The optimization of the physical chemistry protocol has been achieved over 28 samples. The present study focuses on the samples (four samples from the silanization set (Si) and three samples from the chromic–sulfuric set (CS)) that have been tested with both ultrasonic C-scan and mechanical tests. The results from the mechanical measurements are summarized in Table 3 for the two adherend treatments, silanization and chromic–sulfuric etching. The best adhesive strength has been obtained for the chromic–sulfuric surface treatment. At the end of the test, joint failure has been observed. In all cases, the failure mode is adhesive, sometimes with one or more jumps of the fracture from one interface to the other or with some adhesive remaining on one of the aluminum substrates.

3.3. Ultrasonic Testing Results

Each adhesive joint sample tested using the transmission method produces a C-scan of the bonded area. Our first goal is to verify the quality of the joint. Indeed, before making a prediction regarding the adhesion strength, it is important to assess the joint homogeneity. C-scan images of the samples Si-1 and CS-2 are presented in Figs 5 and 6.

A first qualitative observation can be done as images textures are very different. For the sample Si-1 (Fig. 5), large homogeneous areas with little differences in amplitudes are observed. In these large areas, some localized defects are also present probably due to large gas entrapment as our bond is too liquid. Gas entrapment is a true difficulty for manufacturing adhesive joints and resulting voids should be taken into account for modes of failures [25]. The epoxy is degassed during 210 sec using UIP1000hd device (Hielscher, Teltow, Germany) [26]. For the CS-2 sample, the image texture, corresponding to ultrasonic amplitude distribution, is more heterogeneous

TABLE 3 Mechanical Results

Final sets	Surface treatment	Meanτ (MPa) / std (MPa)	Number of samples
Si	Silanization	9.2/0.7	4
CS	Chromic–sulfuric	12.6/0.7	3

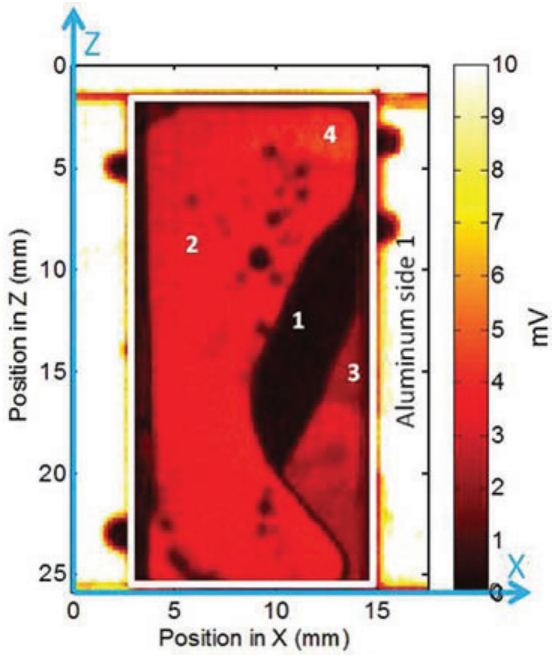

FIGURE 5 C-scan of sample Si-1 (amplitude in mV).

and the spatial scale of the distribution is lower. The texture aspect can be created by small voids distributed on all the joint surface. The adherend surface roughness contributes also to the texture aspect of C-scan images.

As the transmission method is used, if the joint is properly bonded, the received signal should have a high amplitude; in the opposite case, if there is a defect involving the presence of air, the amplitude of the signal should be very low. A-scan data have been recorded at various locations (X, Z) for each sample. The obtained results are presented in Figs3 and 4, which correspond to samples one of the silane set (Si-1) and the second of the chromic–sulfuric set (CS-2), respectively. The first echo corresponds to the direct travel of the ultrasound through the first aluminum plate, the joint and the second aluminum plate. The second echo corresponds to the same travel path plus a round trip into the aluminum.

All images have been obtained with the same transducer settings. In area 1 of sample Si-1, the amplitude is very low (dark blue), which allows us to define the amplitude threshold below which the joint is considered not bonded. The corresponding threshold is 0.45 mV; thus, we can calculate the size of the bonded area and the size of the disbonded one, if any. The C-scan analyses have been conducted with MATLAB. The surface size of the adhesive joint is first visually defined. This surface is represented in Figs5 and 6 by the bold rectangle. Next, the size of the bonded area is automatically calculated depending on the threshold value. Thus, for sample Si-1, the surface of the joint is 234.6 mm^2, the bonded area is found to be 211.3 mm^2, and the disbonded zone is 23.2 mm^2. For sample CS-2, the surface of the adhesive joint

is 273.7 mm^2, and there is no disbonded surface. Considering the geometry of the specimens (Fig. 1), the theoretical bonded area should be equal to 312.5 mm^2; however, the epoxy formulation used has a very low viscosity, and some leaks may occur in the joint. These leaks are the origin of the smaller-than-expected measured bonded area and of the observed defects.

3.4. Correlation Between Mechanical Tests and NDT

This section presents the correlation between the mechanical tests and the ultrasonic tests. To search for a link between the mechanical strength and the bonded surface area, a plot representing the bonded surface area as a function of the failure load is shown in Fig. 7. Two different populations are found; set CS has higher failure strengths and greater bonded surface areas than set Si. Not surprisingly, no simple linear relation exists between the bonded area and the mechanical strength [3]. It is known that in a single-lap shear test, the eccentricity of the tensile axis results in peel and transverse stresses. The stress distribution is highly nonuniform, so the strength is much more sensitive to the integrity of some areas of the joint than to others. Therefore, measurement of the bond area, without taking the localization of this bonded area into account, does not necessarily provide a linear correlation with the strength. Literature indicates that the presence of large defects may not modify the ultimate strength if there are localized in the middle of the joint. This behavior depends also of the ductility of the adherend [27].

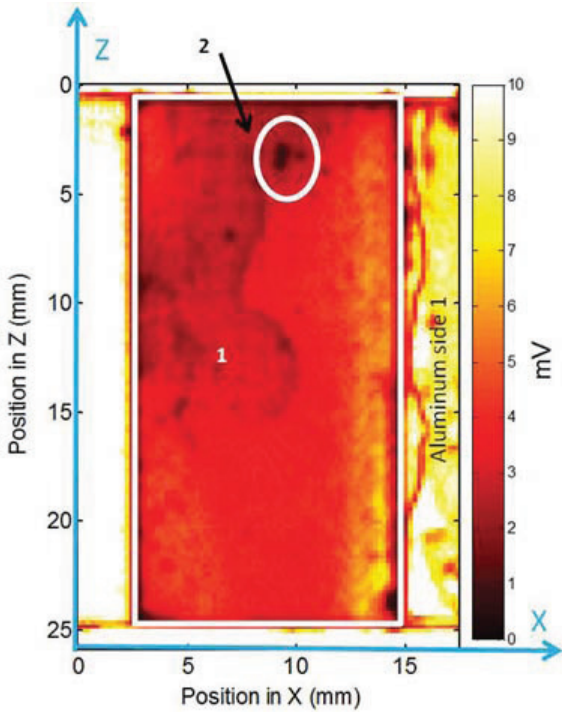

FIGURE 6 C-scan of sample CS-2 (amplitude in mV).

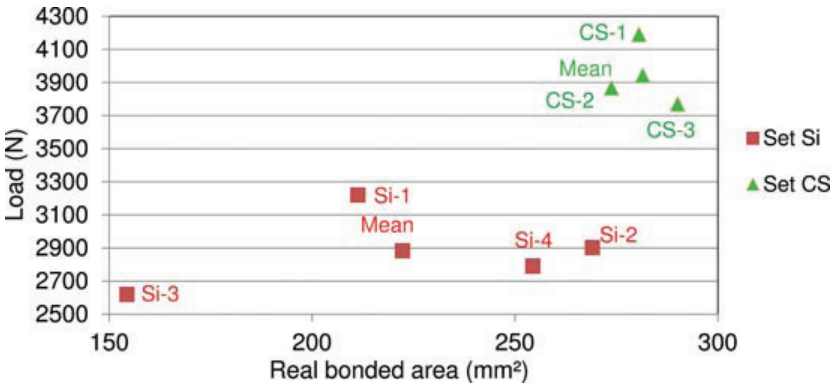

FIGURE 7 Bonded area versus load.

With the knowledge of the real bonded area, we can evaluate a more accurate joint adhesive strength using formula (1). Table 4 presents the corrected strengths. It reveals that the silane treatment may yield the same adhesion strength as the chromic–sulfuric acid treatment, as the average strengths are very similar. It also reveals that in this study, the silane treatment produces less reproducible results. Such information is not evident from only the results obtained with the mechanical tests (see Table 3). Using strength results, no significant difference arises between the two surface treatments. It is due to the presence of voids identified through the ultrasonic dataset. Moreover, additional interesting correlations between C-scan images and the fracture surface are described below.

The mechanical tests continue until failure of the samples. Therefore, at the end of these tests, the fracture surfaces can be optically observed (Figs 8 and 9). A strong similarity in shape can be observed between the visible features of the fracture surfaces and the ultrasonic C-scans. Traces of epoxy are indicated with the letter E on the fracture photographs (Figs 8 and 9), while apparent aluminum surfaces are indicated with Al. Various indications of likely failure modes are thus obtained:

- adhesive failure when the photographs give Al–E or E–Al indications
- cohesive failure when the photographs give E–E indications
- defect presence when the photographs give Al–Al indications

TABLE 4 Mechanical Results Corrected for the Bonded Area Measured with the UT Through-Transmission Method

Final sets	Surface treatment	Meanbonded area (mm^2)	Meanτ (MPa)/std (MPa)	Number of samples
Si	Silanization	222.3/51.5	13/3.1	4
CS	Chromic–sulfuric	281.5/8.20	14.0/1	3

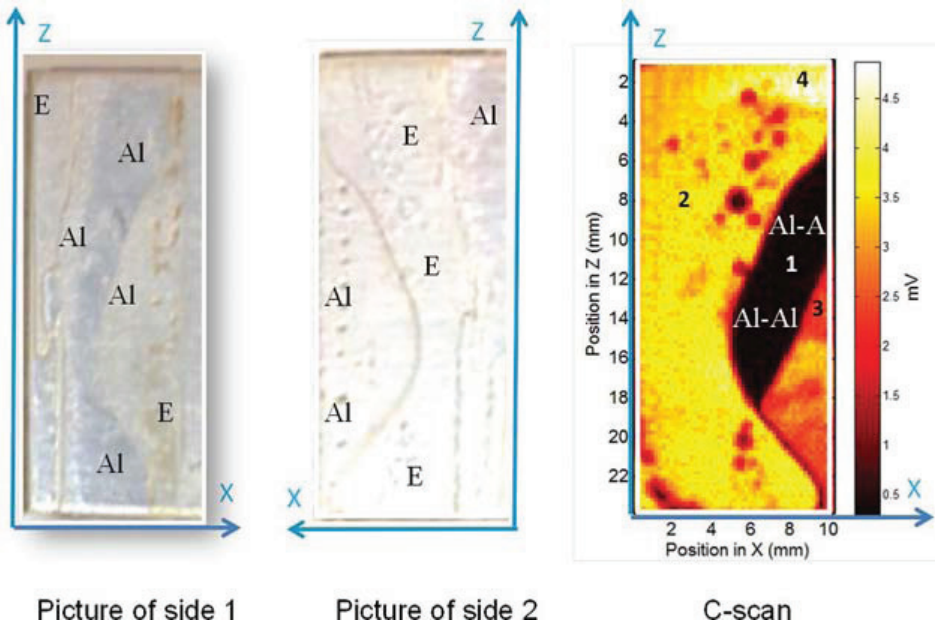

FIGURE 8 Sample Si-1: fracture surfaces and C-scan (amplitude in mV).

The adhesive failure mode is the most commonly observed in Figs 8 and 9. It is the expected failure mode, as the surface treatment is the variable parameter in this study. Also as expected, the cohesive failure mode is not observed. The third case, the presence of one or more defects, is apparent in zone 1 (defined in Fig. 5 above) of sample Si-1, which is consistent with

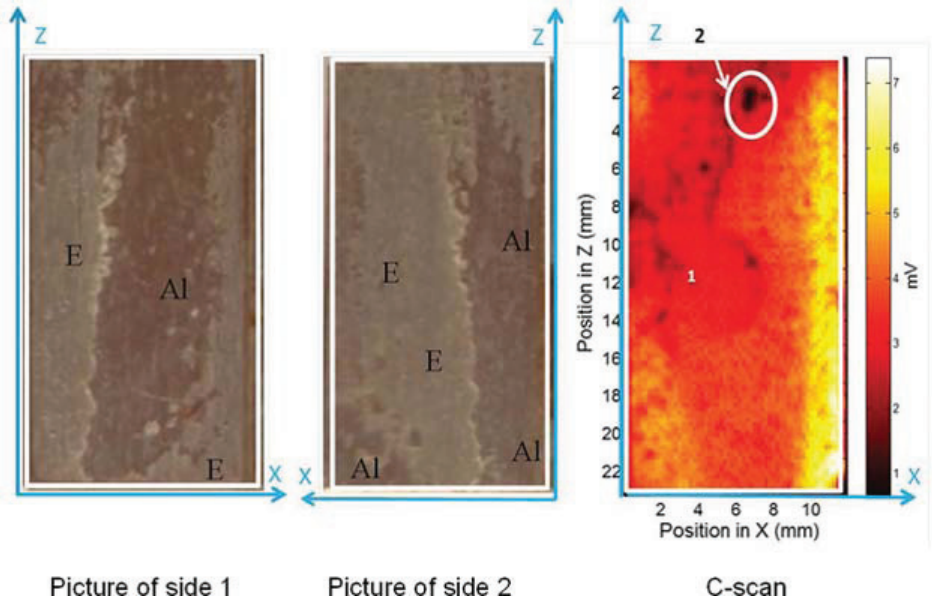

FIGURE 9 Sample CS-2: fracture surfaces and C-scan (amplitude in mV).

our analysis of signal 1: there is no ultrasound transmission. This case is not expected and is attributed to an excessively fluid epoxy adhesive.

The position of the defect in zone 1, where there is no stress concentration, could explain why this sample demonstrates a similar strength to the other samples during the shear test despite the presence of a large defect.

The pictures of the fracture surfaces and the C-scans corresponding to samples Si-1 and CS-2 are presented in Figs 8 and 9. The bonded area is more homogeneous for sample CS-2. The small, circular, weakly adhesive areas that are visible on the C-scans (darker areas of the image) are also apparent on the fracture surfaces.

4. CONCLUSION

This study shows how the combination of mechanical and ultrasonic NDT methods can provide additional information in the view of a better understanding of adhesion strength. For the material aspect of this challenge, the use of different surface treatment is the preferred solution. Using a high-frequency C-scan, it is possible to obtain a corrected value for the bonded surface area, allowing the proper evaluation of the adhesive strength. It is also shown that these ultrasonic images exhibit a notably good correlation with the fracture surfaces obtained after failure.

Efforts in progress aim at improving the C-scan method using higher frequencies as well as the epoxy adhesive which will be more viscous. It should allow separating echoes in ultrasonic data, increasing the information available such as speed of sound and attenuation. A complementary approach using C-scan images associated with a detailed analysis of the stress concentrations would greatly help multidisciplinary studies concerning adhesion strength.

ACKNOWLEDGMENTS

The authors wish to thank Erwin Taviot (Aix-Marseille Université) for his contribution to the ultrasonic experiments, and Professor R. Adams for useful discussions and comments about this study. The collaboration with *Aircelle and Safran Composites* is gratefully acknowledged.

FUNDING

This work was supported under the PRC Composites, French research project funded by DGAC, involving SAFRAN Group, ONERA, and CNRS.

REFERENCES

[1] Adams, R. D., *Adhesive bonding: Science, technology and applications* (Wood head Publishing Ltd., University of Bristol, UK, 2005).
[2] da Silva, L. F. M., and Öchsner, A., *Modeling of Adhesively Bonded Joints*, (Springer-Verlag, Berlin, 2008).
[3] Guyott, C. C. H., Cawley, P., and Adams, R. D., *J. Adhes.* **20**, 129–189 (1986).
[4] Michaloudaki, M., Lehmann, E., and Kosteas, D., *J. Adhes. Adhes.* **25**, 257–267 (2005).
[5] Adams, R., and Drinkwater, B., *J. Mater. Prod. Technol.* **14**, 385–398 (1999).
[6] Nagy, P. B., *J. Adhes. Sci. Technol.*, **5**, 619–630 (1991).
[7] Brotherhood, C. J., and Drinkwater, B. W., Dixon, S., *Ultrasonics* **41**, 521–529 (2003).
[8] Bockenheimer, C., Fata, D., Possart, W., Rothenfusser, M., Netzelmann, U., and Schaefer, H., *Int. J. Adhes. Adhes.* **22**, 227–233 (2002).
[9] Yan, D., Drinkwater, B. W., and Neild, S. A., *NDT E Int.* **42**, 459–466 (2009).
[10] Santos, M. J., Pardigao, J., and Faia, P., *J. Adhes.* **84**, 421–438 (2008).
[11] Le Crom, B., and Castaings, M., *J. Acoust. Soci. Am.* **127**, 2220–2230 (2010).
[12] Vijaya Kumar, R. L., Bhat, M. R., Murth, C. R. L., *Int. J. Adhes. Adhes.* **42**, 60–68 (2013).
[13] Smith, N. R., Kollgaard, J. R., and Dickinson, L., *SAMPE J.* **47**, 25–31 (2011).
[14] Vijaya Kumar, R. L., Bhat, M. R., Murthy, C. R. L., *Ultrasonics* **53**, 1150–1162 (2013).
[15] Challis, R. E., Holmes, A. K., Tebbutt, J. S., and Cocker, R. P., *J. Acoust. Soc. Am.* **103**, 1413–1420 (1998).
[16] May, M., Wang, H. M., Akid, R., *Int. J. Adhes. Adhes.* **30**, 505–512 (2010).
[17] da Silva, L. F. M., Carbas, R. J. C., Critchlow, G. W., Figueiredo, M. A. V., and Brown, K., *Int. J. Adhes. Adhes.* **29**, 621–632 (2009).
[18] Baldan, A., *J. Mater. Sci.* **39**, 1–49 (2004).
[19] Jastrzebski, M. U., Sinclair, A. N., Raizenne, D. D., and Spelt, J. K., *Int. J. Adhes. Adhes.* **29**, 372–379 (2009).
[20] Cognard, J. Y., Créac' Hcadec, R., and Maurice, J., *Int. J. Adhes. Adhes.*, **31**, 715–724 (2011).
[21] Abel, M. L., Allington, R. D., Digby, R. P., Porritt, N., Shaw, S. J., and Watts, J. F., *Int. J. Adhes. Adhes.* **26**, 2–15 (2006).
[22] Owens, D. K., and Wendt, R. C., *J. Appl. Polym. Sci.* **13**, 1741–1747 (1969).
[23] Harris, A. F., and Beevers, A., *Int. J. Adhes. Adhes.* **19**, 445–452 (1999).
[24] Kahramana, R., Sunar, M., and Yilbas, B., *J. Mater. Process. Technol.* **205**, 183–189 (2008).
[25] da Silva, L. F. M., Adams, R. D., Gibbs, M., *Int. J. Adhes. Adhes.* **24**, 69–83 (2004).
[26] Kapustina, O. A., *Physical principles of ultrasonic technology* (LD. Rosenberg, Plenum Press, New York, 1973).
[27] Karachalios, E. F., Adams, R. D., da Silva, L. F. M., *Int. J. Adhes. Adhes.* **45**, 69–76 (2013).

Applying diffuse ultrasound under dynamic loading to improve closed crack characterization in concrete

C. Payan,[a] A. Quiviger,[b] V. Garnier, and J. F. Chaix
Aix Marseille Université, Laboratory of Mechanics and Acoustics, LMA CNRS UPR 7051, 31 chemin Joseph-Aiguier 13402 Marseille CEDEX 20, France
cedric.payan@univ-amu.fr, audrey.quiviger@univ-amu.fr, vincent.garnier@univ-amu.fr, jean-francois.chaix@univ-amu.fr

J. Salin
EDF R&D STEP, 6 quaiWatier, BP 49, 78401 Chatou, France
jean.salin@edf.fr

Abstract: Recent studies show the ability of diffuse ultrasound to characterize surface breaking cracks in concrete. However, derived parameters are sensitive to the presence of partially opened zones along the crack whose pattern may differ from one sample to another. The aim of this letter is to study the variation of diffuse ultrasound parameters while the sample is driven by a low frequency bending load which alternatively opens and closes the crack, allowing to access supplementary information about its morphology. The results show the sensitivity of the method for various crack depths and highlight its potential for concrete nondestructive evaluation.

PACS numbers: 43.20.Fn, 43.25.Lj [OG]
Date Received: May 17, 2013 **Date Accepted:** July 1, 2013

1. Introduction

Concrete is a highly complex material influenced by its environment during its life. In Civil Engineering structures, the multi-scale nature of concrete damage ranges from the structure scale (∼m: large cracks) to the microscopic scale (∼nm: chemical reactions). This paper focuses on the detection and characterization of surface breaking cracks present in the first centimeters of concrete, i.e., the concrete cover. This layer of concrete protects the rebar from environmental aggression (CO_2, water, chemical agents…) which can lead to a corrosion of the latter. Consequently, the early detection of cracks in concrete structures is challenging, especially in nuclear energy structures, for which the cost of repairs increases exponentially in time.[1]

Several nondestructive methods are employed for probing concrete mechanical properties, but the only one directly related with the elastic properties is ultrasound. The use of elastic waves for crack characterization is standardized.[2] However, its requirements, based on low frequency wave (below 100 kHz) time of flight measurements, can only detect a large opened crack. To decrease the detection threshold, the use of higher frequencies would be welcomed but, in this frequency range, wavelengths are on the order scale of the aggregates size which implies a strong multiple scattering phenomena making it impossible to use standard signal processing. The basic idea is to take advantage of the information carried into the coda (term used in seismology to describe the late arrivals of seismic waves on seismograms after an earthquake) of

[a]Author to whom correspondence should be addressed.
[b]Also at: EDF R&D STEP, 6 quaiWatier, BP 49, 78401 Chatou, France.

these signals to improve macro crack characterization. Recent studies highlight the potential of using coda waves for various topics related to concrete evaluation. Most of them are related with Coda Wave Interferometry, a method developed by Snieder *et al.*[3] to measure small changes in the earth crust. Payan *et al.*[4] evaluate the third order elastic constants of concrete and Zhang *et al.*[5] improve the method by taking into account the influence of temperature changes during experiments. In the multiple scattering regimes, the ultrasonic energy propagated in concrete follows a diffusion equation[6] driven by two parameters: the diffusivity D, and the dissipation σ. The diffusivity (unit $m^2\ s^{-1}$) is related to the composition. It depends on the density of the aggregates, their geometry, and their average spacing. The dissipation (unit s^{-1}) is an indicator of the viscoelastic properties of the medium, which in the case of concrete are mainly related to the cement paste.

The study of diffuse ultrasound in the presence of cracks in concrete is reported in the literature. Ramamoorthy *et al.*[7] study the influence of the depth of notches (simulated cracks with no contact between its lips) on diffuse ultrasound. Jacobs *et al.*[8] show the ability to follow self-healing of artificially opened surface breaking cracks. Quiviger *et al.* show both experimentally[9] and numerically[10] the feasibility of using diffuse ultrasound for real macro cracks characterization. These studies show the sensitivity of diffuse ultrasound to the presence of opened zone either for notches or opened cracks. This is also the case for closed cracks which exhibit partially opened zone along its lips.[9,10]

The aim of this paper is to acquire information about the closed part of the crack. Within that goal, the superimposition of a low frequency dynamical loading to diffuse ultrasound is proposed. It thus allows probing of the crack at various tension and compression states. The idea of probing the material during a dynamic loading (namely, Dynamic Acouto Elastic Testing) was developed by Renaud *et al.*[11] It was applied to the measurement of nonlinear elastic and dissipative constants of materials. The main interest of this method is its ability to probe the nonlinearity of a material at several load level. It allows some interesting nonlinear signatures to be identified.[11,12] The following sections present the samples and performed experiments. The results are exposed and discussed regarding the nature of the crack and its dynamical behavior.

2. Experiments

The samples studied here are those employed by Quiviger *et al.*[9] Four samples (15 cm $\times$ 15 cm $\times$ 60 cm) containing real closed cracks at various depth (0, 1, 3, and 5.5 cm) are available. These real cracks were designed by the use of a three point bending load and initiated by a 1 cm depth and 3 mm width notch at the sample center

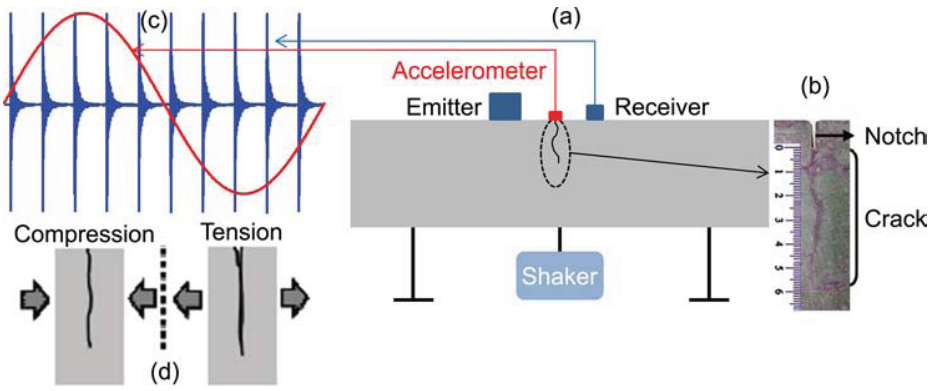

Fig. 1. (Color online) (a) Experimental scheme. (b) Zoom on the 5.5 cm crack. (c) Schematic of recorded signals which does not match real signals. It is shown for explaining the method. (d) Behavior of the crack during dynamic bending.

[Figs. 1(a) and 1(b)]. The load was released when the desired crack depth was reached. It is important to notice that the resulting cracks are completely closed and not visible by naked eye. The crack visible Fig. 1(b) was revealed by liquid penetrant inspection.

Diffuse ultrasound is scrupulously measured with the protocol described by Quiviger *et al.*[9] Ultrasound transducers are placed in contact with the upper surface of the sample, on both sides of the crack as shown in Fig. 1(a) with a constant 60 mm separation between them. The transmitter (Panametrics V101, diameter 25.4 mm) has a central frequency of 500 kHz and is driven by a pulsed source. The receiver is a small diameter (4 mm), broad-band transducer centered at 500 kHz. The only change is the superimposition of the low frequency generated by the shaker, recorded by the accelerometer [Figs. 1(a) and 1(c)]. Note that the shaker is driven at constant force (30 N) for each sample. The sequence of pulses sent to the emitter is designed with the maximal repetition rate and making sure that the received high frequency signal does not overlap with the following. The low frequency (LF) is set so as to be uncorrelated from the pulses repetition rate (100 Hz) and as low as possible to be able to reasonably assume the LF amplitude to be constant over the propagating time. Additionally, the efficiency of the shaker at low frequency is taken into account, resulting in a LF frequency of 137 Hz. This forced bending load allows the crack to be alternatively in tension and in compression while diffuse ultrasound probes the crack as shown [Fig. 1(d)].

The total recorded signal length is 1 s, with a sampling frequency of 20 MHz, averaged 500 times to increase signal to noise ratio. Each high frequency is isolated as shown in Fig. 2. It is made possible because the trigger of the high frequency is also recorded but not shown for clarity. The Arrival Time of the Maximum Energy (ATME) is evaluated by fitting the energy curve [Fig. 2(b)] with the 2D solution of the diffusion equation:[9]

$$\log \langle E(r,t,f\rangle \ = C_0 - \log(Dt) - \frac{r^2}{4Dt} - \sigma t, \tag{1}$$

where E is the energy if the considered frequency band, r is the distance between transducers, C_0 is a constant depending on the energy injected by the source. The energy envelope is determined by time-frequency analysis. Diffusion parameters are then evaluated by fitting the 2D solution from the received signals with a time window of 50 μs and a frequency window of 80 kHz. Each time window have a 90% overlap with the preceding window. The ATME is derived in frequency band for which a maximum

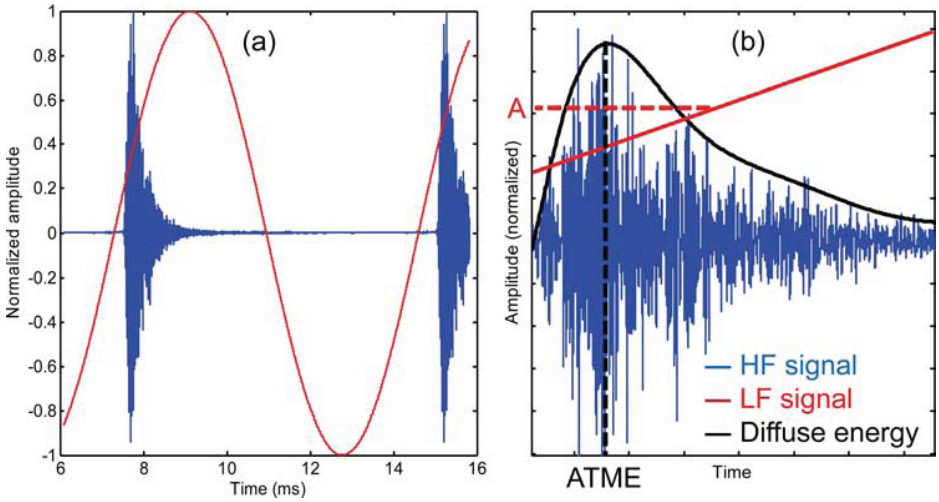

Fig. 2. (Color online) (a) Experimental HF and LF signals. (b) ATME and LF amplitude evaluation.

quantity of energy is transmitted [240–320 kHz]. For further details about fitting procedure and signal processing, the reader is invited to refer to Quiviger *et al.*[9] Each ATME is then related with the low frequency amplitude [noted A in Fig. 2(b)] as the average amplitude during the diffusion process. The acceleration amplitude is converted to displacement u in steady state conditions by $u = -\ddot{u} / (4\pi^2 f^2)$, where f is the LF frequency. The only evaluated parameter is ATME due to the fact that it is known to be the more sensitive and the more robust one to probe cracks.[9]

3. Results and discussion

The evolution of ATME as a function of the dynamic displacement is shown Fig. 3. Several observations arise from that curves. Hysteresis is present in each case, even in the sample with no crack [Fig. 3(a)]. As a reminder, this sample, like other ones, has a 1 cm notch. One can notice that the 3 cm cracked [Fig. 3(c)] sample does not exhibit as much hysteresis as the other ones and that the 5.5 cm cracked sample exhibits a particular behavior. The slope increases with crack depth except for the 5.5 cm cracked sample for which the slope does not really relate the dynamics. The maximal excursion of ATME during a complete cycle regularly increases with crack depth.

The dynamical behavior of the crack is complex and, to our knowledge, no former study deals with this topic. ATME is shown to decrease when the contact density along the crack increases.[9,10] Present data are in agreement with that statement. When the crack is under tension, the contact density decreases, leading to an increase of the ATME [Figs. 3(b)–3(d)]. The evolution of the ATME for the uncracked sample [Fig. 3(a)] can be explained by the intrinsic nonlinearity of concrete. It is important to notice that this nonlinearity is not due to the presence of the notch which is known to be a linear type defect, i.e., detected by linear diffusion techniques.[7,9]

The residual uncracked depth decreases with increasing crack depth. Thus, as the shaker is driven at constant force, the maximum displacement increases with crack depth.

The presence of hysteresis may be due to the viscoelastic nature of cement as well as the hysteretic opened/closed behavior of the crack. A real crack in concrete exhibits some partial contacts all along its lips.[10] It is reasonable to assume that these contact zones are hysteretic during dynamical loading. However, the low hysteretic behavior of the 3 cm crack [Fig. 3(c)] is probably due to a particular crack morphology which makes the open state occurring at the same stress than the closed state.

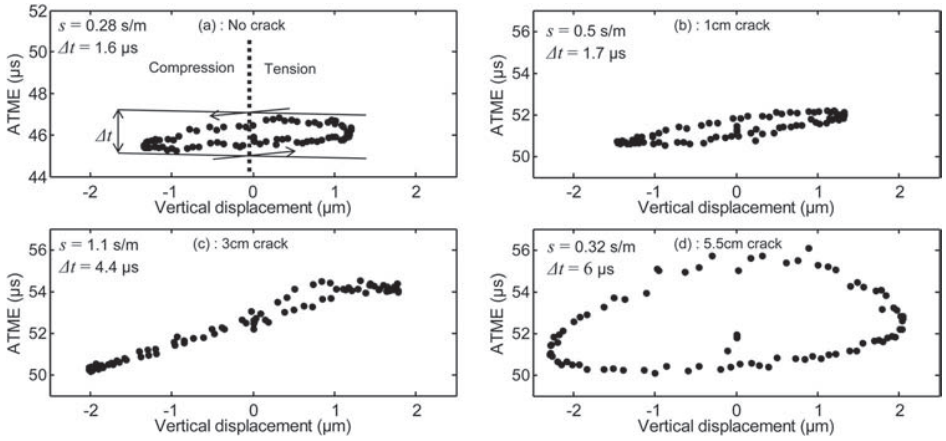

Fig. 3. ATME as a function of the dynamical vertical displacement recorded by the accelerometer. Both vertical and horizontal scales are kept constant for comparison purpose. (a) Uncracked sample. The arrows indicate the displacement way which is the same for others plots. The dotted line is the linear fitting of the data with a slope s and Δt the maximal ATME excursion during a cycle. Sample with, (b) a 1 cm crack, (c) 3 cm crack, and (d) 5.5 cm crack.

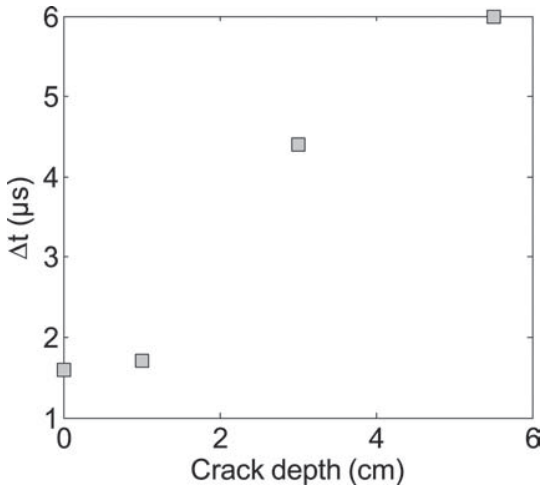

Fig. 4. Evolution of the maximum ATME excursion during a cycle (Δt) as a function of crack depth.

The postulate is done that the complex signature of the 5.5 cm crack [Fig. 3(d)] is due to its large opening during oscillations which can lead to a redistribution of contacts location. Starting from 0 to positive displacements Fig. 3(d), ATME increases with a similar trend than the 3 cm crack [Fig. 3(c)]. Because of the size of the crack compared with sample width (~half the width), when the shaker starts coming down, contact zones can be rearranged into another state while the crack remains in tension. As soon as the compression stage starts, the crack morphology comes back to its original state.

The maximum ATME excursion over a full cycle (Δt) increases with crack depth (Fig. 4). Previous studies[7,9] report an ATME variation of the order of 15 μs for 5 cm notches. Unlike notches, real closed cracks exhibit a distribution of contact along its depth, thus it is not surprising that the present Δt remains inferior to 10 μs. The correlation between Δt and crack depth may indicate that the whole crack is affected by the low frequency, even if it is not entirely opened or closed. From a qualitative point of view, one can notice the large sensitivity of Δt to the depth of the crack with a maximum variation of about 500%. Quiviger *et al.*[10] numerically show that even a single, 1 mm size, contact can lead to a few microseconds ATME variation in the present samples. At the same time, the contact density makes the ATME varying in the same range.[10] Thus present variations and complex signatures are mostly due to a combination of these effects.

As the ATME depends on elastic diffusivity, it also depends on elastic properties of concrete.[6] It is worth noticing that concrete is a nonlinear medium,[13] meaning that its elastic behavior depends on the low frequency amplitude in experiments. The nonlinearity measured for the uncracked sample relates the "intrinsic" nonlinearity of present samples under dynamic loading. This quantity could be de-correlated from cracked samples but the physics of nonlinear phenomena under dynamic conditions in concrete is complex and not yet fully understood. For a comparison purpose, a previous study carried out on the same samples[14] shown that the measured nonlinearity, using nonlinear interaction, exhibits a similar sensitivity than the modulated ATME.

4. Conclusion

The present letter shows the feasibility of applying diffuse ultrasound under low frequency loading to probe a real closed crack in concrete. The derived parameters exhibit a large sensitivity to crack depth (~500%). The main advantage of the method is the opportunity to get a signature of the crack depending on its morphology. As for

DAE experiments, even if interesting, this kind of data are directly related to the physics but its analysis remains complex.[11,12] Answers should arise from the knowledge of the crack morphology and its behavior under loading. Future works will be aimed at imaging a real closed crack in concrete by X ray micro-tomography. In addition to these data, numerical simulation of diffuse ultrasound[10] should provide the means to quantitatively relate the crack morphology to the measurements.

Acknowledgments

Authors wish to thank Electricité de France (EDF) for funding this research. The Laboratory of Materials and Durability of Constructions (LMDC) is also acknowledged for manufacturing the samples.

References and links

[1]P. Stephan and J. Salin, "Ageing management of concrete structure: Assessment of EDF methodology in comparison with SHM and AIEA guides," Con. Build. Mat. **37**, 924–933 (2012).
[2]ISO 1920-7:2004, *Testing of concrete, Part 7: Non-destructive tests on hardened concrete* (International Organization for Standardization, Geneva, Switzerland, 2004).
[3]R. Snieder, A. Grêt, H. Douma, and J. Scales, "Coda wave interferometry for estimating nonlinear behavior in seismic velocity," Science **295**, 2253–2255 (2002).
[4]C. Payan, V. Garnier, J. Moysan, and P. A. Johnson, "Determination of third order elastic constants in a complex solid applying coda wave interferometry," Appl. Phys. Lett. **94**, 011904 (2009).
[5]Y. Zhang, O. Abraham, V. Tournat, A. Le Duff, B. Lascoup, A. Loukili, F. Grondin, and O. Durand, "Validation of a thermal bias control technique for Coda Wave Interferometry (CWI)," Ultrasonics **53**(3), 658–664 (2013).
[6]P. Anugonda, J. Wiehn, and J. Turner, "Diffusion of ultrasound in concrete," Ultrasonics **39**(6), 429–435 (2001).
[7]S. K. Ramamoorthy, Y. Kane, and J. A. Turner, "Ultrasound diffusion for crack depth determination in concrete," J. Acoust. Soc. Am. **115**(2), 523–529 (2004).
[8]C.-W. In, R. Brett Holland, J.-Y. Kim, K. E. Kurtis, L. F. Kahn, L. J. Jacobs, "Monitoring and evaluation of self-healing in concrete using diffuse ultrasound," NDT E Int. **57**, 36–44 (2013).
[9]A. Quiviger, C. Payan, J.-F. Chaix, V. Garnier, and J. Salin, "Effect of the presence and size of a real macro-crack on diffuse ultrasound in concrete," NDT E Int. **45**(1), 128–132 (2012).
[10]A. Quiviger, A. Girard, C. Payan, J. F. Chaix, V. Garnier, and J. Salin, "Macro-crack characterization in concrete by diffuse ultrasound under low frequency dynamic loading," POMA **16**, 045016 (2012).
[11]G. Renaud, P.-Y. Le Bas, and P. A. Johnson, "Dynamic measures of elastic nonlinear (anelastic) behavior: Dynamic acousto-elasticity testing (DAET)," J. Geophys. Res. **117**, B06202, doi:10.1029/2011JB009127 (2012).
[12]C. La Rocca, C. Payan, and J. Moysan, "Evaluation of epoxy bonded joint quality using nonlinear acoustics," Proc. Meet. Acoust. **10**, 045001 (2010).
[13]C. Payan, T. J. Ulrich, P. Y. Le Bas, T. A. Saleh, and M. Guimaraes, "Probing materials damage at various depths by use of Time Reversal Elastic Nonlinearity Diagnostic: Application to concrete," POMA **16**, 045013 (2012).
[14]J.-P. Zardan, C. Payan, V. Garnier, and J. Salin, "Effect of the presence and size of a localized nonlinear source in concrete," J. Acoust. Soc. Am. **128**(1), EL38–EL42 (2010).

NDT&E International 60 (2013) 11–16

Contents lists available at ScienceDirect

NDT&E International

journal homepage: www.elsevier.com/locate/ndteint

Influence of the depth and morphology of real cracks on diffuse ultrasound in concrete: A simulation study

A. Quiviger [a,b], A. Girard [b], C. Payan [a,*], J.F. Chaix [a], V. Garnier [a], J. Salin [b]

[a] Aix Marseille Université, LMA CNRS UPR 7051, LCND IUT Aix en Provence, 13100 Aix en Provence, France
[b] EDF-R&D-STEP, 6 Quai Watier, BP 49, 78401 Chatou, France

ARTICLE INFO

Article history:
Received 24 April 2013
Received in revised form
2 July 2013
Accepted 9 July 2013
Available online 16 July 2013

Keywords:
Diffuse ultrasound
Numerical simulation
Crack
Concrete

ABSTRACT

The aim of the present paper is to simulate the propagation of diffuse ultrasonic energy in concrete in the presence of a real crack. The numerical model is presented and validated by the comparison with experimental data from the literature. Unlike most of the studies which consider a crack as a notch, a realistic crack morphology exhibits partial contacts along its lips. These contacts are modeled in order to study their influence on the diffusion parameters. The feasibility of determining the contact density of the crack is shown, revealing practice implications for non-destructive crack sizing and imaging in concrete.

1. Introduction

Cracking is critical for the structural integrity of civil engineering structures, as a consequence of the risks of mechanical failure and loss of impermeability which it can produce. In particular, the latter effect is induced by cracking of the concrete cover located between the surface and the first layer of rebar. This leads to the penetration of aggressive agents into the core of the structure, thus promoting corrosion of the rebar, leading to a degradation of the mechanical properties of the structure. The detection and characterization of such cracks is thus necessary, to allow the remaining lifetime of the structure to be predicted and its maintenance to be optimized.

Several difficulties are encountered in the use of acoustic techniques for the characterization of concrete in an industrial context. ISO and ASTM standards [1,2] state that ultrasound frequencies in the range between 20 kHz and 150 kHz should be used. The wavelength is thus greater than 3 cm, which does not allow real cracks to be detected efficiently before reaching the rebar located at few centimeter depth. When the frequency is increased, ultrasound measurements become more complex, in particular due to multiple scattering, resulting from the presence of aggregates similar in size to the ultrasound wavelength [3,4]. Various authors [5–7] have studied the ultrasonic characterization of cracks in concrete. They revealed a change in the waves' time of flight in the presence of a crack with controlled dimensions: a notch, whose walls have no contact points. Analogous results were observed with cracks produced by bending loads [8]. However, these cracks were opened artificially by applying a bending force to the test specimens, thus placing limitations on the accuracy with which they can represent real cracks.

A second approach [9], based on the analysis of diffuse ultrasound, was also studied for the purposes of concrete characterization. It shows that the complex propagation of multiple scattered waves in concrete can be simplified into a standard diffusion law. It is founded on the analysis of the ultrasonic energy diffusion by two parameters: the diffusivity D (with dimensions $[m]^2[s]^{-1}$), characteristic of the material's structure, and the dissipation σ (with dimensions $[s]^{-1}$), which reflects the medium's viscoelastic properties. Anugonda et al. [9] demonstrated the validity of this approach for concrete, both analytically and experimentally. They thus opened up numerous possibilities for the non-destructive characterization of microstructural damage in concrete. Becker et al. [10] thus studied the variation of diffusion parameters as a function of the aggregate diameters, whereas Punurai et al. [11] determined such variations in cement as a function of the quantity of occluded air. Deroo et al. [12] studied the influence of alkali silicate reaction on the diffusion parameters. Diffuse ultrasound was also analyzed in order to characterize cracks in concrete by Ramamoorthy et al. [13]. They showed that the diffusion parameters vary as a function of the length of a notch in concrete. Authors introduced another parameter: the arrival time of maximum energy (ATME). Quiviger et al. [14] confirmed the ability of ATME to characterize the opened portion of a real

* Corresponding author. Tel.: +33 442939055.
E-mail address: cedric.payan@univ-amu.fr (C. Payan).

0963-8695/$ - see front matter © 2013 Elsevier Ltd. All rights reserved.
http://dx.doi.org/10.1016/j.ndteint.2013.07.003

crack. According to the same authors, the ATME also varies as a function of the length of the closed portion of the crack. The presence of partial contacts along the length of the crack is assumed to be the cause of the observed variations.

The aim of the present study is to verify the influence of real crack morphology on the measured diffusion parameters. The morphology of a real crack in concrete and the numerical model are presented. This model is validated by the comparison with experimental data from concrete samples containing controlled notches. A real crack is then introduced by the study of the influence of partial contacts on diffuse ultrasound. Then, the numerical model is applied to the case of real cracks in concrete and compared to experimental data from the literature [14].

2. Crack morphology

The morphology of a crack, which is open at the concrete surface, has been described in [14]. The crack comprises two portions: the first is the open portion, located at the surface at the outer end of the crack. The second, in which the two walls are partially or totally in contact, is considered to be closed. The particularity of a real closed crack lies in the number and nature of the contact points or areas present between the walls. These modify the mechanical behavior of the crack, in particular as a result of local stress redistribution.

Turatsinze et al. [15] revealed a disparity in the profile of a crack produced by bending, similarly to the test specimens shown in Fig. 1(a) and (b) used in the present study. The crack exhibits a variable morphology, depending on its depth in the sample. These authors revealed the presence of discontinuities in the profile of the crack, lying in the median plane [Fig. 1(c) and (d)]. This is not a simple crack, but it can be represented in this zone by an interfacial crack with contact zones and interlocking effects.

Diffuse ultrasound in a concrete sample was numerically modeled by Ramamoorthy et al. [13] who studied the influence of a numerical notch on ATME. Seher et al. [16] numerically modeled diffusion in the presence of partially closed cracks. However, this study was performed using a commercial heat transfer software, thus the dissipation was taken into account by a post processing procedure (exponential decay). In the following, the numerical model including dissipation is presented and a realistic numerical crack is introduced.

3. Numerical simulation

3.1. The model

The computer code developed in the present study is based on a 2D finite difference method. This method is chosen mainly as a result of the simple geometry of the problem, the functional regularity of the energy, and the uniform diffusion which can be achieved inside the material. The results given by the numerical simulations are then compared with the experiments carried out by Quiviger et al. [14], with the decision to use a 2D model motivated by the symmetry of the test specimens used in the latter study, as well as by the resulting gain in computing time. The code is developed using Matlab®.

The concrete in which diffuse ultrasound propagates has fixed dissipation and diffusivity values. The size, the position of the sensors and the boundary conditions of the model are also fixed, to ensure that they match the experimental conditions. A rectangular mesh, with a horizontal resolution of 2 mm and a vertical resolution of 1 mm is used. It results from a compromise between maximum resolution along the axis of the crack, and lower resolution along the axis perpendicular to the crack, thus allowing the computing time to be optimized.

Diffuse energy is initiated by the experimentally determined energy spectrum of the 500 kHz sensor used in [14]. Ultrasonic energy diffusion is simulated by directly applying the general diffusion equation (Eq. (1)), using the energy emitted by the source (x_{exc},y_{exc}), expressed in the form of a Dirichlet condition (Eq. (2)).

$$\frac{\partial}{\partial t}\langle E(x,y,t)\rangle + \sigma\langle E(x,y,t)\rangle = D\Delta\langle E(x,y,t)\rangle, \tag{1}$$

$$\langle E(x_{exc},y_{exc},t)\rangle = E_0(t), \tag{2}$$

Using $E_{i,j}^{(n)}$ to note the energy at point $(x_i,y_i)=(i\Delta x+x_0,\ j\Delta y+y_0)$, and at instant $n\Delta t$, the resolution scheme can be written in an explicit temporal form

$$\frac{E_{i,j}^{(n+1)}-E_{i,j}^{(n)}}{\Delta t} = -\sigma E_{i,j}^{(n)} + D\frac{E_{i-1,j}^{(n)}-2E_{i,j}^{(n)}+E_{i+1,j}^{(n)}}{\Delta x^2} + D\frac{E_{i,j-1}^{(n)}-2E_{i,j}^{(n)}+E_{i,j+1}^{(n)}}{\Delta y^2}, \tag{3}$$

This explicit form implies that the Courant-Friedrich-Lévy (CFL) condition is respected, i.e. that the temporal interval remains

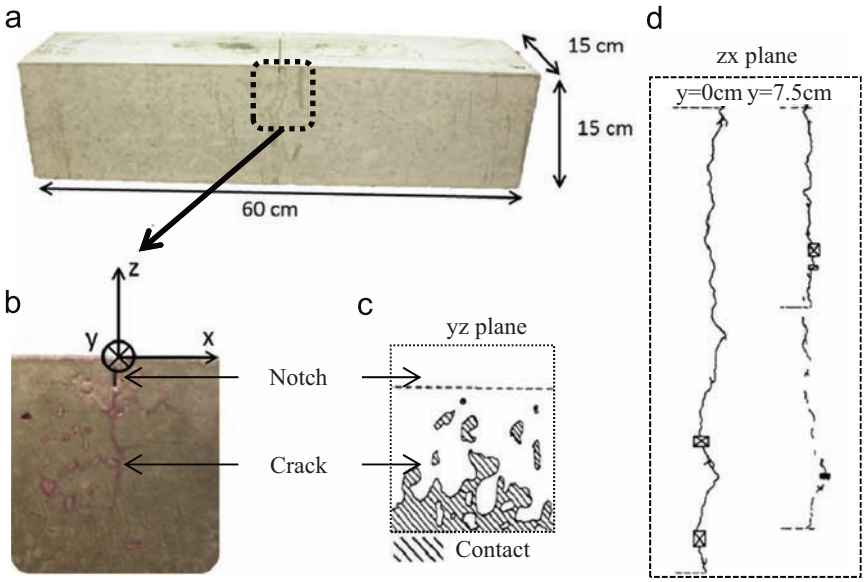

Fig. 1. Map of a real crack in concrete: (a) concrete samples used in the present study, (b) zoom on the crack region revealed by dye penetrant inspection at the surface (present study), (c) crack observation from [15] in a longitudinal plane at $y=0$ (surface) and $y=7.5$ cm (center), and (d) transverse observation at $x=0$ from [15].

below a certain maximum value, which depends on the spatial interval, such that the information supplied by a given point is correctly transmitted to the adjacent ones. In the case of the present equation, the CFL condition is given by

$$\Delta t \leq \frac{\min(\Delta x^2, \Delta y^2)}{D} \tag{4}$$

In the following simulations, this leads to the requirement: $\Delta t < 1.7 \times 10^{-7}$ s, which is of a similar order to the value of Δt needed to account for the highest signal frequency. It is of the order of 700 kHz, thus, in this simulation the CFL does not lead to any limitation.

In order to optimize the computation time, only a 10×30 cm portion of the concrete surrounding the crack (Fig. 2) is modeled. The boundary conditions of the model are chosen as: no energy at the concrete–concrete interfaces (in green, Fig. 2), Neumann conditions at the concrete–air interface (shown in red, Fig. 2). The dissipation in concrete is sufficiently great to avoid having to take the absorbent layers onto account. This corresponds to a so-called "*Perfectly Matched Layer*" (PML), and prevents reflections. Diffusion parameters in Eq. (3) are assumed to be frequency independent: taking a frequency dependence into account would require frequency domain analysis, which would add considerable complexity to the resolution scheme, involving the management of parasitic oscillatory effects arising from the inverse Fourier transform.

This numerical model allows crack parameters such as depth and geometry to be modified. It also allows the real

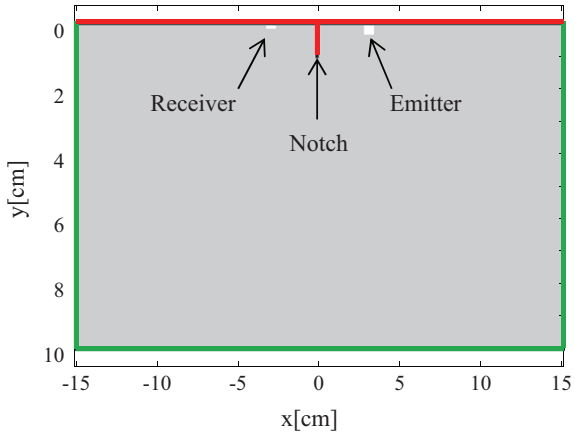

Fig. 2. Cross-section of the modeled 10×30 cm concrete specimen. A (1 cm) notch is positioned at the origin. The positions of the two transducers are shown, on either side (at $x=+3$ and -3 cm) of the notch. No energy boundary condition in green and Neumann boundary condition in red. (For interpretation of the references to color in this figure legend, the reader is referred to the web version of this article.)

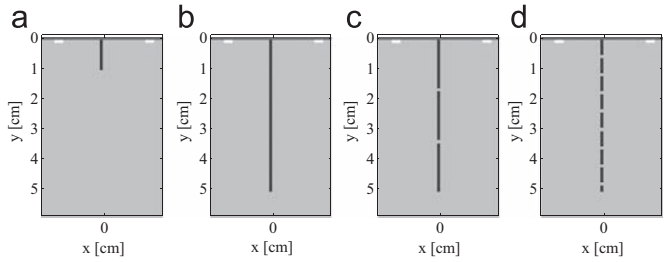

Fig. 3. (a, b) Detailed views of the concrete test specimen, showing two examples of an open crack, with depths equal to 1 and 5 cm. (c, d) Detailed views of the concrete test specimen, showing two examples of a 5 cm deep closed crack, with respectively 2 and 8 points of contact.

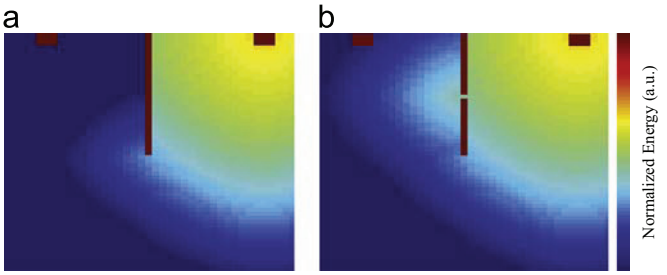

Fig. 4. Snapshot at the same time of diffuse ultrasound energy with (a) a notched sample and (b) the same one with a single contact point at the notch center.

crack morphology to be accounted for, by creating partial contacts along the length of the crack. An opened crack, or a crack with partial opened portions, is produced in the numerical model by imposing the Neumann conditions on the walls of the crack

$$\frac{\partial}{\partial n}\langle E(x,y,t)\rangle\Big|_{\Gamma} = 0, \tag{5}$$

where Γ indicates the walls of the crack and n is the normal at a point on this wall. In the simulation, in which vertical cracks are considered, this amounts to writing the expressions for the left and right walls of the crack, respectively as

$$\frac{E^{(n)}_{i-1,j} - E^{(n)}_{i,j}}{\Delta x} = 0, \quad \frac{E^{(n)}_{i+1,j} - E^{(n)}_{i,j}}{\Delta x} = 0. \tag{6}$$

This condition ensures that no energy can flow through the crack. The so-called open crack is defined by its depth (Fig. 3a, b). A realistic crack is introduced by the addition of partial contacts (Fig. 3c, d). To study their influence on diffuse ultrasound, the number and distribution of these contacts are parameterized. These points allow a part of diffuse energy to be transmitted through the crack as shown in Fig. 4.

In the following section, the model is validated by comparing its predictions with the experimental results presented by Quiviger et al. [14] for the case of open cracks (notches). The influence of contact points along the length of the crack is then studied. A realistic crack morphology is proposed in order to compare the model with experimental results obtained by Quiviger et al. [14] for the case of real cracks.

3.2. Validation of the model

The validation of the model is performed by comparing its predictions with the experimental results presented by Quiviger et al. [14], for the case of open cracks (notches). In the simulations, the diffusivity and dissipation parameters, D and σ, are constants. The experimental values from [14] of D and σ of concrete without cracks are introduced as inputs in the model. Following the signal processing proposed in [14], the apparent diffusion parameters are determined, in order to compare the numerical results with those found experimentally. They are evaluated through the use of a least squares fit to the solution of the 2D energy diffusion equation from the energy measured by the numerical receiver. Further details about diffusion constant determination are available in [14]. The results of the numerical simulations are shown in Fig. 5 with notches with depths ranging from 1 to 5 cm.

The numerical results show that the variation in these apparent parameters, as a function of the depth of the open crack, lies within the range of uncertainty of the experimental values, with the exception of the dissipation determined for a 2 cm notch. Also, the ATME values reveal a similar variation, with a difference which could arise from the boundary

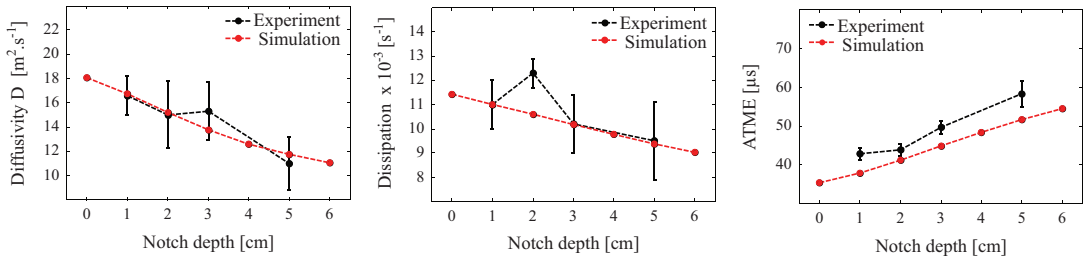

Fig. 5. Comparison of apparent diffusion parameters derived from the simulation, with those determined experimentally, for a notch of variable length.

conditions of the simulation as well as the 2D limitations of the model. These results allow the diffuse energy simulator, as well as the data processing, to be validated.

3.3. Simulation of partial contacts

In the presence of a closed crack, Quiviger et al. [14] assume that the contact zones between the walls of the crack play a predominant role. The present study focuses on the ability of the proposed simulation to accurately simulate diffuse ultrasound propagation through a realistic 2D numerical crack. Due to the mesh defined previously and the 2D nature of the simulation, the crack is assumed to represent the projection of the 3D crack morphology in the simulation plane. In order to reduce the parametrical study, the contact zones are defined as single mesh points (1×2 mm²) located along a line. In the following, the influence of the number of contact points on the diffusion phenomenon is evaluated. The influence of the position of a single contact point along the crack is determined. Then, the experimental data from real cracks [14], together with the detailed morphology described in the second part of this paper, are used to optimize the model. The experimental data shows that the most relevant parameter is the ATME [14]. Thus, the remaining part of the study is restricted to the use of the latter parameter.

3.3.1. Number of contacts

In order to evaluate the consequences of a variation in the density of contact points on the diffusion properties through a closed crack, a crack is simulated with a total length of 5 cm, including from 1 to 24 contacts, linearly distributed along the crack [Fig. 6(a, b)].

The simulations and data processing are carried out according to the same procedures as those described in the foregoing descriptions. The results plotted Fig. 6 show that the ATME decreases as a function of the number of contact points. It is noticeable that the presence of a single contact point located half length of the crack leads to a 5 µs, i.e. approximately 10%, change in ATME. With increasing contact density, the ATME decreases, approaching the direct trajectory time.

3.3.2. Contact point locations

The position of a contact point along the crack is the second parameter influencing diffuse energy propagation. Fig. 7 shows the influence of a single contact point located along the length of the crack at a depth ranging from 1 to 50 mm.

The distance between the contact point and the surface has an influence on the propagation of diffuse energy through the crack. ATME increases with the depth of the contact point. Note that for the given crack depth (5 cm), the different contact point locations lead to an ATME variation of the order of 10 µs.

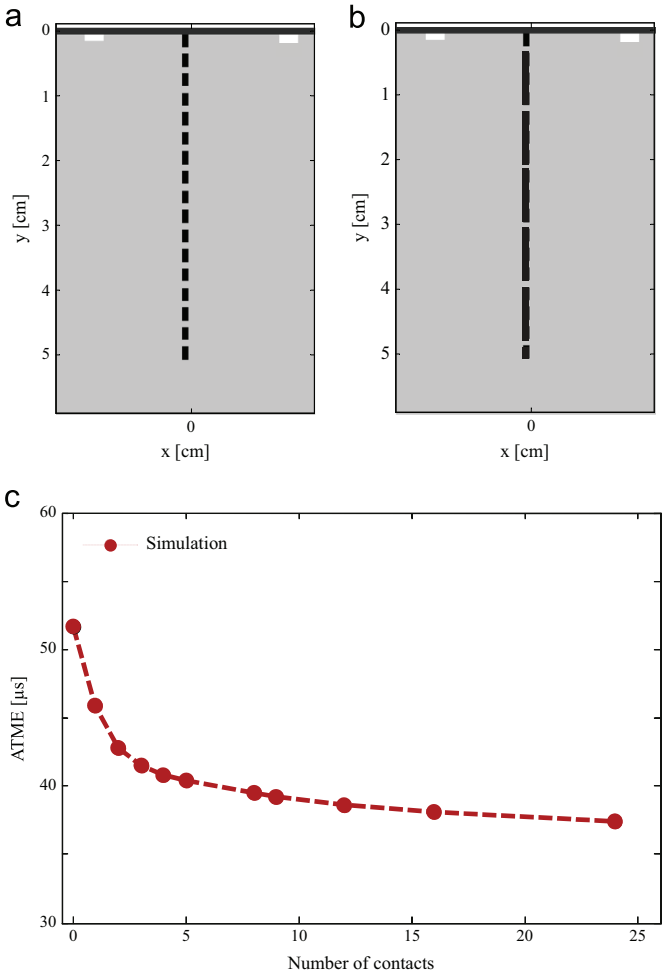

Fig. 6. (a, b) Example of spatial distribution of contacts along the length of the crack, and (c) variation in ATME as a function of the number of linearly distributed contact points along a total crack length of 5 cm.

3.3.3. Real cracks

This section deals with the variations in ATME as a function of the depth of the cracks observed experimentally by Quiviger et al. [14]. The cracks were generated using three-point bending, initiated by a 1 cm notch at the center of the test specimen. It is also modeled in the following simulations. The simulated cracks, identical to those analyzed experimentally (1, 3 and 5.5 cm), are represented by a linear distribution of contact points along the length of the crack (Fig. 8). This distribution is in agreement with observations made by Turatsinze et al. [15], described in Section 2. The contact density is the optimization parameter used in the numerical model to match experiments from [14]. An iteration process modifies this contact density, in order to optimize the morphology of the numerical crack with respect to the experimental results. The results are shown in Fig. 9.

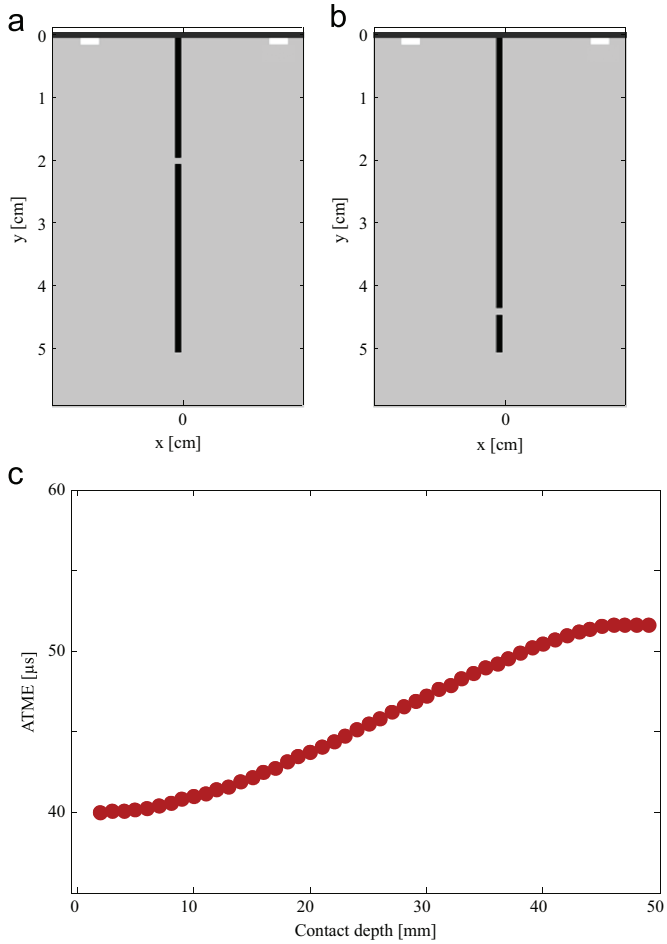

Fig. 7. (a, b) Example of position of a single contact along a 5 cm crack and (c) variation in ATME as a function of the contact position.

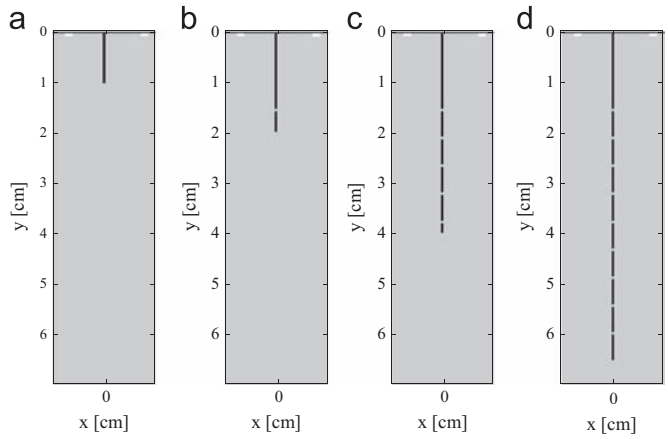

Fig. 8. Numerical simulation of the cracks analyzed during the experiments. (a) 0 cm, (b) 1 cm, (c) 3 cm and (d) 5.5 cm.

It shows that the variations in the simulated and experimental results are in agreement. Into this optimized configuration, the contact density is found to represent 6.5% of the total length of the crack. It should be noted that the numerical results for the ATME reach a maximum value at a depth of 4 cm, and then fall to a lower value at a depth of 6.5 cm, whereas the experimental results show a continuous increase in ATME. Nevertheless, the numerical variations remain within the range of uncertainty of the experimental results. This difference may be due to the crack description

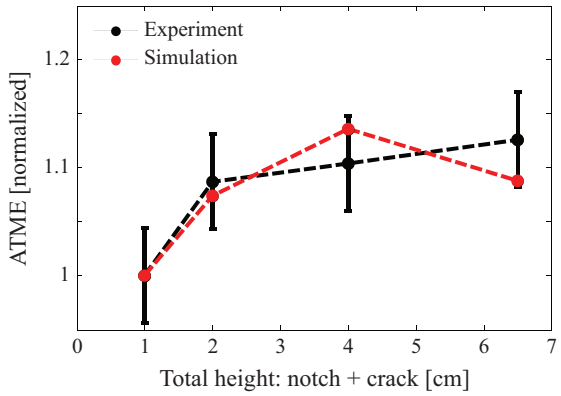

Fig. 9. Variation of the ATME as a function of the depth of the crack, for an optimized contact density. Comparison with experimental results.

which takes into account a linear contact point distribution along the crack.

4. Conclusion

The simulation tool and the numerical description of a crack allow a better understanding of diffuse wave's interactions with a real crack. A realistic numerical diffusion model including dissipation is proposed and validated through the use of experimental results from the literature. The simulations reveal the influence of the number of contacts, and their spatial distribution on the measured ATME. A realistic crack morphology is described numerically which makes possible the model to be optimized. It is shown that a linear contact density of 6.5% can explain the experimental variations in ATME, for cracks varying between 1 and 5.5 cm in depth. A more complex distribution could have been used but there is a lack of knowledge about crack morphology to validate such a study.

Fig. 1 shows the 3D characteristics of the crack, with varying contact densities between the test specimen's outer surfaces and its center. However it is important to note that Turatsinze et al. produced an image of the crack by slicing the samples. That leads to internal stress release, which can produce openings which are not present in bulk of the samples.

In this study, as regard with the symmetric location of the transducers and the position of the cracks, the 2D simulation is accurate. A 3D extension of this simulation is currently being evaluated. It will allow to model non-symmetric samples as well as various transducer locations. However, the main issue concerns the knowledge of the crack morphology in the bulk of the material. Non-destructive 3D observation of the morphology of this type of crack is to be considered in future studies, using X-ray microtomography for example. The complementarity of these data should ultimately allow the 3D crack morphology to be imaged in concrete.

The numerical model presented in this paper will also be of interest in future studies dealing with gradual changes in depth. As this simulation method includes the dissipation, it allows to simulate some concrete pathologies such as carbonation by introducing gradual changes of porosity (which mainly drives the dissipation) in the first centimeters of concrete.

Acknowledgments

Authors wish to thank Electricité de France for funding this study. Jean-Paul Balayssac (LMDC, France) is also acknowledged for helpful comments and suggestions about crack morphology in concrete.

References

[1] ISO 1920-7:2004, Testing of concrete, Part 7: Non-Destructive Tests on Hardened Concrete.
[2] ASTM C597-09, Standard Test Method for Pulse Velocity through Concrete.
[3] Chaix JF, Garnier V, Corneloup G. Ultrasonic wave propagation in heterogeneous solid media: theoretical analysis and experimental validation. Ultrasonics 2006;44:200–10.
[4] Payan C, Garnier V, Moysan J, Johnson PA. Determination of third order elastic constants in a complex solid applying coda wave interferometry. App Phys Lett 2009;94:011904.
[5] Van Hauwaert A, Thimus JF, Delannay F. Use of ultrasonics to follow crack growth. Ultrasonics 1998;36:209–17.
[6] Hévin G, Abraham O, Pedersen HA, Campillo M. Characterization of surface cracks with rayleigh waves: a numerical model. NDT&E Int 1998;31:289–97.
[7] Liou T, Hsiao C, Cheng CC, Chang N. Depth measurement of notches as models for shallow cracks in concrete. NDT&E Int 2009;42(1):69–76.
[8] Aggelis DG, Kordatos EZ, Soulioti DV, Matikas TE. Combined use of thermography and ultrasound for the characterization of subsurface cracks in concrete. Constr Build Mater 2010;24(10):1888–97.
[9] Anugonda P, Wiehn J, Turner J. Diffusion of ultrasound in concrete. Ultrasonics 2001;39(6):429–35.
[10] Becker J, Jacobs LJ, Qu J. Characterization of cement-based materials using diffuse ultrasound. J Eng Mech 2003;129(12):1478–84.
[11] Punuraia W, Jarzynskib J, Qub J, Kurtisa KE, Jacobs LJ. Characterization of dissipation losses in cement paste with diffuse ultrasound. Mech Res Comm 2007;34(3):289–94.
[12] Deroo F, Kim JY, Qu J, Sabra K, Jacobs LJ. Detection of damage in concrete using diffuse ultrasound. J Acoust Soc Am 2010;127(6):3315–8.
[13] Ramamoorthy SK, Kane Y, Turner JA. Ultrasound diffusion for crack depth determination in concrete. J Acoust Soc Am 2004;115(2):523–9.
[14] Quiviger A, Payan C, Chaix JF, Garnier V, Salin J. Effect of the presence and size of a real macro-crack on diffuse ultrasound in concrete. NDT&E Int 2012;45(1):128–32.
[15] Turatsinze A, Bascoul A. Restrained crack widening in mode i crack propagation for mortar and concrete. Adv Cem Based Mater 1996;4(3–4):77–92.
[16] Seher M, In CW, Kim JY, Kurtis KE, Jacobs LJ. Numerical and experimental study of crack depth measurement in concrete using diffuse ultrasound. J Nondestr Eval 2013;32(1):81–92.

NDT&E International 45 (2012) 128–132

Contents lists available at SciVerse ScienceDirect

NDT&E International

journal homepage: www.elsevier.com/locate/ndteint

Effect of the presence and size of a real macro-crack on diffuse ultrasound in concrete

A. Quiviger [a,b], C. Payan [a,*], J.-F. Chaix [a], V. Garnier [a], J. Salin [b]

[a] Laboratoire de Caractérisation Non Destructive, Université de la Méditerranée, IUT Aix-Provence, Avenue Gaston Berger, 13100 Aix en Provence, France
[b] EDF-R&D-STEP, 6 quai Watier, BP 49, 78401 Chatou, France

ARTICLE INFO

Article history:
Received 15 February 2011
Received in revised form
9 September 2011
Accepted 16 September 2011
Available online 22 September 2011

Keywords:
Diffusion
Cracks
Damage
Elastic waves
Wave scattering

ABSTRACT

In civil engineering structures, the first layer of concrete plays a role in terms of water-tightness, and contributes to the protection of metal frames from corrosion by external chemical agents (water, CO_2, chlorine etc.). In concrete, a crack is comprised of an external part with a surface opening, and a completely or partially closed part below the surface. The aim of this paper is to identify the contribution of a real macro-crack on the diffuse ultrasound parameters. The methods ability to characterize the open part of the crack is confirmed. The results reveal the influence of the closed part of the crack, with regions in partial contacts, on the diffusion parameters.

1. Introduction

Cracking is a major problem for the integrity of concrete constructions in civil engineering. Indeed, the mechanical properties of such constructions depend mainly on the steel frames they contain. In general, the first layer of reinforcing steel is located only a few centimeters below the surface, and is protected by the concrete cover. The role of the latter is mainly to ensure that the steel is protected from the aggression of naturally present agents: water, CO_2 present in air etc. Poor water-tightness of concrete leads to corrosion of the frame, which in turn produces macro-cracking, the consequence of which is an acceleration of the structure's degradation process. It is thus of particular importance to be able to characterize a crack present in the concrete cover, in order to forestall, as early as possible, any damage to the structure. The aim of the present study is thus to achieve, *in fine*, the detection, localization, and characterization of macro-cracks present in the concrete coating.

The morphology of a real macro-crack in concrete is shown Fig. 1. This can be described in two parts: the first, in which the two lips do not come into contact, is referred to as an opened crack zone (Fig. 1). The second part, in which the two lips of the crack are partially or totally in contact, is considered to be closed (closed crack zone in Fig. 1).

Standard methods [1,2], such as pulse velocity, based on low frequency (10–100 kHz) wave propagation, cannot provide information related to the presence of localized defects, at the scale of a few centimeters. In order to increase the resolution of such methods, higher frequency ultrasonic waves are required. However, when the wavelengths are of the order of the size of the aggregates, the observed signals are strongly influenced by the multiple scattering phenomenons. In concrete, which contains a large quantity of scatterers, of varying composition, size and shape, the ultrasound energy is dispersed in time and space. The ultrasonic field, influenced by multiple scattering effects, is thus composed of coherent and incoherent components. The former, which resists to a spatial average, describes a wave which has propagated in an effective medium, represented by a homogenized version of the real medium [3]. The incoherent field describes waves, which have followed extremely complex paths. It is often treated as if it was noise, although the information it contains is a representation of the microstructure of the material, at the scale of one wavelength.

It was only towards the end of the 1960s, at the time of the studies made by Aki [4], that geophysicists started to take interest in this part of the signal, which was then referred to as the "coda", by analogy with the finale of a musical composition. The idea was thus to exploit the full signal, thereby extracting all of the information available in it. Recent coda applications, based on signal correlations, have been implemented in concrete. Payan et al. [5] used it to

* Corresponding author. Tel.: +33 4 42 93 90 55; fax: +33 4 42 93 90 84.
E-mail addresses: audrey.quiviger@univmed.fr (A. Quiviger), cedric.payan@univmed.fr (C. Payan), jean_francois.chaix@univmed.fr (J.-F. Chaix), jean.salin@edf.fr (V. Garnier), vincent.garnier@univmed.fr (J. Salin).

0963-8695/$ - see front matter © 2011 Elsevier Ltd. All rights reserved.
doi:10.1016/j.ndteint.2011.09.010

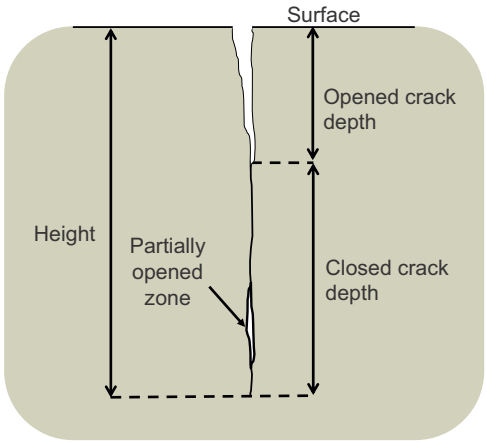

Fig. 1. Macro-crack morphology in concrete.

measure very weak relative variations in velocity, induced by static stress, and was thus able to determine the nonlinear elastic properties of concrete. A refined version of the method proposed by Aubry and Derode [6], and used by Larose et al. [7], demonstrate that it is possible to detect and locate the appearance of a millimeter-sized defect (holes) in concrete.

The incoherent part of the signal can be represented by an approximation to the diffusion regime, which describes the temporal variations of the energy density in the received signal. This notion of diffusion of the ultrasonic energy has been described and validated by Weaver [8] in the case of aluminum foams with variable porosities. In the domain of concrete, Anugonda et al. [9] determined the diffusion parameters at a central frequency of 500 kHz, in other words at considerably higher frequencies than those normally used for this type of material. Their work thus opens up a large number of possibilities in terms of the non-destructive characterization of micro-structural damage in concrete. Becker et al. [10] studied the variation of diffusion parameters as a function of the diameters and volume fraction of aggregates, represented by glass beads. Punuraia et al. [11] characterized this variation in cement paste, as a function of the volume of entrained air voids. The influence of diffuse damage (Alkali Silicate Reaction and thermal damage) has recently been demonstrated [12].

Ramamoorthy et al. [13] have demonstrated a correlation between the latter parameters and the depth of a notch (opened crack depth). The authors have shown the ability of inverting the problem by means of 2D numerical simulation. To be consistent, these simulations need a priori on the diffusion properties of undamaged concrete. The present study is presented from the point of view of the "Non-Destructive Tester" who needs to link some indicator's variation to a potential damage without needing to know whether a crack is present or not. Therefore, the diffusion parameters are treated as indicators. That would be useful to identify how the whole set of parameter evolves as a function of the type of damage in presence. As an example, thermal damage affects two parameters (dissipation and diffusivity) [12], while the presence of entrained air in cement only affects diffusivity. The aim of the present paper is to follow the measured diffuse ultrasound parameters in the presence of real cracks, which are able to transmit all or part of the ultrasonic energy from regions in partial contact. For that goal, a simple diffusion model associated with a simple data fitting procedure will be employed so as to follow the parameters evolution. The following sections describe the theory of diffuse ultrasound, the experiments carried out on notches in order to validate the method, and finally those carried out on real cracks.

2. Theory of diffuse ultrasound

The diffusion equation expresses the frequency-dependent spatio-temporal variation of the energy E, for a point source P [8]:

$$\frac{\partial \langle E(x,t,f)\rangle}{\partial t} - D\Delta\langle E(x,t,f)\rangle + \sigma\langle E(x,t,f)\rangle = P(x,t,f) \quad (1)$$

where x is the position, t is the time, f is the frequency, D is the diffusivity, and σ is the dissipation. The diffusivity (unit $m^2\,s^{-1}$) is characteristic of the material's microstructure, and depends on the density of the aggregates, their geometry and their average spacing [9]. The dissipation (unit s^{-1}) is indicative of the viscoelastic properties of the medium, which in the case of concrete are essentially related to the properties of the cement paste [9].

The solution to Eq. (1) can be found in 1D as described by [9], in 2D as given by [13], or in 3D, according to [12]. Here, we are interested in the 2D solution, which can be written in logarithmic form as

$$\log(\langle E(r,t,f\rangle) = C_0 - \log(Dt) - \frac{r^2}{4Dt} - \sigma t \quad (2)$$

where r is the distance from the sound source and C_0 is a constant depending on the energy injected by the source. Fig. 2(a) shows a typical diffuse ultrasound signal in concrete. In order to derive a fit to Eq. (2), the temporal signal (Fig. 2a) is divided into windows of duration Δt. The energy spectral density of each window is then determined for certain frequencies, by integrating the spectrum over a frequency band of width Δf, centered on the frequency of interest. Each spectral density value is associated with a discrete instant in time, corresponding to the center of the relevant temporal window. It is thus possible to follow the variations of energy as a function of time, and to determine the associated values of dissipation and diffusivity (Fig. 2b) using Eq. (2). We note that an additional parameter can be studied: the Arrival Time of the Maximum energy (ATME in Fig. 2b), which seems to be a sensitive indicator of the length of the notch [13].

Even if this model only apply for medium with homogeneous diffusion properties and does not match the physical problem, i.e., specific boundary conditions (zero flux condition at the crack/notch faces), it remains useful for data processing, and so, for measuring the diffusion parameters. The evolution of the full set of diffusion parameter as a function of the crack depth is presented in the next section.

3. Experiments

Two series of concrete samples of equivalent geometry ($150 \times 150 \times 600\ mm^3$) were studied. The first of these included four samples notched to different depths, which is devoted to simulating the opened crack depth (Fig. 1). The second included four samples, each having notches with a length if 1 cm, and of which three had cracks of different lengths (1, 3, and 5.5 cm). In the second series, the notches were introduced in order to initiate a crack during manufacture at the samples center. These samples were placed under four-point flexure loading, by controlling the press as a function of the crack opening, rather than by its displacement, using the signals provided by LVDT transducers. When the desired depth was attained, the press is stopped. It is important to note that when the loading is released, the cracks close again. Thus this series is devoted to simulating real cracks with various closed crack depth (Fig. 1). Note that the two series of samples were not made at the same time, and had different concrete compositions.

Ultrasound transducers are placed in contact with the upper surface of the sample, on both sides of the crack as shown in Fig. 3. The 60 mm separation between the transducers is achieved by means of a shim, which is systematically centered with respect

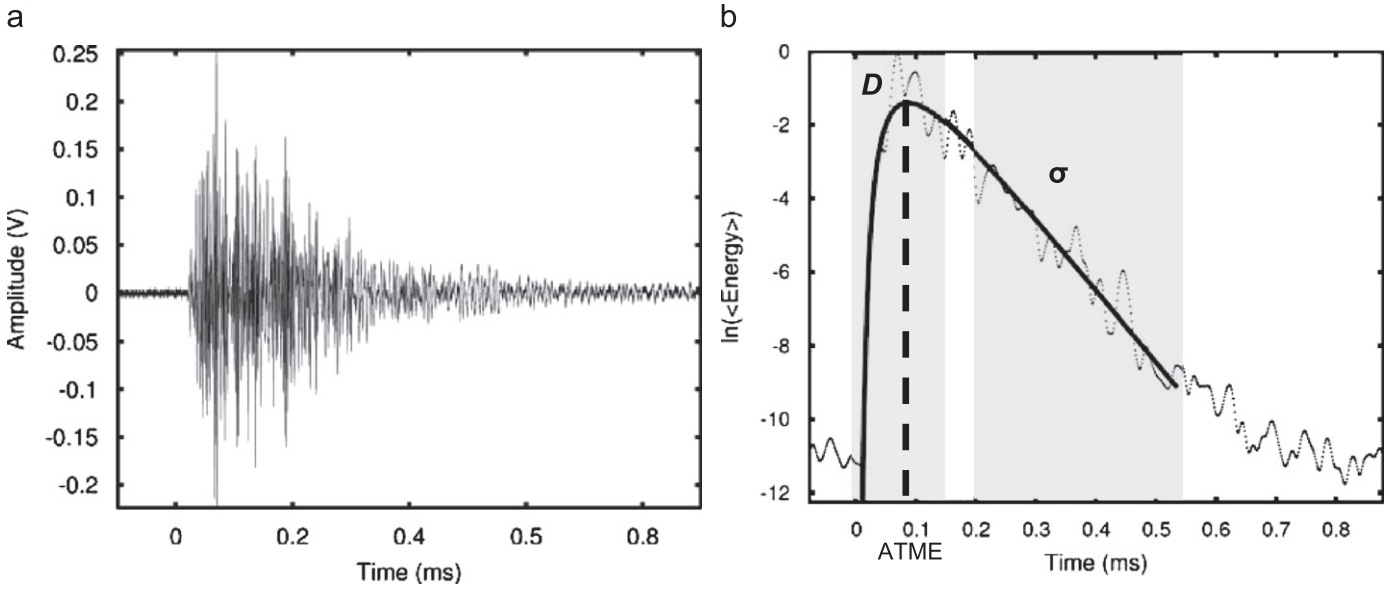

Fig. 2. (a) Diffuse ultrasound time signal. (b) Representation of the energy spectral density as a function of time (dashed curve) and the smoothed function (continuous line) given by Eq. (2).

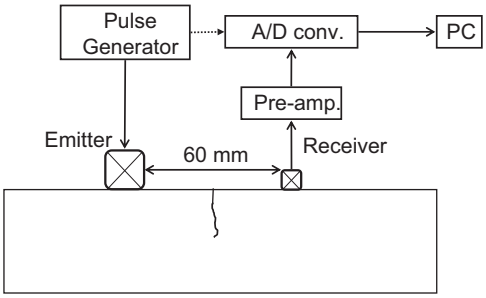

Fig. 3. Experimental setup.

to the opening point of the crack. The transmitter (Panametrics V101, diameter 25.4 mm) has a central frequency of 500 kHz, and is driven by a pulsed source (Olympus 5072PR). The receiver is a small diameter (4 mm), broad-band transducer centered at 500 kHz. The choice of a small diameter receiver is driven by the need to limit phase cancellation phenomena [14]. The time signals are averaged over 100 recordings in order to reduce the noise level. In addition, in order to ascertain the uncertainties in the evaluation of the diffusion parameters, each measurement is repeated 25 times by removing, and then repositioning the sensors. The time-frequency analysis described in Section 2 is implemented on signals received with $\Delta t = 50$ μs and $\Delta f = 80$ kHz, with each time window having a 90% overlap with the preceding window. To illustrate the results of the signal processing, the frequency evolution of both diffusivity (D) and dissipation (σ) is shown in Fig. 4 for the cracked samples. These trends are coherent with those found in the literature [9], with a global increase in dissipation (from 10 to 25 ms^{-1}) and a global decrease in diffusivity (from 20 to 10 $m^2 s^{-1}$), as a function of frequency. The error bars in Fig. 4 are evaluated according to Weaver [8] from Δt and Δf.

4. Results and discussion

The complete set of results is presented in Fig. 5. The selected frequency band is that for which a maximum quantity of energy is transmitted [240–320 kHz].

4.1. Notched samples

For notched samples, the measured values of dissipation σ (Fig. 5b) and diffusivity D (Fig. 5a) are in agreement with those found in the literature for various concrete composition [9,11,14]. The trend of ATME with the notch depth is in agreement with Ramamoorthy et al. [13]. But to validate our results, we evaluated D from the data available in [13] with our data processing procedure: D decreases from 12 (no notch) to 9 (3.75 cm notch), up to 3 (7.5 cm notch). This trend is comparable to the present study.

As the dissipation refers to the viscoelastic nature of the material, it does not reveal any noticeable variability as a function of the opened crack depth (Fig. 5b).

The diffusivity D (Fig. 5a) tends to decrease with the opened crack depth. Notches modify the energy transport between transmitter and receiver. However, one can also note the significant range of uncertainties, as revealed by the difficulty in making an exact determination of the diffusivity. The time-frequency analysis starts only at an energy level greater than that of the noise, which is systematically set by thresholding (mean noise level + 3 standard deviations, statistically corresponding to more than 99% of the population). In the diffusion equation, the diffusivity predominates in the first part of the energy signal (Fig. 2b), which represents only a reduced number of points with respect to the total energy signal. Since a variation in the noise level leads to a threshold at the next highest point, it then also produces a significant variation in the determination of the value of D.

The Arrival Time of the Maximum Energy (ATME in Fig. 5(c)) varies noticeably as a function of the opened crack depth. Furthermore, we note that, since the latter parameter is representative of the full set of signal data points, it is less strongly influenced by the thresholding, and its associated uncertainty is considerably lower than that of the diffusivity.

4.2. Real cracks

As for notched samples, the dissipation does not evolve noticeably (Fig. 5b). The observed difference between both sample set is related to their different compositions. Therefore, this could be a source of information about the nature of concrete.

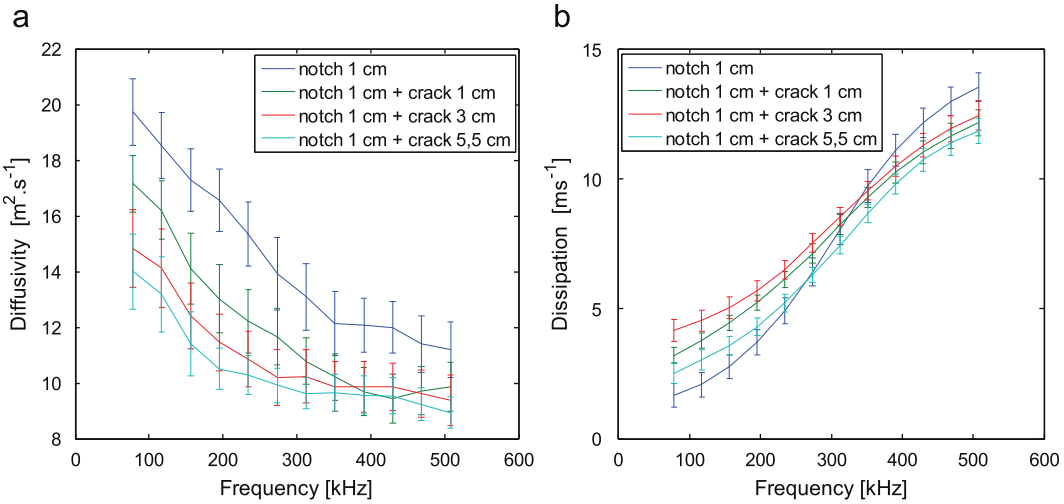

Fig. 4. Variation of (a) diffusivity and (b) dissipation, in cracked samples as a function of frequency.

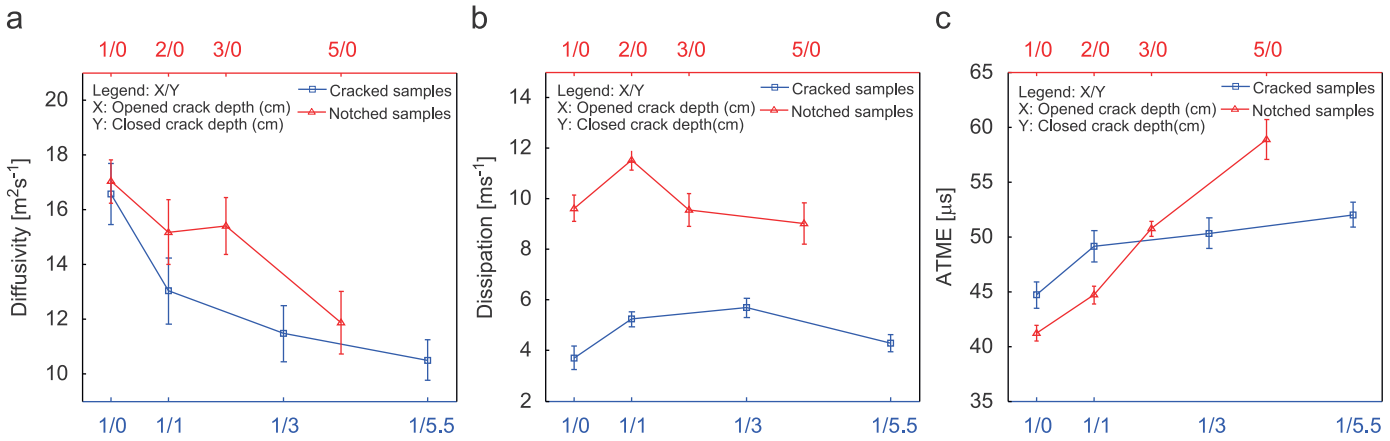

Fig. 5. Variation of diffusion constants in cracked (blue) and notched (red) samples, as a function of crack height, for the frequency range [240–320 kHz]. (a) Dissipation, (b) diffusivity and (c) arrival time of the maximum energy (for interpretation of the references to colour in this figure legend, the reader is referred to the web version of this article).

The diffusivity is affected by the presence of a closed crack (Fig. 5a), probably due to the presence of partially opened zones along the crack lips (Fig. 1). However, for the same reason as for notched samples, this indicator presents a high uncertainty that does not allow discerning the closed crack depth.

The ATME (Fig. 5c) exhibits a sensitivity lower than for the notched samples but as for these last, the uncertainty remains to a lower level than the diffusivity. However, this indicator does not manage to a sufficient dynamic to allow characterizing the closed crack depth.

5. Conclusion and prospects

This paper analyses how the presence and the size of a real macro-crack modify the diffusion parameters of concrete, obtained from the 2D diffusion equation. This study highlights the effects of the presence of multiple contacts and localized voids along the closed crack zone.

It has been shown that the ATME is a good indicator for the characterization of the opened crack depth. However, in view of the amount of uncertainties, it appears difficult to extract reliable information related to the depth of closed cracks. Future studies will be concentrated on the analysis of new samples with controlled crack morphologies, which, when associated with numerical simulations, should allow conclusions to be drawn concerning the influence of partially opened zones along the crack. In addition, due to high spatial variability, it would not be straightforward to discern the presence of a macro-crack in large concrete structures. As a consequence, the comparative study of the variations of the whole set of diffusion parameters for diverse kind of damage (distributed or localized) and composition should be revealing.

Recent laboratory studies [15] show that the methods derived from nonlinear acoustics can provide information related to the closed crack depth. The complementarity of these two approaches should in the long term allow macro-cracks in concrete to be completely characterized, with possible applications in civil engineering.

Acknowledgments

The authors wish to thank the Laboratoire Matériaux et Durabilité des Constructions (LMDC, France) for having manufactured the cracked samples, as well as EDF R&D for their financial support.

References

[1] ISO 1920-7:2004. Testing of concrete, part 7: non-destructive tests on hardened concrete.

[2] ASTM C597-09. Standard test method for pulse velocity through concrete.
[3] Chaix JF, Garnier V, Corneloup G. Ultrasonic wave propagation in heterogeneous solid media: theoretical analysis and experimental validation. Ultrasonics 2006;44:200–10.
[4] Aki K. Analysis of the seismic coda of local earthquakes as scattered waves. J Geophys Res 1969;74:615–31.
[5] Payan C, Garnier V, Moysan J, Johnson PA. Determination of third order elastic constants in a complex solid applying coda wave interferometry. Appl Phys Lett 2009;94:011904.
[6] Aubry A, Derode A. Random matrix theory applied to acoustic backscattering and imaging in complex media. Phys Rev Lett 2009;102:084301.
[7] Larose E, Planes T, Rossetto V, Margerin L. Locating a small change in a multiple scattering environment. Appl Phys Lett 2010;96:204101.
[8] Weaver R. Ultrasonics in an aluminium foam. Ultrasonics 1998;36:435–42.
[9] Anugonda P, Wiehn J, Turner J. Diffusion of ultrasound in concrete. Ultrasonics 2001;39(6):429–35.
[10] Becker J, Jacobs LJ, Qu J. Characterization of cement-based materials using diffuse ultrasound. J Eng Mech 2003;129(12):1478–84.
[11] Punuraia W, Jarzynskib J, Qub J, Kurtisa KE, Jacobs LJ. Characterization of dissipation losses in cement paste with diffuse ultrasound. Mech Res Commun 2007;34(3):289–94.
[12] Deroo F, Kim JY, Qu J, Sabra K, Jacobs LJ. Detection of damage in concrete using diffuse ultrasound. J Acoust Soc Am 2010;127(6):3315–8.
[13] Ramamoorthy SK, Kane Y, Turner JA. Ultrasound diffusion for crack depth determination in concrete. J Acoust Soc Am 2004;115(2):523–9.
[14] Page JH, Schriemer HP, Bailey AE, Weitz DA. Experimental test of the diffusion approximation for multiply scattered sound. Phys Rev E 1995;52:3106–14.
[15] Zardan JP, Payan C, Garnier V, Salin J. Effect of the presence and size of a localized nonlinear source in concrete. J Acoust Soc Am 2010;128(1):EL38–42.

Microbubble cloud characterization by nonlinear frequency mixing

M. Cavaro,[a] C. Payan,[b] and J. Moysan
Laboratoire de Caractérisation Non Destructive, Université de la Méditerranée, IUT Aix-Provence, Avenue Gaston Berger, 13100 Aix en Provence, France
matthieu.cavaro@cea.fr, cedric.payan@univmed.fr, joseph.moysan@univmed.fr

F. Baqué
Commissariat à l'Énergie Atomique et aux Énergies Alternatives - Cadarache, Direction de l'Energie Nucléaire, Laboratoire d'Instrumentation et d'Essais Technologiques, Bâtiment 202, 13108 Saint Paul lez Durance, France
francois.baque@cea.fr

Abstract: In the frame of the fourth generation forum, France decided to develop sodium fast nuclear reactors. French Safety Authority requests the associated monitoring of argon gas into sodium. This implies to estimate the void fraction, and a histogram indicating the bubble population. In this context, the present letter studies the possibility of achieving an accurate determination of the histogram with acoustic methods. A nonlinear, two-frequency mixing technique has been implemented, and a specific optical device has been developed in order to validate the experimental results. The acoustically reconstructed histograms are in excellent agreement with those obtained using optical methods.

PACS numbers: 43.25.Yw, 43.35.Zc, 43.30.Lz, 43.25.Zx [MH]
Date Received: November 16, 2010 **Date Accepted:** February 18, 2011

1. Introduction

Among the candidates envisaged for the next generation of nuclear reactors, France has chosen to develop the SFR design (sodium fast reactor: fast neutron reactors cooled with liquid sodium, see Fig. 1), which is expected to be commissioned toward the year 2040. Improvements in the demonstration of safety and monitoring of the operation of this type of reactor depend, today, among other factors, on the characterization of microbubbles of gas in the liquid sodium used as a coolant. This presence is normal and continuous: it arises mainly from the entrainment of the argon cover gas present above the sodium and from the nucleation of bubbles resulting from the gas dissolution phenomena.

The consequences of this gasification are various. Among the most significant of these, we cite the risk of gas pocket accumulation. The control of the causes and consequences of this presence of microbubbles requires their characterization, i.e., the determination of the bubble radius histogram.

It is important to note that liquid sodium is perfectly opaque, thus making it impossible to optically characterize this presence of bubbles. Moreover, its electric properties, together with the very low values of the radii together with the expected vacuum levels ($r \sim 10$ μm, void fraction $\sim 10^{-6}$), render most other bubble characterization methods inapplicable. We therefore studied the potential use of acoustic methods. Safety requirements also impose the development of measurement techniques for which no *a priori* data are necessary. However, the acoustic methods based on the measurement of attenuation or scattering by the bubbles have an ambiguity, since the scattering of a

[a]Present address: CEA Cadarache, DEN/DTN/STPA/LIET, Bâtiment 202, 13108 Saint Paul lez Durance, France.
[b]Author to whom correspondence should be addressed.

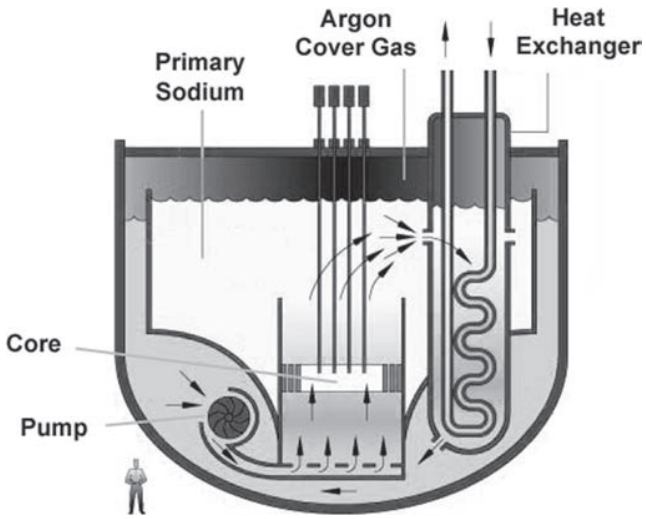

Fig. 1. Schematic diagram of a SFR type of nuclear reactor.

resonant bubble is identical to that of a considerably larger non-resonant bubble. As for propagation velocity measurements, these allow the void fraction to be determined only for a frequency range, which depends on the size of the bubbles which are present. Linear acoustic methods thus appear to be inadequate under these conditions.

The dynamic behavior of a bubble in an acoustic field can be described by the modified Raleigh equation[1]

$$\rho R\ddot{R} + \frac{3}{2}\rho\dot{R}^2 = \left(p_0 + \frac{2\sigma}{R_0} - p_v\right)\left(\frac{R}{R_0}\right)^{3\gamma} - \frac{2\sigma}{R_0} - \frac{4\mu}{R}\dot{R} + p_v - p_0 - P(t) \tag{1}$$

where ρ is the mass density of the liquid, R is the instantaneous radius of the bubble, R_0 is its rest radius, p_0 is the static pressure, p_v is the saturation vapor pressure, γ is the polytropic gas pressure, σ is the surface tension, and μ is the dynamic viscosity of the liquid. The acoustic field $P(t)$ takes the form $p_a \sin(\omega t)$. This equation is strongly nonlinear, which explains our decision to investigate the nonlinear resonant behavior of bubbles, in order to unambiguously reconstruct the radius histogram of a cloud of bubbles, without the need for any *a priori* data. From Eq. (1), the Minnaert[2] equation can be derived, relating the resonance frequency of a bubble to its radius:

$$f_{\text{res}} = \frac{1}{2\pi R_0}\sqrt{\frac{3\gamma p_0}{\rho}}. \tag{2}$$

The excitation of a bubble at its resonant frequency (f_1) leads to the appearance of multiple and sub-multiple frequencies, such as its harmonics ($n.f_1$) and, eventually, its ultra-harmonics [$(2n+1).f_1/2$] and sub-harmonic ($f_1/2$). In the case of a bi-frequency excitation ($f_1 < f_2$), if f_1 corresponds to the bubble's resonant frequency, the mixing of the different frequencies leads in addition to the appearance of sum and difference frequencies ($f_2 \pm nf_1$) and, possibly, to various ultra-harmonic and sub-harmonic combinations.

Although the idea of applying mixed frequencies to bubbles appeared in the early 1970s,[3] it was not before the 1980s that the first experimental applications of this principle were made with bubbles.[4] In 1985, Chapelon *et al.*[5] obtained a radius histogram for air bubbles of a few tens of microns in water by mixing one high frequency (HF) and one low frequency (LF). Validation of their results by means of an optical

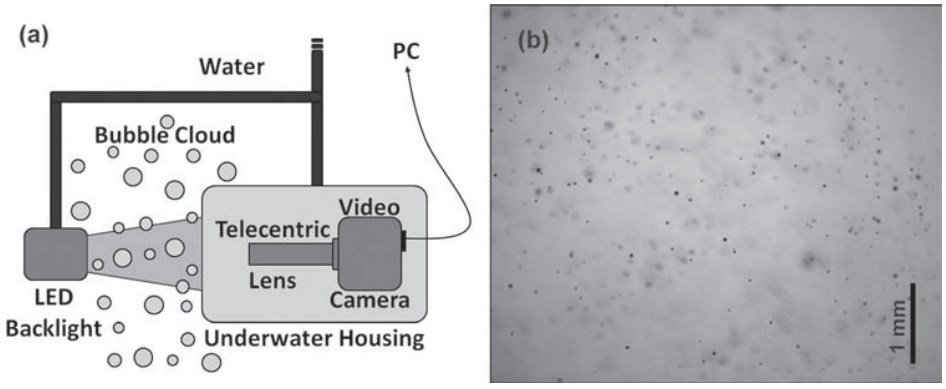

Fig. 2. (a) Optical device. (b) Photograph of the microbubble cloud obtained using the optical device.

technique demonstrated the results' coherence, without achieving a higher degree of agreement. The correlation coefficient between optical and acoustic histograms was estimated at 0.8. A nonlinear mixing technique with two HFs then allowed Sutin *et al.*[6] to reconstruct microbubble radius histograms, but without being able to validate them. More recently, Buckey *et al.*[7] and Leighton *et al.*[8] obtained bubble radius histograms by means of frequency mixing techniques, again without being able to validate their measurements.

The aim of this letter is determine micron-sized bubble radius histograms, with the best possible reliability. As the temperature of liquid sodium in a SFR lies in the range between 450 and 550 °C, and this substance is highly reactive with water and air, an experimental breadboard is presented, enabling clouds of microbubbles of air to be generated and optically tested in water. The acoustic behavior of the air/water pair at 20 °C is very closed to that of argon/sodium one at 500 °C. The histograms obtained by means of nonlinear mixing of one HF and one LF are then compared with the optical measurements.

2. Experiments

The bubble production was achieved here by means of aeroflotation, a technique based on the supersaturated state of dissolved gas, which leads to a bubble nucleation phenomenon. The radius histogram of the thus produced bubble cloud is then determined using an immerged optical device comprising a 5 megapixel camera equipped with a telecentric lens, having a magnification of 1.5 and a focal length of 660 μm, and a light-emitting diode (LED) light source [Fig. 2(a)]. We can thus obtain images such as that shown in Fig. 2(b).

The image processing designed to eliminate the blurry bubbles is achieved by the "Image Processing" toolbox of MATLAB. This allows the radius histogram of the present bubbles to be reconstructed. The optical device and the image processing were validated by means of simultaneous measurements made with a granulometric laser from Malvern (Orsay, France) Spraytech.

The acoustic device used is shown in Fig. 3(a). An Imasonic (Voray sur l'Ognon, France) LF transducer, centered at 250 kHz and connected to an Agilent (Santa Clara, CA) 33250A function generator, produces the pump frequency. The imaging frequency is emitted and received by a pair of Panametrics (Wamltham, MA) V304 HF transducers centered at 2.25 MHz, which are focused at a distance of 30 mm and aligned at 90° with respect to each other. The emission is achieved using an HP (Palto Alto, CA) 3314A function generator. The receiver is connected to a 12 bit analog-to-digital (A/D) converter, which is in turn connected to a personal computer (PC).

In order to limit potentially perturbing electronic nonlinearities, the electronic emitter and receiver circuits are completely decoupled. In addition, the use of power

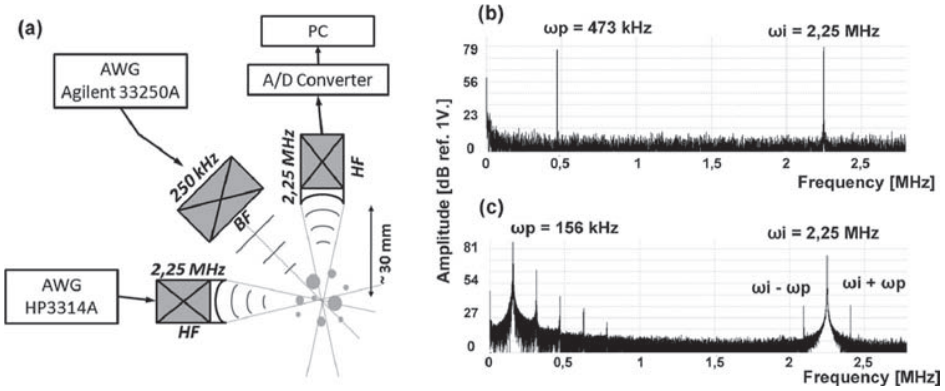

Fig. 3. Experimental device: (a) acquisition chain. Spectrum produced in the case of, respectively, (b) the absence and (c) the presence of a resonant bubble at the acoustic focal spot.

amplifiers in the emission electronics and preamplifiers in the receiver electronics is avoided.

The pump and imaging frequencies are emitted continuously. The HF at 2.25 MHz and the LF chirped between 10 and 500 kHz allow the full range of resonant frequencies of the present bubble sizes (between 7 and 330 μm) to be covered.

The intersection between the focal spots of the two HF transducers corresponds to a volume of the order of 2 mm^3 at -6 dB. The LF emitter is not focused, such that a resonant bubble close to the focal spot can be detected. Since the void fraction estimated by the optical device is approximately 8×10^{-5}, the probability of more than one resonant bubble being present at the acoustic focal spot is very low. This is a mandatory condition for our measurement validity.

When there is no bubble having a radius corresponding to the pump frequency present in the acoustic focal spot, a spectrum similar to that shown in Fig. 3(b) is obtained. Only the pump (473 kHz) and imaging (2.25 MHz) frequencies are observed. This result confirms the linearity of our setup. Figure 3(c) shows a spectrum revealing the presence of a bubble, which is resonant at the pump frequency (156 kHz). The harmonics of the sum and difference pump frequencies can be observed.

3. Results

The algorithm used to reconstruct the acoustic histogram is quite simple. A threshold above the noise level is defined on the frequency spectrum. As soon as a component appears in the interval $[\omega i - 500$ kHz, $\omega i[\cap]\omega i + 500$ kHz], the position of the maximum in this zone indicates the resonant frequency of the bubble.

As the frequency is known, Eq. (2) allows the bubble's radius to be found, and the radius histogram can thus be incremented. The analysis of approximately two thousands 5 ms acoustic sequences thus allowed to construct the histogram shown in Fig. 4. For comparison purpose, the optically determined histogram is also shown.

The histograms obtained by optical and acoustic methods are thus seen to be in very good agreement, with a correlation coefficient of 0.94. Such an agreement has, to the best of our knowledge, never before been reported in the literature. Contrary to most previous studies, we made the decision not to work with the amplitudes of the sum and difference frequencies, but rather with their presence (or absence). This allowed the data reduction to be simplified which, when associated with 12 bit electronics and the absence of amplifiers, led to conclusive results.

4. Conclusions and prospects

The ability to reconstruct accurate microbubble radius histograms, thanks to the use of nonlinear mixing of two frequencies, has been demonstrated for the air/water pair. The

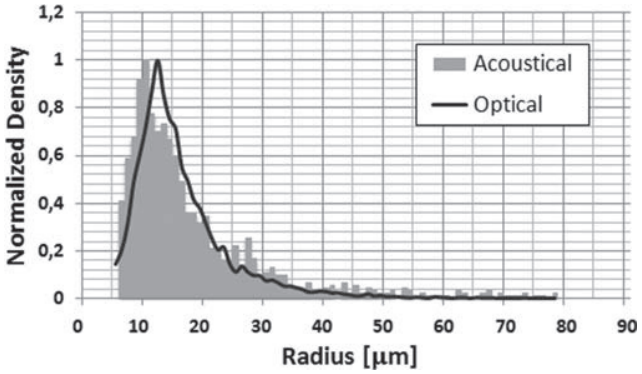

Fig. 4. Normalized bubble radius histograms, reconstructed using the acoustic method (gray histogram) and the optical method (black curve).

results are validated by optical measurements and are in excellent agreement. It is important to note that these results were obtained on microbubbles, without using amplifiers, and this could have implications in other domains, for biomedical applications in particular.

The uncertainty on the acoustical interaction zone resulting from the use of an unfocused LF means that the reconstructed histograms show a relative distribution only. Consequently, they do not yet allow the void fraction of the bubble cloud to be determined. The use of two focused, HF emissions would allow this uncertainty to be removed. Indeed, preliminary results obtained with the same device are encouraging. However, the number of detected bubbles is too low because the bubble generator, which operates in open loop, can be operated for only a few minutes at a time.

As a consequence of the complexity of developing the transposition of this setup to the industrial conditions of liquid sodium, with acoustic transducers compatible with this medium, under the operating conditions of a nuclear reactor, such a validation is planned for the coming years.

Acknowledgments

The authors wish to thank the French Commissariat à l'Energie Atomique et aux Energies Alternatives (CEA), the regional council of Provence-Alpes-Côte d'Azur for financing this study, and the RMS company (France) for technical support. We acknowledge the Laboratoire de Mécanique et d'Acoustique (CNRS UPR-7051, France), especially the Propagation and Imaging team for helpful comments, discussions, and technical support.

References and links

[1]W. Lauterborn, "Numerical investigation of nonlinear oscillations of gas bubbles in liquids," J. Acoust. Soc. Am. **59**(2), 283–293 (1976).
[2]M. Minnaert, "On musical air bubbles and the sound of running water," Philos. Mag. **16**(7), 235–248 (1933).
[3]E.A. Zabolotskaya and S. I. Soluyan, "Emission of harmonic and combination frequency waves by air bubbles," Sov. Phys. Acoust. **18**(3), 396–398 (1973).
[4]V.L. Newhouse and P. M. Shankar, "Bubble size measurements using the nonlinear mixing of two frequencies," J. Acoust. Soc. Am. **75**(5), 1473–1477 (1984).
[5]J. Y. Chapelon, P. M. Shankar, and V. L. Newhouse, "Ultrasonic measurement of bubble cloud size profiles," J. Acoust. Soc. Am. **78**(1), 196–201 (1985).
[6]A. M. Sutin, S. W. Yoon, E. J. Kim, and I. N. Didenkulov, "Nonlinear acoustic method for bubble density measurements in water," J. Acoust. Soc. Am. **103**(5), 2377–2384 (1998).
[7]J. C. Buckey, D. A Knaus, D. L. Alvarenga, M. A. Kenton, and P. J. Magari, "Dual-frequency ultrasound for detecting and sizing bubbles," Acta Astronaut. **56**, 1041–1047 (2005).
[8]T. G. Leighton, A. Mantouka, P. White, and Z. Klusek, "Towards field measurements of population of methane gas bubbles in marine sediments: An inversion method required for interpreting two-frequency insonification data from sediment containing gas bubbles," Hydroacoustics **11**, 203–224 (2008).

Cement and Concrete Research 41 (2011) 557–559

Contents lists available at ScienceDirect

Cement and Concrete Research

journal homepage: http://ees.elsevier.com/CEMCON/default.asp

Short communication

Carbonation assessment in concrete by nonlinear ultrasound

F. Bouchaala [a], C. Payan [a,*], V. Garnier [a], J.P. Balayssac [b]

[a] Laboratoire de Caractérisation Non Destructive, Université de la Méditerranée, IUT Aix-Provence, Avenue Gaston Berger, 13625 Aix en Provence Cedex, France
[b] Université de Toulouse; UPS, INSA; LMDC (Laboratoire Matériaux et Durabilité des Constructions); 135, avenue de Rangueil, 31077 Toulouse Cedex 04, France

ARTICLE INFO

Article history:
Received 10 September 2010
Accepted 25 February 2011

Keywords:
Carbonation (C)
Characterization (B)
Nonlinear acoustics

ABSTRACT

The carbonation process results in a change in the elastic properties of concrete, resulting in a variation of standard acoustic indicators such as wave speed. However, this evolution is too low to ensure an efficient carbonation assessment. The present communication focuses on the feasibility of carbonation assessment in concrete by applying Nonlinear Resonant Ultrasound Spectroscopy (NRUS). The results show that the nonlinear parameter is significantly affected by the presence of carbonation, which is interpreted with respect to the evolution of concrete microstructure in the presence of this pathology.

Carbonation is a chemical reaction in concrete between the calcium hydroxide ($Ca(OH)_2$) contained in cement and the carbon dioxide (CO_2) in the air. The following chemical reactions can be identified:

- Dissolution of carbon dioxide in water:

$$CO_2 + H_2O \rightarrow H_2CO_3$$

$$H_2CO_3 + H_2O \rightarrow HCO_3^- + H_3O^+$$

$$HCO_3^- + H_2O \rightarrow CO_3^{2-} + H_3O^+$$

- Reaction of carbonic acid with calcium hydroxide $Ca(OH)_2$, after its dissolution:

$$H_2CO_3 + Ca(OH)_2 \rightarrow CaCO_3 + 2H_2O \quad (1)$$

One of the consequences is the decrease of the pH due to the liberation of ions H_3O^+. The pH value of concrete ranges from 12 to 13 and after carbonation, the pH drops to 9 for fully carbonated concrete. It was observed that the ability of carbon dioxide to be fixed by calcium hydroxide depends on the quantity of alkalis (NaOH, KOH) contained in the cement because the alkalis decreases the solubility of calcium hydroxide. But once the alkalis are carbonated higher amounts of calcium hydroxide can be carbonated [1].

Carbonation also affects the other hydrates of the cement paste (silicates and aluminates). Particularly, it was observed that the C–S–H can be carbonated following the reaction:

$$1.7H_2CO_3 + 1.7CaO.SiO_2.2.5H_2O \rightarrow 1.7CaCO_3 + 1.7SiO_2.2.5H_2O + 1.7H_2O$$

Nevertheless it must be noticed that the carbonation of calcium hydroxide is faster than for the other hydrates. The speed of carbonation essentially depends on the humidity of concrete and is maximal for values about 65%.

After carbonation it was observed that the porosity of concrete decreases due to a highest molar volume of carbonation products in comparison to the volume of hydrates. For instance, the molar volume of $Ca(OH)_2$ is about 33.2 cm^3/mol while the molar volume of $CaCO_3$ is about 36.9 cm^3/mol which corresponds to an increase of 11%. The consequence of this difference was observed on cement pastes [2] and on concrete [3], essentially by Mercury Intrusion Porometry (MIP). For concrete, the difference of porosity between non carbonated and carbonated concrete is higher for concrete with low porosities and can attain 10% [3]. The same studies emphasized that carbonation also modifies the size distribution and it was generally observed a coarsening of the pore structure after carbonation. For instance, it was observed an increase of the volume of capillary pores after full carbonation of cement pastes mixed with different cements [2]. For the authors the coarsening of the pore structure may be associated with the formation of additional silica gel due to the decomposition of the C–S–H gel in the matrices following prolonged exposure to CO_2. Another study aiming to compare the effect of CO_2 concentration on the carbonation process demonstrated that the carbonation of C–S–H is significantly enhanced when high concentration is used (50% of CO_2 in this study) [4]. This consideration again supports the assumption that the reduction of porosity is due to the carbonation of C–S–H, but specifically at high pressure of CO_2.

The most important consequence of carbonation for reinforced concrete structures is the decrease of pH. In fact, it will lead to a destruction of the passive film which is formed by non-carbonated concrete around the reinforcing steel [5]. Then, in presence of oxygen and water the corrosion process can be initiated. Such corrosion products are expansive, so very quickly the concrete is mechanically damaged and a spalling of cover can be observed with the reinforcement

* Corresponding author.
E-mail address: cedric.payan@univmed.fr (C. Payan).

0008-8846/$ – see front matter © 2011 Elsevier Ltd. All rights reserved.
doi:10.1016/j.cemconres.2011.02.006

directly exposed to the environment. A very usual and reliable tool for assessing the phenomenon consists in measuring the carbonated depth by means of phenolphthalein [6]. But this needs to extract a sample or to drill the concrete which is slightly destructive. The aim of this paper is to provide a non-destructive indicator of carbonation, absolutely non intrusive, allowing the characterisation of an important quantity of points on large structures.

Chang et al. [7] have shown that for a Portland cement based concrete, standard mechanical indicator such as elastic modulus is slightly increased by carbonation. This evolution results in an increase of wave speed (linear indicator) to a 2% order magnitude. This poor sensitivity makes difficult the use of standard ultrasonic non destructive techniques to discern this pathology. Therefore, this study focuses on the potentialities of nonlinear ultrasonic indicators to discern the presence of carbonation.

The complex nonlinear mechanical behaviour of nonlinear mesoscopic media such as concrete [8] is not well described as regards physics. The origin of this so called "non-classical" nonlinearity is thought to come from the mesoscopic scale by the breakage/overlap phenomena of the cohesive properties of grains bonds, contact friction, and the opening/closing of micro-cracks. The nonlinear elastic theory, introduced in the 1960's by Landau and Lifchitz [9], provides no explanation about phenomena such as hysteresis, end point memory effect observed in these materials [10]. However, the introduction of a phenomenological stress strain relationship allows one to describe nonlinear elasticity [10]:

$$\sigma = K_0\varepsilon\left[1 + \beta\varepsilon + \delta\varepsilon^2 \ldots\right] + \alpha(\varepsilon, sign(\dot{\varepsilon})), \quad (2)$$

where K_0 is the elastic modulus, ε is the strain, β and δ represent the classical Landau and Lifchitz [9] type of nonlinearity, the dot relates to the time derivative of ε , and α is the non-classical nonlinear parameter. The *sign* function is equal to $+1$ when the time derivative of the strain is positive, and -1 when it is negative.

Extensive studies of the nonlinear parameter α, have highlighted its sensitivity to damage in various media and fields of applications, and in civil engineering for the monitoring of thermal damage [11] and mechanical damage [12,13]. The influence of structural changes in concrete such as water saturation [14] or alkali silicate reaction [15] has been recently shown. On the other hand, to our knowledge, no former studies have dealt with the effect of carbonation on the nonlinear behaviour of concrete.

In this study, to gain more insight into the influence of carbonation on the nonlinear behaviour of concrete, the nonlinearity of carbonated and non-carbonated samples are compared. The six samples under study are cylindrical cores (5 cm in diameter, 12 cm in length), extracted from slabs prepared in laboratory. Table 1 gives the samples characteristics. Note that the samples S1 and S2 have exactly the same composition but are manufactured in two different batches. The slabs destined to carbonation were exposed to particular conditions with 50% of CO_2 and a 65% relative humidity so as to accelerate their carbonation process. After acoustic measurements, the carbonation depth has been measured by spraying the samples with phenolphthalein after having split them.

To assess the nonlinearity, we develop an experimental device based on NRUS technique. It consists on the measure of the resonance frequency shift versus the resonance peak amplitude for a given resonance mode, while increasing excitation amplitude. From Eq. (2), the nonlinear α parameter is evaluated by $\Delta f/f_0 = \alpha.\Delta\varepsilon$ [11], where f_0 is the linear (low amplitude) resonant frequency and $\Delta\varepsilon$ the strain wave amplitude. Based on the method proposed by Chen et al. [15], the samples were clamped at one end with a chuck and let free at the other end in order to favour the first flexural mode (around 11 kHz for our samples). The vibrations are recorded via an accelerometer (B&K 8339), a signal conditioner (B&K 4416B) connected to an A/D converter (Picoscope 3204) and stored by a computer. The linearity of the acquisition system has been checked by using a cylindrical Aluminium sample. Each concrete sample was subjected to sixteen impacts with an intensity progressively increased.

Table 1
Concrete samples characteristics. C: Carbonated samples, NC : Non-carbonated samples.

Aggregate	Siliceous				Limestone	
Codification	S1-NC	S1-C	S2-NC	S2-C	L-NC	L-C
Carbonation depth (mm)	–	~15	–	~20	–	~30
Cement CEM I (kg)	370		370		370	
Sand 0/2 or 0/4 (kg)	774		774		474	
Gravel 4–14 or 10–14 (kg)	1069		1069			
Fine gravel 2/4 (kg)					284	
Gravel 4–6 (kg)					284	
Gravel 6–10 or 6–14 (kg)					854	
Water (kg)	212		212		214	

Fig. 1 shows that the distribution followed by the variation of the relative frequency shift versus the resonance peak amplitude (acceleration) is linear. The slopes of the dashed lines provide the nonlinear parameter for each sample. Note that the nonlinear parameter is a quantity proportional to α but not an absolute value. The summary of the whole set of results presented Fig. 2a highlights the impact of carbonation on the nonlinear parameter. The amplitude on the nonlinearity is not significantly affected by the concrete composition but we can notice that the L samples are less sensitive to the presence of carbonation.

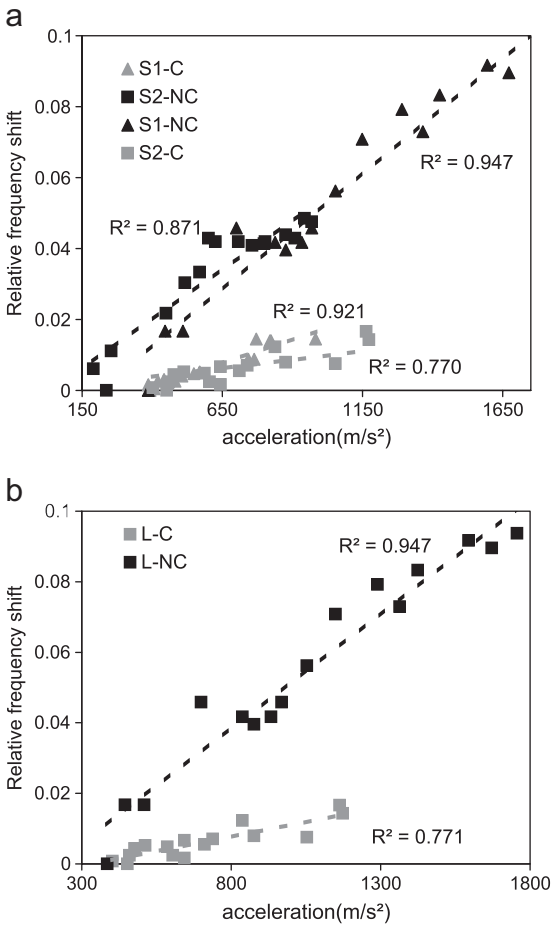

Fig. 1. Relative frequency shift as a function of amplitude. (a) Siliceous aggregates samples, (b) limestone aggregates samples. Dashed lines are the linear fits of these evolutions.

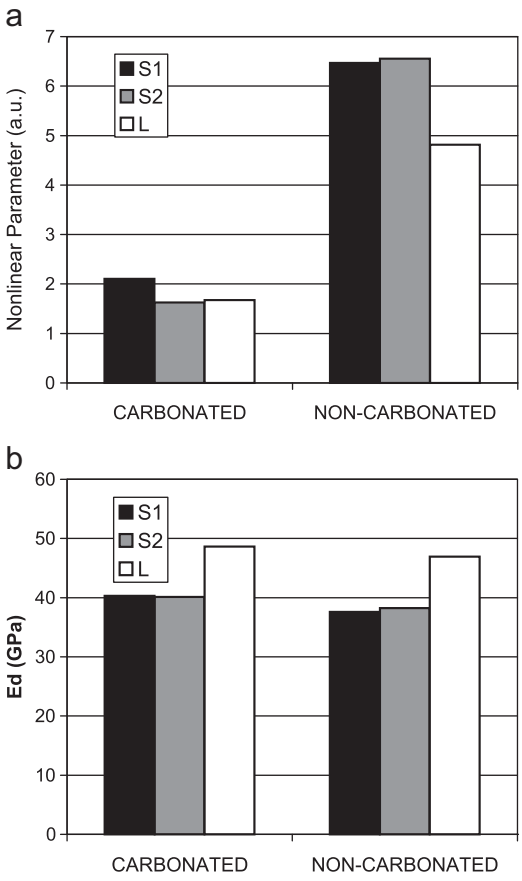

Fig. 2. Comparison of nonlinear (a) and linear (b) parameters of carbonated and non-carbonated samples.

The general decrease of the nonlinear parameter can be explained by the change of concrete microstructure as follow:

- SEM pictures from Chang et al. [7] show that cubic shapes of $CaCO_3$ are deposited in the concrete pores and micro-cracks. This should reduce the contact between grains and micro-cracks lips which is thought to be one of the main sources of nonlinear phenomena.
- It is worth noticing that C–S–H gel plays a key role in the viscoelastic nature of cement pastes [16]. Even if the linear global viscoelastic nature of concrete do not influence the measured nonlinearity (amplitude dependant), the presence of soft inclusions into hard matrix [10] is known to cause some non classical nonlinear phenomena. Since our samples have been carbonated in accelerated conditions, the carbonation of C–S–H gel is a central reaction that can contribute to the decrease of the nonlinear parameter.

For comparison, the dynamical Young modulus has been evaluated (see Fig. 2b) by shear and compressional wave velocities measurements. As in previous studies [7], the presence of carbonation affects slightly this indicator with a maximum increase of 5%, corresponding to a 100 m/s wave speed variation, while the mean variation of the nonlinear parameter reaches more than 300%.

Further to this qualitative study that shows that the presence of carbonation has a large influence on the nonlinear parameter, it can be considered as a good indicator for the detection of this pathology. To have a quantitative result, it would be worth studying the variations of the nonlinear parameter versus carbonation depth. That is uneasy because the sample response characterised by the NRUS method is not a local but a global one. Thus future study will be aimed at identifying a method able to provide the nonlinear parameter as a function of the wave propagating depth. In addition, that would be worth studying an extended carbonation depth scale, up to fully carbonated samples.

It is likely that the study of carbonation phenomenon within materials and rocks would have numerous applications in the CO_2 storage field, which is among the very important current topics [17].

Acknowledgements

We acknowledge Maxime Lion (EDF CEIDRE TEGG) for the carbonation depth measurements and Jean-Philippe Zardan (LCND, France) for helpful comments and discussions.

References

[1] K. Kobayashi, Y. Uno, Influence of alkali on carbonation of concrete, part 2 — influence of alkali in cement on rate of carbonation of concrete, Cem. Concr. Res. 20 (4) (1990) 619–622.
[2] V.T. Ngala, C.L. Page, Effects of carbonation on pore structure and diffusion properties of hydrated cement pastes, Cem. Concr. Res. 27 (7) (1997) 995–1007.
[3] M. Thiery, G. Villain, G. Platret, in: D.A. Lange, K.L. Scrivener, J. Marchand (Eds.), Effect of carbonation on density, microstructure and liquid water saturation of concrete, Advances in Cement and Concrete, 2003, pp. 481–490.
[4] N. Hyvert, A. Sellier, F. Duprat, P. Rougeau, P. Francisco, Dependency of C–S–H carbonation rate on CO_2 pressure to explain transition from accelerated tests to natural carbonation, Cem. Concr. Res. 40 (11) (2010) 1582–1589.
[5] H. Pourbaix, Atlas of electrochemical equilibria in aqueous solutions, Pergamon press, Oxford, 1966.
[6] R. Jones, R.K. Dhir, M.D. Newlands, A.M.O. Abbas, A study of the CEN test method for measurement of the carbonation depth of hardened concrete, Mater. Struct. 33 (2000) 135–142.
[7] J.J. Chang, W. Yeih, R. Huang, J.M. Chi, Mechanical properties of carbonated concrete, J. Chin. Inst. Eng. 26 (4) (2003) 295–308.
[8] R.A. Guyer, P.A. Johnson, Nonlinear mesoscopic elasticity: the complex behaviour of granular media including rocks, concrete, soil, Wiley, New York, 2009.
[9] L.D. Landau, E.M. Lifshitz, Theory of Elasticity, Pergamon Press, New York, 1959.
[10] R.A. Guyer, P.A. Johnson, Nonlinear mesoscopic elasticity: evidence for a new class of materials, Phys. Today 52 (1999) 30–35.
[11] C. Payan, V. Garnier, J. Moysan, P.A. Johnson, Applying nonlinear resonant ultrasound spectroscopy to improving thermal damage assessment in concrete, J. Acoust. Soc. Am. 121 (4) (2007), EL125-EL130,.
[12] P. Antonaci, C.L.E. Bruno, P.G. Bocca, M. Scalerandi, A.S. Gliozzi, Nonlinear ultrasonic evaluation of load effects on discontinuities in concrete, Cem. Concr. Res. 40 (2010) 340–346.
[13] J.-P. Zardan, C. Payan, V. Garnier, J. Salin, Effect of the presence and size of a localized nonlinear source in concrete, J. Acoust. Soc. Am. 128 (1) (2010), EL38-EL42.
[14] C. Payan, V. Garnier, J. Moysan, Effect of water saturation and porosity on the nonlinear elastic response of concrete, Cem. Concr. Res. 40 (2010) 473–476.
[15] J. Chen, A.R. Jayapalan, J.Y. Kim, K.E. Kurtis, L.J. Jacobs, Rapid evolution of alkali-sillica reactivity of aggregates using a nonlinear resonance spectroscopy technique, Cem. Concr. Res. 40 (2010) 914–923.
[16] A. Rouhollah, J.J. Beaudoin, L. Raki, Viscoelastic nature of calcium silicate hydrate, Cem. Concr. Comp. 32 (2010) 369–376.
[17] P.Y. Le Bas, P.A. Johnson, J.W. Carey, T.W. Darling, Probing mechanical change due to CO_2 exposure in carbonate sandstone applying Nonlinear Resonance Ultrasound Spectroscopy, American Geophysical Union, Fall Meeting, abstract MR41A-1832, 2009.

Effect of the presence and size of a localized nonlinear source in concrete

J.-P. Zardan, C. Payan,[a] and V. Garnier
Laboratoire de Caractérisation Non Destructive, Université de la Méditerranée IUT Aix-Provence, Avenue Gaston Berger, 13100 Aix en Provence, France
jean-philippe.zardan@univmed.fr; cedric.payan@univmed.fr; vincent.garnier@univmed.fr

J. Salin
EDF-R&D-STEP, 6 quai Watier, BP 49, 78401 Chatou, France
jean.salin@edf.fr

Abstract: The aim of the present letter is to identify the contribution of a macroscopic source of elastic nonlinearity in concrete, a medium which by nature is nonlinear, and belongs to the nonlinear mesoscopic class of materials. The influence of real, localized macro-cracks is characterized with respect to the intrinsic nonlinearity of the material. The influence of the size of the source on the amplitude of the measured nonlinearity is qualitatively demonstrated. A comparison is made between the changes in linear and nonlinear parameters.

PACS numbers: 43.25.Ba, 43.25.Dc, 43.25.Lj [MH]
Date Received: February 26, 2010 **Date Accepted:** May 12, 2010

1. Introduction

The complex, elastic nonlinear behavior of heterogeneous media such as rocks, granular media, or concrete has been extensively reported.[1] Various hypotheses have been proposed to explain its physical origin at different scales, and solutions have been proposed for its analysis. At the atomic scale using nonlinear elastic theory, introduced in the 1960s by Landau and Lifshitz,[2] and at other scales by the breakage/overlap phenomena of the cohesive properties of grains bonds (order scale $<\mu$m), contact friction, and the opening/closing of micro-cracks (order scale $>\mu$m). On a scale ranging from nano to millimeter, the presence of free water in the porosities or at the points of contact, also plays a major role,[3] through capillary, fluid/solid interaction, or lubricated contact phenomena. When placed under static load, these media exhibit hysteresis and discrete memory phenomena in their stress strain relationship.[4] In addition, under dynamic loads with high strain levels (order 10^{-6}), the elastic modulus decreases to a degree, which is not predicted by Landau's "classical" nonlinear theory of elasticity. This phenomenon is called fast dynamics or anomalous fast dynamics. When the load is removed, the material's initial elastic properties are slowly restored, over a period of time of the order of 1000 s. This phenomenon is referred to as slow dynamics. They are also thought to exhibit conditioning effect, resulting from the mutual coupling between slow and fast dynamics. These materials are said to belong to the nonlinear mesoscopic class or the nonequilibrium class.[1]

To date, this mechanical behavior is not accurately described, when compared with the physics of the relevant phenomena. However, the introduction of a phenomenological parameter allows the nonlinear elasticity as well as the material's hysteresis to be described:[4]

$$\sigma = K_0[1 + \beta\varepsilon + \delta\varepsilon^2 \ldots] + \alpha(\varepsilon, \mathrm{sign}(\dot{\varepsilon})), \quad (1)$$

where K_0 is the elastic modulus, ε is the strain, and β and δ represent the Landau and Lifshitz type of nonlinearity, the dot corresponds to the time derivative of ε, and α is the nonlinear

[a]Author to whom correspondence should be addressed.

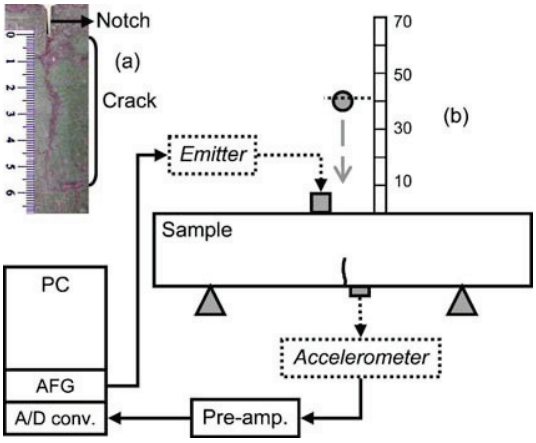

Fig. 1. (Color online) (a) Zoom on the crack (56.5 mm). (b) Experimental setup.

hysteretic parameter. The *sign* function is equal to +1 if the time derivative of the strain is positive, and −1 if it is negative. Although it does not describe slow dynamics, nor conditioning, this model allows the nonlinearity to be estimated.

The nonlinear parameter α has been widely studied and reported in the literature for its sensitivity to the presence of damage in a medium, for various fields of applications.[5,6] In all cases, it has a sensitivity often 10-fold greater than that of linear parameters such as the velocity or attenuation of waves. However, these studies deal with the sensitivity of the nonlinear parameter to diffuse damage, at the micro/meso scale. Recently, Antonaci *et al.*[7] show that a discontinuity has an effect on the nonlinear response of two concrete cubes coupled by cement joint.

For homogeneous materials which naturally have no, or very little hysteretic nonlinearity, a localized crack is clearly visible.[8] To the best of our knowledge, there have to date been no studies dealing with a nonlinearity source, localized in a medium which is itself nonlinear.

From this observation, in the present letter we wish to advocate the study of the potentiality of the nonlinear parameter α for the detection and gauging of a single macroscopic nonlinearity (macro-crack) in concrete, a naturally nonlinear medium. The challenge is to know whether the nonlinearity induced by the presence of a macro crack has a signature arising above the nonlinear response of the medium itself; and in this case, whether the amplitude of the nonlinearity can be correlated with the size of the source.

2. Experiments

We used four identical, parallelepiped concrete samples ($150 \times 150 \times 600$ mm^3). Each sample is pre-notched [Fig. 1(a)] at its center, in order to initiate the crack at that location. The different crack depths are obtained by means of four-point flexure loading. The press is driven, while measuring the crack openings with LVDT transducers. This procedure allows the loading to be stopped as soon as the desired crack depth is reached. It is important to note that the crack closes again when it is unloaded. It thus remains invisible to the naked eye. A penetrant inspection dye was used to reveal cracks [Fig. 1(a)]. A pre-notched, but non-cracked sample was used as a reference. The three other samples were cracked to depths of respectively 9 mm, 27.0 mm and 56.5 mm.

Estimation of the nonlinear parameter α is achieved by wave interaction. This method is based on the interaction of a high frequency wave with a low frequency wave. The low frequency allows mechanical energy to be injected, thereby exciting the nonlinearities. The monochromatic high frequency is used to inspect the medium subjected to this dynamic stress, and based on Eq. (1), is thus modulated in amplitude, giving rise to new frequency components. These, referred to as side bands, appear on either side of the high frequency (Fig. 2). In our experiments, the low frequency is produced by exciting the resonant frequency of the sample by

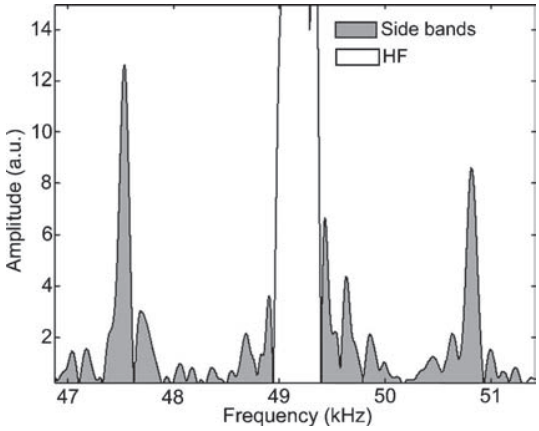

Fig. 2. Typical high frequency spectrum obtained in experiments.

means of mechanical impact. This method, introduced by Abeele *et al.*[6] is referred to by its authors as Nonlinear Wave Modulation Spectroscopy. The nonlinear parameter α is computed from the ratio of the energy contained in the side bands, to the product of the energy contained in the frequency components from which these are produced:

$$\alpha \propto \frac{E_{SB}}{E_{HF}E_{LF}}, \tag{2}$$

where E_{HF} and E_{LF} are the energies contained respectively in the high frequency (49 kHz) and in the low frequency components, E_{SB} is the energy contained in the side bands. These energies are estimated by the power spectrum illustrated Fig. 2 for E_{HF} and E_{SB}. The same treatment is performed in the low frequency band for E_{LF}.

The experimental setup is described in Fig. 1(b). The sample is placed on two linear supports separated by 40 cm. A steel ball (66 g) is released near to the center of the sample in order to favor excitation of the first flexural mode, which concentrates the strain energy in the cracked zone. The high frequency is generated by a piezoelectric transducer driven by a function generator in continuous mode at 49 kHz (EPA ARB 1410). Detection of the high and low frequencies is achieved using a high frequency accelerometer (B&K 8339), via a signal conditioner (B&K 4416B) connected to a 12 bit A/D converter (Picoscope 4424). The accelerometer and the transmitter are placed in semi-direct transmission configuration through the crack. This arrangement is chosen with respect to results obtained by Antonaci *et al.*[7] who illustrate the effect of transducers location on the measured nonlinearity. The ball is released from 7 increasing heights (10 … 70 cm), thus allowing us to estimate the α parameter from the slope of the straight line $E_{SB}=\alpha\ E_{HF}.E_{LF}$ [from Eq. (2)]. The experiments are carried out under stable atmospheric conditions of temperature and humidity.

3. Results

The variations in the nonlinear α parameter as a function of crack depth are shown in Fig. 3. The influence of the presence of a macro-crack on the nonlinear response can be clearly seen. Moreover, the depth of the crack plays a major role. For the purposes of comparison, we also illustrate the change in a linear parameter, the resonant frequency (1st flexural mode), at low amplitude. Whereas the linear parameter remains insensitive to presence and variations in crack depth, the relative change in the nonlinear parameter reaches a factor of 6. A repeatability study was carried out with a sample (27 mm crack), resulting in a relative uncertainty of 23% in the measured value. It is likely that this outcome is the consequence of the slow dynamics, which were not accounted for, and of the repeatability of the ball's impact on the sample. Perhaps, other meth-

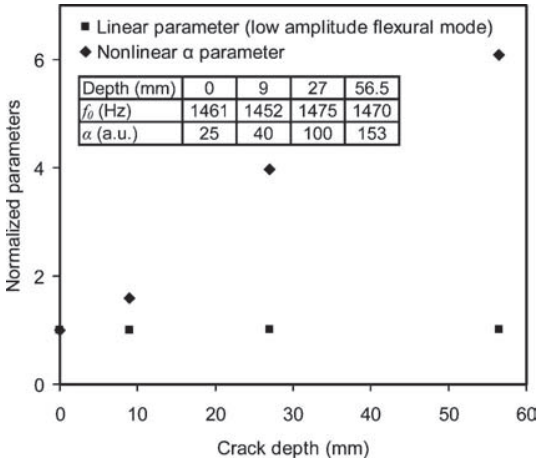

Fig. 3. Relative variation of both linear and nonlinear parameter as a function of crack depth.

ods such as Scaling Subtraction Method[9] or Nonlinear Resonant Ultrasound Spectroscopy[5] should provide much more accuracy, but imply the need of power amplification and the great coupling of transducers.

We note that the nonlinear α parameter varies quasi-linearly with crack depth, which suggests a relationship between the size of the crack and possible contacts between its edges, which can lead to hysteretic nonlinearities. The activation of the latter is rendered complex by the load distribution along, and at the extremities of the crack, as described by fracture mechanics.[10] This relationship is therefore to be verified in the near future by a larger set of samples (different geometries, materials…).

4. Conclusion and prospects

In the present letter we describe the strong contribution of a localized macroscopic nonlinear source on the response of a medium, which is naturally nonlinear at the mesoscopic scale. The influence of the size of the nonlinearity is also demonstrated. Future studies will aim at understanding the physical mechanisms governing the nonlinear response of a macro-crack, in order to provide a quantitative relationship between its characteristics and the amplitude of the nonlinearity. In addition, particular attention will be paid to improving the measurement methodology in order to reduce uncertainties. These results also open new avenues for the localization of nonlinear sources through the application of methods such as Time Reversal Nonlinear Elastic Wave Spectroscopy.[8] All of these approaches should ultimately lead to an assessment procedure, with possible applications in the fields of civil engineering, aeronautics (composites), geophysics (rocks) and medicine (bones).

Acknowledgments

The authors wish to thank Electricité de France (EDF) for financing this study and the Laboratoire Matériaux et Durabilité des Constructions (LMDC, Toulouse, France) for manufacturing the samples.

References and links

[1]R. A. Guyer and P. A. Johnson, *Nonlinear Mesoscopic Elasticity: The Complex Behaviour of Granular Media Including Rocks, Concrete, Soil* (Wiley, New York, 2009).
[2]L. D. Landau and E. M. Lifshitz, *Theory of Elasticity* (Pergamon, New York, 1959).
[3]C. Payan, V. Garnier, and J. Moysan, "Effect of water saturation and porosity on the nonlinear elastic response of concrete," Cem. Concr. Res. **40**, 473–476 (2010).
[4]R. A. Guyer and P. A. Johnson, "Nonlinear mesoscopic elasticity: Evidence for a new class of materials," Phys. Today **52**(4), 30–36 (1999).

[5]C. Payan, V. Garnier, J. Moysan, and P. Johnson, "Applying nonlinear resonant ultrasound spectroscopy to improving thermal damage assessment in concrete," J. Acoust. Soc. Am. **121**, EL125–EL130 (2007).
[6]K. Van Den Abeele, A. Sutin, J. Carmeliet, and P. A. Johnson, "Micro-damage diagnostics using nonlinear wave spectroscopy (NEWS)," NDT Int. **34**, 239–248 (2001).
[7]P. Antonaci, C. L. E. Bruno, P. G. Bocca, M. Scalerandi, and A. S. Gliozzi, "Nonlinear ultrasonic evaluation of load effects on discontinuities in concrete," Cem. Concr. Res. **40**, 340–346 (2010).
[8]T. J. Ulrich, P. A. Johnson, and R. A. Guyer, "Interaction dynamics of elastic waves with a complex nonlinear scatterer through the use of a time reversal mirror," Phys. Rev. Lett. **98**, 104301 (2007).
[9]C. L. E. Bruno, A. S. Gliozzi, M. Scalerandi, and P. Antonaci, "Analysis of elastic nonlinearity using the scaling subtraction method," Phys. Rev. B **79**, 064108 (2009).
[10]G. R. Irwin, "Analysis of stresses and strain near the end of a crack traversing a plate," Trans. ASME, J. Appl. Mech. **24**, 361–364 (1948).

Cement and Concrete Research 40 (2010) 473–476

Contents lists available at ScienceDirect

Cement and Concrete Research

journal homepage: http://ees.elsevier.com/CEMCON/default.asp

Effect of water saturation and porosity on the nonlinear elastic response of concrete

Cédric Payan *, Vincent Garnier, Joseph Moysan

Laboratoire de Caractérisation Non Destructive, Université de la Méditerranée, IUT Aix-Provence, Avenue Gaston Berger, 13625 Aix-en-Provence Cedex 1, France

ARTICLE INFO

Article history:
Received 14 May 2008
Accepted 29 October 2009

Keywords:
Characterization (B)
Spectroscopy (B)
Mechanical Properties (C)
Nonlinear acoustics

ABSTRACT

Nonlinear interaction of a monochromatic elastic wave with a low frequency should be a good tool for non-destructive evaluation of existing concrete structures. Nonlinear indicators have already proved efficient in detecting global damage by exhibiting a significant sensitivity regarding classical linear ultrasonic methods like wave speed or attenuation. However, it is necessary to understand the influence of some structural parameters such as porosity, stress state, or water saturation on the nonlinear processes. In this way, a recent model containing all of these potential contributors is presented in this paper. It is sustained by nonlinear interaction experiments in impact mode. This method reveals a great potential for in situ measurements with a low frequency propagating into the whole structure. We make use of a calibrated concrete sample's series, conditioned at different water saturation states, to quantify the influence of water content and porosity on the nonlinear response of concrete.

1. Introduction

Nonlinear acoustics based methods offer promising means of on site non-destructive testing of concrete structures. Linear indicators, like wave speed or attenuation, have a limited sensitivity and significant variations appear late in the microstructure evolution process. Often, nonlinear based methods present a sensitivity more than one order magnitude greater than linear ones. This great sensitivity regarding damage is hopeful but the influence of structural and environmental parameters on the nonlinear elastic properties of concrete should be understood. In case of in situ measurements, there is a need to uncouple the influence of damage and the one of structural or environmental conditions on the nonlinear indicators.

Concrete is a naturally highly heterogeneous and microcracked media. It exhibits a strong nonlinear elastic response, which can be physically explained by the classical Landau and Lifschitz theory [1] and at different scales by dislocations, rupture and recovery of intergrain cohesive bonds, porosity, clapping contacts, etc. As a result, concrete and cement based materials fall into the nonlinear nonequilibrium class [2] known to exhibit "nonlinear nonclassical effects" [3] termed slow dynamic and anomalous fast dynamic [2].

Fast dynamic relates the quasi-instantaneous decrease of the elastic modulus with increasing wave amplitude. The fact that this decrease is unexpected regarding the classical Landau theory, and that these materials also exhibit hysteresis and end point memory effects [3], has been termed "anomalous" or "nonclassical". Slow dynamic relates the slow, logarithmic in time, recovery of initial elastic properties after the disturbance (order 10^3–10^4 s in microcracked or damaged materials).

Van Den Abeele et al. show that this nonclassical nonlinear behaviour largely dominates the global nonlinear response of heterogeneous and microcracked materials such as concrete [4]. Thus, this behaviour can be phenomenologically described by a nonlinear elastic modulus [4,5]:

$$M = M_0[1-\alpha(\Delta\varepsilon + sign(\dot{\varepsilon})\varepsilon)], \quad (1)$$

where M_0 is the linear elastic modulus, α the nonlinear parameter, $\Delta\varepsilon$ the average strain wave amplitude, and the *sign* function equals $+1$ if the strain rate is positive and -1 if negative.

Nonlinear properties of materials can be non-destructively evaluated by harmonic generation, nonlinear wave interaction or nonlinear resonant ultrasound spectroscopy (NRUS). Nonlinear indicators reveal high potential for monitoring thermal [6], mechanical [7] damage, curing [8] of concrete or pre-stress state [9]. Nonlinear wave interaction is a good candidate for on site inspection, with a low frequency (LF) propagating in the whole structure. Moreover, this LF can be easily generated by a mechanical impact or by the natural solicitations of the structure like wind or traffic.

Assuming two harmonic sources, $S_1(t) = \Delta\varepsilon_1\cos(\omega_1 t)$ and $S_2(t) = \Delta\varepsilon_2\cos(\omega_2 t)$, in case of $\omega_2 \gg \omega_1$, the HF signal is amplitude modulated by the LF one. The resulting transmitted signal spectrum Fig. 1 provides means to extract the nonlinear α parameter [10] by the ratio of the fundamental amplitudes with the side lobes:

$$\alpha \propto \frac{A(\omega_2 \pm 2\omega_1)}{A(\omega_1)A(\omega_2)}. \quad (2)$$

This method is valid for monochromatic waves, and experimentally, the LF has to be sufficiently energetic to excite nonlinear phenomena.

* Corresponding author.
E-mail address: cedric.payan@univmed.fr (C. Payan).

0008-8846/$ – see front matter © 2009 Elsevier Ltd. All rights reserved.
doi:10.1016/j.cemconres.2009.10.021

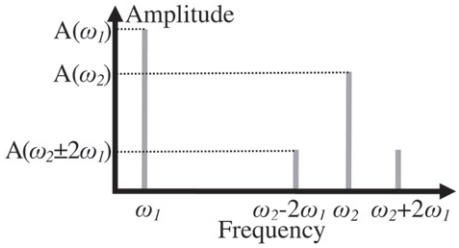

Fig. 1. Frequency spectrum result of nonlinear continuous wave's interaction.

Keeping in mind that the goal is on site inspection, generating high amplitude continuous waves seems to be difficult. Consequently, a simple apparatus will be employed with a mechanical impact that provides means to generate the high amplitude LF. However, the complexity of the resonant modes and the HF modulation deny using Eq. (2) to extract the nonlinear parameter (see Fig. 2). Van Den Abeele et al. [10] suggest and prove experimentally that the nonlinear parameter can be extracted not by the amplitude, but by the energy ratio:

$$\alpha \propto \frac{E_{SL}}{E_{LF}E_{HF}}, \tag{3}$$

where E_{SL}, E_{LF} and E_{HF} are respectively, the energy contained into side lobes, the LF, and the HF spectrum components.

Damage has a great influence on the nonlinear α parameter in concrete [6,7]. However, this large sensitivity may be also induced by environmental or structural parameters such as water saturation or porosity. In order to uncouple these potential contributors, a recent model containing all of them is described in the next section. Then, the experimental setup is presented and afterwards the study of these parameters' influence on the nonlinear response of concrete is achieved and discussed.

2. Model

Up to now, the most employed model was phenomenological, based on hysteresis description into the Preisach–Mayergoyz space [5]. The present model [11], quantitatively validated in sedimentary rocks, describes both slow and anomalous fast dynamic phenomena by the dependence of defect concentration on temperature and water saturation. Then, this concentration is related in the elastic modulus by:

$$M(c,\varepsilon,t) = M_0\left[1-f(s,T)\left(1+\frac{\delta c(\varepsilon,t)}{c_0}\right)\right], \tag{4}$$

where M_0 is the linear elastic modulus, $f(s,T)$ a function depending on water saturation (s) and temperature (T), δc is the instantaneous defect concentration variation and c_0 the initial defect concentration. Under an alternative strain drive (frequency ω and amplitude $\Delta\varepsilon$), the defect concentration variation associated with the excitation can be written to the first order:

$$\delta c_\sigma = \frac{\upsilon c_0 M_0}{kT}\Delta\varepsilon \sin(\omega t), \tag{5}$$

with k being the Boltzmann constant, T the temperature, and υ the typical volume of a single defect. Authors [11] assume that both fast and slow dynamic effects result from the interaction of two elastic subsystems: a fast elastic subsystem governed by the λ parameter in Eq. (6), and a slow elastic subsystem governed by the τ parameter in Eq. (6). It is interpreted by the defect concentration that evolves as a function of strain and time following a kinetic equation:

$$\frac{d(\delta c)}{dt} = -[\tau\theta(\delta c-\delta c_\sigma) + \lambda\theta(\delta c_\sigma-\delta c)](\delta c-\delta c_\sigma), \tag{6}$$

where λ is the defect creation rate, τ the defect annihilation rate, and θ is the Heaviside step function. Solving this equation at each t time allows estimating the instantaneous elastic modulus M (Eq. (4)). The large disparity between slow and fast dynamic time scales makes $\lambda \gg \tau$, and thus implies that solutions of Eq. (6) are stable and tend to track the amplitude of δc_σ [11].

The present study focuses on the fast dynamic effect that enables evaluating the nonlinear α parameter by the interaction of the HF continuous wave with the high amplitude LF. In the experiments, the typical wavelength of the LF is order 20 times larger than the HF one. Consequently, it can be reasonably assumed that experiments are performed in permanent regime ($\delta c \to \max(\delta c_\sigma)$). Therefore, assuming the temperature and water saturation are not influential during a single experiment, the elastic modulus can be written:

$$M = M_0\left[1-\frac{\upsilon M_0}{kT}\Delta\varepsilon\right]. \tag{7}$$

This equation demonstrates the analogy between the phenomenological model [5] and this one [11] (see Eq. (1)). The nonlinear α parameter can also be expressed:

$$\alpha = \frac{\upsilon M_0}{kT}. \tag{8}$$

Measuring the nonlinear α parameter of concrete samples for varying water saturation states will make possible the $f(s,T)$ function (Eq. (4)) determination. The next section presents performed experiments, results, and comments.

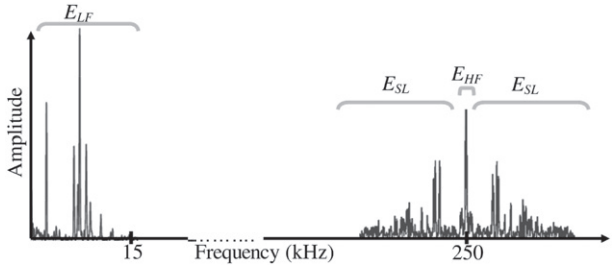

Fig. 2. Typical spectrum obtained in experiments.

3. Experiments

To study the influence of porosity and water saturation on the nonlinear behaviour of concrete, a battery of measurements is performed on a concrete sample ($50\times25\times12$ cm^3) series with a water cement ratio varying from 0.3 to 0.8 conditioned at 0, 40, 60, 80 and then 100% saturation. Five series of six identical samples are studied. All samples of the same series have the same water cement ratio (w/c) and composition. First, every sample is conditioned at 0% water saturation in a steam room at 80 °C during months with a very slow increase then decrease in temperature. Then, they are conditioned at 100% by immersing samples in water. Finally, a part of each series is conditioned at 40, 60 or 80% saturation in a carefully controlled atmosphere.

The experimental setup Fig. 3 consists of a monochromatic HF wave (250 kHz) transmitting through the sample. The LF wave is generated by the impact of a steel ball (24.8 g) unhanded from a constant height (20 cm). The resulting LF signal is recorded and synchronizes the acquisition.

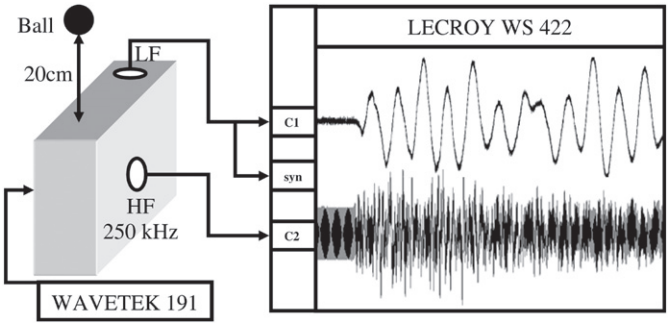

Fig. 3. Experimental apparatus.

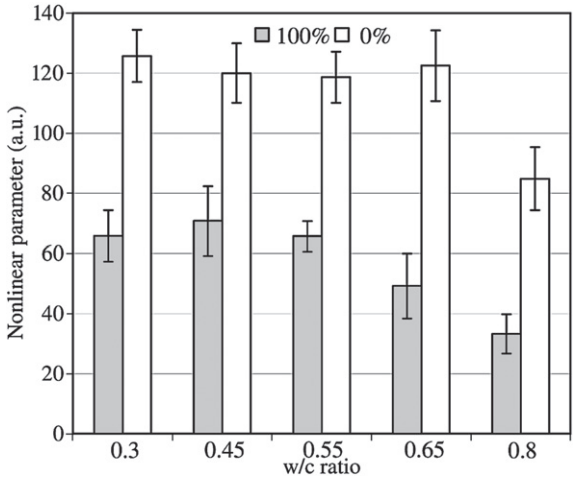

Fig. 5. Evolution of nonlinear α parameter as a function of w/c ratio for 0% (white) and 100% (grey) water saturation.

Van Den Abeele et al. [10] suggest estimating the energies by a time frequency analysis (Fig. 4a). Recorded signals have a 200,000 points length with a sampling frequency of 10 MHz. A sliding Blackman time window of 0.8 ms is used with a time step of 0.3 ms. In view of increasing frequency resolution, the power spectrum is obtained by a chirpZ transform (See [7] for more details) instead of standard FFT. The HF frequency spectrum is normalized with respect to the HF amplitude assumed to be a constant. The SL energy is estimated all around the 250 kHz spectrum component so as to take into account all the energy contained in the side lobes. The energies of the side lobes (E_{SL}) and of the low frequency (E_{LF}) are extracted in each time window. We then plot E_{SL} in function of E_{LF} (Fig. 4c). The signal processing is illustrated Fig. 4b. The analysis stops when the LF signal reaches noise level. The nonlinear parameter is obtained by the slope of the fitted line (Fig. 4c). The determination coefficient (R^2) of this fitting has a mean value of 0.84 over all experiments. The time frequency image (Fig. 4a), is obtained by a reduced time step (0.03 ms). We show it to illustrate the signal processing method and the decay of the side lobes and the low frequency in time after the impact but not used in this form for calculation.

Note that the resulting nonlinear parameter is not an absolute value, and depends on the transducers. Nevertheless, the same transducers are employed during experiments. Thus, the obtained values are comparable to each others, obtained in the same manner.

Each sample is conditioned at 0 then 100% water saturation. That is not the case of intermediate values for which only a portion of each series is conditioned at 40, 60 or 80%. For that reason, the influence of water cement ratio on the nonlinear α parameter is studied for these extreme water saturation states (see Fig. 5).

Two essential observations appear. The first is that porosity rate (w/c) does not seem having a notable influence on the nonlinear parameter into the usual w/c range ($0.3<w/c<0.65$ or $12.5<$porosity in %<16). The second one is that water saturation has a large influence on the nonlinear parameter, with a mean decrease of 102% between dried and wetted state.

The limited influence of porosity rate allows averaging the nonlinear parameter values of every sample over each saturation state, in the common w/c range. The result obtained in the full water saturation range is plotted in Fig. 6.

There are few measurements of the nonlinear α parameter for varying water saturation states in the literature [12,13], and none to our knowledge in concrete and cement based materials, meaning these values are the first reported for these materials. Without reference results and with the purpose of optimising the model, experimental points (♦ in Fig. 6) are fitted with an exponential type function (solid curve in Fig. 6). Experiments were conducted at constant temperature, so the f function (Eq. (3)) can be written as $f(s,T=cst)=K\exp(-2.3s^3+4.65s^2-3s)$, with s being the water saturation ($0<s<1$). These experiments provide

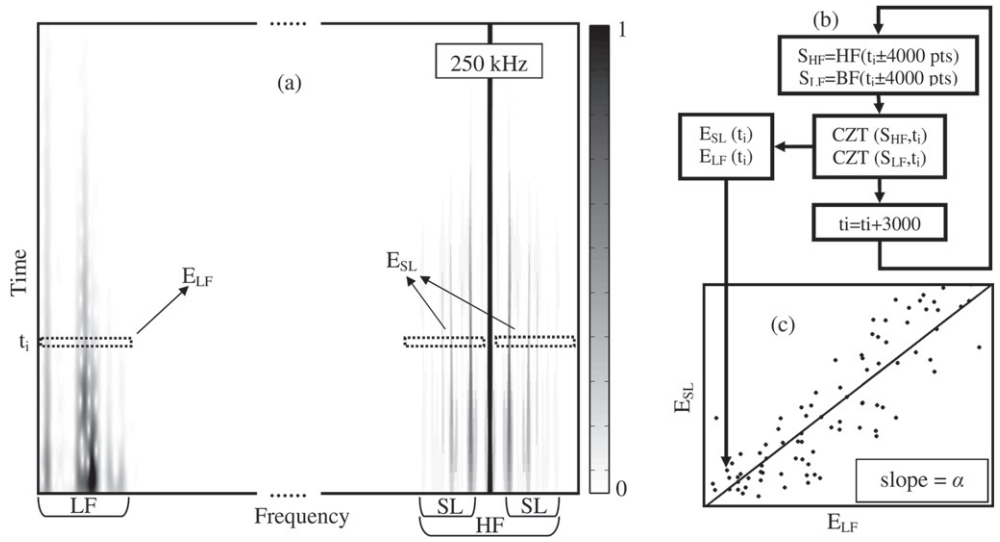

Fig. 4. Illustration of the signal processing method used to evaluate the nonlinear parameter. (a) Time frequency analysis. (b) Signal processing algorithm and (c) extraction of the nonlinear parameter for a concrete sample conditioned at 0% (log scale). Note that the frequency scale is not the same for the HF and LF components. The LF frequency axis has been stretched in order to clearly show the resonant modes.

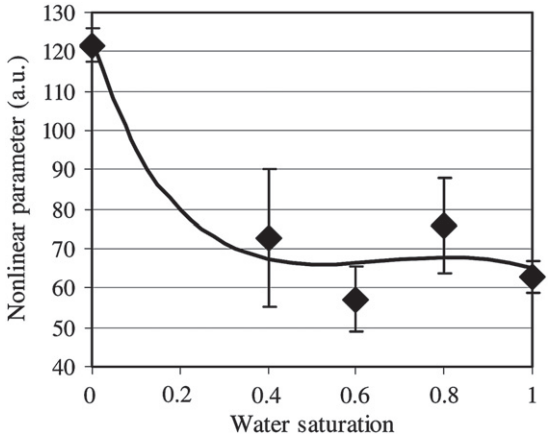

Fig. 6. Evolution of the nonlinear α parameter with water saturation ($0<s<1$). ♦ Present experimental values of the nonlinear parameter, error bars are the associated uncertainty. The solid line is the fit of experiments ($f(s,T=cst)$ function).

relative values, so K is a constant to be determined by a reference measurement. The determination coefficient of this fitting is $R^2=0.94$.

4. Discussion

The sudden decrease of the nonlinear α parameter from 0% saturation is qualitatively equivalent to observations made in chalk [12] but very different from those made in rocks such as sandstone or limestone [12,13]. As for rocks, in the low saturation range (up to 20%), authors assume that the increase of the nonlinear parameter is due to solid–fluid interactions. In the latter saturation range, capillarity condensation dominates.

This physical interpretation, valid for rocks with small pores (typically $<10\,\mu m$ for sandstone), does not hold in concrete. The porosity scale is much larger and varies from nano (smallest pores) to millimetre (microcracks). Moreover, in intact concrete, "natural" microcracks are located in mortar or at the aggregate/mortar interface but not into aggregates. Thus, it is not surprising that the evolution of the nonlinear behaviour of concrete is different from rocks.

Physically, we posit that the abrupt decrease of the nonlinear parameter in the low saturation range may be due to larger porosities. Dried rough contacts are very nonlinear and it can be presumed that like for granular media [14], a small quantity of fluid added is sufficient to greatly modify the mechanical behaviour. Water lubes scrapping microcracks, and as a result, the nonlinear behaviour falls. In the latter saturation range, like for rocks [13], the capillarity condensation phenomenon dominates in the smallest pores. These results show that in the typical w/c range, it is not the rate but the size of porosities that seems to manage the nonlinear response of concrete. This is in accordance with the presented modelling, where the influential parameter is v (Eq. (5)), the typical volume accounting by a single defect.

5. Conclusion and prospects

A promising method, with a high potential for on site inspection, is presented to extract the nonlinear parameter of concrete. The poor influence of porosity rate on the typical w/c range is shown and the influence of water saturation is quantified. A recent model that describes the influence of water saturation on the nonlinear response of concrete is presented and optimised.

Regarding the evolution of the nonlinearity with water saturation from 20% to 100%, the nonlinear parameter can be considered as constant in this range. As concrete structures are exposed to atmospheric conditions, between 30% and 100% of water saturation, nonlinear acoustics should not be used for water saturation characterization. However, this insensitivity makes this method a better candidate to process damage characterization.

Future research will be aimed at studying the influence of some concrete pathologies such as carbonization and chlorination on the nonlinear response of concrete.

Acknowledgements

This study was conducted in the French national project SENSO (Non-destructive evaluation strategy for concrete structures monitoring) supported by the French Research National Agency. Authors thank Paul Allan Johnson (Los Alamos National Laboratory, USA) for helpful comments and discussions.

References

[1] L.D. Landau, E.M. Lifshitz, Theory of Elasticity, Pergamon Press, New York, 1959.
[2] P.A. Johnson, Nonequilibrium nonlinear-dynamics in solids: state of the art, in: P.P. Delsanto (Ed.), Universality of Nonclassical Nonlinearity: Applications to Non-Destructive Evaluations and Ultrasonics, Springer, New York, 2006, pp. 49–69.
[3] P.P. Delsanto, M. Scalerandi, Modeling nonclassical nonlinearity, conditioning, and slow dynamics effects in mesoscopic elastic materials, Phys. Rev. B 68 (2003) 064107–064116.
[4] K. Van Den Abeele, J. Carmeliet, J. TenCate, P.A. Johnson, Nonlinear elastic wave spectroscopy (NEWS) techniques to discern material damage. Part II: single-mode nonlinear resonance acoustic spectroscopy, Res. Nondestruct. Eval. 12 (2000) 31–43.
[5] R.A. Guyer, P.A. Johnson, Nonlinear mesoscopic elasticity: evidence for a new class of materials, Phys. Today 52 (1999) 30–35.
[6] C. Payan, V. Garnier, J. Moysan, P.A. Johnson, Applying nonlinear resonant ultrasound spectroscopy to improving thermal damage assessment in concrete, J. Acoust. Soc. Am. 121 (4) (2007) EL125–EL130.
[7] K. Warnemuende, H.C. Wu, Actively modulated acoustic nondestructive evaluation of concrete, Cem. Concr. Res. 34 (2004) 563–570.
[8] J.C. Lacouture, P.A. Johnson, F. Cohen-Tenoudji, Study of critical behavior in concrete during curing by application of dynamic linear and nonlinear means, J. Acoust. Soc. 113 (2003) 1325–1332.
[9] C. Payan, V. Garnier, J. Moysan, P.A. Johnson, Determination of third order elastic constants in a complex solid applying coda wave interferometry, Appl. Phys. Lett. 94 (2009) 011904.
[10] K. Van Den Abeele, et al., Micro-damage diagnostics using nonlinear elastic wave spectroscopy (NEWS), NDT E Int. 34 (2001) 239–248.
[11] O. Vakhnenko, V. Vakhnenko, T.J. Shankland, Soft-ratchet modeling of end-point memory in the nonlinear resonant response of sedimentary rocks, Phys. Rev. B 71 (2005) 174103.
[12] P.A. Johnson, B. Zinszner, P. Rasolofosaon, F. Cohen-Tenoudji, K. Van Den Abeele, Dynamic measurements of the nonlinear elastic parameter α in rock under varying conditions, J. Geophys. Res. 109 (2004) B02202.
[13] K. Van Den Abeele, J. Carmeliet, P.A. Johnson, B. Zinzsner, Influence of water saturation on the nonlinear mesoscopic response of earth materials and the implications to the mechanism of nonlinearity, J. Geophys. Res. 107 (B6) (2002) 2121.
[14] T. Brunet, "Sound propagation in dry and wet granular materials," PhD thesis, Université de Marne la Vallée, France (2006).

Determination of third order elastic constants in a complex solid applying coda wave interferometry

C. Payan,[a] V. Garnier, and J. Moysan
Laboratoire de Caractérisation Non Destructive, Université de la Méditerranée, IUT Aix Provence, Avenue Gaston Berger, 13625 Aix-en-Provence Cedex 1, France

P. A. Johnson
Geophysics Group, Earth and Environmental Sciences Division, Los Alamos National Laboratory of the University of California, Los Alamos, New Mexico 875454, USA

(Received 25 September 2008; accepted 12 December 2008; published online 6 January 2009)

In this letter we describe the development of coda wave interferometry to determine acoustoelastically derived third order nonlinear coefficients of a highly complex material, concrete. Concrete, a structurally heterogeneous and volumetrically mechanically damaged material, is an example of a class of materials that exhibit strong multiple scattering as well as significant elastic nonlinear response. We show that intense scattering can be applied to robustly determine velocity changes at progressively increasing applied stress using coda wave interferometry, and thereby extract nonlinear coefficients. © *2009 American Institute of Physics*. [DOI: 10.1063/1.3064129]

Acoustoelasticity refers to measurement of material wave speed while progressively increasing stress and is the acoustical analog of photoelasticity in optics. Acoustoelastic-derived nonlinear properties of isotropic homogeneous materials have been obtained for at least half a century. Such measurements provide insight into the nano-to-mesoscale features that determine the elastic nonlinear response and can be used to obtain important physical characteristics, such as material modulus, and to predict material strength. Hughes and Kelly[1] derived expressions for the speeds of elastic waves in a stressed solid using Murnaghan's[2] theory of finite deformations and third order terms in the strain-energy expression. In complex materials, determining the third order constants accurately can be challenging due to significant intrinsic dissipation, as well as heterogeneity leading to strong wave scattering. Most Earth materials fall into this class, known as the nonlinear nonequilibrium class[3] or also the nonlinear mesoscopic class,[4] and an extreme example is concrete. It is highly complex both chemically and mechanically, is porous and permeable, heterogeneous, and highly elastically nonlinear.[5] In typical laboratory acoustic measurements on concrete, frequencies range from 200 kHz to 1 MHz. Associated wavelengths and typical aggregate sizes are equivalent, leading to strong multiple scattering. In this paper, we make use of the information imprinted in the wave form coda generated by multiple scattering. Applying successively larger stresses in combination with coda wave interferometry (CWI) provides the means to obtain velocity as a function of pressure and thereby extract the third order nonlinear coefficients.

The study of multiple scattering in the Earth (termed "coda" originally by Aki[6] more than 50 years ago) has been of interest to the geoscience community for at least 50 years.[7] Poupinet *et al.*[8] developed a method for monitoring velocity variations employing coda, termed "doublets" [referring to successive nearly identical signals from the same earthquake source]. The method was refined in laboratory studies by the addition of monitoring changes in attenuation by applying an active source by Roberts *et al.*,[9] where it was termed the "active doublet method." More recently developments have been aimed at detecting small changes in the scattering field due to modifications in the Earth's crust, including velocity changes induced by thermal stress or stress accumulation in the crust, and source location (earthquake localization). This more recent version of the method has been broadly termed "CWI."[10]

The purpose of this letter is to report the development of CWI in conjunction with incremental changes in the applied stress to a specimen, for determining the third order elastic constants of concrete, a method that can be applied to any solid but is particularly appropriate for complex solids. The essence of the method is to extract velocity and/or attenuation change between two time signals obtained at different stresses, by analyzing wave form coda changes. This is accomplished by cross-correlating moving time windows between time signals captured under different pressure conditions. By inverting results from a number of pressure increments the nonlinear coefficients are calculated. Recently CWI was applied to monitor thermally induced velocity variations in a solid,[11] as well as to observations of velocity changes in a sample of Berea sandstone.[12] In the following, we describe details of how the CWI method is implemented to extract the Murnaghan constants of a concrete sample, and how the CWI results are used to obtain the nonlinear coefficients. This is followed by results and analysis.

In the case of uniaxial loading in the 1 direction (1,2,3 designates an orthonormal basis), the strain-induced velocity variations in an initially isotropic medium can be analyzed to extract the Murnaghan third order elastic constants l, m, and n by a first order approximation assuming small changes in velocities.[13] We define here the acoustoelastic constants L_{ij} as $dV_{ij}/V_{ij}^0 = L_{ij} d\varepsilon$, where $\varepsilon = du/dx$ is strain in the 1 direction, V_{ij} the speed of a wave propagating in the i direction polarized in the j direction, and V_{ij}^0 designates the wave speed in the unstrained state.

[a]Electronic mail: cedric.payan@univmed.fr.
[b]Also at Geophysics Group, Earth and Environmental Sciences Division, Los Alamos National Laboratory of the University of California, Los Alamos, NM 875454, USA.

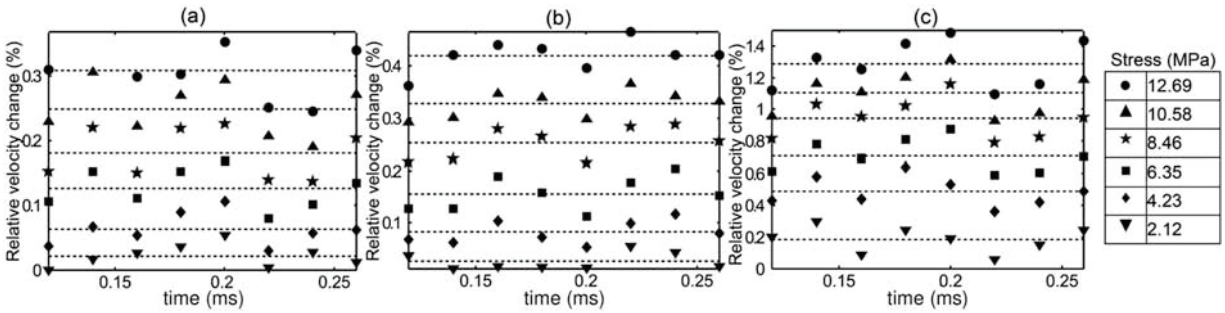

FIG. 1. Result of CWI. Dashed lines are the mean values of dV_{2j}/V_{2j}^0: (a) dV_{23}/V_{23}^0, (b) dV_{22}/V_{22}^0, and (c) dV_{21}/V_{21}^0.

Following a change in the material, by cross-correlating piecewise-in-time two wave forms w and w_0, a sequence of the correlation functions R^{t,t_w} can be determined. In the case of a velocity (modulus) perturbation, the distinct wave packets arrive at the receiver at different times with respect to the corresponding unperturbed packets. It has been demonstrated that the time of the maximum of R^{t,t_w} corresponds to the mean value of these timelags $\langle\tau\rangle_{(t,t_w)}$, where (t,t_w) refer to the center and the half width, of the evaluation time window, respectively, assuming the time window length $\Delta t=2t_w$ is small and $t\gg t_w$. The relative velocity variation in the entire perturbed signal is then $dV/V^0=-\langle t/\tau\rangle$, where $\langle\cdots\rangle$ refers to the average over all time windows.[10]

To summarize, in order to obtain the nonlinear coefficients we must measure the second order (linear) coefficients λ and μ and Poisson's ratio ν (as described below). We then must extract the velocity changes dV_{2j}/V_{2j}^0. The quantities dV_{2j}/V_{2j}^0 are obtained from CWI by three separate measures of wave speed, one compressional (dV_{22}), and two polarized shear wave measurements at 90° from each other (dV_{21}, dV_{23}). From these quantities L_{2j} are obtained by the relation $dV_{2j}/V_{2j}^0=L_{2j}d\varepsilon$. The uniaxial strain ε in the 1 direction is obtained from strain gauges. The third order coefficients l, m, and n are then calculated from Ref. 13. In contrast to classical acoustoelastic measurements, an advantage of this approach is that we do not require a velocity reference in the unstrained state, which is challenging to obtain in a highly scattering medium like concrete.

Our study is performed on a cylindrical concrete sample 160 mm long by 75 mm diameter. Destructive measurements of identical samples to that used in this study yielded a Young's modulus E of 42.39 GPa, an ultimate strength of 76.6 MPa, with a Poisson's ratio ν of 0.21. A hydraulic press (MTS 318.25) was programed to apply a stress protocol of six stress steps from 0 to 13 MPa, and strain gauges were attached to the sample in order to monitor the strain in the direction of loading. The loading protocol is determined so as not to exceed 30% of the ultimate strength in order to remain in the elastic regime.[14] Shear and compressional ultrasonic transducers 25 mm in diameter (500 kHz central frequency) are attached to the bar center using ultrasonic coupling gel and maintained in position applying constant force using springs located in holders. They are oriented facing each other on either side of the sample and shot in the 2 direction. The transducers are driven by a high voltage system using an impulse (Panametrics 5058PR). From these quantities L_{2j} are obtained by the relation $dV_{2j}/V_{2j}^0=L_{2j}d\varepsilon$. The third order coefficients l, m, and n are then calculated from Ref. 13.

Much empirical evidence[12,15] suggests that computing the intercorrelation function using ten signal periods is optimal. In order to satisfy the assumption $t\gg t_w$, we begin the coda analysis at $t=10t_w$ ($t=0.1$ ms, while compressional-mode time of flight is 14 μs.) and continue up to $t=0.26$ ms. In this manner the relative velocity variation is computed for eight nonoverlapping windows for each stress step. These eight windows provide a robust average of the relative velocity change. Figure 1 presents the results obtained for dV_{2j}/V_{2j}^0. We observe that the relative velocity variation dV_{2j}/V_{2j}^0 is a constant for each stress step and increases with stress. The fact that the velocity is constant over the entire signal duration at a given step indicates that compressional wave coda dominates the measurement for dV_{22} [Fig. 1(b)]. If it did not, the relative velocity variation would evolve to a different value associated with the shear waves. We benefit from the geometry of the sample in this regard. The measurements of P waves are performed by using P transducers as emitter and receiver. In this case we have a geometry such that the P waves are reflected at normal incidence back and forth across the sample multiple times. During this process, energy leaks away to the rest of the sample and is eventually converted to shear. Had we used the full coda, eventually one sees a change in dV_{22} due to the mode conversion.

For dV_{21} and dV_{23} shear waves are inputted into the sample, and shear wave coda dominates. The large difference

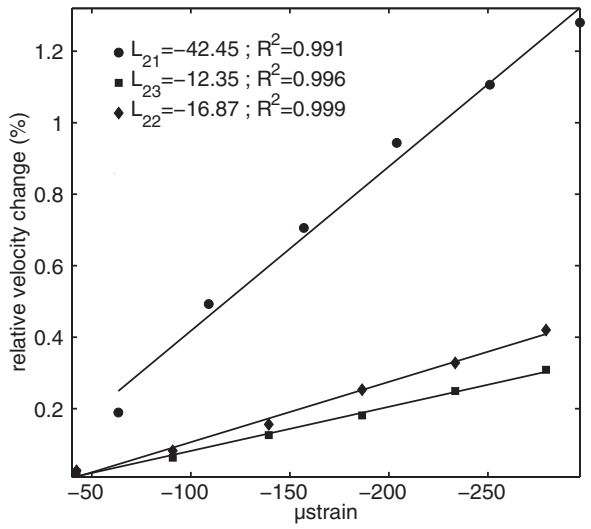

FIG. 2. Relative velocity changes vs quasistatic strain used for inversion of the third order constant (see Table I). Solid lines are the fits of experimental values. R^2 is the determination coefficient of the linear regression.

TABLE I. Third order elastic constants and the nonlinear parameter β in concrete.

l (GPa)	m (GPa)	n (GPa)	β
$-3007 \pm 2.8\%$	$-2283 \pm 1.2\%$	$-1813 \pm 3.4\%$	$-157 \pm 1.9\%$

between these two polarized shear waves implies that coda waves carry polarization information due to stress-induced birefringence. They carry it for the full coda used in the study. The relative uncertainty in dV_{2j}/V_{2j}^0 decreases from 12% to 2.3% with increasing stress. These values are similar to those reported in literature.[12] The repetitiveness in the pattern of the data scatter for each successive stress step suggests that the waves follow the same path. We posit that the scatter is due to local stress field inhomogeneities due to inclusions.

The fits of dV_{2j}/V_{2j} as a function of the measured strain for each applied load for the 2 direction are given in Fig. 2. The slopes of the fits are the acoustoelastic constants L_{ij} used for calculation of l, m, and n. The associated third order constants are shown in Table I. As in less complex materials such as iron or glass,[1] we observe that the most sensitive waves to stress are those which have particle displacement in the 1 direction, i.e., V_{21}.

The nonlinear behavior is not characterized by the absolute values of l, m, and n but by the ratio of second and third order elastic constants. A nonlinear one dimensional stress-strain relationship can be written as $\sigma = E\varepsilon(1+\beta\varepsilon)$, where the nonlinear β parameter can be written as a combination of Murnaghan's and Lame's elastics coefficients[16] by $\beta = 3/2 + (l+2m)/(\lambda+2\mu)$. The large negatives values reported in Table I are similar to those found in rocks such as quartz-rich sandstone, marble, and granite,[17–19] and are around two orders of magnitude greater than an ordinary nonlinear material such as steel or iron and pyrex glass.[1] For comparison, the nonlinear parameter β can be extracted from quasistatic measurements. Our results are in agreement with those reported in literature[20] for a concrete sample of similar composition.

We have presented a robust method by which to extract the third order nonlinear parameters, the Murnaghan coefficients, of concrete. CWI and acoustoelasticity have been combined to extract nonlinear parameters, and illustrate yet another of the rich applications of CWI. A unique aspect of the reported work is the development of a method by which to link the measured velocity changes dV/V^0 to L_{ij} in order to calculate the Murnaghan coefficients l, m, and n. The method is highly accurate and precise for determining the third order constants in any material, and is especially appropriate for materials exhibiting strong scattering. The approach overcomes much of the difficulty in acoustoelastic measurements of shear waves in particular, resulting in more accurate calculation of l, m, and n. We note that the method should work well for homogeneous materials with little internal scattering as long as there is sufficient scattering from the free surfaces.

This study was conducted in the ACTENA program supported by the French Research National Agency and Electricité De France (EDF). P.A.J. was supported by the U.S. DOE Office of Basic Energy Science. We acknowledge the Laboratoire de Mécanique et d'Acoustique (CNRS UPR 7051) for technical support. We thank M. Griffa for helpful comments.

[1] D. S. Hughes and J. L. Kelly, Phys. Rev. **92**, 1145 (1953).
[2] F. D. Murnaghan, *Finite Deformations of an Elastic Solid* (Wiley, New York, 1951).
[3] R. Guyer and P. A. Johnson, Phys. Today **52**(4), 30 (1999).
[4] P. A. Johnson, in *Universality of Nonclassical Nonlinearity: Applications to Non-Destructive Evaluations and Ultrasonics*, edited by P. P. Delsanto (Springer, New York, 2006), p. 49.
[5] J. C. Lacouture, P. Johnson, and F. Cohen-Tenoudji, J. Acoust. Soc. Am. **113**, 1325 (2003).
[6] K. Aki, J. Phys. Earth **4**, 71 (1956).
[7] K. Aki, J. Geophys. Res. **74**, 615 (1969).
[8] G. Poupinet, W. L. Ellsworth, and J. Frechét, J. Geophys. Res. **89**, 5719 (1984).
[9] P. M. Roberts, W. S. Phillips, and M. C. Fehler, J. Acoust. Soc. Am. **91**, 3291 (1992); P. M. Roberts, M. C. Fehler, P. A. Johnson, and W. S. Phillips, U.S. Patent No. 5369997 (December 1994).
[10] R. Snieder, A. Grêt, and H. Douma, Science **295**, 2253 (2002).
[11] E. Larose, J. De Rosny, L. Margerin, D. Anache, P. Gouédard, M. Campillo, and B. Van Tiggelen, Phys. Rev. E **73**, 016609 (2006).
[12] A. Grêt, R. Snieder, and J. Scales, J. Geophys. Res. **111**, B03305 (2006).
[13] D. M. Egle and D. E. Bray, J. Acoust. Soc. Am. **60**, 741 (1976).
[14] T.T. C. Hsu, Mater. Struct. **17**, 51 (1984).
[15] A. Grêt, R. Snieder, and U. Ozbay, Geophys. J. Int. **167**, 504 (2006).
[16] L. Ostrovsky and P. A. Johnson, Riv. Nuovo Cimento **24**, 1 (2001).
[17] P. A. Johnson and P. N. J. Rasolofosaon, J. Geophys. Res. **101**, 3113 (1996).
[18] A. Nur and G. Simmons, J. Geophys. Res. **74**, 6667 (1969).
[19] M. Zamora, Ph.D. thesis (in french), Paris VII University, 1990.
[20] I. E. Shkolnik, Cem. Concr. Compos. **27**, 747 (2005).

Applying nonlinear resonant ultrasound spectroscopy to improving thermal damage assessment in concrete

C. Payan, V. Garnier, and J. Moysan
Laboratoire de Caractérisation Non Destructive, Université de la Méditerranée, IUT Aix-en-Provence, Avenue Gaston Berger, 13625 Aix-en-Provence Cedex 1, France
cedric.payan@univmed.fr, garnier@iut.univ-aix.fr, moysan@iut.univ-aix.fr

P. A. Johnson
Geophysics Group, Earth and Environmental Sciences Division, Los Alamos National Laboratory, Los Alamos, NM 875454, USA
paj@lanl.gov

Abstract: Nonlinear resonant ultrasound spectroscopy (NRUS) consists of evaluating one or more resonant frequency peak shifts while increasing excitation amplitude. NRUS exhibits high sensitivity to global damage in a large group of materials. Most studies conducted to date are aimed at interrogating the mechanical damage influence on the nonlinear response, applying bending, or longitudinal modes. The sensitivity of NRUS using longitudinal modes and the comparison of the results with a classical linear method to monitor progressive thermal damage (isotropic) of concrete are studied in this paper. In addition, feasibility and sensitivity of applying shear modes for the NRUS method are explored.

PACS numbers: 43.25.Ba, 43.25.Gf, 43.35.Zc [MH]
Date Received: September 1, 2006 **Date Accepted:** January 17, 2007

1. Introduction

Nonlinear acoustics based methods offer promising means for nondestructive evaluation because of their sensitivity in comparison with linear methods (velocity, attenuation). Methods have been, and are currently, in development to apply nonlinear means to detect and image localized damage with, for example, time reversal nonlinear elastic wave spectroscopy (TR NEWS[1]), and distributed damage with NRUS[2] as well as other nonlinear methods. Concrete is a structural heterogeneous and microcracked material exhibiting strong elastic nonlinearity similar to rock[3] and geomaterials[4] in general, including granular media.[5] In addition to classical Landau and Lifschitz[6] theory, their nonlinear response may be physically explained at different scales by dislocations, rupture, and recovery of intergrain cohesive bonds, porosity, opening/closing of micro-cracks, etc. As a result, these materials exhibit hysteresis in their pressure-strain response, the phenomenon of slow dynamics, and are thought to also exhibit end point memory.[7,8] A phenomenological description based on the Preisach-Mayergoyz space representation describing both second- and higher-order nonlinearity and hysteretic behavior has been proposed.[7,8] Note that this model does not contain the slow dynamics (a time dependant recovery process of elastic properties occurring after a disturbance) present in these materials. A nonlinear and hysteretic modulus[9] in the stress strain relationship in one dimension can be written

$$M(\varepsilon,\dot{\varepsilon}) = M_0(1 - \beta\varepsilon - \delta\varepsilon^2 - \cdots - \alpha(\Delta\varepsilon + \mathrm{sign}(\dot{\varepsilon})\varepsilon)), \quad (1)$$

where M_0 is the linear modulus, ε is strain, $\dot{\varepsilon}$ the strain rate, β and δ the second and third order nonlinearity, α being the nonlinear hysteretic parameter, $\Delta\varepsilon$ the average strain amplitude, and the sign function equals +1 if the strain rate is positive and −1 if negative.

This model predicts a softening or hardening of the material with increasing driving amplitude depending on the signs of β, δ, and α. If the net effect is negative (as it is in geomaterials, for instance), the resonant frequency decreases as a function of wave amplitude. At large strain amplitude levels in these materials, much empirical evidence suggests that the nonlinear hysteretic behavior proportional to α dominates,[2] and a first order approximation gives

$$\frac{f_0 - f}{f_0} \approx \alpha \Delta\varepsilon, \tag{2}$$

where f_0 is the linear resonant frequency and f the resonant frequency for an increasing driving amplitude. The evaluation of this linear (slope α) relative frequency shift dependence with strain amplitude is the basis of the NRUS method.

Some studies have already explored the potential of nonlinear methods on evaluating the physical/mechanical properties of concrete. For instance, curing of concrete has been monitored by harmonic generation[10] and damage evaluation has been studied by the nonlinear wave modulation[11] method. NRUS has already been employed in mechanically damaged concrete,[12,13] providing promising results which indicate that the method has potential to monitor thermal damage.

NRUS on damaged concrete exploits longitudinal[13] (P) or flexural[12] mode to estimate the nonlinear α parameter.

To our knowledge, the nonlinear hysteretic behavior of concrete has not been studied applying shear (S) waves. Potentially, S waves propagating in nonlinear hysteretic material should be efficient for nondestructive evaluation.[14] We can reasonably expect that sliding of rough contacts at grain boundaries and microcracks lips may be hysteretic. Note that excitation of these phenomena take place in P modes by coupling between P and S waves due to Poisson effect, nonlinear processes,[15] and scattering[16] from inhomogeneities.

The aim of this paper is to study the evolution of concrete thermal damage applying NRUS and comparing the results to ultrasonic velocities. We then examine S wave sensitivity to thermal damage by applying the NRUS method for shear.

2. Thermal damage process of concrete

Concrete is a complex multiphasic solid material composed, before curing, of anhydrous cement, aggregates, sand, and water. Anhydrous cement is principally composed of silica (SiO_2), alumina (Al_2O_3), lime (CaO), and calcium sulphate ($CaSO_4$). Most of the contained aggregates are limestone and silica. The aggregate size is generally between 3 and 16 mm. Cohesion of concrete is guaranteed by a water cement ratio (w/c) of typically $0.3 < w/c < 0.6$. Chemical processes occur with heat generated during curing, producing an increase of porosity and mi-

Table 1. Chemical process occurring in concrete while increasing temperature. The top three lines are the temperature range studied here.

Temperature	Chemical process
$\rightarrow$105 °C	$\langle\langle$Free$\rangle\rangle$ water evaporation
$\rightarrow$300 °C	First step of dehydration. Breaking of cement gel and uprooting of water molecules into hydrated silicates
400$\rightarrow$500 °C	Portlandite decomposition: $Ca(OH)_2 \rightarrow CaO + H_2O$
600 °C	Structural transformation of quartz α into β—swelling of quartziferous aggregates
$\rightarrow$700 °C	Second dehydration step: dehydration of hydrated calcium silicates
$\rightarrow$900 °C	Limestone decomposition: $CaCO_3 \rightarrow CaO + CO_2$
1300 °C	Aggregates and cement paste fusion

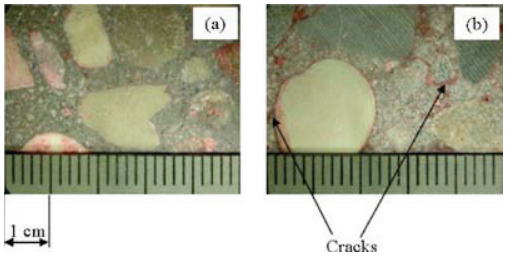

Fig. 1. (Color online) Macrography of intact sample (a) and thermally damaged sample (b) (Ref. 18).

crocracks. Thermal damage process of concrete is well known[17] and synthesized in Table 1. Evidence of cracking is obtained applying macrography[18] which provides the means for estimating the crack density (Fig. 1). For intact concrete we observe 10^3 cracks/m^2. For 200 °C thermally damaged concrete (held at temperature for 3 hours) we observe 33×10^3 cracks/m^2. These measures reveal two essential observations: (i) there is no preferential cracking direction validating our hypothesis of isotropic damage; (ii) most of cracks appear at the cement-aggregate interface and in the cement matrix but never inside the aggregates, following the chemical process described in Table 1 (the first aggregate transformation appears at 600 °C).

3. Experiments

Four samples were studied. The first is a reference (20 °C), while three others have been (1) heated for 3 hours, to 120 °C; (2) to 250 °C, and (3) to 400 °C, respectively. These samples are parallelepipeds of dimension $10 \times 10 \times 5$ cm. P wave transducers (Panametrics V1012, central frequency: 100 kHz) are glued (Salol) on both polished sides of the sample (Fig. 2) and driven by a function generator with high voltage output. In order to find the first compressional resonance mode, a P wave time of flight t measurement is performed. Due to the free surface boundary conditions, the resonant frequency is given by

$$f_0 = 1/2t. \tag{3}$$

For each amplitude (at least 7), a monochromatic tone burst is transmitted. The duration of the burst is selected so as to perform an RMS measurement at steady-state conditions (order Q-cycles, or about 100 cycles). The frequency of the tone burst is fixed around f_0 to obtain a resonance curve. The same scheme is repeated at each amplitude level. Figure 3 presents typical NRUS curves. The system linearity was checked with a reference steel sample using the identical system. We exploit measured RMS amplitude V_{RMS}, which is proportional to the strain amplitude

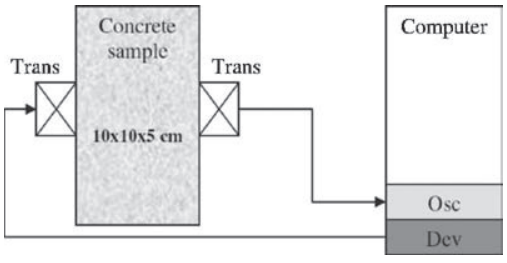

Fig. 2. Scheme of the NRUS experiment. Osc: A/D converter; Dev: high voltage ultrasonic device; Trans: Panametrics transducers (V1012 for P modes and V1548 for S modes).

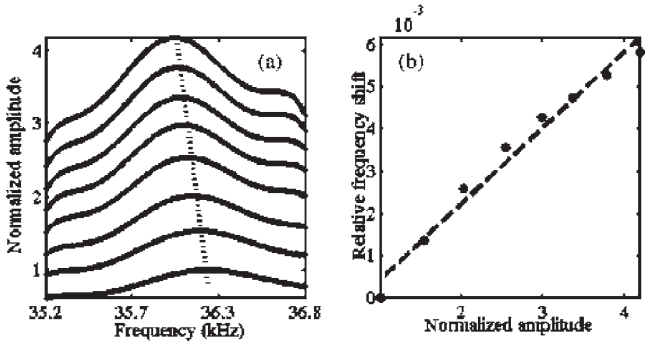

Fig. 3. 120 °C damaged sample frequency shift (a) and extraction of α from the slope of the frequency change with amplitude (b).

$$V_{\mathrm{RMS}} = K\Delta\varepsilon, \tag{4}$$

with K the transducer constant. The value of nonlinear parameter αK is obtained in Fig. 3 by Eq. (2).

In order to compare the sensibility of the NRUS with a linear parameter, velocity is obtained via the linear resonant frequency

$$\nu = 2Lf_0, \tag{5}$$

with L the length of the sample.

As expected, results show the high sensitivity of NRUS to thermal damage applying compression (Fig. 3). Its dynamic evolution is far greater than the classical linear method (Fig. 4). The relative variation of α is 230% while relative velocity variation is only 35%.

The implementation of S modes for NRUS follows the same scheme. The only difference is that the mode is selected so that the half wavelength corresponds to a third of the sample length (third bulk S-resonance mode). This mode is used in order to employ the S-wave transducers (Panametrics V1548, central frequency 100 kHz) near their central frequency, and to be

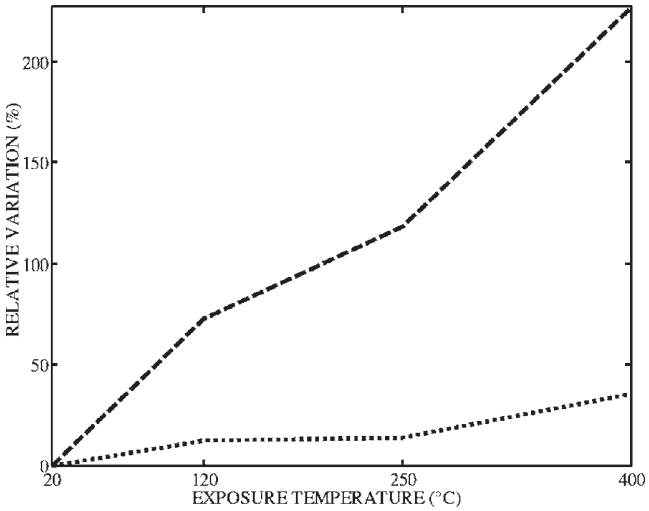

Fig. 4. Relative variation of nonlinear α parameter for first Young mode (dashed line) compared to relative variation of velocity (dotted line) in function of exposure temperature.

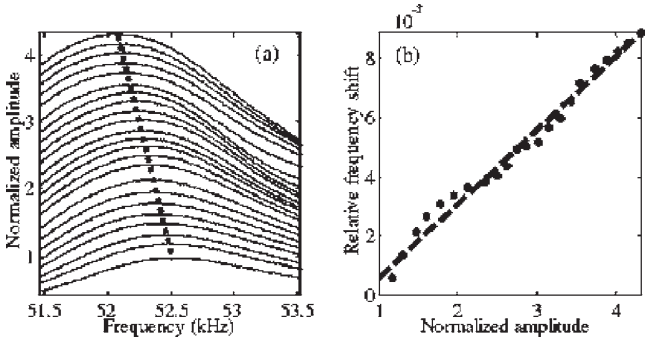

Fig. 5. 250 °C damaged sample frequency shift (a) and extraction of α parameter (b) in shear mode.

sure that the mode explored is the mode expected. Higher modes, for this particular geometry, are not exploitable because of increasing mode density with frequency. Time of flight measurement of S waves is more difficult because S transducers generate a small P wave as well (less than 30 dB/S wave) and concrete causes mode conversion by multiple scattering. Thus the arrival is masked by P-wave coda. For our frequency range (~50 kHz) and length of sample (~5 cm), it is nearly impossible to separate S and P waves. Therefore, the time-of-flight is measured at higher frequency (500 kHz) with another transducer (Panametrics V151).

The feasibility of applying S modes for NRUS method is achieved (Fig. 5). Moreover, sensitivity to thermal damage of the nonlinear α parameter extracted from the S mode (Fig. 5), is very close, less than 8% to that of the P one (Fig. 6).

Note that the fits of the change in frequency vs amplitude for extraction of α in both the compressional [Fig. 3(b)] and shear experiments [Fig. 5(b)] are not perfect, and could be fit with other functions. The shear result is particularly complex. In future experiments we will explore in more detail these behaviors and whether they may change with increasing damage. It may be that the simple model presented here based on hysteresis is only partially correct.

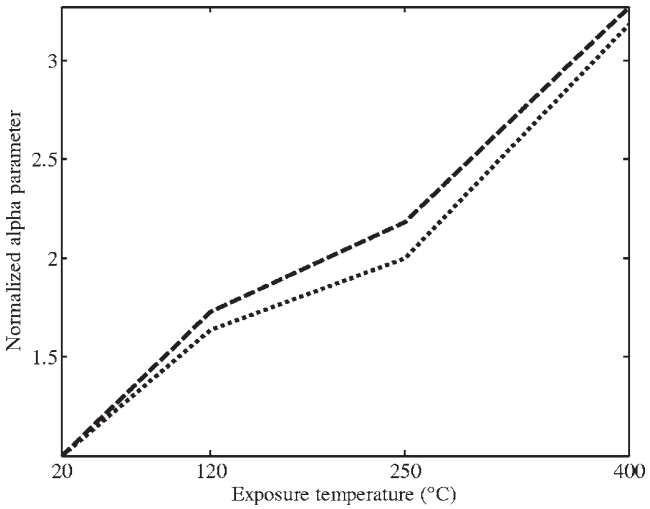

Fig. 6. Comparison of nonlinear α parameter for the P mode (dashed line) with the S mode (dotted line) as a function of exposure temperature.

4. Conclusions and prospects

The significant sensitivity of the nonlinear response to thermal damage in concrete is demonstrated. The method, when compared with linear velocity measurement, exhibits greater sensitivity which should be useful for nondestructive evaluation.

Shear modes have also been tested. Their feasibility for NRUS method and their sensitivity to thermal damage have been illustrated. Qualitative values of the nonlinear α parameter have been obtained for both P and S modes and their dynamic evolutions are very similar for this isotropic damage. Therefore, the same study should be performed to monitor the evolution of the P and S modes responses for different anisotropic mechanical states.

References and links

[1]T. J. Ulrich, P. A. Johnson, and A. Sutin, "Imaging nonlinear scatterers applying the time reversal mirror," J. Acoust. Soc. Am. **119**, 1514–1518 (2006).
[2]K. Van Den Abeele, J. Carmeliet, J. TenCate, and P. A. Johnson, "Nonlinear elastic wave spectroscopy (NEWS) techniques to discern material damage. Part II: Single-mode nonlinear resonance acoustic spectroscopy," Res. Nondestruct. Eval. **12**, 31–43 (2000).
[3]R. A. Guyer and P. A. Johnson, "Nonlinear mesoscopic elasticity: Evidence for a new class of materials," Phys. Today **52**, 30–35 (1999).
[4]L. Ostrovsky and P. A. Johnson, "Dynamic nonlinear elasticity in geomaterials," Riv. Nuovo Cimento **24**, 1–46 (2001).
[5]P. A. Johnson and X. Jia, "Nonlinear dynamics, granular media and dynamic earthquake triggering," Nature (London) **437**, 871–874 (2005).
[6]L. D. Landau and E. M. Lifshitz, *Theory of Elasticity* (Pergamon Press, New York, 1959).
[7]K. R. McCall and R. A. Guyer, "Equation of state and wave propagation in hysteretic nonlinear elastic material," J. Geophys. Res. **99**, 23887–23897 (1994).
[8]R. A. Guyer, K. R. McCall, and G. N. Boitnott, "Hysteresis, discrete memory, and nonlinear wave propagation in rock: A new paradigm," Phys. Rev. Lett. **74**, 3491–3494 (1995).
[9]K. Van Den Abeele, P. A. Johnson, and A. Sutin, "Nonlinear elastic wave spectroscopy (NEWS) techniques to discern material damage. Part I: Nonlinear wave modulation spectroscopy (NWMS)," Res. Nondestruct. Eval. **12**, 17–30 (2000).
[10]J. C. Lacouture, P. A. Johnson, and F. Cohen-Tenoudji, "Study of critical behavior in concrete during curing by application of dynamic linear and nonlinear means," J. Acoust. Soc. Am. **113**, 1325–1332 (2003).
[11]K. Warnemuende and H. C. Wu, "Actively modulated acoustic nondestructive evaluation of concrete," Cem. Concr. Res. **34**, 563–570 (2004).
[12]K. Van Den Abeele and J. De Visscher, "Damage assessment in reinforced concrete using spectral and temporal nonlinear vibration techniques," Cem. Concr. Res. **30**, 1453–1464 (2000).
[13]M. Bentahar, H. El Aqra, R. El Guerjouma, M. Griffa, and M. Scalerandi, "Hysteretic elasticity in damaged concrete: Quantitative analysis of slow and fast dynamics," Phys. Rev. B **73**, 014116 (2006).
[14]V. Gusev, C. Glorieux, W. Lauriks, and J. Thoen, "Nonlinear bulk and surface shear acoustic waves in materials with hysteresis and end-point memory," Phys. Lett. A **232**, 77–86 (1997).
[15]A. Goldberg, "Interaction of plane longitudinal and transverse elastic waves," Sov. Phys. Acoust. **6**, 306–310 (1960).
[16]V. V. Varadan and V. K. Varadan, "Scattering matrix for elastic waves. III. Application to spheroids," J. Acoust. Soc. Am. **75**, 896–905 (1979).
[17]N. A. Noumowé, "Effet de hautes températures (20 °C–600 °C) sur le béton. Cas particulier du BHP ("Effect of high temperatures (20 °C–600 °C) on high performance concrete")," Ph.D. thesis, INSA de Lyon, 1995.
[18]J. F. Chaix, "Caractérisation non destructive de l'endommagement de bétons: apport de la multidiffusion ultrasonore ("Nondestructive evaluation of concrete damage: Contribution of the ultrasonic multiple scattering")," Ph.D. thesis, Université de la Méditerranée, 2003.